

CONSEJO SUPERIOR DE INVESTIGACIONES CIENTÍFICAS

INSTITUTO DE CIENCIA DE MATERIALES DE MADRID

**LOW-TOXIC CHEMICAL SOLUTION DEPOSITION
METHODS FOR THE PREPARATION OF
MULTI-FUNCTIONAL $(\text{Pb}_{1-x}\text{Ca}_x)\text{TiO}_3$ THIN FILMS**

Ph.D Thesis

ÍÑIGO BRETOS ULLÍVARRI

Supervisor: Dra. M^a Lourdes Calzada Coco

UNIVERSIDAD AUTÓNOMA DE MADRID

MADRID, JUNE 2006

CONSEJO SUPERIOR DE INVESTIGACIONES CIENTÍFICAS

INSTITUTO DE CIENCIA DE MATERIALES DE MADRID

DEPARTAMENTO DE MATERIALES FERROELÉCTRICOS

**LOW-TOXIC CHEMICAL SOLUTION DEPOSITION
METHODS FOR THE PREPARATION OF
MULTI-FUNCTIONAL $(\text{Pb}_{1-x}\text{Ca}_x)\text{TiO}_3$ THIN FILMS**

**This thesis submitted in partial fulfillment of the requirements for the Degree of
European Doctor in Chemistry at the “Universidad Autónoma de Madrid”**

ÍÑIGO BRETOS ULLÍVARRI

Supervisor: Dra. M^a Lourdes Calzada Coco

DEPARTAMENTO DE QUÍMICA INORGÁNICA

UNIVERSIDAD AUTÓNOMA DE MADRID

MADRID, JUNE 2006

*A mis padres,
Rosa y "Buli"*

A Pilar

La presente Tesis Doctoral se ha realizado en el Departamento de Materiales Ferroeléctricos del Instituto de Ciencia de Materiales de Madrid (ICMM-CSIC) bajo la dirección de la Dra. M^a Lourdes Calzada Coco, gracias a la concesión de una beca del Programa de Formación de Personal Investigador (FPI) del Ministerio de Ciencia y Tecnología, asociada al proyecto de investigación “Láminas ferroeléctricas de alta permitividad para microdispositivos” (MAT2001-1564).

Muchas han sido las personas que durante estos cuatro años han formado parte, algunas quizás sin saberlo, de esta apasionante “novela científica” que hoy toca a su fin. A todos estos “Dramatis Personae” les dedico de corazón los siguientes párrafos, ya que sin ellos no hubiese sido posible acabar esta historia.

En primer lugar, tengo que agradecer a la Dra. M^a Lourdes Calzada su infatigable capacidad de trabajo y su constante dedicación durante todos estos años, por confiar en mí desde el primer día y por haberme dado la oportunidad de enriquecerme como científico y como persona gracias a las numerosas salidas al extranjero de las que pude disfrutar.

Mi agradecimiento a la Prof. Dra. Carmen Navarro del Departamento de Química Inorgánica de la Universidad Autónoma de Madrid (UAM), por aceptar ser mi tutora y por su ayuda con todos los trámites requeridos para presentar esta Tesis.

A la Dra. Lorena Pardo, que siempre ha tenido buenas palabras conmigo, por su sincero interés en la marcha de mi trabajo y su preocupación en los momentos más duros e inciertos de estos últimos meses.

Al Dr. Ricardo Jiménez, con quien he compartido tantos viajes y aventuras durante estos años, por todos esos buenos momentos que hemos pasado juntos y por toda su ayuda en las numerosas horas que hemos metido en el laboratorio de medidas eléctricas, donde he aprendido tantas cosas aparte de las meramente teóricas.

Al Dr. Jesús Ricote, por ser un modelo de científico a seguir, por ayudarme con la complicada estructura y microestructura de mis láminas y por las excelentes sesiones didácticas de las que he podido disfrutar.

Al Dr. Miguel Algueró, por su desbordante alegría y por haber animado tantas cenas de congreso con sus ingeniosos comentarios. Al Dr. Pablo Ramos, por interesarse siempre por la buena marcha de mi Tesis.

Quiero agradecer también al resto de los miembros del Departamento de Materiales Ferroeléctricos, comenzando por aquellos que ya se fueron, los ya jubilados Dres. Jesús Mendiola, Basilio Jiménez, Carlos Alemany y Enrique Maurer, por su grata predisposición a ayudarme y por su trato tan agradable que siempre me hizo sentir como en casa. Y siguiendo por los últimos en doctorarse, Dra. Rosalía Poyato, por preocuparse por mí durante mis primeros días en el departamento y Dr. Alberto Moure, por tantas conversaciones interesantes acerca de la vida, de la ciencia y sobre todo, de fútbol.

I would like to thankfully acknowledge Profs. Drs. Marlies K. Van Bael and Jules Mullens for accepting me in his group in the Laboratory of Physical and Inorganic Chemistry of the University of Hasselt at Diepenbeek (Belgium), from 1st March to 27th May 2005, within the framework of a short-term stay in a foreign laboratory granted by the FPI Program. Special thanks are due to Dr. An Hardy for her efficient and patient help with the fabrication of the films by the aqueous solution-gel method and to Dr. Dirk Van Genechten for his friendly teaching about some topics of sol-gel processing. I would like to express my sincere gratitude to the rest of the group for making my stay there a real pleasure; Heidi, Jorge, Marjoleine, Elke, Dirk Mondelaers, John, Annick, Ine and Kristof.

Agradezco también a mi antiguo tutor y profesor de carrera, Dr. Rafael Sirera, de la Universidad de Pamplona, la realización de las medidas de dispersión dinámica de luz (“Dynamic Light Scattering”) y sobre todo su constante apoyo a lo largo de estos años.

Agradezco al Dr. Javier García, del Centro Nacional de Aceleradores de Sevilla, la realización de las medidas de espectroscopía de iones retrodispersados (“Rutherford Backscattering Spectroscopy”), y su ayuda con la simulación de los resultados experimentales.

Mi agradecimiento también al Prof. Dr. Enrique Rodríguez-Castellón, de la Universidad de Málaga, por la realización de las medidas de espectroscopía de fotoelectrones (“X-ray Photoelectron Spectroscopy”) y su ayuda en la interpretación de los resultados.

I would like to thank Dr. Hervé Guillon for all his help with the experiments on thin films crystallisation at low temperatures by using the ultraviolet-assisted rapid thermal processor installed at the research+development department of JIPELEC-QUALIFLOW in Grenoble (France), during my stay in his group from 16th to 28th February 2003 inside the COST528 project “Low temperature processing of ferroelectric films for computer memories and piezoelectric applications”.

I am grateful also to Prof. Dr. Daniel Chateigner for introducing me to quantitative texture analysis of ferroelectric thin films at the “Laboratoire de Cristallographie et Sciences des Matériaux (CRISMAT), Ecole Nationale Supérieure d’Ingénieurs de Caen-Centre de Recherche (ENSICAEN)” associated with the “Centre National de la Recherche Scientifique (CNRS)” at Caen (France), from 13th to 25th June 2004 inside the 2004FR0030 project “Influence of the crystallographic texture on the properties of polycrystalline ferroelectric materials”. Specially thanks to him and to Dr. Magali Morales for the cultural weekend trip along the Normandy landing beaches, and also to Dr. Gérald Leclerc for taking care of me when I arrived at Caen.

I am grateful also to Prof. Dr. Antonio Sergio Bezerra Sombra for accepting me in his group in the “Laboratório de Telecomunicações e Ciência e Engenharia de Materiais-LOCEM-Departamento de Física da Universidade Federal do Ceará” at Fortaleza (Brasil), from 27th August to 18th September 2005, inside the 2004BR0003 project “Estudio de materiales con estructura perovskita de alta permitividad”. Special thanks are due to Prof. Dr. José Airton Cavalcante de Paiva for the help and warm care he bestowed on me.

Y no me puedo olvidar de todos los becarios del ICMM cuyas vidas han corrido paralelas a la mía durante estos cuatro años. En especial, agradezco; a Alberto y Rosalía, por tantos buenos momentos compartidos con ambos en el despacho 230 y en algún que otro congreso; a Jose, Celia y Elisa, por ser gente que merece la pena; a Carmen y Tere, por su alegría y buen humor; a Luismi, porque, aunque lamentablemente sólo coincidimos un año, durante ese año lo pasamos en grande; a Pilar Ferrer y Merce, por su gran simpatía.

A Álvaro, por haber vestido a esta Tesis de etiqueta, por tantas lecciones de informática y por haber compartido tantas risas. A Gonzalo (“Boludo”), Fer, Isabel, Carolina y Elvira por aguantar mis “payasadas”. Y a la última hornada de gente en llegar, a Alfonso, Virginia, Inma, María, Raquel y Abel, por haber traído nuevos aires al Instituto, por toda vuestra energía e ilusión.

También quiero agradecer a todos mis compañeros del fútbol de los miércoles, por disfrutar tanto jugando con vosotros todas las semanas. No daré la alineación, ya que nuestra plantilla se renueva año tras año, pero todos vosotros sabéis bien quiénes sois.

Y por supuesto a mis amigos de Vitoria, juntos todos desde preescolar, porque también habéis sufrido mi ausencia en estos últimos meses de la escritura, por vuestro apoyo y por tantas juergas corridas en Gasteiz. A Rodrigo (“KP”), Ricardo (“Ricart”), Miguel (“Palankas”), Eduardo (“Melón”), Alejandro (“Bogarde”), Iñigo (“Pepo”) y Juan Carlos (“Charlie”), por hacerme sentir “Orgullo Colega”.

Esta Tesis está especialmente dedicada a mis padres, por haberme apoyado y animado en todos mis proyectos durante toda mi vida. A mi madre, de quien seguro he heredado la capacidad de trabajo y el optimismo y alegría con que intento afrontar la vida. Y a mi padre, porque “las cosas, Íñigo, o se hacen bien o no se hacen...”. Gracias a vosotros soy lo que soy.

Y por supuesto, no habría podido acabar esta Tesis sin tu ayuda, Pilar. Tú me das la energía con la que afronto mi feliz existencia todos los días. Has estado siempre conmigo, en los buenos y malos momentos, en la difícil etapa de la escritura (que con tu ayuda ha sido un verdadero placer). Estoy orgulloso de tenerte a mi lado, “Meu”, ahora y siempre, contigo da igual dónde acabe, porque siempre me sentiré capaz de comerme el mundo.

Resumen

El titanato de plomo modificado con calcio, $(\text{Pb}_{1-x}\text{Ca}_x)\text{TiO}_3$ (PCT), es un material tipo perovskita cuya estructura cristalina y propiedades dieléctricas y ferroeléctricas varían con el contenido de Ca^{2+} . Las composiciones con sustituciones de Pb^{2+} por Ca^{2+} por debajo de 40 at% ($x \leq 0.40$) se han estudiado ampliamente en materiales de distinta conformación (monocristales, cerámicas densas o láminas delgadas). En el caso de la lámina, los métodos de depósito químico de disoluciones (“*Chemical Solution Deposition*”, CSD) han sido muy utilizados en la preparación de estas películas. Durante los últimos años, el estudio de composiciones de PCT con contenidos de Ca^{2+} mayores ($x > 0.40$) ha suscitado un gran interés investigador, tanto desde el punto de vista básico como aplicado. Estos trabajos se han llevado a cabo sobre polvos cerámicos o cerámicas densas de PCT. Sin embargo, hasta la fecha no se ha publicado ningún estudio sobre lámina delgada, debido fundamentalmente a las dificultades que entraña su preparación.

En la presente Tesis Doctoral se han desarrollado distintos procesos químicos en disolución para la fabricación de láminas delgadas de PCT con sustituciones de Pb^{2+} por Ca^{2+} desde 0 a 50 at% ($0 \leq x \leq 0.50$). Se ha puesto especial énfasis en el uso de tecnologías relativamente limpias (en comparación con las ya publicadas para este sistema) dadas las estrictas exigencias medioambientales surgidas durante los últimos años particularmente en la producción de materiales funcionales avanzados. En general, los métodos CSD conllevan riesgos a la salud y a la seguridad, derivados del uso de determinadas sustancias peligrosas reconocidas como altamente tóxicas (carcinógenos, teratógenos, etc), como por ejemplo algunos de los disolventes orgánicos y reactivos químicos normalmente empleados en el laboratorio. Además, los tratamientos térmicos de cristalización de materiales que contienen plomo en su composición producen la emisión de sustancias volátiles de elevada toxicidad.

Los procesos aquí propuestos para la preparación por CSD de láminas delgadas de PCT se basan en el uso de dos sistemas sintéticos; una ruta disolución-gel acuosa y una ruta sol-gel basada en dioles. En el primer caso, los disolventes orgánicos empleados tradicionalmente en sistemas sol-gel se han reemplazado por agua, disminuyendo así los riesgos a la salud y además los costes del procesado. Para ello, primero se preparó un complejo estable de peroxo-citrato de Ti(IV), el cual fue mezclado posteriormente con los reactivos de Pb^{2+} y Ca^{2+} (citratos) en la relación molar deseada para obtener disoluciones acuosas precursoras de $(\text{Pb}_{0.76}\text{Ca}_{0.24})\text{TiO}_3$ (PCT24) y $(\text{Pb}_{0.50}\text{Ca}_{0.50})\text{TiO}_3$ (PCT50). La concentración de Ca^{2+} afectó notablemente a la estabilidad de las disoluciones con el tiempo. Para preparar láminas delgadas, se tuvo que potenciar la hidrofiliadad de los substratos de $\text{Pt}/\text{TiO}_x/\text{Ti}/\text{SiO}_2/\text{Si}$, ya que la elevada tensión superficial del agua dificulta el óptimo mojado del substrato por la disolución acuosa, obteniéndose así recubrimientos defectuosos. Para ello se utilizó un tratamiento químico basado en las mezclas SPM y APM (Ácido sulfúrico/Peróxido de hidrógeno y Amoníaco/Peróxido de hidrógeno, respectivamente). Las láminas fueron cristalizadas a 650 °C con RTP (“*Rapid Thermal*

Processing”). Mediante medidas dieléctricas y ferroeléctricas se analizó la viabilidad de estas láminas para su uso en dispositivos microelectrónicos.

En el caso de la ruta sol-gel basada en dioles, se utilizaron como disolvente mezclas de 1,3-propanodiol y agua. La toxicidad de este diol es sensiblemente menor que la de compuestos como el 2-metoxietanol, xileno, etc, ampliamente utilizados en la preparación de láminas ferroeléctricas por CSD. Con este sistema químico, se ha estudiado la cristalización de láminas de PCT en función del contenido de Ca^{2+} y de la temperatura. Así pues, se observó que la temperatura de cristalización de la lámina era dependiente del contenido de Ca^{2+} , desplazándose la cristalización de la perovskita hacia temperaturas mayores a medida que aumentaba la concentración de Ca^{2+} en el sistema. Además, se pudo apreciar una inhibición de los fenómenos de nucleación y crecimiento en los cristales de PCT para altas concentraciones de Ca^{2+} . La estructura cristalina y la microestructura de las láminas de PCT también se vieron influenciadas por el contenido de Ca^{2+} . Las láminas de PCT24 depositadas sobre substratos de silicio presentaron una estructura tetragonal, con microestructuras formadas por granos de ~ 150 nm de diámetro. Por el contrario, las láminas de PCT50 mostraron una fase perovskita pseudocúbica con granos de mucho menor tamaño (~ 50 nm). En estas últimas láminas se detectaron reflexiones de tipo superred atribuidas al giro de los octaedros de TiO_6 , en concordancia con estudios previos realizados en cerámicas densas de la misma composición.

Con el sistema diólico, se desarrollaron varios métodos sintéticos diferentes para la obtención de precursores de PCT. Para ello se ensayaron distintos reactivos de calcio y distintos protocolos de reacción. De esta forma, se obtuvieron *soles reales* (rutas B y C) o *disoluciones* (ruta A), precursores de $(\text{Pb}_{1-x}\text{Ca}_x)\text{TiO}_3$. Los soles B y C resultaron ser más homogéneos que las disoluciones obtenidas a partir de la ruta sintética A. Como consecuencia, las láminas cristalinas de PCT derivadas de estos soles mostraron perfiles composicionales homogéneos, sin interfases resultantes de la reacción del sustrato y la película de PCT, y con microestructuras formadas por granos de mayor tamaño que en el caso de las láminas derivadas de la ruta A. Debido a esto, las láminas obtenidas a través de las rutas B y C presentaron unas mejores propiedades eléctricas. Así, en las láminas de PCT24 se obtuvieron polarizaciones remanentes (P_r) de $22.9 \mu\text{C}/\text{cm}^2$, coeficientes piroeléctricos (γ) de $1.2 \times 10^{-8} \text{ C}/\text{cm}^2\text{°C}$ y elevadas retenciones (el 90% de la polarización después de 10 años). Por el otro lado, en las láminas de PCT50 se midieron altas constantes dieléctricas a temperatura ambiente ($k' = 545$) y bajas densidades de corriente de fugas ($< 10^{-8} \text{ A}/\text{cm}^2$). Estos resultados mostraron la competitividad de estos materiales en posibles aplicaciones dentro de un amplio rango de dispositivos microelectrónicos, como Memorias Ferroeléctricas No Volátiles de Acceso Aleatorio (NVFeRAMs) o sensores de infrarojo en el caso de las láminas de PCT24, y Memorias Dinámicas de Acceso Aleatorio (DRAMs) o componentes de alta frecuencia para las láminas de PCT50.

Finalmente, otro reto de esta Tesis Doctoral fue la reducción de la temperatura utilizada en el tratamiento térmico de cristalización de las láminas. Esto tiene un doble interés; por una parte, evitar la emisión de plomo a la atmósfera durante el procesado del material; y por otra, utilizar temperaturas de fabricación compatibles con las empleadas en la tecnología del silicio (facilitando así la integración del material ferroeléctrico en el dispositivo microelectrónico). La técnica empleada con este fin ha sido el depósito fotoquímico de disoluciones (“*PhotoChemical Solution Deposition*, PCSD”), también llamado “*ultraviolet (UV) sol-gel photoannealing*”, que utiliza disoluciones precursoras fotosensibles y RTP asistido por luz ultravioleta. De esta forma, se obtuvieron láminas cristalinas de PCT24 y PCT50 con estructura perovskita a 450 y 500 °C, respectivamente, en atmósferas de aire u oxígeno. En las láminas de PCT24 se midieron ciclos de histéresis ferroeléctricos con valores de P_r de 11 $\mu\text{C}/\text{cm}^2$. Para las láminas de PCT50 se obtuvo una transición difusa tipo relaxor con valores de k' relativamente altos a temperatura ambiente (179). Estas propiedades avalan el posible uso de estos materiales en dispositivos multifuncionales. La respuesta eléctrica de las láminas mejoró sensiblemente cuando el procesado por PCSD se llevó a cabo en atmósfera de oxígeno. Aquí, la foto-excitación de los orgánicos contenidos inicialmente en la película amorfa depositada unida a un fenómeno de ozonolisis, permite disminuir el número de defectos (vacantes, subóxidos, etc) del material dando lugar a láminas con unas mejores propiedades dieléctricas y ferroeléctricas, y por ello más competitivas para su uso en dispositivos microelectrónicos.

Abstract

Calcium modified lead titanate, $(\text{Pb}_{1-x}\text{Ca}_x)\text{TiO}_3$ (PCT), is a perovskite-type material whose crystalline structure and dielectric and ferroelectric properties are influenced by the Ca^{2+} content. Compositions with substitutions of Pb^{2+} by Ca^{2+} below 40 at% ($x \leq 0.40$) have been widely studied in materials of different form (single crystals, bulk ceramics or thin films). In the case of the film, Chemical Solution Deposition (CSD) methods have been highly used in the preparation of these coatings. During the last years, a great deal of research has arisen from the study of PCT compositions with larger Ca^{2+} contents ($x > 0.40$), either from the basic or practical point of view. These works have been carried out on PCT ceramic powders or bulk ceramics. However, studies on thin films have not been reported until the present time mainly due to the difficulties that involves their preparation.

In the present Ph.D Thesis, different CSD approaches have been developed for the fabrication of PCT thin films with substitutions of Pb^{2+} by Ca^{2+} from 0 to 50 at% ($0 \leq x \leq 0.50$). Special emphasis has been placed on the use of relatively clean technologies (as compared with those already reported for this system) due to the stringent environmental requirements arisen during the last years in the production of advanced functional materials. In general, CSD methods involves healthy and safety risks derived from the use of certain hazard substances recognised as highly toxic (carcinogens, teratogens, etc), such as some of the organic solvents and chemical reagents usually employed in the laboratory. Furthermore, the thermal treatments carried out for the crystallisation of materials that contain lead in their composition lead to the emission of hazardous substances to the atmosphere.

The processes here proposed for the preparation of PCT thin films by CSD are based on the use of two synthetic systems, an aqueous solution-gel route and a diol-based sol-gel route. In the first case, the hazardous organic solvents usually employed in sol-gel chemistry are totally replaced by water, thus reducing healthy risks and moreover the costs of the technique. A stable peroxo-citrato complex of Ti(IV) was first synthesised and combined next with the Pb^{2+} and Ca^{2+} reagents (citrates) in the desired molar ratio to obtain $(\text{Pb}_{0.76}\text{Ca}_{0.24})\text{TiO}_3$ (PCT24) and $(\text{Pb}_{0.50}\text{Ca}_{0.50})\text{TiO}_3$ (PCT50) precursor aqueous solutions. The Ca^{2+} concentration highly affected the stability of the solutions with time. In order to prepare thin films, the hydrophilicity of the Pt/TiO_x/Ti/SiO₂/Si substrates had to be enhanced, since the high surface tension of water prevents the correct wetting of the substrate by the aqueous solution, and therefore defective coatings are obtained. A chemical treatment, based on SPM and APM mixtures (Sulphuric acid/hydrogen Peroxide and Ammonia/hydrogen Peroxide mixtures, respectively) was used to overcome this problem. Films were crystallised at 650 °C by Rapid Thermal Processing (RTP). The feasibility of these films for their use in microelectronic devices was analysed through dielectric and ferroelectric measurements.

In the case of the diol-based sol-gel process, mixtures of 1,3-propanediol and water were used as solvent of the reactions. The toxicity of this diol is considerably lower than that of the compounds widely used in the preparation of ferroelectric thin films by CSD (2-methoxyethanol, xylene, etc). With this chemical system, the crystallisation of the PCT films has been studied as a function of the Ca^{2+} content and of the temperature. Thus, it was observed how the crystallisation temperature of the film was dependent on the Ca^{2+} content, delaying the crystallisation of the perovskite towards higher temperatures as the Ca^{2+} concentration in the system increased. Furthermore, nucleation and growth phenomena of the PCT crystals seemed to be hindered for large Ca^{2+} concentrations. The crystal structure and microstructure of the PCT films were also influenced by the amount of Ca^{2+} content. A tetragonal structure was detected in the PCT24 films, with microstructures formed by grains of ~ 150 nm diameter. On the contrary, the PCT50 films showed a pseudocubic perovskite phase with grains of much lower size (~ 50 nm). In these films, superlattice reflections ascribed to the tilting of TiO_6 octahedra were detected, in agreement with previous studies carried out on bulk ceramics of the same composition.

Several diol-based sol-gel synthetic methods were developed for the preparation of the PCT precursor solutions. To this aim, different calcium reagents and synthetic pathways were tested. Thus, stable PCT *real sols* (routes B and C) or *solutions* (route A) were obtained. Sols derived from routes B and C resulted more homogeneous than solutions obtained through the route A. Consequently, the PCT crystalline films derived from the sols presented homogeneous compositional profiles, with no interfaces resulting from reactions between the substrate and the PCT film, and microstructures formed by larger grain sizes when compared with the films derived from the route A. This led to improved electrical properties in the films obtained through the routes B and C. Remanent polarisations (P_r) of $22.9 \mu\text{C}/\text{cm}^2$, pyroelectric coefficient (γ) of $1.2 \times 10^{-8} \text{ C}/\text{cm}^2\text{°C}$ and a large retention (90% of polarisation after 10 years) were obtained in the PCT24 films. On the other hand, high dielectric constant at room temperature ($k' = 545$) and low leakages current densities ($< 10^{-8} \text{ A}/\text{cm}^2$) were measured for the PCT50 films. The results show the competitiveness of these materials for possible applications in a wide range of microelectronic devices, such as Non-Volatile Ferroelectric Random Access Memories (NVFeRAMs), infrared sensors and MicroElectroMechanical Systems (MEMS) in the case of the PCT24 films, and Dynamic Random Access Memories (DRAMs) and high-frequency components for the PCT50 films.

Finally, another challenge of this Ph.D Thesis was the reduction of the processing temperature for the crystallisation of the films. This has two-fold interests; first, to avoid the lead emission to the atmosphere during the material processing; and second, to use processing temperatures compatible with those employed in the silicon IC (Integrated Circuit) technology (thus making possible the integration of the ferroelectric material with the microelectronic device). PhotoChemical Solution Deposition, PCSD (also called

ultraviolet (UV) sol-gel photoannealing) has been the technique used to this aim, which uses photo-sensitive precursor solutions and UV-assisted RTP. Thus, full-perovskite PCT24 and PCT50 films were prepared at 450 and 500 °C, respectively, in air or oxygen atmosphere. Well-defined ferroelectric hysteresis loops were measured in the PCT24 films, with P_r values of $11 \mu\text{C}/\text{cm}^2$. For the PCT50 films, a diffuse transition with a relaxor-like character and relatively high k' values at room temperature (179) was obtained. These properties fulfill the possible use of these materials in multifunctional devices. Furthermore, the electrical response of the films was improved when the processing was carried out in oxygen atmosphere. Here, the photo-excitation of the organics joined to a phenomenon of ozonolysis promotes the removing of defects (vacancies, suboxides, etc) from the material, giving rise to enhanced dielectric and ferroelectric responses, and therefore more competitive for their use in microelectronic devices.

TABLE OF CONTENTS

AGRADECIMIENTOS/ACKNOWLEDGMENTS.....	i
RESUMEN.....	v
ABSTRACT.....	ix
LIST OF FIGURES.....	xvii
LIST OF TABLES.....	xxiii
CHAPTER I. INTRODUCTION.....	
1.1. INTRODUCTION AND PURPOSE OF THE WORK.....	3
1.2. THEORY AND LITERATURE REVIEW.....	7
1.2.1. Basic concepts of dielectrics and ferroelectrics.....	7
1.2.2. Structure and properties of Ca ²⁺ modified PbTiO ₃ perovskite bulk materials.....	13
1.2.3. From ferroelectric bulk ceramics to thin films.....	20
1.2.4. Applications of ferroelectric thin films.....	21
1.2.4.1. Computer memories.....	22
1.2.4.2. High-frequency components.....	23
1.2.4.3. Infrared sensors.....	24
1.2.4.4. MicroElectroMechanical Systems (MEMS).....	25
1.2.5. Preparation techniques of ferroelectric thin films.....	25
1.2.5.1. Sputtering techniques.....	27
1.2.5.2. Laser ablation.....	27
1.2.5.3. Chemical vapor deposition.....	28
1.2.5.4. Chemical solution deposition.....	29
1.2.6. Motivation to fabricate PCT thin films by CSD.....	36
1.2.7. Low-toxic CSD methods.....	38
1.2.8. PhotoChemical solution deposition.....	42
CHAPTER II. EXPERIMENTAL METHOD.....	
<i>PART 1: CALCIUM MODIFIED LEAD TITANATE (PCT) PRECURSOR SOLUTIONS</i>	
2.1.1. SYNTHESIS OF THE PRECURSOR SOLUTIONS.....	49
2.1.1.1. Experimental setup.....	49
2.1.1.2. The aqueous solution-gel synthetic route.....	51
2.1.1.3. The diol-based sol-gel synthetic route.....	52
2.1.1.3.1. Incorporation of Ca ²⁺ through a calcium acetate water solution.....	53
2.1.1.3.2. Incorporation of Ca ²⁺ through a calcium acetylacetonate water solution.....	54
2.1.1.3.3. Incorporation of Ca ²⁺ through a calcium	

acetate or calcium acetylacetonate diol solution	55
2.1.1.3.4. Incorporation of Ca ²⁺ through a calcium acetate diol-water solution	55
2.1.1.3.5. Incorporation of Ca ²⁺ through a calcium acetylacetonate diol-water solution	56
2.1.2. PHYSICO-CHEMICAL CHARACTERISATION OF SOL-GEL PRECURSOR SOLUTIONS	57
2.1.2.1. Viscosity, density and concentration	57
2.1.2.2. Ultraviolet spectrophotometry analysis (UV)	58
2.1.2.3. Infrared spectroscopy analysis (IR)	60
2.1.2.4. Dynamic light scattering analysis (DLS)	61
2.1.2.5. Differential thermal analysis and thermogravimetric analysis (DTA-TGA)	62
2.1.2.5.1. Evolved gas analysis (EGA)	62
2.1.2.5.1.1. Thermogravimetric analysis-Fourier transform infrared spectroscopy (TGA-FTIR)	63
2.1.2.5.1.2. Thermogravimetric analysis-mass spectroscopy (TGA-MS)	63

PART 2: CALCIUM MODIFIED LEAD TITANATE (PCT) THIN FILMS

2.2.1. PREPARATION OF THE THIN FILMS	64
2.2.1.1. Substrates	64
2.2.1.2. Deposition, drying and pyrolysis of the thin films	65
2.2.1.3. Crystallisation of the thin films	67
2.2.1.3.1. Rapid thermal processing (RTP)	67
2.2.1.3.2. Ultraviolet-assisted rapid thermal processing (UV-RTP)	68
2.2.2. THIN FILMS CHARACTERISATION	70
2.2.2.1. Thickness measurements	70
2.2.2.1.1. Profilometry	71
2.2.2.2. Compositional and heterostructural analyses	72
2.2.2.2.1. Rutherford backscattering spectroscopy (RBS)	72
2.2.2.2.2. X-ray photoelectron spectroscopy (XPS)	73
2.2.2.3. Crystal structure	75
2.2.2.3.1. X-ray diffraction with the Bragg-Brentano geometry (XRD)	75
2.2.2.3.2. X-ray diffraction with the grazing incidence geometry (GIXRD)	76
2.2.2.4. Microstructural and nanoscopic studies	78
2.2.2.4.1. Scanning electron microscopy (SEM)	78
2.2.2.4.2. Transmission electron microscopy (TEM)	79
2.2.2.4.3. Scanning force microscopy (SFM)	81
2.2.2.4.4. Brillouin spectroscopy (BS)	83
2.2.2.5. Electrical characterisation	84
2.2.2.5.1. Dielectric constant	84
2.2.2.5.2. Leakage current density	85
2.2.2.5.3. Capacitance-voltage curves	86
2.2.2.5.4. Hysteresis loops	88
2.2.2.5.4.1. Piezoresponse force microscopy (PFM)	89
2.2.2.5.5. Fatigue and retention	90

CHAPTER III. PCT THIN FILMS FROM THE AQUEOUS SOLUTION-GEL SYNTHETIC ROUTE	
3.1. AQUEOUS PCT PRECURSOR SOLUTIONS	96
3.2. THERMAL DECOMPOSITION OF THE AQUEOUS PCT GELS.....	98
3.3. THIN FILM PREPARATION	105
3.3.1. Spinnability of the aqueous precursor solutions	105
3.3.2. Crystal structure and microstructure of the PCT films.....	106
3.3.3. Dielectric and ferroelectric properties of the PCT films	112
3.3.4. Applications in microelectronic devices	117
3.4. REMARKS.....	118
CHAPTER IV. PCT THIN FILMS FROM THE DIOL-BASED SOL-GEL SYNTHETIC ROUTE	
<i>PART 1: Ca²⁺ CONTENT AND CRYSTALLISATION OF THE PCT THIN FILMS</i>	
4.1.1. SOLUTIONS, GELS AND FILMS USED FOR THE CRYSTALLISATION STUDY	122
4.1.2. PCT GELS.....	122
4.1.2.1. Thermal evolution of the gels by Differential Thermal and Thermogravimetric Analysis (DTA-TGA).....	122
4.1.3. PCT THIN FILMS	127
4.1.3.1. Compositional depth profile of the films by X-ray Photoelectron Spectroscopy (XPS)	127
4.1.3.2. Microstructure and crystal structure of the films by Transmission Electron Microscopy (TEM) and Selected Area Electron Diffraction (SAED)	131
4.1.3.3. Crystal phases in the films by Grazing Incidence X-Ray Diffraction (GIXRD) analysis.....	136
4.1.3.4. Crystallinity of the perovskite films by X-Ray Diffraction (XRD) analysis.....	138
4.1.3.5. Surface morphology of the films by Scanning Force Microscopy (SFM)	143
4.1.3.6. Crystallisation of the films at nano-scale by Brillouin Spectroscopy (BS).....	145
4.1.4. REMARKS.....	148
<i>PART 2: SOL-GEL PROCESSING AND PROPERTIES OF THE PCT THIN FILMS</i>	
4.2.1. PCT PRECURSOR SOLUTIONS	154
4.2.1.1. Synthetic routes	154
4.2.1.2. Precursor solutions studied by Infrared spectroscopy (IR) analysis	157
4.2.1.3. Particle size distributions by Dynamic Light Scattering (DLS) and viscosity measurements of the solutions	161
4.2.1.4. Aging of the solutions with time	165
4.2.2. PCT GELS.....	170

4.2.2.1. Thermal evolution of the gels by Differential Thermal and Thermogravimetric Analysis (DTA-TGA)	170
4.2.3. PCT THIN FILMS	175
4.2.3.1. Crystalline phases in the films as a function of temperature	175
4.2.3.2. Crystalline structure of the films by X-Ray Diffraction with the Grazing Incidence (GIXRD) and with the Bragg-Brentano (XRD) geometry.....	177
4.2.3.3. Films microstructure by Scanning Force Microscopy (SFM) and Scanning Electron Microscopy (SEM).....	180
4.2.3.4. Films heterostructure by Rutherford Backscattering Spectroscopy (RBS)	185
4.2.3.5. Dielectric and ferroelectric properties of the PCT films. Applications in microelectronic devices.....	190
4.2.3.5.1. PCT24 thin films.....	190
4.2.3.5.1.1. Evaluation of the PCT24 films for applications in multifunctional microelectronic devices .	193
4.2.3.5.2. PCT50 thin films.....	196
4.2.3.5.2.1. Evaluation of the PCT50 films for applications in DRAMs and high-frequency components	197
4.2.4. REMARKS	202
 <i>PART 3: LOW-TEMPERATURE PROCESSING OF PCT THIN FILMS BY PHOTOCHEMICAL SOLUTION DEPOSITION</i>	
4.3.1. PHOTO-ACTIVATION OF THE PCT SOLUTIONS AND UV-ASSISTED LOW-TEMPERATURE PROCESSING OF THE PCT FILMS	208
4.3.2. LOW-TEMPERATURE PCT THIN FILMS	212
4.3.2.1. Crystalline structure of the films by X-Ray Diffraction with the Grazing Incidence (GIXRD) and with the Bragg-Brentano (XRD) geometry.....	212
4.3.2.2. Microstructure of the films by Scanning Electron Microscopy (SEM) and Scanning Force Microscopy (SFM)	216
4.3.2.3. Films heterostructure by Rutherford Backscattering Spectroscopy (RBS)	220
4.3.2.4. Dielectric and ferroelectric properties of the PCT films. Applications in microelectronic devices	225
4.3.2.4.1. Low-temperature processed PCT24 thin films	225
4.3.2.4.2. Low-temperature processed PCT50 thin films	231
4.3.3. REMARKS	236
 CAPÍTULO V. CONCLUSIONES GENERALES.....	241
 CHAPTER V. GENERAL CONCLUSIONS	247
 REFERENCES	251

List of Figures

Figure 1.1. <i>Ferroelectric hysteresis loop</i>	9
Figure 1.2. <i>Surface charge associated with spontaneous polarisation in a ferroelectric material and formation of 180° domains to minimise electrostatic energy (a). Schematic diagram of 180° and 90° domains minimising mechanical strain (b)</i>	10
Figure 1.3. <i>Domain structure in a ferroelectric ceramic before (a) and after (b) the polarisation process</i>	11
Figure 1.4. <i>A classification scheme for the 32 crystallographic point groups in relation to ferroelectric properties. Subcategories of ceramic ferroelectrics are also included</i>	12
Figure 1.5. <i>Different representations of the PbTiO₃ perovskite unit cell</i>	13
Figure 1.6. <i>Lattice parameters (a) and dielectric constant with temperature (b) of PCT bulk ceramics as a function of the Ca²⁺ content</i>	17
Figure 1.7. <i>Representation of the oxygen octahedra tilt in the perovskite structure</i>	18
Figure 1.8. <i>Phase diagram of the (Pb_{1-x}Ca_x)TiO₃ system with temperature as a function of the composition</i>	19
Figure 1.9. <i>Towards the miniaturisation of ferroelectric materials and their integration into microelectronic devices</i>	21
Figure 1.10. <i>Applications of ferroelectric thin films</i>	22
Figure 1.11. <i>Flow chart of a typical CSD process, with representative drawings of the structural status evolution of the metal components during the process (right-hand)</i>	32
Figure 1.12. <i>Different coating techniques used for the deposition of thin films</i>	33
Figure 1.13. <i>Fundamental effects induced by UV-irradiation and their applications</i>	44
Figure 2.1. <i>Experimental setup used in the synthesis of the aqueous (a) and diol-based (b) PCT precursor solutions</i>	50
Figure 2.2. <i>Structure of the titanium di-isopropoxide bis(acetylacetonate) (a) and acetylacetonate (b) chemical reagents</i>	50
Figure 2.3. <i>Schematic diagram of the aqueous solution-gel synthetic route</i>	52
Figure 2.4. <i>Schematic diagram of the diol-based sol-gel synthetic route A</i>	54
Figure 2.5. <i>Structure of the calcium acetylacetonate chemical reagent</i>	55
Figure 2.6. <i>Schematic diagrams of the diol-based sol-gel synthetic routes B* and C**</i>	56
Figure 2.7. <i>Cone/plate viscosimeter (Brookfield rheometer)</i>	58
Figure 2.8. <i>Electronic transitions among the molecular orbitals of an organic compound</i>	58
Figure 2.9. <i>Different steps of the spin-coating deposition process</i>	66
Figure 2.10. <i>Equipments used for the deposition, drying and pyrolysis of the PCT films; spinner (a), hot-plate (b) and general view of the deposition and pyrolysis equipments (c), inside the clean-room</i>	67
Figure 2.11. <i>Photograph of the rapid thermal processor (a), scheme of the furnace arrangement (b) and thermal budget (c) used for the crystallisation of the films</i>	68
Figure 2.12. <i>Photograph of the UV-assisted RTP processor (a), scheme of the furnace arrangement (b) and thermal budget (c) used for the crystallisation of the films</i>	69
Figure 2.13. <i>Diagram of the procedure followed for the fabrication of PCT thin films (a) and drawing (b) of the heterostructure of the resulting material</i>	70
Figure 2.14. <i>Example of a film-substrate profile obtained by profilometry (raw data) (a) and resulting profile (b) after subtraction of the substrate curvature</i>	71
Figure 2.15. <i>Experimental setup for the RBS measurements of the PCT films</i>	73

Figure 2.16. Scheme of the process of photoelectron emission	74
Figure 2.17. Schematic illustration of Bragg-Brentano (a) and grazing incidence (b) geometries for x-ray diffraction.....	78
Figure 2.18. Schematic diagram of SEM (a) and TEM (b) columns	80
Figure 2.19. Schematic representation of a scanning force microscope.....	82
Figure 2.20. Experimental setup of the BS technique.....	84
Figure 2.21. Schematic diagram of the measurement for the leakage current determination.....	86
Figure 2.22. Schematic diagram of the measurement for the capacitance versus voltage curves determination	87
Figure 2.23. $P(E)$ hysteresis loop (a) and $J(E)$ ac current density loop (b).....	88
Figure 2.24. Experimental setup used for the PFM measurements on the films.....	90
Figure 2.25. Schematic diagram of the fatigue measurements on the films.....	91
Figure 3.1. TGA-DTG of the aqueous solutions derived PCT24 (a) and PCT50 (b) gels	99
Figure 3.2. TGA-FTIR of the aqueous solutions derived PCT24 (a) and PCT50 (b) gels. Windows; 940-913 cm^{-1} (NH_3), 2217-2137 cm^{-1} (CO), 2268-2395 cm^{-1} (CO_2) and 4000-400 cm^{-1} (Gram-Schmidt).....	100
Figure 3.3. TGA-MS of the aqueous solutions derived PCT24 (a) and PCT50 (b) gels.....	101
Figure 3.4. Thermal decomposition sequence of citric acid ²³⁰	103
Figure 3.5. Aqueous solutions derived films deposited onto Pt-substrates previously cleaned with trichloroethylene/acetone/2-propanol (a) and SPM/APM (b) mixtures	106
Figure 3.6. Crystalline films derived from aqueous PCT24 precursor solutions of ~0.30 (left) and ~0.35 (right) molar concentration.....	107
Figure 3.7. GIXRD (a) and XRD (b) patterns of the aqueous solutions derived PCT24 and PCT50 films (Pv: perovskite, Pt: platinum)	109
Figure 3.8. SEM micrographs (plan-view) of the aqueous solutions derived PCT24 (a) and PCT50 (b) films. Magnifications of each micrograph are embedded shown	110
Figure 3.9. SEM micrographs (cross-section) of the aqueous solutions derived PCT24 (a) and PCT50 (b) films.....	111
Figure 3.10. Variation of the dielectric constant (k') with temperature of the aqueous solution derived PCT24 (a) and PCT50 (b) films, measured at various frequencies. Continuous lines are depicted as a guide for the eye for the temperature maximum shift. Insets show the variation of the loss tangent ($\tan \delta$) with temperature for the PCT24 (i) and PCT50 (ii) films	112
Figure 3.11. Ferroelectric hysteresis loop of the aqueous solution derived PCT24 film. Non-switching contribution to ferroelectric domains is also depicted.....	114
Figure 3.12. Field dependence of leakage currents for the aqueous solutions derived PCT24 and PCT50 films.....	115
Figure 4.1.1. DTA curves for heating (i) and cooling (ii), and TGA curves (iii) of the diol sol-gel derived PCT0 (a), PCT24 (b) PCT30 (c), PCT40 (d) and PCT50 (e) powders. Insets show the DTA, TGA and DTG curves of the PCT0 and PCT24 powders.....	124/125
Figure 4.1.2. Photoelectron peak intensities during depth profiling of a diol sol-gel derived PCT50 film deposited on Pt/TiO ₂ /SiO ₂ /(100)Si	128
Figure 4.1.3. C1s (a) and O1s (b) core levels measured at different Ar ⁺ sputtering times (beginning of the analysis and after 1 min of Ar ⁺ sputtering) in the diol sol-gel derived PCT50 film. (c) Signal of C1s measured in the film as a function of depth and binding energy.....	130

Figure 4.1.4. Bright-field TEM micrograph (a) and indexed SAED patterns (b and c) of the diol sol-gel derived PCT24 film (plan-view). Magnified micrograph to appreciate crystal size (d) and corresponding SAED pattern (e) are also shown. Continuous rings observed in the SAED patterns are ascribed to copper of the sample-holder grid.....	132
Figure 4.1.5. Bright-field TEM micrograph (a) and indexed SAED patterns (b and c) of the diol sol-gel derived PCT35 film (plan-view). Magnified micrograph to appreciate crystal size (d) is also shown. Continuous rings observed in the SAED patterns are ascribed to copper of the sample-holder grid.....	133
Figure 4.1.6. Bright-field TEM micrographs at different magnifications to appreciate the heterostructure (a, b and c) and the crystal size (d) of the diol sol-gel derived PCT50 film (cross-section). Corresponding indexed SAED pattern (e) is also shown	134
Figure 4.1.7. GIXRD patterns of the diol sol-gel derived PCT films treated at 400 °C (a), 425 °C (b), 450 °C (c) and 650 °C (d) by RTP (Py: pyrochlore). Indexed peaks correspond to the perovskite. Inset shows the GIXRD pattern of the PCT50 film treated at 450 °C.....	137
Figure 4.1.8. Pseudo-Voigt curves corresponding to the 111 perovskite peaks of the diol sol-gel derived PCT films treated at different temperatures.....	139
Figure 4.1.9. Variation with temperature of FWHM values of the 111 perovskite peak measured by XRD with the Bragg-Brentano geometry of the diol sol-gel derived PCT films	140
Figure 4.1.10. Crystallite size and micro-strains calculated with the variance method ²⁵² from the XRD diffraction data of the 111 perovskite reflection for the diol sol-gel derived PCT0 (a) and PCT50 (b) films treated at different temperatures by RTP. Graph (c) shows both values for PCT films treated at 650 °C by RTP as a function of the Ca ²⁺ content.....	142
Figure 4.1.11. SFM images of the surfaces of the diol sol-gel derived PCT0 (a) and PCT50 (b) films, treated at 450 and 650 °C. Note the lower magnification used in the photograph of the PCT0 film at 650 °C than that of the other photographs.....	144
Figure 4.1.12. The variation of the sound velocity of acoustic waves travelling through the diol sol-gel derived PCT0 (a) and PCT50 (b) films, as a function of the processing temperature. Inset i shows the BS spectrum of the PCT0 film at 400 °C. Inset ii shows a schematic graph of the different stages (A, B and C) of the crystallisation process with temperature of the PCT films	146
Figure 4.2.1. IR spectra of the distilled liquids (a) and of the precursor solutions (b) corresponding to the diol sol-gel synthesis of the PCT24 solution following the routes A and C. Insets correspond to the wavenumber interval where the $\nu(\text{C}=\text{O})$ stretching vibrations of acetic acid (1720-1710 cm^{-1}) and isopropylacetate ester (1740-1730 cm^{-1}) are observed.....	158
Figure 4.2.2. IR spectra of the distilled liquids (a) and of the precursor solutions (b) corresponding to the diol sol-gel synthesis of the PCT50 solution following the routes A and B. Insets correspond to the wavenumber interval where the $\nu(\text{C}=\text{O})$ stretching vibrations of acetic acid (1720-1710 cm^{-1}) and isopropylacetate ester (1740-1730 cm^{-1}) are observed.....	159
Figure 4.2.3. Particle size distributions in a lognormal representation of the diol sol-gel PCT24-A and PCT24-C solutions (a) and of the diol sol-gel PCT50-A and PCT50-B solutions (b) determined by DLS. Inset shows the two Gaussian curves separated from the asymmetrical particle size distribution measured by DLS in the PCT50-A solution.....	162
Figure 4.2.4. Viscosity of the diol sol-gel PCT24-A, PCT24-C, PCT50-A and PCT50-B solutions, as a function of shear rate.....	163
Figure 4.2.5. A proposed Pb(II)-Ti(IV) sol network with occluded calcium acetate molecules for the diol sol-gel PCT solutions derived from the synthetic route A (proposed for barium or strontium titanate precursors ²⁶¹).....	164
Figure 4.2.6. Lognormal representation of the particle size distributions of the diol sol-gel PCT50-A and PCT50-B solutions determined by DLS on the fresh solutions (a) and after 6 (b), 14 (c) and 20 (d) months of aging	166/167
Figure 4.2.7. Variation of the viscosity and of the thickness of the derived crystallised film with the aging time of the diol sol-gel PCT50-A (a) and PCT50-B (b) solutions	169

Figure 4.2.8. DTA-TGA of the diol sol-gel derived PCT24-A (a) and PCT24-C (b) gels. Inset shows the DTA-TGA curves of the calcium acetylacetonate chemical reagent.....	171
Figure 4.2.9. DTA-TGA of the diol sol-gel derived PCT50-A (a) and PCT50-B (b) gels.....	172
Figure 4.2.10. GIXRD patterns of the diol sol-gel derived PCT24-A (a), PCT24-C (b), PCT50-A (c) and PCT50-B (d) films RTP treated at different temperatures.....	176
Figure 4.2.11. GIXRD (a) and XRD (b) patterns of the diol sol-gel derived PCT films.....	178
Figure 4.2.12. SFM images of the diol sol-gel derived PCT24-A (a) and PCT24-C (b) films, and PCT50-A (c) and PCT50-B (d) films. Calculated grain sizes are shown in the figures.....	181
Figure 4.2.13. SEM micrographs (plan-view) obtained in the diol sol-gel derived PCT24-A (a) and PCT24-C (b) films, and PCT50-A (c) and PCT50-B (d) films. Magnifications of each micrograph are embedded shown.....	182
Figure 4.2.14. SEM micrographs (cross-section) obtained in the diol sol-gel derived PCT24-A (a) and PCT24-C (b) films, and PCT50-A (c) and PCT50-B (d) films.....	183
Figure 4.2.15. RBS spectra and heterostructure deduced from RBS data for the diol sol-gel derived PCT24-A (a) and PCT24-C (b) films.....	186
Figure 4.2.16. RBS spectra and heterostructure deduced from RBS data for the diol sol-gel derived PCT50-A (a) and PCT50-B (b) films.....	187
Figure 4.2.17. Variation of the dielectric constant (k') with temperature of the diol sol-gel derived PCT24 films, measured at various frequencies.....	191
Figure 4.2.18. Pulsed hysteresis loops of the diol sol-gel derived PCT24 films.....	192
Figure 4.2.19. Compensated hysteresis loop of the ~300 nm thick diol sol-gel derived PCT24-C film.....	193
Figure 4.2.20. Fatigue of the ~300 nm thick diol sol-gel derived PCT24-C film.....	194
Figure 4.2.21. Evolution of the pyroelectric coefficient (γ) of the ~300 nm thick diol sol-gel derived PCT24-C film after poling (retention).....	195
Figure 4.2.22. Variation of the dielectric constant (k') with temperature of the diol sol-gel derived PCT50 films, measured at various frequencies.....	197
Figure 4.2.23. Leakage current behaviour of an ~80 nm thick PCT50-B film.....	198
Figure 4.2.24. Time voltage drop after the writing pulse in a ~100 nm thick PCT50-B capacitor, for the two signs of voltage charge.....	199
Figure 4.2.25. Capacitance-voltage (C-V) curves for a ~1200 nm thick diol sol-gel derived PCT50-B film measured at various temperatures (-20, 20, 70 and 100 °C).....	200
Figure 4.2.26. Relative tunability, figure of merit and $\tan \delta$ of the diol sol-gel derived PCT50-B film at different temperatures, measured at 1 kHz.....	201
Figure 4.3.1. Molecular structure of the titanium di-isopropoxide bis-acetylacetonate chemical reagent (a) and UV absorption spectrum of the PCT solutions (b).....	209
Figure 4.3.2. DTA-TGA of the diol sol-gel derived PCT24 (a) and PCT50 (b) gels, showing the optimum temperatures for the UV-irradiation of the gel films.....	210
Figure 4.3.3. FTIR spectra of the gel layers derived from the photosensitive diol sol-gel solutions and treated at 250 °C for 240 s with and without UV-irradiation.....	211
Figure 4.3.4. GIXRD patterns of the UV-irradiated PCT24 (a) and PCT50 (b) films processed in air at different temperatures, and of the UV-irradiated PCT24 films at 450 °C (c) and PCT50 films at 500 °C (d) processed in air or oxygen atmosphere.....	213
Figure 4.3.5. XRD patterns of the UV-irradiated PCT24 films crystallised at 450 °C (a) and of the UV-irradiated PCT50 films crystallised at 500 °C (b), using air or oxygen atmosphere.....	215

Figure 4.3.6. SEM micrographs (plan-view) obtained in the; PCT24 film processed by UV-assisted RTP at 450 °C in air (a), PCT24 film processed by UV-assisted RTP at 450 °C in oxygen (b), PCT50 film processed by UV-assisted RTP at 500 °C in air (c) and PCT50 film processed by UV-assisted RTP at 500 °C in oxygen (d).....	217
Figure 4.3.7. SEM micrographs (cross-section) obtained in the; PCT24 film processed by UV-assisted RTP at 450 °C in air (a), PCT24 film processed by UV-assisted RTP at 450 °C in oxygen (b), PCT50 film processed by UV-assisted RTP at 500 °C in air (c) and PCT50 film processed by UV-assisted RTP at 500 °C in oxygen (d).....	218
Figure 4.3.8. SFM images of the PCT24 film processed by UV-assisted RTP in air (a) and oxygen (b). Insets show line profile of the images	219
Figure 4.3.9. RBS spectra and heterostructure deduced from the RBS data of the low-temperature PCT24 films processed in air (a) or oxygen (b)	221
Figure 4.3.10. RBS spectra and heterostructure deduced from the RBS data for the low-temperature PCT50 films processed in air (a) or oxygen (b).....	222
Figure 4.3.11. Variation of the dielectric constant (k') and loss tangent ($\tan \delta$) with temperature of the PCT24 films processed by UV-assisted RTP at 450 °C in air or oxygen, measured at various frequencies.....	225
Figure 4.3.12. Ferroelectric hysteresis loops (a) and non-switching contribution to the polarisation loops (b) of the PCT24 films processed by UV-assisted RTP at 450 °C in air or oxygen.....	227
Figure 4.3.13. Leakage current densities measured for the PCT24 films processed by UV-assisted RTP at 450 °C in air or oxygen	229
Figure 4.3.14. Variation of the pyroelectric coefficient (γ) with time for the PCT24 films processed by UV-assisted RTP at 450 °C in air or oxygen.....	229
Figure 4.3.15. Local piezoelectric hysteresis loop of the PCT24 film processed by UV-assisted RTP at 450 °C in oxygen	231
Figure 4.3.16. Variation of the dielectric constant (k') and loss tangent ($\tan \delta$) with temperature of the PCT50 films processed by UV-assisted RTP at 500 °C in air or oxygen, measured at various frequencies.....	232
Figure 4.3.17. Ferroelectric hysteresis loops of the PCT50 films processed by UV-assisted RTP at 500 °C in air or oxygen (a). Ferroelectric hysteresis loops measured in these films at temperatures below and over the transition temperature, in air (b) or oxygen (c)	233
Figure 4.3.18. Leakage current densities measured for the PCT50 films processed by UV-assisted RTP at 500 °C in air or oxygen	234

List of Tables

Table 1.1. <i>Properties of the PCT bulk ceramics as a function of the Ca^{2+} content</i>	16
Table 1.2. <i>Comparison of main features of common methods of ferroelectric thin film preparation</i>	26
Table 1.3. <i>Low-temperature CSD methods for ferroelectric thin films</i>	41
Table 1.4. <i>Ultraviolet light sources</i>	43
Table 3.1. <i>Physicochemical properties of the aqueous PCT precursor solutions</i>	97
Table 3.2. <i>TGA and EGA data of the aqueous solutions derived PCT24 and PCT50 gels</i>	104
Table 3.3. <i>Dielectric and ferroelectric parameters of the aqueous solutions derived PCT24 and PCT50 films</i>	116
Table 4.1.1. <i>Summary of the results obtained by DTA-TGA in the diol sol-gel derived PCT powders</i>	126
Table 4.2.1. <i>Physicochemical characteristics of the different diol-based sol-gel synthetic routes tested for the preparation of PCT solutions</i>	155
Table 4.2.2. <i>Physicochemical characteristics of the PCT precursor solutions prepared from the diol-based sol-gel synthetic routes A, B and C</i>	156
Table 4.2.3. <i>DTA-TGA data of the diol sol-gel derived PCT gels</i>	174
Table 4.2.4. <i>RBS data obtained in the diol sol-gel derived PCT films</i>	189
Table 4.3.1. <i>RBS data obtained in the PCT films processed at low temperatures</i>	224

CHAPTER I

INTRODUCTION

1.1. INTRODUCTION AND PURPOSE OF THE WORK

Since the past two decades, electroceramic materials have become increasingly important in key technologies such as computers and telecommunications, constituting a billion-dollar/euro global market owing to their unique applications in the electronic industry.¹ Among these materials, ferroelectric ceramics show a wide range of properties of high interest for microelectronic devices; high permittivity values (Dynamic Random Access Memories, DRAMs), spontaneous polarisation that can be switched with the electric field (Non Volatile Ferroelectric Random Access Memories, NVFeRAMs), piezoelectric activity (sensors and actuators) or pyroelectric response (sensors).²

However, the fabrication of these devices involves the integration of the ferroelectric material with the Complementary Metal Oxide Semiconductor (CMOS) Integrated Circuit (IC). To this aim, the thin film technology together with the recent advances in deposition methods have allowed the integration of these films into functional heterostructures, mainly using semiconductor substrates based on silicon.

Several ferroelectric compositions have proved to have interesting properties when deposited as thin films. As examples, solid solutions of lead zirconate titanate, $\text{Pb}(\text{Zr,Ti})\text{O}_3$ (PZT)³ or strontium bismuth titanate, $\text{SrBi}_2\text{Ta}_2\text{O}_9$ (SBT)⁴ have been prepared in thin film form by different methods and their applications, mainly for sensors and actuators in the first case, and for non-volatile memories in the second one, have been widely reported in the literature. Other compositions based on the partially A-site substituted PbTiO_3 perovskite have also shown significant properties in thin film form. Among them, the author wants to point up the calcium modified lead titanate solid solution, $(\text{Pb}_{1-x}\text{Ca}_x)\text{TiO}_3$ (PCT), which has been the composition studied in the present work.

PCT thin films are currently under investigation for a wide number of applications, including computer memory storage devices (NVFeRAM),⁵ MicroElectroMechanical Systems MEMS⁶ (pressure sensors, accelerometers, inkjet printers, ultrasonic micromotors, micropumps) and pyroelectric sensors (infrared detectors).^{7,8} Particularly, PCT compositions with partial substitutions of Pb^{2+} by Ca^{2+} of 24 at% ($x = 0.24$), have been very studied due to their excellent ferro-, pyro- and piezoelectric properties.⁹ Films of this composition have a well-defined dielectric and ferroelectric character, a large piezoelectric activity with a stable piezoelectric coefficient that does not significantly change with the dc field removal (attractive for MEMS) or high pyroelectric coefficients of interest in infrared sensors.

Recently, PCT bulk ceramics with high Ca^{2+} contents ($0.40 \leq x \leq 0.50$) have shown diffuse ferro-paraelectric transitions with high values of the dielectric constant at room temperature and a large non-linearity with voltage.¹⁰ These characteristics could be exploited in DRAMs and high-frequency components (consumer portable communications, radar systems) if they could be prepared in thin film form.

Therefore, the PCT solid solution shows a broad compositional range (substitutions of Pb^{2+} by Ca^{2+} from 0 up to 50 at%) in which the material results highly competitive for an extensive deal of applications. Furthermore, the properties of the PCT films can be easily tuned depending on the Ca^{2+} content introduced in the PCT composition. This results of high technological interest, since a wide spectrum of different microelectronic components of different functionality can be fabricated with PCT thin films by only modifying the partial substitution of Pb^{2+} by Ca^{2+} .

Different physical and chemical methods have been used for the fabrication of PCT thin films, being Chemical Solution Deposition (CSD) that which has received most attention. Sol-gel is included within CSD methods, and it offers several advantages such as the low cost, the compositional control of the chemical reagents at molecular level or the ability to tailor the solution chemistry.

However, one of the main problems found when solution techniques (e.g. sol-gel) are used is the compatibility among starting reagents (raw materials) in a stable multi-component (multi-oxide) precursor solution. In the case of the PCT solutions, the calcium precursor is an additional problem, since calcium compounds exhibit a low solubility in the solvents usually employed in sol-gel processing (alcohols, carboxylic acids, etc). Thus, literature on sol-gel derived PCT films has been mainly focused on compositions with Ca^{2+} contents below 40 at% ($x \leq 0.40$). The preparation of PCT films with larger Ca^{2+} contents shows critical difficulties as a result of the low stability of the solutions and the formation of non-ferroelectric phases during the crystallisation of the perovskite film. At the present time, and to the author's knowledge, the fabrication of PCT thin films with Ca^{2+} contents over 40 at% has indeed not been reported.

Since the physical properties of the crystalline PCT thin films are dependent on the Ca^{2+} concentration, a deep study of the perovskite phase crystallisation in these films as a function of the Ca^{2+} content is required to understand the different structures, microstructures and electrical properties resulting in the oxide films. The progressive substitution of Pb^{2+} by Ca^{2+} in the PCT films leads to a decrease on the tetragonality (c/a) of the system and on the ferro-paraelectric transition temperature. The spontaneous polarisation (P_s) and coercive field (E_c) also decrease with

the Ca^{2+} content, whereas the values of the dielectric constant (k') at room temperature are increased.^{11,12} Thus, the understanding of the effects of the Ca^{2+} content on the nucleation and growth phenomena of the PCT perovskite would shed light upon the functional features of the crystalline films obtained.

One of the major advantages of sol-gel processing is the ability to prepare solutions with tailored physicochemical properties. The use of different synthetic pathways, chemical reagents or thermal treatments can strongly affect the microstructure, heterostructure and electrical response of the films. Control over solution homogeneity, composition, rheology (i.e. viscosity, flow behaviour) or aging characteristics (i.e. the change of solution properties with time) is therefore extremely important to improve the processing and the properties of the films. To maximise the dielectric and ferroelectric properties of the PCT films through the solution chemistry is one of the approaches carried out in this Ph.D Thesis.

Advanced materials with sophisticated functions and high performances are each time more demanded (even needed) by the modern society. However, the remarkable development of these materials during the last past decades has led to a vast consumption of energies and resources, causing serious damages to the environment. Consequently, a global trend towards clean technologies has arisen during the last years mainly supported by recently relevant and strict law enactment.^{13,14} Sol-gel processing involves healthy and safety risks related to the use of certain substances, such as some of the organic solvents and chemical reagents usually employed in the laboratory. The emission of organic volatiles during the thermal treatment of the films is also a constant object of concern nowadays, since volatilisation of lead from lead based-on perovskite compositions can arise at high temperatures. Therefore, another challenge of this work will be the reduction of the processing temperature of the PCT films that would minimise hazardous exhaust emissions towards the atmosphere.

Furthermore, the low-temperature processing of these films would not only provide significant benefits to the environment, but also to the microelectronic industry. The fabrication of reliable microelectronic devices based on ferroelectric materials requires their integration with the silicon substrate, which involves processing temperatures of the film that should be compatible with those used in the Si-technology (<550 °C). Silicon and other elements of the microelectronic device are seriously damaged at the common crystallisation temperatures of ferroelectric films (over 600 °C). This is currently one of the hot-topics in ferroelectric materials,¹⁵ and significant efforts are being made nowadays in order to achieve this objective.

In this work, the following approaches will be necessary to attain the objectives previously discussed:

- (1) Development of novel chemical solution processes and thermal treatment procedures for the preparation of $(\text{Pb}_{1-x}\text{Ca}_x)\text{TiO}_3$ thin films by CSD, with a decreased environmental hazard as compared with others traditionally used in the literature.
- (2) Synthesis of stable and homogeneous $(\text{Pb}_{1-x}\text{Ca}_x)\text{TiO}_3$ precursor solutions for the whole compositional perovskite range here studied ($0 \leq x \leq 0.50$) that lead to crystalline thin films with homogeneous compositional profiles and appropriate crystal structures and microstructures.
- (3) Preparation of $(\text{Pb}_{1-x}\text{Ca}_x)\text{TiO}_3$ thin films with different properties and applications by tuning the Ca^{2+} content of the perovskite composition.
- (4) To establish relationships between solution processing and film properties, thus determining those processing parameters that directly affect the dielectric and ferroelectric responses of the $(\text{Pb}_{1-x}\text{Ca}_x)\text{TiO}_3$ thin films.

1.2. THEORY AND LITERATURE REVIEW

1.2.1. Basic concepts of dielectrics and ferroelectrics

A dielectric can be defined as a material which presents high resistance to flow of electric current and hence, as an electrical insulator (non-conducting), can show the ability to accumulate electric charges. One of the main applications of dielectric materials is their use as capacitive elements in electronic circuits. Ceramic materials are extensively used in capacitors because of their excellent electrical properties and potential integration as part of an electronic device. For a large plate capacitor of area A and thickness d subjected to an applied voltage V , the capacitance (i.e. the ability to storage an electrical charge Q) in vacuum is:

$$C_0 = \epsilon_0 (A/d) \quad [\text{eq. 1}]$$

where ϵ_0 is the vacuum permittivity. If a dielectric material (e.g. ceramic) of permittivity ϵ' is placed between the capacitor plates, then:

$$C' = \epsilon' (A/d) = \epsilon' (C_0/\epsilon_0) = (\epsilon'/\epsilon_0) C_0 = k C_0 \quad [\text{eq. 2}]$$

from which it can be deduced that the capacitance of the capacitor has been increased by a factor of k ; the *relative dielectric constant* of the material. Therefore, this material property affects the capacitance of the circuit element.

The additional charge that has been generated in the capacitor arises from the displacement of charge carriers present in the dielectric material, resulting from the application of the electric field. This phenomenon is known as polarisation, and the consequent charge displacements within the dielectric can neutralise part of the applied field.

However, when an alternating field is applied, the relative dielectric constant of the material is often treated as a complex function (frequency dependent) given by:

$$k = k' - ik'' \quad [\text{eq. 3}]$$

where k' is the real part of the complex dielectric constant, also named *dielectric constant*, and k'' is the imaginary part of the complex dielectric constant, named *loss factor*. The k' value (amount of electrical energy stored) is related to the polarisation generated in the material, whereas k'' depends on the energy loss of the process. The ratio between k'' and k' gives rise to the *loss tangent*, $\tan \delta$, also known as dissipation factor ($\tan \delta = k''/k'$).

There are various possible mechanisms for polarisation in a dielectric material,¹⁶ such as i) the shift of the gravity center of the negative electron cloud in relation to the positive atom nucleus (electronic polarisation), ii) the displacement of positive and negative ions from their equilibrium positions (ionic polarisation), iii) the orientation of permanent electric dipoles with the applied field (dipole polarisation) and iv) the accumulation of free charges at the interfaces of the material (interface polarisation). A special kind of behaviour resulting from these polarisation mechanisms is the ferroelectricity.

The phenomenon of *ferroelectricity* was discovered in single crystal materials (Rochelle salt, $\text{NaKC}_4\text{H}_4\text{O}_6 \cdot 4\text{H}_2\text{O}$) by Joseph Valasek in 1921.¹⁷ However, it was not up to the early 1940 when ferroelectricity was extended to polycrystalline ceramics, with the aim to demonstrate the unusually high dielectric constant found in barium titanate (BaTiO_3 , BT) ceramic capacitors.³ Since then, several books and papers have been published dealing with the history of ferroelectricity, to which the reader is openly encouraged to be introduced.¹⁸⁻²²

A ferroelectric material can be defined as a crystallographically non-centrosymmetric dielectric, which presents a phase transition from a polar (ferroelectric phase) to a non polar state (paraelectric phase) at a temperature at which its dielectric constant shows a maximum value (*dielectric anomaly*). Typically, ferroelectrics loose their ferroelectric properties above this temperature, known as the transition temperature.

Ferroelectric materials posses a crystallographic axis, or polar axis, in which along its direction it exists a spontaneous polarisation (P_s) in the polar phase, consequence of a non-centrosymmetric arrangement of ions in its unit cell that produces an electric dipole moment in the material. The main feature of a ferroelectric material is that the sign of this spontaneous polarisation can be reversed (switched) by applying a suitable electric field (E), giving rise to the characteristic non-linear “polarisation-electric field” plot. Figure 1.1 shows the polarisation dependence with the electric field of a ferroelectric material (*ferroelectric hysteresis loop*). The representative parameters that define the ferroelectric loop are; the remanent polarisation, P_r , the spontaneous/saturation polarisation, P_s , and the coercive field, E_c .

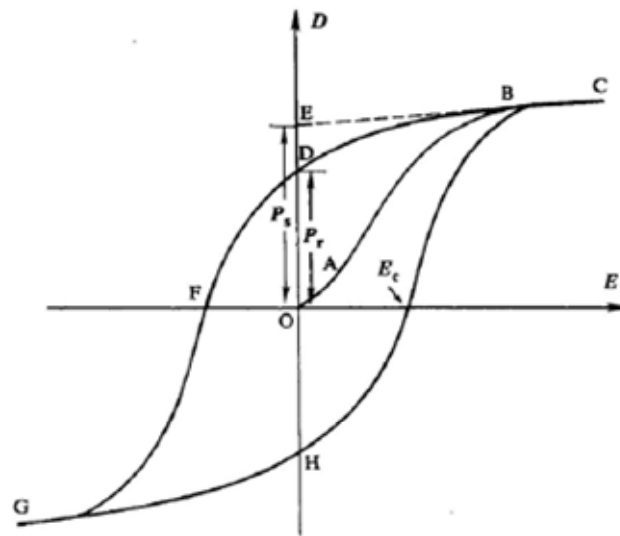


Figure 1.1. Ferroelectric hysteresis loop

In order to minimise the electric and elastic energies within the material, ferroelectrics are structured into a *domain configuration*. Ferroelectric domains are regions of the material with uniform spontaneous polarisation, that is, within each individual domain all the electric dipoles are aligned in the same direction. These domains are separated by interfaces where the polarisation direction changes abruptly, known as domain walls. Domain configurations may be signified as 180° and 90° (for tetragonal systems), which differ in the direction of the polar axis and hence in the lattice dimensions along particular directions within a crystal. The 180° and 90° orientations occurring in a simple domain structure are schematically shown in Figure 1.2.²² The 180° domain configuration reduces the surface charge and minimise the electrostatic strain, whereas the 90° domains minimise the mechanical strain associated with the tetragonal distortion of the unit cell.

In polycrystalline ferroelectric materials (e.g. ceramics), the electric dipoles and therefore also the domains are randomly oriented prior to the application of an electric field, that is, at $E = 0$, the net polarisation of the material equals to zero. The application of a low electric field generates a linear relationship between P and E , since the field is not large enough to switch any domains and the material behaves as a normal dielectric material (paraelectric). This behaviour corresponds to the segment OA of the P - E hysteresis loop in Fig. 1.1.

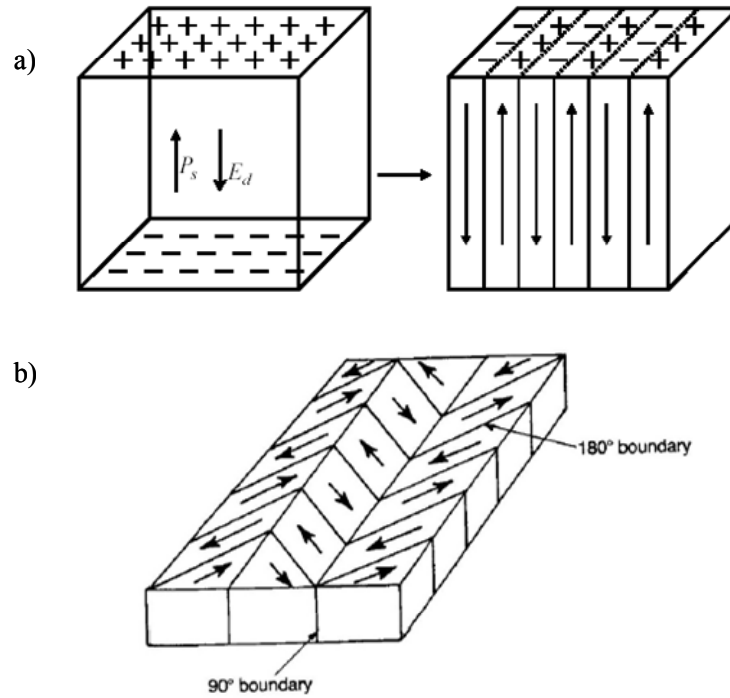


Figure 1.2. Surface charge associated with spontaneous polarisation in a ferroelectric material and formation of 180° domains to minimise electrostatic energy (a). Schematic diagram of 180° and 90° domains minimising mechanical strain (b)

As the electric field strength increases, a number of the domains with opposite polarisation direction will switch towards the field direction, producing a rapid increase in polarisation (segment AB). When all the domains as possible are aligned in the field direction, a saturation state is reached (BC). As the field strength decreases, the polarisation will decrease (BD) but does not go back to zero. When the field is reduced to zero, some of the domains will remain aligned and the material will exhibit a remanent polarisation (P_r). The extrapolation of the linear segment BC of the hysteresis loop back to the polarisation axis (CBE) represents the value of the spontaneous/saturation polarisation (P_s), in the case of an appropriately oriented, fully poled polycrystalline material.

The remanent polarisation in a ferroelectric material cannot be removed until the applied electric field in the opposite direction reaches a certain value (at point F in Fig. 1.1). Thus, the strength of the field required to reduce the polarisation back to zero is called the coercive field strength (E_c). Further increase of the field in the negative direction will cause an alignment of the dipoles in this direction and the cycle can be completed by reversing the field direction once again.

A representation of the domain structure for a ferroelectric polycrystalline ceramic prior to the application of the electric field, and after the polarisation process (poling), is shown in Figure 1.3. Note that at $E = 0$, the net polarisation is zero and the material would not show ferroelectric activity. After poling, a net polarisation different to zero has been induced through the mechanism of domain motion and the material exhibits ferroelectric response, as consequence of its non-centrosymmetric arrangement of electric dipoles.

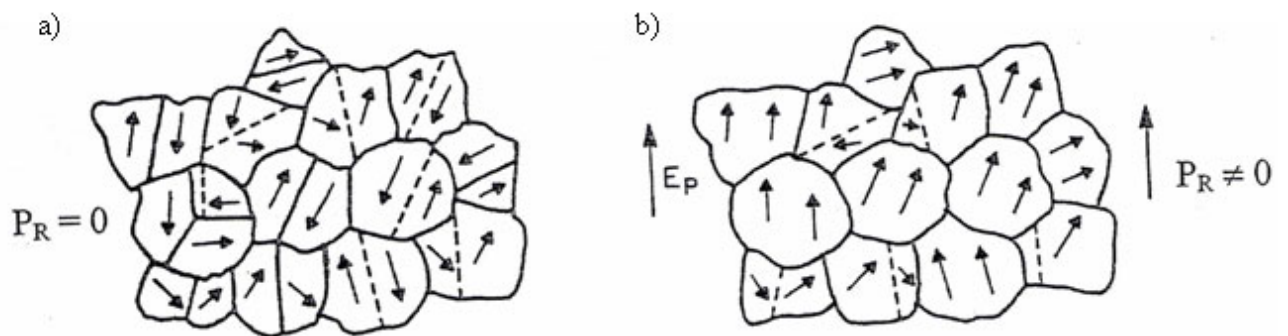


Figure 1.3. Domain structure in a ferroelectric ceramic before (a) and after (b) the polarisation process

The spontaneous polarisation of a ferroelectric material can be also altered by the temperature (*pyroelectricity*) and by the mechanical stress (*piezoelectricity*). Pyroelectricity results when the material is subjected to thermal variations generating thus an electric current, named pyroelectric current. In piezoelectricity (from the Greek “piezo”, meaning “to press”), when a mechanical stress is applied to a non-centrosymmetric crystal, an electric charge or polarisation is generated (direct piezoelectric effect). Conversely, when an electric field is applied to a piezoelectric crystal, the resulting atomic displacements produce a mechanical strain (converse piezoelectric effect). All the ferroelectric materials are piezoelectrics and pyroelectrics. Note that both piezoelectricity and pyroelectricity are inherent properties of the material, requiring only the crystal structure to contain a polar axis along which atomic displacement can occur asymmetrically. Ferroelectricity lies on the property of polar crystals to reverse the spontaneous polarisation by applying an electric field.

Figure 1.4 depicts the interrelationship between piezoelectrics and subgroups on the basis of internal crystal symmetry. Furthermore, four types of ceramic ferroelectrics have been also introduced as subcategories of the general group of ferroelectric materials (based on its unit cell structure),²³ focusing in the perovskite (ABO_3) group category, to which the composition studied in this Ph.D Thesis, the calcium modified lead titanate system ($Pb_{1-x}Ca_x$)TiO₃, belongs. The perovskite type composition families listed, represent the bulk of the ferroelectric ceramics manufactured in the world today.

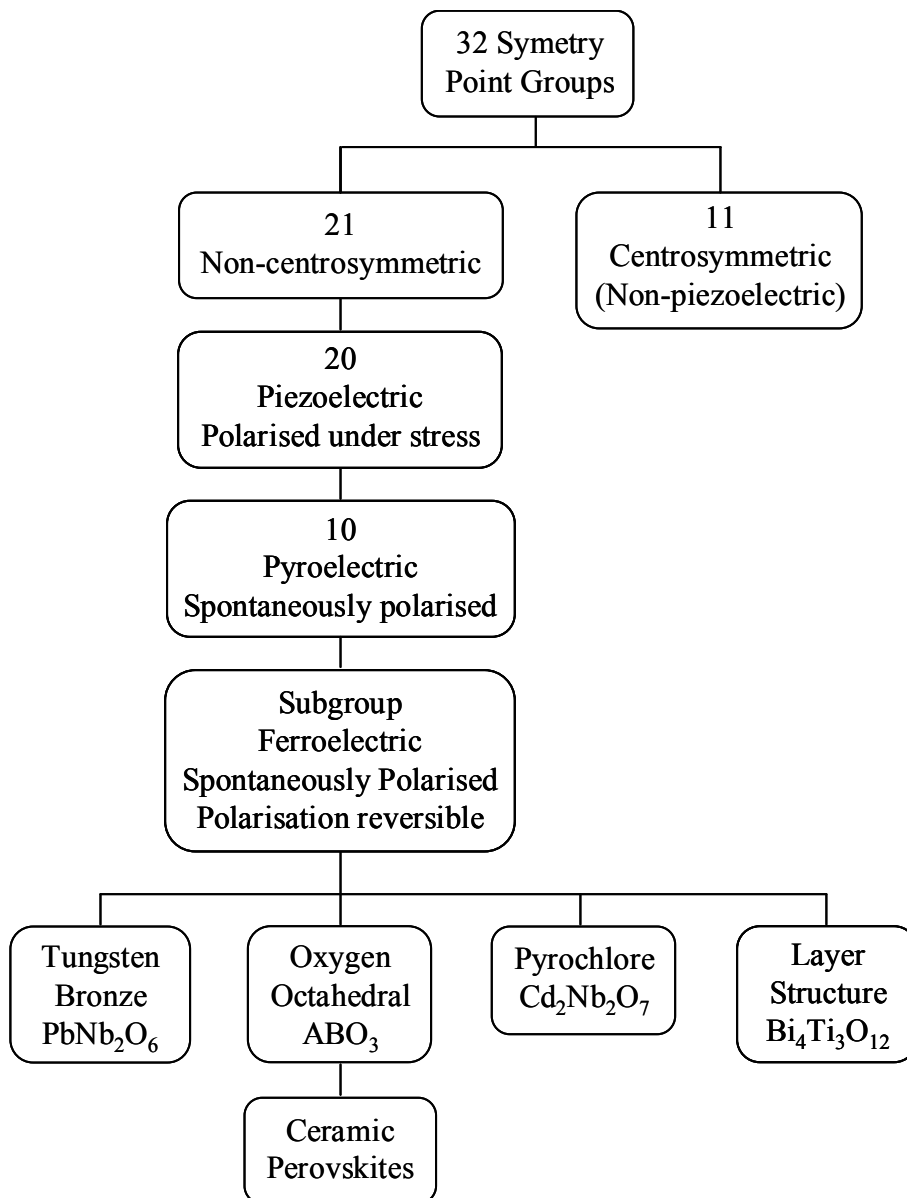


Figure 1.4. A classification scheme for the 32 crystallographic point groups in relation to ferroelectric properties. Subcategories of ceramic ferroelectrics are also included

1.2.2. Structure and properties of Ca^{2+} modified PbTiO_3 perovskite bulk materials

The calcium titanate (CaTiO_3 , CT) mineral discovered in 1839 by the Russian mineralogist Rose, owes its particular name (*perovskite*) to the Russian minister L.A. Perovskiy. Nowadays, this mineral has transferred its name to a wide family of compounds with general formula ABO_3 . Thus, the perovskite type solid solutions present a great variety of systems (see previous Fig. 1.4), which strive to please the each time more demanded requirements in the field of the ferroelectric ceramics. The lead titanate system (PbTiO_3 , PT) belongs to this family whose ferroelectric properties as bulk ceramic have been studied since the 50s.²⁴ Figure 1.5 shows the unit cell of the PbTiO_3 perovskite.

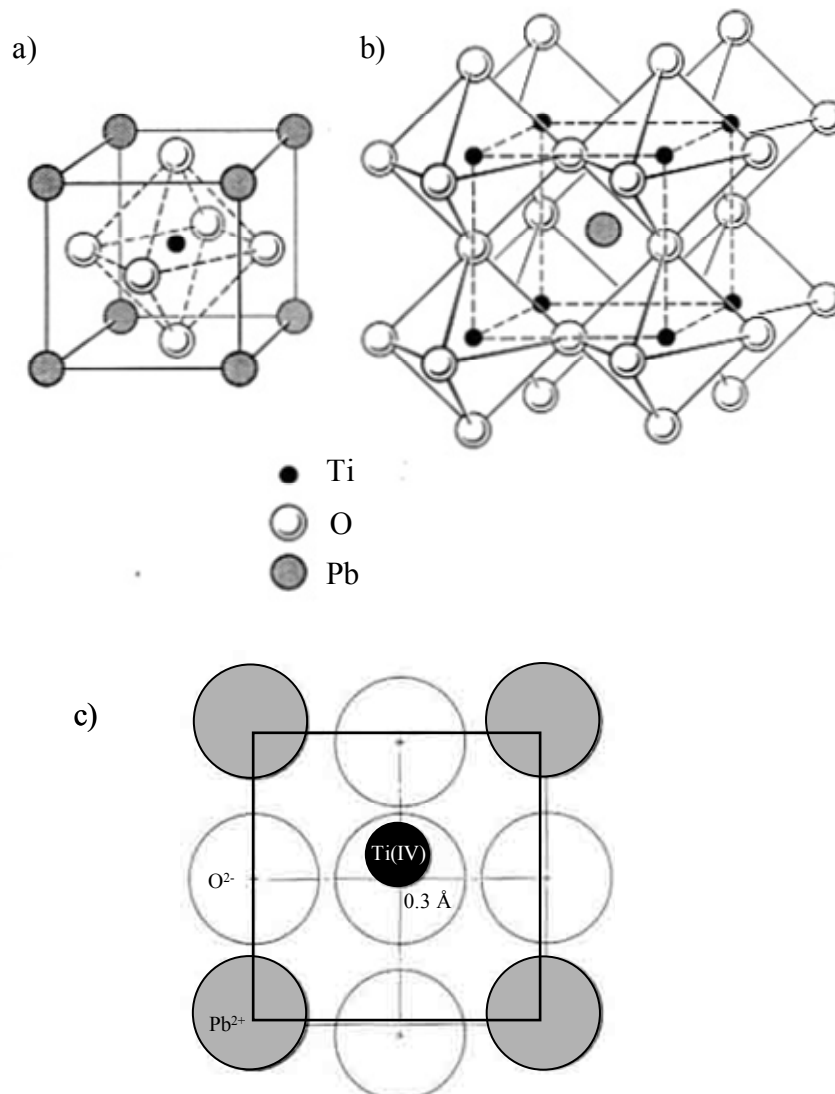


Figure 1.5. Different representations of the PbTiO_3 perovskite unit cell

The PbTiO_3 perovskite structure consists in a cubic close-packed arrangement of large Pb(II) (A-site) and O ions with smaller Ti(IV) (B-site) ions filling the octahedral interstitial positions (Fig. 1.5a). Thus, in the formula ABO_3 , A and B would be cations and O would be oxygen. This structure can be also regarded as corner-sharing oxygen octahedra (BO_6) arranged in three dimensions with smaller, highly charged Ti(IV) cations located in the middle of the octahedra, and lower charged, larger Pb(II) cations in between the octahedra (Fig. 1.5b).

The PbTiO_3 perovskite has a tetragonal structure at room temperature (space symmetry P4mm) and shows ferroelectric behaviour as consequence of the slight off-center displacement of the B-site cation ($\delta_{\text{ZTi}} = 0.30 \text{ \AA}$)²¹ respect to its body-centered position in the unit cell (see Fig. 1.5c). The high transition temperature (Curie point of 490 °C) of this compound together with its large tetragonality ($c/a \sim 1.064$), leads to a relatively high spontaneous polarisation at room temperature ($P_s > 50 \mu\text{C}/\text{cm}^2$). Above 490 °C, the PbTiO_3 system becomes cubic (space symmetry Pm3m), non-ferroelectric. Thus, when cooling from the paraelectric (cubic) to the ferroelectric (tetragonal) phase, a distortion of the oxygen octahedra is produced giving rise to the displacement of the Ti(IV) cation along the c-axis. This results in the appearance of an electric dipole moment along this direction (polar axis).

The inherent large anisotropy of lead titanate along the c-axis prevents the preparation of dense ceramics of pure PbTiO_3 , since the volume variation coming from the cubic-to-tetragonal phase transition is so high that causes cracking of the ceramic body during the cooling process after firing.²⁵ The difficulties in its preparation together with the high coercive field of lead titanate made that the first publications reporting switching measurements and ferroelectric loops on bulk materials appeared in 1970.^{26,27} In order to overcome this handicap, several modifier cations have been incorporated to the PbTiO_3 system to reduce the tetragonality of the system, but maintaining relative high values of polarisation. Thus, substitutions of Pb^{2+} by isovalent elements (Ca^{2+} , Sr^{2+} and Ba^{2+}) or off-valent donors (Bi^{3+} , La^{3+} , Sm^{3+}) have been carried out at the A-site of the perovskite, whereas substitutions of Ti(IV) by isovalent elements (Zr(IV) , Sn(IV)), off-valent donors (Nb(V) , Ta(V)) or off-valent acceptors (Mn(III) , Sc(III) , Fe(III)) are reported for the B-site. As example, interesting properties were found by McQuarrie in the 50s when studying several solid solutions of PbTiO_3 with substitutions at the A-site by Ca^{2+} , Ba^{2+} , Sm^{3+} and La^{3+} cations.²⁸ Also, the partial substitution of Ti(IV) by Zr(IV) have led to the most widely used ferroelectric material in the field of piezoelectric transducers nowadays, the Pb(Zr,Ti)O_3 (PZT) solid solution.²⁹ However, is in the 80 years of the past century when the first works on modified- PbTiO_3 bulk ceramics reporting

ferroelectric measurements are published. Thus, Takeuchi et al.³⁰ studied the viability of (Pb,Ln)(Ti,Mn)O₃ (Ln = rare earths) ceramics for piezoelectric applications with directional electromechanical coupling factors in ultrasonic transducers of medical diagnoses.

The partial substitution of Pb²⁺ by Ca²⁺ at the A-site of the perovskite leads to the calcium modified lead titanate system, (Pb_{1-x}Ca_x)TiO₃ (hereinafter, denoted as PCT), which has been the composition studied in this Ph.D Thesis. The first works about the effect of Ca²⁺ on the PbTiO₃ system concern structural features. In the 50s, Sawaguchi et al.³¹ confirmed a decrease on the tetragonality of the PCT system as the Ca²⁺ content increases, and the crystal structure was reported to be tetragonal at room temperature for compositions with Ca²⁺ contents between 0 and 40 at%, and cubic for compositions above 40 at%. However, another contemporary study³² indicated that the tetragonal phase seems to be present at room temperature for PCT compositions up to a 50 at% of Ca²⁺. Furthermore, a cubic phase for Ca²⁺ contents between 50 and 63 at%, and two-coexisting phases (cubic and antiferroelectric orthorhombic phases) from 63 to 77 at%, with only the orthorhombic phase present for remaining compositions, were proposed by these authors³² for the PCT system.

Thirty years later, in 1982, Yamashita et al.^{33,34} found the disappearance of the planar electromechanical coupling factor (radial mode $k_p \sim 0$) in (Pb_{0.76}Ca_{0.24})(Co_{0.5}W_{0.5})Ti_{0.96}O₃ bulk ceramics with a 2% of MnO, when increasing the polarisation voltage bias (45 kV/cm and 100 °C), together with high values of the transversal electromechanical coupling factor (thickness mode $k_t = 0.53$) and high piezoelectric d_{33} coefficient ($d_{33} = 63$). A high k_t/k_p ratio is thus obtained that practically eliminates the radial vibration modes of the bulk ceramic improving the resolution of the ultrasonic transducers that use this type of materials. Therefore and from the viewpoint of applications, these studies indicated that substitutions of Pb²⁺ by Ca²⁺ of 24 at% in the PbTiO₃ system seemed to be very promising, due to the high electromechanical anisotropy (k_t/k_p) obtained in bulk ceramics.³⁵ Also in the 80s, Yamamoto et al.¹¹ and Mendiola et al.¹² published a complete work on (Pb_{1-x}Ca_x)TiO₃ bulk ceramics with $12 \leq x \leq 50$, reporting permittivity and polarisation measurements, hysteresis loops, electromechanical coupling factors, electron diffraction analysis, microstructural features and domain observations. The results revealed that the increase of the Ca²⁺ content in the PCT system produces an appreciable increase of the dielectric constant at room temperature, an almost linear decrease of the transition temperature and a strong decrease of the spontaneous polarisation and coercive field. Furthermore, satellite spots owing to the presence of a superlattice structure were observed by electron diffraction in bulk ceramics with $x \geq 0.35$. This was

ascribed to the chemical ordering of the Pb^{2+} and Ca^{2+} cations in these PCT compositions. Now, the typical 90° domains of the tetragonal PbTiO_3 phase were observed for $x < 0.42$, and they could not be detected at higher Ca^{2+} concentrations, where only grain boundaries were observed.

Table 1.1 summarises the main properties of the $(\text{Pb}_{1-x}\text{Ca}_x)\text{TiO}_3$ bulk ceramics as a function of the Ca^{2+} content, according to the works reported by all these authors.

Table 1.1. Properties of the PCT bulk ceramics as a function of the Ca^{2+} content

Properties	Ca^{2+} content (x in $\text{Pb}_{1-x}\text{Ca}_x\text{TiO}_3$)			
	$x < 0.35$	$0.35 \leq x \leq 0.40$	$0.40 \leq x \leq 0.42$	$0.42 < x$
Dielectric permittivity (room temperature)	200	200-400	400-800	800-1500
Remanent polarisation ($\mu\text{C}/\text{cm}^2$)	25-30	25-30	20-15	10
Coercive field (kV/cm)	4	2.5-4	1	0.8
90° domains	Yes >>>	Yes >>	Yes >	No
Superlattice	No	Yes >	Yes >>	Yes >>>
Transition temperature ($^\circ\text{C}$)	~ 230	~ 140	~ 84	~ 34

The variation of the reticular parameters and of the tetragonality of PCT bulk ceramics, together with the thermal behaviour of the dielectric constant for different amounts of Ca^{2+} as reported in the literature, are depicted in Figure 1.6.

Note that until that time, the ferroelectric experiments on the PCT system with substitutions of Pb^{2+} by Ca^{2+} did not go beyond $x \geq 0.50$ (i.e. the 50 % of the Ca^{2+} content). In other words, the studies focused on the PbTiO_3 side of the PbTiO_3 - CaTiO_3 solid solution. It was in the 90s when first works dealing with the ferroelectric behaviour of PCT ceramics close to the CaTiO_3 side were reported.

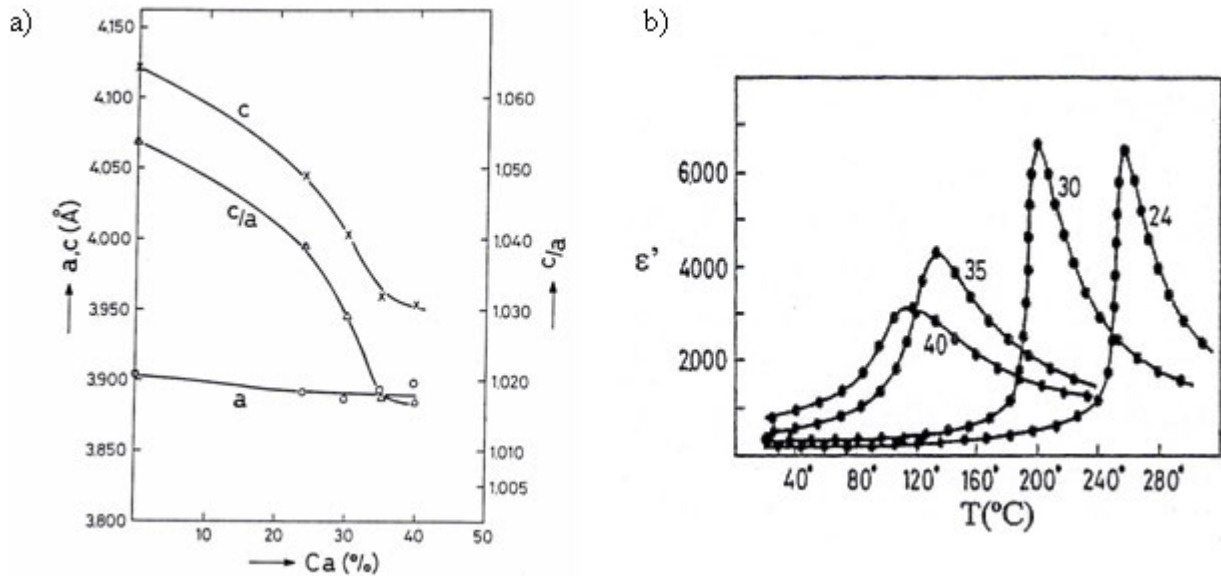


Figure 1.6. Lattice parameters (a) and dielectric constant with temperature (b) of PCT bulk ceramics as a function of the Ca^{2+} content

Thus, Eremkin et al.³⁶ proposed a phase diagram for the $(\text{Pb}_{1-x}\text{Ca}_x)\text{TiO}_3$ solid solution system with $0 \leq x \leq 0.62$ based on investigations carried out by optical studies (birefringence) on single PCT crystals. Now, these authors suggest the presence of three different crystallographic phases at room temperature in this system; i) a ferroelectric tetragonal phase for $x < 0.42$, ii) a ferroelectric orthorhombic phase for $0.42 < x < 0.48$ and iii) a non-ferroelectric orthorhombic phase for $x > 0.48$. Previous to this work, conflicting reports assumed the boundary between the ferroelectric and paraelectric phases to be located at $x = 0.38$,²⁸ $x = 0.50$,^{11,32,37} or $x = 0.60-0.62$ ³⁸ (at room temperature). In order to settle this controversy, different investigations were carried out on the structural features of the high-Ca PCT compositions ($x > 0.40$).

Thus, a tilting of oxygen octahedra³⁹ was proposed by some authors as responsible of the superlattice reflections observed in the electron diffraction patterns of PCT bulk ceramics with high Ca^{2+} contents, instead of the chemical ordering of the Pb^{2+} and Ca^{2+} cations.^{11,40-42} Ranjan et al.⁴³ concluded that the superlattice reflections observed in the room temperature powder neutron diffraction patterns of the $(\text{Pb}_{0.50}\text{Ca}_{0.50})\text{TiO}_3$ composition arise due to an orthorhombic distortion (space group Pbnm) resulting from tilted TiO_6 octahedra and off-center location of Pb^{2+} and Ca^{2+} cations. Recently, Chandra et al.⁴⁴ detected these superlattice reflections by means of x-ray diffraction on $(\text{Pb}_{1-x}\text{Ca}_x)\text{TiO}_3$ ceramic powders and refined the structure for a wide compositional range by Rietveld analysis. These authors confirmed the mechanism of antiphase and inphase tilt of

oxygen octahedra from $x \geq 0.421$, which leads to the orthorhombic structure with $a^-a^-c^+$ tilts (according to Glazer's notation)⁴⁵ for these PCT compositions. A representation of this tilting octahedra mechanism is schematically depicted in Figure 1.7.

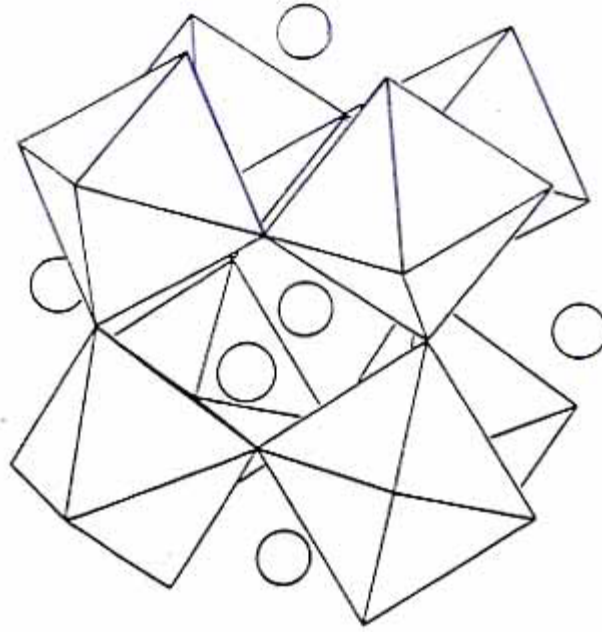


Figure 1.7. Representation of the oxygen octahedra tilt in the perovskite structure

Furthermore, the coexistence of both tetragonal and orthorhombic phases in the range of $0.40 \leq x \leq 0.60$ is also suggested by Chandra et al.⁴⁴. A maximum in the planar electromechanical coupling factor (k_p) has also been reported at this compositional range ($x \sim 0.42$), which seems similar to many other solid solution systems such as $(1-x)\text{PbTiO}_3-x\text{PbZrO}_3$ (PZT)⁴⁶, $(1-x)\text{Pb}(\text{Mg}_{1/3}\text{Nb}_{2/3})\text{O}_3-x\text{PbTiO}_3$ (PMN-PT)⁴⁷ or $(1-x)\text{Pb}(\text{Zn}_{1/3}\text{Nb}_{2/3})\text{O}_3-x\text{PbTiO}_3$ (PZN-PT)⁴⁸, where a maximum piezoelectric response for the Morphotropic Phase Boundary (MPB) region is observed. However, the presence of a MPB region in the PCT system has not been totally confirmed yet, and further studies are needed in this topic.

A proposed phase diagram for the $(\text{Pb}_{1-x}\text{Ca}_x)\text{TiO}_3$ system as a function of the Ca^{2+} concentration is shown in Figure 1.8, according to Eremkin's³⁶ proposal. It can be appreciated a narrow band near $x = 0.50$, where the morphotropic region (MPB) would be located.

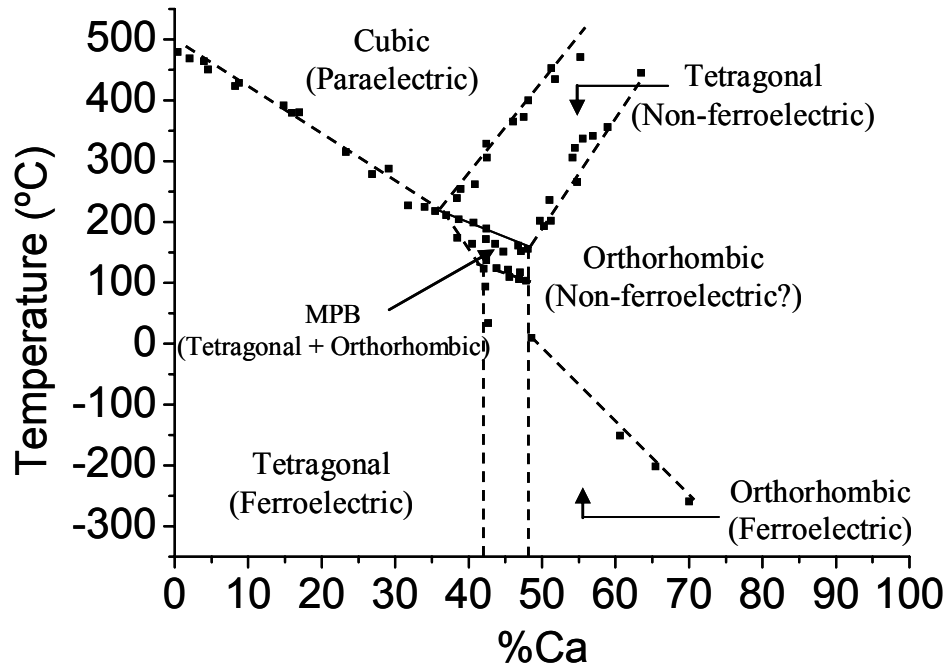


Figure 1.8. Phase diagram of the $(\text{Pb}_{1-x}\text{Ca}_x)\text{TiO}_3$ system with temperature as a function of the composition

The first indication of the relaxor character of PCT materials with Ca^{2+} contents close to 50 at% was reported by Ranjan in 1997.⁴³ Relaxor ferroelectrics differ from normal ferroelectrics by the presence of i) a broad maximum in the thermal dependence of the dielectric permittivity, ii) a frequency dependence of the maximum of the dielectric constant and iii) an important reduction on the dispersion of permittivity above T_m , as well as the existence of local polarisation above this temperature.⁴⁹ These characteristics were found in this work⁴³ from the dielectric studies of $(\text{Pb}_{0.50}\text{Ca}_{0.50})\text{TiO}_3$ bulk ceramics with temperature at various frequencies. The authors proposed the tilt of TiO_6 octahedra and the consequent off-center location of the A-site cations as the main causes to induce the appearance of internal random fields in the material that, if their size is too small, become stable against thermal fluctuations (similar to cluster dipole glass), thus frustrating the ferroelectric character of the system. These small random fields that form the domain structure of a relaxor ferroelectric are usually called *polar micro- or nano-regions*, depending on its size, and are responsible of the polarisation persistence up to temperatures well-above the transition temperature. Recently, Lemanov et al.⁵⁰ confirmed the relaxor character of the PCT system at $x = 0.65$, and suggested a MPB near $x = 0.65$, where both tetragonal and orthorhombic phases should coexist.

Furthermore, they reported that the $(\text{Pb}_{1-x}\text{Ca}_x)\text{TiO}_3$ system behaves as an incipient ferroelectric for $x \geq 0.72$, since the dielectric constant maximum does not appear at $-256\text{ }^\circ\text{C}$ (17 K) until increasing the amount of Pb^{2+} . However, in 2002 Jiménez et al.⁵¹ studied Co and W doped $(\text{Pb}_{0.55}\text{Ca}_{0.45})\text{TiO}_3$ bulk ceramics by neutron diffraction and, although the orthorhombic phase Pbnm of the superlattice was detected, they did not observe relaxor behaviour. The authors concluded that the appearance of Pbnm superlattice is not a sufficient evidence to produce a relaxor behaviour.

1.2.3. From ferroelectric bulk ceramics to thin films

The high dielectric constant found in BaTiO_3 capacitors in 1945 led to the first application of a ferroelectric material with industrial and commercial sights (BaTiO_3 piezoelectric transducer, U.S. Pat. No. 2 486 560).⁵² After the Second World War, the technical exploitation of ferroelectric bulk materials began, based on interesting properties such as a large dielectric permittivity, high piezoelectric and pyroelectric coefficients or non-linear optical effect.

At the beginning, ferroelectric materials were mainly fabricated as single crystals or bulk ceramics. Although the first studies on ferroelectricity were carried out on single crystals, the deal of research on these materials seems to decrease due to the difficulties that involves the preparation of high-quality single crystals and also to the high cost related to the crystal growth techniques.

By far, the largest number of applications using ferroelectric materials has been carried out on bulk ceramic form. As example, ferro-piezoelectric bulk ceramics show a wide range of applications including, for instance, monolithic multilayer capacitors (MLC), piezo-motors (buzzers, loud speakers, actuators), piezo-generators (accelerometers, power supplies, sensors), pressure-sensors (sonars, medical ultrasounds) and resonant devices (ultrasonic cleaners, surface acoustic wave filters).²

However, the 70s witnessed the evolution of the electronic industry towards the miniaturisation of the electronic components, which led to the development of new thin film deposition techniques for ferroelectric oxides. Obviously, thin films are better integrated into the as-low-as-possible scale of microelectronic devices rather than bulk materials are. Ferroelectric thin film devices perform the same electronic functions with only a fraction of the volume of devices based on bulk ceramics or single crystals elements. Furthermore, films are processed at temperatures of several hundred of degree Celsius lower than those used for sintering bulk ceramics, which can be a deciding factor in their applicability. Finally, thin films are convenient

integrated with semiconductor IC technology, showing additional benefits such as lower operating voltages, higher speeds and micro-level designing, and therefore new areas of applications have been identified for these materials (non-volatile memories for computer charge storage, infrared sensors, micro-actuators, multilayer capacitors, etc),⁵³ which will be shown in the next section.

The trend towards the miniaturisation of ferroelectric materials arisen during the last years, as well as their applications related to the material size and form, are summarised in Figure 1.9.

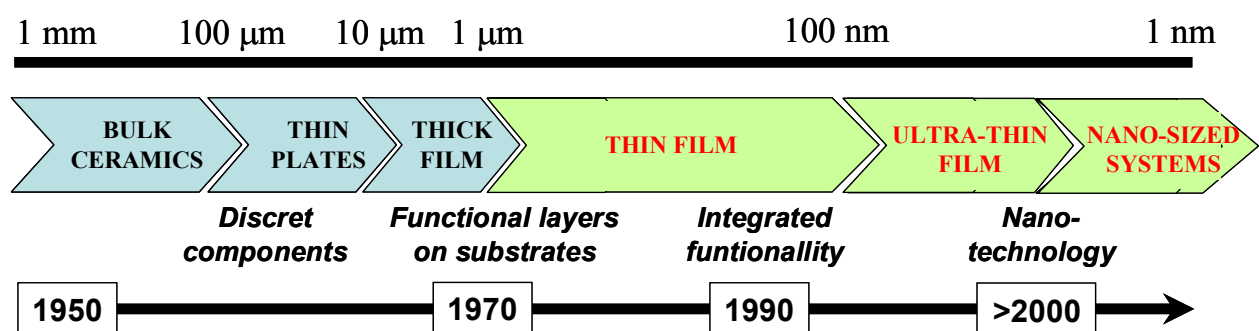


Figure 1.9. Towards the miniaturisation of ferroelectric materials and their integration into microelectronic devices

1.2.4. Applications of ferroelectric thin films

As stated in the previous section, applications involving microelectronic devices are mainly restricted by size limitations and by the needs to process functional materials directly onto integrated circuits. To satisfy these requirements, the development of new materials during this period of time was focused on the conformation (i.e. from bulk to films) rather than on the composition. Thus, almost all the current compositions used in the preparation of ferroelectric thin films have their beginnings in the counterpart bulk ceramics. Early ferroelectric thin films based on the BaTiO_3 composition were fabricated by vacuum deposition techniques (e.g. flash or multi-source evaporations).^{54,55} Afterwards, films of barium strontium titanate $(\text{Ba,Sr})\text{TiO}_3$ (BST), lead zirconate titanate $\text{Pb}(\text{Zr,Ti})\text{O}_3$ (PZT), lead lanthanum zirconate titanate $(\text{Pb,Lu})(\text{Zr,Ti})\text{O}_3$ (PLZT), lead titanate PbTiO_3 (PT), bismuth titanate BiTiO_3 (BIT), strontium bismuth tantalate $\text{SrBi}_2\text{Ta}_2\text{O}_9$ (SBT), lithium niobate LiNbO_3 or potassium niobate KNbO_3 , as most important, have been prepared by different film deposition techniques.

Here, some of the main applications of ferroelectric thin films are stated based on the multifunctional properties that these materials exhibit (i.e. high permittivity, ferroelectricity, pyroelectricity and piezoelectricity).

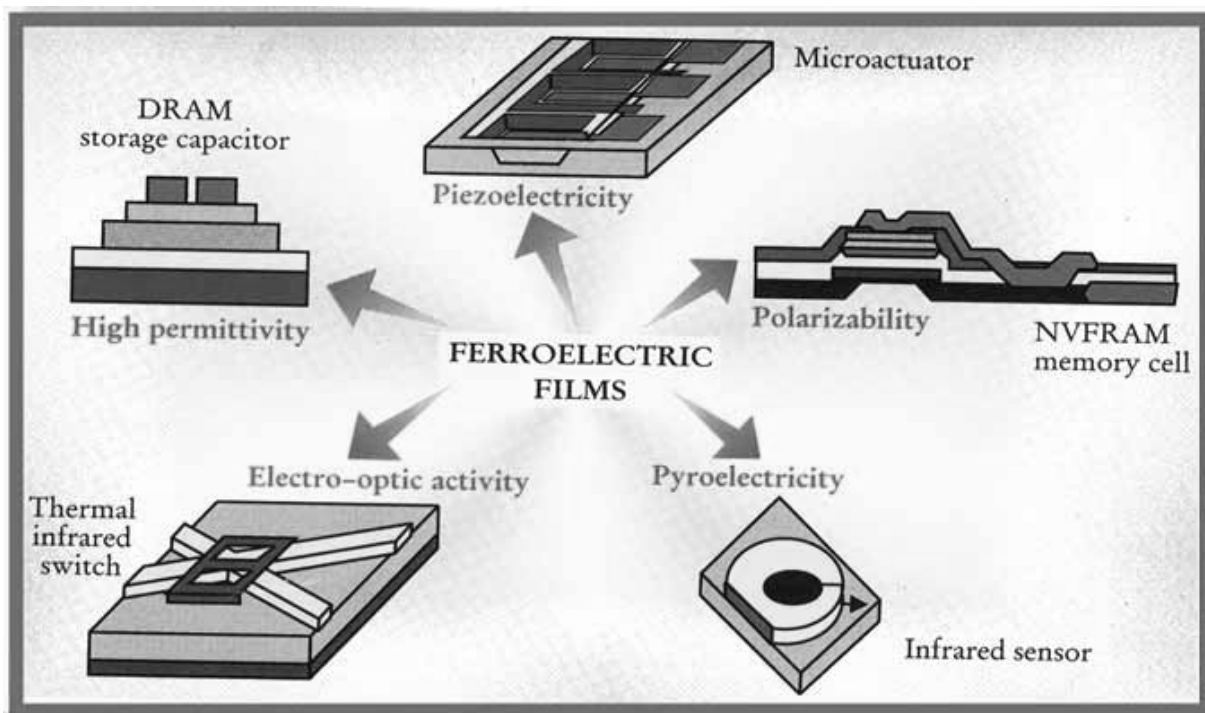


Figure 1.10. Applications of ferroelectric thin films

1.2.4.1. Computer memories

At the present time, the microelectronic industry is based on the technology of silicon which, after reacted with oxygen or nitrogen in a controlled manner, leads to the formation of high-quality insulators used as i) capacitor dielectrics for information storage in *Dynamic Random Access Memories (DRAMs)* and as ii) transistor gate dielectrics in Complementary Metal-Oxide Semiconductor (CMOS) field-effect transistor (FET) logic devices.⁵⁶ However, the trend towards the progressive miniaturisation of these devices (in order to increase its computational capability at a low cost) makes that the thickness of SiO₂, or Si-O-N, had to be reduced (it is predicted that below ~2 nm for 2012)^{15,57}. This scaling trend will hit fabrication and performance problems (e.g. pinholes⁵⁸⁻⁶⁰ or tunnelling effects that lead to high leakage current densities^{57,59}) which predict a near-term end of silicon devices. One solution to this problem is the replacement of the SiO₂ insulator by ferroelectric oxides.

The high dielectric constant of ferroelectric materials makes them potential candidates for DRAMs applications. This device works very simply by using a submicron-sized capacitor, representing 1 bit of memory, to store a given amount of electrical charge. If the charge is present, it represents a digital “1”, if not, then the bit is a “0” (Boolean algebra). Therefore, the logic states of the memory are associated to the charge and charge-release of the capacitor. It is accepted that a DRAM is volatile and charge must be refreshed many times per second (“dynamic” memory), hence the importance of low leakage current densities present in the capacitor. Materials used for DRAMs moreover should not exhibit polarisation-voltage hysteresis loop.⁶¹ Prototypes of 64-megabit DRAM memories based on BST capacitors have been developed by Matsushita Electric Company. Other materials such as PZT, PTL and PLZT have been also studied.⁶²⁻⁶⁴

The ability of ferroelectric materials to switch their polarisation direction between two stable polarised states provides the basis for the binary code-based *Non-Volatile Ferroelectric Random Access Memories (NVFeRAMs)*.⁶⁵ Each IC memory bit has associated with it a ferroelectric capacitor, that will “remember” the memory state (e.g. $+P_r$ for “1” and $-P_r$ for “0”). Within this multi-billion dollar/euro market, PZT, SBT and lanthanum bismuth titanate $(\text{Bi,La})_4\text{Ti}_3\text{O}_{12}$ (BLT) are the three presently most investigated ferroelectric multimetal oxide materials for the fabrication of NVFeRAMs,^{66,67} developed by companies like Samsung and Siemens at present. Applications of embedded these memories in smart IC cards are produced and sold in the market by Matsushita, Panasonic, NEC and Rohm.

1.2.4.2. High-frequency components

The interest in the potential use of ferroelectric thin films in tunable high-frequency (microwave, radio-frequency) components has reemerged since the past decade due to their applications in miniaturised microwave components and integrated microelectronic circuits. This could be exploited into two directions, mainly; consumer portable communications (e.g. mobile phones) and radar systems (e.g. phased array antennas).

The interest of tunable ferroelectrics for their use in these devices lies on the strong dependence of their dielectric constant with the applied bias electric field. Tunability is defined as the ratio of the dielectric constant of the material at zero electric field to that at some non-zero electric field. Ferroelectric thin films used as tunable capacitors (i.e. *varactors*), require high tunabilities, low dielectric losses and low temperature dependence of the tunability.⁶⁸ Thus, high

dielectric constant materials (normally in the paraelectric phase) lead to large values of tunability, although dielectric losses and temperature dependence of these materials are also higher. However, these losses are lower than those exhibited by semiconductor varactors, together with the better power handling and lower consumption of the formers.

High-frequency waves phase shifters are one of the major applications of ferroelectric tunable components. They are used in phased array antennas, consisting in thousands of phase shifters which control and modify the width and the angle of the steered radar beam. Thus, the phase velocity of the electromagnetic wave that passes through the phase shifter (i.e. the ferroelectric thin film) is controlled by the applied dc electric field (via changing the dielectric constant of the film, which in turn controls the wave velocity).⁶⁹ Therefore, the frequency of the electromagnetic wave can be tuned. Among the scarce literature reported for tunable ferroelectric thin films, the BST composition is considered at present as the main alternative for these applications,^{69,70} but device manufacturing is still to come.

1.2.4.3. Infrared sensors

This is one of the areas in which ferroelectric materials have a clear commercialisation potential. Infrared sensors are based on the pyroelectric effect, that is, the change on the temperature of the ferroelectric thin film produced by the infrared radiation that leads to the generation of an electric current (signal) in the material. This can be used in applications such as fire/intruder alarms, older population fall detection and thermal imaging (uncooled infrared cameras).^{71,72}

These devices are more sensitive in thin film form rather than in bulk ceramic, since the small amount of mass displayed by the former leads to a lower thermal capacity, which improves the infrared detector resolution. Furthermore, ferroelectric thin films show the ability to operate at room temperature (“uncooled” detectors), in opposite to the semiconductor materials traditionally employed in these applications that require cooling below $-173\text{ }^{\circ}\text{C}$ (100 K) to reduce thermal noise.

Films based on lead titanate (PT) and modified lead titanate compositions such as PZT, $(\text{Pb},\text{La})\text{TiO}_3$ (PTL) and PCT are the most widely ferroelectric materials used for these applications.⁷³⁻⁷⁵ Pyroelectric thin film-based sensor arrays for uncooled thermal imaging have been fabricated by Siemens and GEC-Marconi companies.

1.2.4.4. MicroElectroMechanical Systems (MEMS)

In recent years, a great deal of novel applications have been collected under this name (MEMS), which are based on the piezoelectric properties of ferroelectric thin films combined with the silicon integration in microelectronic devices.^{76,77} Thin film piezoelectric materials offer a number of advantages in MEMS, due to the large motions that can be generated (often with low hysteresis) the high available energy densities and the low power requirements.⁷⁸ Depending on the use of the direct or converse piezoelectric effect, sensor or actuator components are fabricated, respectively. Thus, a larger number of piezoelectric microdevices has been manufactured in the first field (sensors), such as pressure sensors, accelerometers and cantilevers for Scanning Force Microscopy (SFM). On the other hand, microactuators such as ultrasonic micromotors, micropumps and microfilters are more representative of the converse piezoelectric effect.

1.2.5. Preparation techniques of ferroelectric thin films

The interest in the preparation of ferroelectric thin films began in the 60s when films of BaTiO₃ were prepared by electron beam evaporation.^{54,55} Since then, different deposition techniques have been used for the fabrication of thin films.

Techniques used for deposition of films can be grouped into physical and chemical methods. First ones include sputtering or laser ablation as more relevant. Chemical methods mainly involve deposition in vapour state (chemical vapour deposition, CVD) and solution deposition (CSD), in which sol-gel and metalorganic decomposition (MOD) are included. Table 1.2, reported by R.W. Roy et al.,⁷⁹ shows the comparison of the main features of these techniques. A brief review of the details of the aforementioned techniques is given below.

Table 1.2. Comparison of main features of common methods of ferroelectric thin film preparation

Method	Deposition rate (Å/min)	Temperature (°C)	Stoichiometry (1-10)	Devices	Cost	Miscellaneous problems
RF sputtering	5-50	500-700	3	1-6	High	Negative ions
Magnetron sputtering	50-300	500-700	5	1-6	High	Target surface
Ion beam sputtering	20-100	500-700	8	1-6	High	Uniformity
Evaporation	100-1000	500-700	4	1-6	High	Rate control
Laser ablation	50-1000	500-700	6	1,3,5	High	Uniformity
MOCVD	50-1000	600	7	1-5	High	High substrate temperature
MOD	3000 (Å/coating)	500-800	9	1,3,5	Low	High annealing temperature
CSD Sol-gel	1000 (Å/coating)	450-750	9	1-5	Low	Multiple coating

Numerical scale for stoichiometry: 1-worst, 10-best

“Devices” number: 1-Capacitor, 2-Memory cell, 3-Actuator, 4-Electro-optic, 5-Pyroelectric, 6-Surface Acoustic Wave (SAW)

1.2.5.1. Sputtering techniques

In this technique, an electric field (of the order of kV) is applied to an inert gas (Ar, Xe) confined between a cathode and an anode under reduced pressure, thus generating a plasma of ions (usually positive gas ions) and electrons which is accelerated by the electric field towards the cathode (target) that contains the material to deposit. When the kinetic energy of the ions is high enough to overcome the lattice binding energy, some surface atoms are rejected from the target, and these ejected atoms are deposited onto any substrate (anode) placed in the flux. Thus, coatings with the same composition of the target are obtained. However, if reactive gases such as oxygen and/or nitrogen are used in this process (instead of an inert gas), depositions of oxides and/or nitrides compounds onto the substrate can be carried out. In the case of preparation of multicomponent systems, the target compositions have to be empirically modified to attain the desired film composition. Therefore, the target usually consists in pure metal or alloys compounds.

Within this technique, the term *dc sputtering* is normally used when the plasma is created from a dc power supply, whereas *rf sputtering* is named when radiofrequency sources are used. If magnetic fields are applied to confine the electrons to the target area, the sputtering system is called *magnetron sputtering*. Here, electron confinement increases the ionisation efficient, leading to high deposition rates.

Although sputtering techniques are very good for epitaxial growth of thin films,⁸⁰ difficulties related with the control of the physical and chemical properties of the film (i.e. stoichiometry, crystal structure, microstructure and uniformity over large areas) are found. Furthermore, expensive and complicated equipment is usually required.

1.2.5.2. Laser ablation

This technique is also known as Pulsed Laser Ablation Deposition (PLAD) method, and it has only recently been extensively applied to fabricate ferroelectric thin films as logical extension to the work done on the deposition of high critical temperature superconductors films.⁸¹ It is based on the use of a high-energy pulsed excimer (or Nd:YAG) laser beam which is directed to a target located in a vacuum chamber in such a way that it impacts on the target surface. The impact of the laser beam on the target surface results in various processes including ablation, melting and evaporation of the material, and production of a plasma due to the excitation and ionisation of the

species ejected from the target by the laser photons. The material ejected from the target is then deposited on a substrate generally positioned opposed.

The main advantages of this technique are the ability to work at low temperatures (200 °C),⁸² the high deposition rates obtained and the possibility to use reactive atmospheres (using air or certain gases instead of vacuum) or post-deposition annealing (700-800 °C) to improve film properties.

On the other hand, the difficulty to deposit high surface areas and the presence of macroscopic fragments on the coating coming from the target, are the major problems related to this technique.

1.2.5.3. Chemical vapour deposition

In Chemical Vapour Deposition (CVD) processes, precursors are thermally volatilised at reduced pressure and mixtures of the required precursors in vapour form are transported and deposited onto heated substrates. CVD techniques lead to high-quality thin films, especially when organometallic precursors are used (i.e. MetallOrganic Chemical Vapour Deposition, MOCVD). The use of these precursors (e.g. alkyls, aryls, etc) allows working with substrate temperatures not too high (< 600 °C), since these compounds have higher vapour pressures at lower temperatures than do inorganic precursors usually employed in common CVD.⁸³

It is considered a chemical technique, since coatings are obtained by the reaction among the different compounds present in the chamber. If this process is carried out in the vapour state, the CVD reaction would be homogeneous, whereas if the reaction of the constituent elements of the film is developed onto the substrate surface (e.g. a decomposition), it would be called heterogeneous CVD.

The CVD process can be extremely reproducible once conditions are established to produce a film with a particular composition and crystal structure. However, CVD techniques tend to be strongly influenced by gas flow rate, gas pressure and precursor evaporation rates.⁸⁴ This leads to compositional variations between the source and the film, giving rise to low compositional control of stoichiometry of the complex compositions typical of ferroelectric materials. However, this technique has important advantages in the fabrication of certain devices such as memories, since conformational deposits can be easily prepared by Metalloorganic Chemical Vapour Deposition (MOCVD).

1.2.5.4. Chemical solution deposition

First attempts on solution preparation of oxide-based ferroelectric thin films were carried out in 1976 by Fukushima et al.,⁸⁵ reporting a partially sol-gel and partially organometallic solution process for BaTiO₃ thin films. Subsequent publications by Fukushima et al.⁸⁶ on Metalloorganic Decomposition (MOD), and Budd et al.^{87,88} and Lipeles et al.⁸⁹ on sol-gel processing of simple (PbTiO₃ and PbZrO₃) and complex (Pb(Zr,Ti)O₃ and (Pb,La)(Zr,Ti)O₃) perovskite thin films, date the development of Chemical Solution Deposition (CSD) methods for electronic multi-oxide thin film preparation to the early middle 80s.

Since that date, the number of publications on CSD processing of ferroelectric thin films has grown exponentially, and compositions such as PbTiO₃ (PT), Pb(Zr,Ti)O₃ (PZT), (Bi,La)₄Ti₃O₁₂ (BLT), (Pb,Ca)TiO₃ (PCT), xPb(Mg,Nb)O₃-(1-x)PbTiO₃ (PMN-PT) and SrBi₂Ta₂O₉ (SBT), as more relevant, are nowadays prepared by CSD methods.⁹⁰⁻⁹⁵ The main advantages of these methods are the high compositional control (stoichiometry) and homogeneity of the solutions, the large surface areas deposited or the low cost associated with the materials and experimental setup.

In general, the typical CSD process involves the initial synthesis of a stable, homogeneous precursor solution that contains the multi-metal precursors dissolved in appropriate solvents with the desired molar ratio. Then, this solution is deposited onto the substrate by different coating techniques obtaining the as-deposited film, which is afterwards dried, pyrolysed and crystallised by a thermal treatment. Thicker films can be obtained by successive deposition, drying and annealing of single coatings (layers).

The different and numerous chemical solution strategies used in the fabrication of electronic oxide films can be grouped into three main categories; *Metalloorganic Decomposition (MOD)*, *classical sol-gel processes* and *hybrid routes*. They basically differ on the procedure followed to obtain the precursor solution and the reactions that occur during thermal annealing of the film.⁹⁶

Metalloorganic Decomposition (MOD). The main basis of this process is the use of large carboxylate or β -diketonates reagents, such as 2-ethylhexanoates, neodecanoates and di-methoxy di-neodecanoates. Each of these compounds is dissolved in a common solvent, usually xylene, leading to stable solutions which are then combined in the desired stoichiometric ratio. A fundamental aspect of this technique is the no interaction of the starting compounds among them and neither with the solvent, since these chemical reagents are usually water-insensitive and therefore they do not display oligomerisation behaviour, such as in the case of sol-gel. Both features

make the resulting MOD solutions a simple mixture of components, and hence the solution chemistry involved is considered very straightforward.

However, the large organic ligands used in MOD processing may cause cracking of the thin films, due to the large weight losses and shrinkage phenomena that occur during the thermal treatments. Furthermore, the minimal reactivity of the starting reagents makes that the ability to tailor the physicochemical properties of the solutions to obtain films with improved properties (e.g. structure, microstructure), would be a hard task, restricting process flexibility. The use of short chain carboxylates (e.g. acetate) and β -diketonates (e.g. acetylacetonate) seems to minimise the problems related to cracking.⁹⁷ MOD processing has received special attention in the preparation of Aurivillius phase $\text{SrBi}_2\text{Ta}_2\text{O}_9$ and related materials.^{98,99}

Sol-gel processes. The sol-gel methodology has been historically applied to the field of silica, using the alkoxide TEOS (tetraethylorthosilicate) and the solvent ethanol as most frequently used reagents. In the field of electroceramics, perovskite films have been obtained by sol-gel processing using suitable metallorganic precursors (e.g. alkoxides) which are dissolved in organic solvents (e.g. alcohols) and undergo primarily hydrolysis and polycondensation reactions, in which metal-oxygen-metal (M-O-M) bonds are formed:



Another key issue in this process is the alcohol exchange reaction that occurs, resulting in a decrease in the hydrolysis sensitivity of starting reagents:



Alcohol exchange

On the contrary to the MOD process, the sol-gel chemistry involves the reaction among the starting compounds and allows the easy manipulation of the above reactions by controlling the chemical reagents, catalysis and hydrolysis conditions.

Although other organic compounds are also employed, alcohols are the most extensively used solvents in the sol-gel processing of electronic multi-metal oxides. Processes based on 2-methoxyethanol, $\text{CH}_3\text{OCH}_2\text{CH}_2\text{OH}$ (MOE), present some advantages such as the easy dissolving of carboxylate precursors (acetates) and the alcohol-exchange reaction with the starting reagents that

results in a lowering of the hydrolysis sensitivity. This solvent has been widely used in the sol-gel preparation of ferroelectric thin films, giving place to the synthetic method known as “*methoxyethanol route*”.^{87,88,100} However, as the majority of the organics solvents used in CSD methods, 2-methoxyethanol presents safety hazards (is a known teratogen) and therefore, the use of this solvent in most manufacturing facilities is forbidden.

Since the past decade, the replacement of 2-methoxyethanol by others solvents is being reported,^{92,101,102} trying thus to solve problems related to the toxicity and moisture-sensitivity of the methoxyethanol route.

Hybrid processes. The use of short-chain carboxylate A-site precursors (e.g. acetates) and B-site alkoxide compounds in the sol-gel processing of perovskite-type (ABO_3) solutions is the main characteristic of “hybrid” processes. In addition, the B-site alkoxide species used in these processes are usually modified through reactions with other reagents, such as acetic acid, acetylacetone or amine compounds. The resulting modified alkoxides are less sensitive towards hydrolysis and solutions are therefore more easily handled in air.¹⁰³

Hybrid routes also include “chelate” processes because the chelation reaction is the one of the features that defines the solutions obtained by these processes. Furthermore, hydrolysis and condensation of the oligomeric species obtained are also carried out during the synthesis, which results in a rather complexity of the solution chemistry involved. The presence of acetate ligands in these alcoholic solutions can also lead to esterification, which is proposed to be one of the mechanisms responsible of the aging phenomena exhibited by hybrid solutions.¹⁰⁴ In spite of this, a large number of research groups routinely use sol-gel hybrid processes as the primary method for thin film fabrication.

In all the cases, the fabrication of thin films from chemical solutions (CSD) involves different steps that are detailed below. A schematic representation of these steps, for perovskite titanate solution precursors, is illustrated in Figure 1.11, according to Schwartz et al.⁹⁶ A brief description of the main physicochemical features involved in each step will be also stated below.

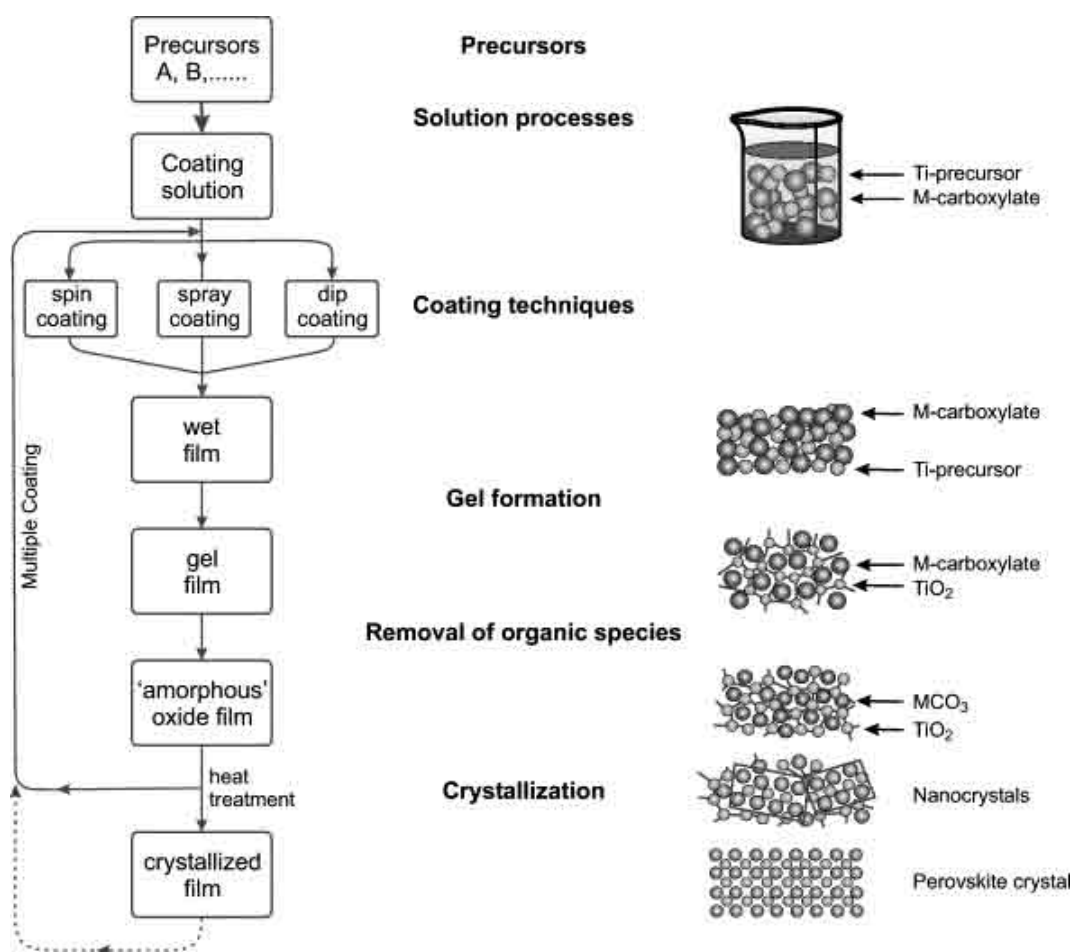


Figure 1.11. Flow chart of a typical CSD process, with representative drawings of the structural status evolution of the metal components during the process (right-hand)

a) Synthesis of the precursor solutions

Precursor solutions can be prepared from the different chemical solution approaches (MOD and sol-gel and hybrid processes) previously described. These solutions must fulfil some requirements such as a high solubility of the metal precursors in the solvent used, a high degree of homogeneity (stoichiometry), optimum rheological properties (e.g. viscosity, flow behaviour) to obtain high-quality coatings and a long-term stability to avoid non-reproducible results. It has been demonstrated that the structure of the species in the solution can affect and even resemble that of the final crystalline phase of the film.¹⁰⁵⁻¹⁰⁸ Thus, a high level of molecular homogeneity would be required to improve the characteristics and the properties of the resulting crystalline films.

b) Deposition of the precursor solutions onto a substrate

Different techniques such as spin-coating, spray coating or dip-coating can be used for the deposition of the solution onto a substrate.⁹⁶ An illustration of these coating techniques is shown in Figure 1.12.

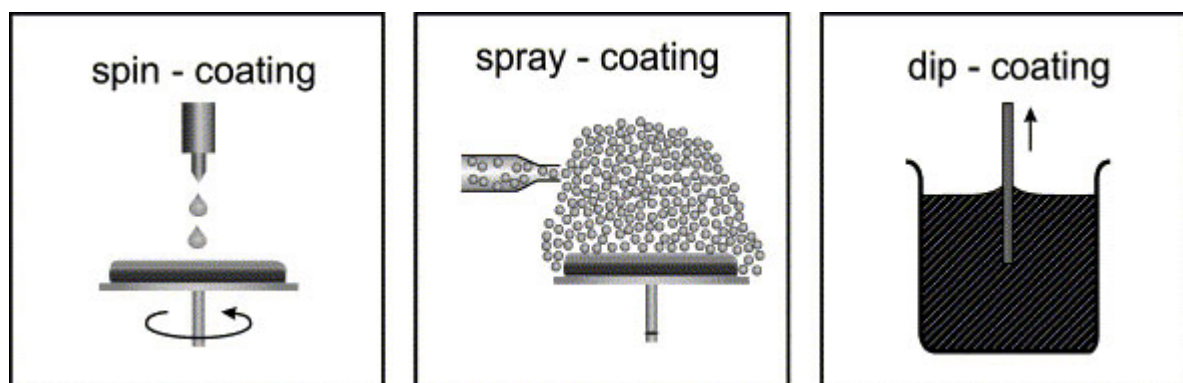


Figure 1.12. *Different coating techniques used for the deposition of thin films*

The spin deposition is probably the most widely used coating technique for the preparation of films. It consists in the deposition of few drops of the solution onto a substrate, which is held on a photoresist spinner. When the spinner is rapidly accelerated, a large centrifugal force is produced that spreads the liquid onto the substrate obtaining a thin and homogeneous layer. Parameters such as the angular velocity of the spinner and the spinning time, besides the solution rheology (i.e. spinnability), affect the final characteristics of the deposited layer (thickness, roughness, etc).

When coatings with non-planar shapes (e.g. steps, stacks or trenches) are required, the film deposition is usually carried out by spray-coating. The coating solution is here converted into an aerosol of small droplets (~100 nm) by an ultrasonic nebulizer or Venturi nozzle, which afterwards is directed by a carrier gas to the substrate surface in which is deposited by gravitation or, more efficiently, by an electrostatic field.¹⁰⁹ In comparison to the other coating-techniques, the rheology of the solution plays a critical role in the spray-coating technique, and normally the viscosity of the coating solutions must be reduced to enhance the nebulizing process.

In dip-coating the substrate is immersed into the solution, and a layer is then obtained either by removing the substrate from the solution or by draining the solution.¹¹⁰ The wet coating leads to the formation of a continuous film after drainage and solvent evaporation. Here, the velocity rate of

substrate withdrawal and the physicochemical characteristics of the solution (viscosity, volatilisation, surface tension) influence the final film thickness. As major disadvantages, a large amount of solution is required and cross contamination can be obtained when multiple deposition is carried out.

Once the solution layer has been deposited by any of the coating techniques described above, the gelation of the film is normally occurred short afterwards. Three types of films can be distinguished depending on the gelation behaviour that is produced. In *chemical gel films*, the formation of chemical bonds among the oligomeric species is produced during or just after their deposition by polymerisation or polycondensation reactions. *Physical gel films* are obtained when gelation is produced by physical aggregation of the oligomers by Van der Waals forces or steric interactions. Therefore, these films can still be redissolved in their parent solvents until condensation reactions with time occurred, and these films become then chemical gels.¹¹¹ Finally, when solvents with a high boiling point (low volatilisation) and precursor species with a low reactivity towards polymerisation are used, *non-gelling films* are obtained, which are characterised by their “wet” appearance after deposition.¹¹² The solvent evaporation in these films occurs at similar temperatures at which pyrolysis starts.

c) Removal of organic species

The as-deposited sol-gel film generally retains solvent still entrapped within the gel network, together with a significant organic fraction. Two general approaches have been used to convert the as-deposited film into the crystalline perovskite phase; the single-step process and the two-step process. During these processes, M-O-C (or M-O-H) bonds of the aggregated oligomeric species must be broken (via dehydration, thermolysis and/or pyrolysis reactions) and M-O-M bonds are formed by rearrangement of the species to form an inorganic amorphous film which must be subsequently crystallised in the desired oxide phase (i.e. perovskite).

In the *single-step process*, the film is heated directly to the crystallisation temperature, which results in both organic removal (pyrolysis) and perovskite crystallisation. High heating rates are usually applied, >100 °C/s (Rapid Thermal Processing, RTP), which enhance thin film densification by delaying the onset of organics removal and crystallisation to higher temperatures.^{111,113} Thus, both processes could occur within time spans as short as 15 s and therefore, formation of intermediate phases is not favoured.

In the *two-step process*, the removal of the organic species is carried out in a separate processing step at lower temperatures (200-400 °C) prior to a high-temperature crystallisation step. It has been proposed that this procedure allows the removal of the organic constituents prior to the collapse of the amorphous network, which minimises cracking and blistering. After pyrolysis of the films, crystallisation is subsequently carried out at higher temperatures.

d) Film crystallisation

Since in the majority of cases pyrolysed films are typically amorphous, crystallisation into the desired oxide phase at high temperatures is accomplished by nucleation and growth phenomena. Thus, the characteristics of these processes will serve to define the resulting microstructure in the film. Films that display microstructures where only interface nucleation of the crystalline phase has occurred (i.e. heterogeneous nucleation), are frequently columnar in nature, whereas those in which nucleation is produced within the bulk film (i.e. homogeneous nucleation) are typically polycrystalline, formed by equiaxed grains.

From a thermodynamic point of view, the driving forces that rule the transformation from the pyrolysed amorphous film to the crystalline ceramic material play a critical role in defining the active nucleation events and, thereby, film microstructure.¹¹⁴ For example, to obtain highly oriented or epitaxial films, the film must be processed so that heterogeneous nucleation at the interface dictates the microstructure. Considering either heterogeneous or homogeneous nucleation of the film, this will depend on diverse parameters related with the free energy (ΔG) for the nucleation event of a perovskite crystal, such as its interfacial energy, the contact angle with the substrate and the driving force for crystallisation. Normally, the energy barriers for interface nucleation are lower than those expected for homogeneous nucleation.¹¹⁵ As crystallisation driving force is increased (e.g. via thermal treatment) bulk nucleation becomes as probable as interface nucleation. Furthermore, films with increased densification and larger grain sizes are obtained when high crystallisation temperatures are used.

To sum up, the thermal processing conditions can significantly affect the microstructure and therefore the functional properties of the (perovskite) thin film. It can be concluded that both kinetic and thermodynamic features of thermal treatments strongly influence the crystallisation of the film.

1.2.6. Motivation to fabricate PCT thin films by CSD

The first work dealing with PCT thin films was published by Yamaka et al.¹¹⁶ in 1988. These authors reported on the structural, ferroelectric and pyroelectric properties of $(\text{Pb}_{1-x}\text{Ca}_x)\text{TiO}_3$ thin films with $x = 0-0.40$ prepared by radio-frequency magnetron sputtering onto Pt/MgO and Pt/SrTiO₃ substrates. Thus, strongly c-axis (001) oriented films were obtained, which led to high values of spontaneous polarisation ($15-60 \mu\text{C}/\text{cm}^2$) and pyroelectric coefficients ($25-50 \times 10^{-9} \text{C}/\text{cm}^2\text{C}$) for Ca^{2+} concentrations between 10 and 40 at%. As it was expected, a similar behaviour to the counterpart bulk ceramics was obtained from the dielectric constant versus temperature measurements of the films, with a broad transition at $x = 0.40$. Furthermore, both polarisation and coercive field values decrease as the partial substitution of Pb^{2+} by Ca^{2+} is bigger. The results of this work showed the feasibility of the PCT films for high infrared detector performance.

By multiple-cathode radio-frequency magnetron sputtering, Maiwa et al.¹¹⁷ also prepared PCT films with a Ca^{2+} content of 30 at% onto Pt/Ti/SiO₂/Si and Pt/MgO substrates, obtaining $\langle 111 \rangle$ and mixed $\langle 001 \rangle / \langle 100 \rangle$ preferred orientations, respectively. Remanent polarisations of 22.5 and 41 $\mu\text{C}/\text{cm}^2$, and dielectric constant values of 225 and 175 were obtained for these films deposited on the Pt/Ti/SiO₂/Si and Pt/MgO substrates, respectively.

M.J. Martín et al.¹¹⁸ reported on PCT films with a Ca^{2+} content of 24 % prepared by pulsed laser deposition, obtaining remanent polarisations up to 30 $\mu\text{C}/\text{cm}^2$.

But, the most widely used method to fabricate PCT thin films has been the Chemical Solution Deposition (CSD) methods. Tsuzuki et al.¹¹⁹ were first to report on the sol-gel preparation of PCT thin films in 1991. Solutions were synthesised through the methoxyethanol route and deposited by dip-coating onto Si-based substrates. After thermal treatments between 500-700 °C for 1 h, films with remanent polarisations of 8 $\mu\text{C}/\text{cm}^2$ were obtained for compositions with substitutions of 20 at Ca%.

After then, a great deal of research has been carried out in the Chemical Solution Deposition of PCT films with Ca^{2+} contents of 24 at% at the “*Departamento de Materiales Ferroeléctricos*” of ICMM-CSIC (see refs. 9 and 120). The introduction of Rapid Thermal Processing (RTP), with heating rates up to $\sim 300 \text{ °C}/\text{s}$, for the crystallisation of the PCT films resulted in significant improvements in the films, such as the absence of undesired secondary phases or the minimised formation of detrimental interfaces between the ferroelectric layer and the substrate.¹²¹ The optimisation of the fabrication of $(\text{Pb}_{0.76}\text{Ca}_{0.24})\text{TiO}_3$ films led to improved ferroelectric properties

such as polarisation values of $25 \mu\text{C}/\text{cm}^2$, coercive fields of $82 \text{ kV}/\text{cm}$, pyroelectric coefficients of $20 \times 10^{-9} \text{ C}/\text{cm}^2\text{C}$, retention of $2 \mu\text{C}/\text{cm}^2$ after $4 \times 10^{11} \text{ s}$ and moderate fatigue (50% of polarisation loss after 4×10^{10} switching cycles).^{5,75,122} Recently, Poyato et al.⁷ obtained polarisation values of $43 \mu\text{C}/\text{cm}^2$ and pyroelectric coefficients of $42 \times 10^{-9} \text{ C}/\text{cm}^2\text{C}$ on $(\text{Pb}_{0.76}\text{Ca}_{0.24})\text{TiO}_3$ films RTP-treated at $650 \text{ }^\circ\text{C}$ and subjected to further thermal conditioning treatments. These values are optimum for ferroelectric and pyroelectric applications (e.g. infrared sensors). Furthermore, electromechanical properties of these films have also been studied, obtaining an effective piezoelectric coefficient d_{33} of $70 \text{ pm}/\text{V}$ (similar to that of the counterpart bulk ceramic), which also makes these films competitive to PZT ones in microelectromechanical applications (MEMS).¹²³

Other groups have also investigated the properties of chemical solution deposited PCT films. Seifert et al.^{6,124,125} prepared $(\text{Pb}_{1-x}\text{Ca}_x)\text{TiO}_3$ thin films with $x = 0-0.30$ using methoxyethanol as solvent. These authors studied the influence of the RTP treatment on the resulting porosity of the films, which led to a lowering of the dielectric constant ($k' = 60-80$) and an increase in the figure of merit for pyroelectric applications.

Pontes et al.¹²⁶ reported on the preparation of $(\text{Pb}_{0.76}\text{Ca}_{0.24})\text{TiO}_3$ thin films by a polymeric precursor sol-gel method based on the Pechini route, using the dip-coating technique for the deposition on $\text{Pt}/\text{Ti}/\text{SiO}_2/\text{Si}$ substrates. A remanent polarisation of $17 \mu\text{C}/\text{cm}^2$ and a coercive field of $75 \text{ kV}/\text{cm}$ were obtained in the films.

Works on the preparation and properties of PCT thin films have always placed emphasis on compositions with low Ca^{2+} contents, and their ferroelectric properties and pyroelectric and piezoelectric responses. However, a resurgent interest in PCT thin films has recently emerged, specifically for high Ca^{2+} contents ($> 40 \text{ at}\%$). These films should have a high charge storage and varactor characteristics that would be useful in DRAM and tunable components, respectively.

To the author's knowledge, PCT thin films with Ca^{2+} contents of $50 \text{ at}\%$ have not been reported until the present date. The reason for this may be related to the problems that the techniques used for the preparation of PCT thin films present when large Ca^{2+} contents have to be added to the PCT system. Physical deposition methods usually lead to films with a badly adjusted stoichiometry, because of the different vapor pressures of the elements and the preferential sputtering of Pb. In the case of solution methods, the low solubility of the calcium compounds in the solvents usually used in CSD (alcohols or carboxylic acids) is the main drawback for the synthesis of PCT solutions containing high Ca^{2+} concentrations.

In the fabrication of $(\text{Pb}_{0.76}\text{Ca}_{0.24})\text{TiO}_3$ thin films by CSD, calcium has been incorporated into the solution as a metal,^{119,127} an acetate^{120,128-130}, an acetylacetonate,¹³¹ a carbonate,^{126,132,133} or a nitrate^{128,134-136}. But, all these CSD methods have clearly shown the difficulty in preparing precipitate-free precursor solutions with Ca^{2+} contents over 30 at%. Only few authors have reported on the preparation of PCT films with a maximum Ca^{2+} content of 40 at% by CSD.^{129,132,137}

Therefore, the fabrication of PCT thin films with different Ca^{2+} contents is of interest first, from the technological point of view. The change of the Ca^{2+} content in the PCT perovskite is a way for tuning the properties of the resulting material. This opens a wide spectrum for the applications of $(\text{Pb}_{1-x}\text{Ca}_x)\text{TiO}_3$ thin films in multifunctional microelectronic devices. But, secondly, the preparation of PCT films with large Ca^{2+} contents by CSD turns into an important challenge, where basic and fundamentals studies on the preparation chemistry of these materials should be carried out for a better understanding of the properties of the films and their relation with the processing.

1.2.7. Low-toxic CSD methods

In 1992, the United Nations Conference on Environment and Development held in Rio de Janeiro (Brazil) addressed an international debate focused on worldwide environmental key issues.¹³⁸ With the aim to achieve a sustainable development, the global states should cooperate towards international agreements that respect the interests of all the citizens and protect the integrity of the global environmental and developmental system. The concept of *Ecomaterial* (abbreviation of “Environmentally Conscious Material”) was born under these circumstances and its development early affected the electroceramic materials field.

D. Xiao¹³ was first to introduce the basic points that must concern the environmentally conscious ferroelectric research. In the particular case of CSD methods, the solution processing should comprise non-hazardous substances with minimum environmental load. However, the majority of works reported on chemical solution preparation (mainly through sol-gel and MOD) of multimetal precursors¹³⁹⁻¹⁴⁵ use organic solvents that are recognised as: carcinogens (benzene), reproductive hazards (2-methoxyethanol, 2-ethoxyethanol), neurotoxins (toluene, n-hexane) or central nervous system depressants (xylene, butoxyethanol). These hazardous substances involve healthy and safety risks in addition to the environmental impact produced by the waste products or the generated byproducts.

A first approach to overcome this problem is the replacement of these hazardous substances by other compounds with identical functionality but a less degree of toxicity. Thus, although 2-methoxyethanol has been extensively used in sol-gel processing of perovskite films, this solvent is a known teratogen and its use in most manufacturing facilities is sometimes forbidden. Therefore, alternative sol-gel routes (mainly hybrid processes) in which the total substitution of 2-methoxyethanol by either carboxylic acids¹⁴⁶ (e.g. acetic acid) or glycols¹⁰¹ (e.g. 1,3-propanediol) have received increased attention because of the lower healthy risks that involved the manipulation of these solvents.

Thus, films of PZT and PLZT compositions have been prepared by an alternative MOD process, using the Deposition by the Aqueous Acetate Solution (DAAS) technique.^{97,147} Here, the hazardous metal 2-ethylhexanoates and di-neodecanoates reagents commonly used in this process are replaced by metal carboxylates and β -diketonates compounds. Also, stable aqueous solutions of BaTiO₃ and SrBi₂Nb₂O₉ (SBN) have been obtained by sol-gel processing using respectively a modified titanium alkoxide¹⁴⁸ (titanium bis(ammoniumlacto) dihydroxide), highly stable towards hydrolysis, or water-soluble complexes of citrate and ethylenediaminetetraacetic (EDTA) compounds¹⁴⁹. Powders of PZT have also been prepared by sol-gel from an aqueous based citrate-nitrate/oxynitrate process,¹⁵⁰ although NO_x gases are released during the processing.

Recently, a new aqueous solution-gel process for various ferroelectric thin films such as BLT, SBT, SBN and PZT has been reported.⁹² This method is based on the use of water, instead of any organic solvent, and coordinating ligands such as citrates and peroxides.¹⁵¹ These chelating agents show the ability to coordinate the different metal cations present in the solution, hence preventing their solvation by the water molecules that would lead to the uncontrolled hydrolysis and subsequent precipitation of the hydroxides/oxides formed.¹⁵²

But, the major environmental problem of electroceramic materials at present is ascribed to the design and fabrication of microelectronic devices basing on ferroelectric compositions containing lead. The RoHS directive¹⁴ (*“Restriction Of the use of certain Hazardous Substances in electrical and electronic equipment”*) of the European Parliament and of the Council mentions that *“from 1st July 2006 new electrical and electronic equipment put on the market does not contain lead, mercury, cadmiun...”*. These compounds are considered as hazardous substances with a potential environmental load.

The preparation of lead-free piezoelectric materials is apparently the simplest way to overcome that problem. Compositions based on alkaline niobates (LiNbO₃, NaNbO₃, KNbO₃),

barium titanate (BaTiO_3 , $\text{Ba}(\text{Ti,Zr})\text{O}_3$), bismuth sodium titanates ($\text{Bi,Na})\text{TiO}_3$ and Aurivillious strontium bismuth tantalate ($\text{SrBi}_2\text{Ta}_2\text{O}_9$) are the main candidates to replace lead based-on compositions (mainly PT, PZT and PMN-PT). However, lead-free ceramics have much smaller ferroelectric, pyroelectric and piezoelectric responses than lead-based ceramics.¹⁵³ Fortunately, “lead in electronic ceramic parts (e.g. piezoelectric devices)” has been exempted from RoHS directive for the next years.

A noticeable lowering of the processing temperature of the ferroelectric thin film is expected to reduce lead volatilisation (emission of toxic volatiles), besides energy consumption and thermal load. In general, amorphous films are usually converted into the crystalline oxide phase at high temperatures (over 550 °C). Low temperature treatments of solution derived layers only lead to films in which an incipient ferroelectric phase is immersed in a matrix containing organic residuals and second phases, which has a detrimental ferroelectric response. Different low-temperature CSD methods have been reported for preparing ferroelectric thin films,^{91,114,154-161} which are summarised in Table 1.3, and some of them described below.

Thus, T. Kijima et al.¹⁵⁶ prepared films from precursor solutions of a ferroelectric material (BT, SBT or PZT) containing Bi_2SiO_5 (BSO) in a high molar ratio to the ferroelectric phase. Crystallisation temperatures of ultrathin films (<25 nm thick) were lowered by 150-200 °C with the addition of BSO, which is expected to incorporate into the single perovskite phase of the ferroelectric. Well-saturated hysteresis loops were measured in these films prepared at 450 °C, at an applied voltage of 0.5 V.

Control of the solution chemistry has also been used for decreasing the processing temperature of ferroelectric films. It is known that the crystallisation of the PZT perovskite depends on the Zr and Ti ratio in the PbZrO_3 - PbTiO_3 solid solution. Crystallisation temperature decreases with decreasing Zr/Ti ratio. Thus, M. Kosec et al.⁹¹ prepared Ti-rich PZT and PLZT films at 400 °C, by controlling the structure of the precursors and the type of solvent.

Basing on the approach that activation energy for the nucleation of the perovskite is usually higher than that for growth, the nucleation rate of a perovskite film can be controlled by the introduction of a seeding layer that enhances this phenomenon. A. Wu et al.¹¹⁴ used nanometric crystalline PZT perovskite powders (seeds) dispersed in PZT sols to induce the perovskite formation at low temperatures. Single perovskite phase was obtained in the seeded films after treatment at 410 °C for 30 h, but appearance of ferroelectric hysteresis loops began at annealing temperatures of 500 °C ($P_r = 20.8 \mu\text{C}/\text{cm}^2$).

Table 1.3. Low-temperature CSD methods for ferroelectric thin films

Material	Method	Reference	Temperature (°C)	Pr ($\mu\text{C}/\text{cm}^2$)	Ec (kV/cm)	Observations
BaTiO ₃	Ferrons	155	200	0.06	38	Very poor ferroelectric response
PZT (52/48)	Bi ₂ SiO ₅	156	450	20	165	Only ultrathin films (<25 nm)
PZT (52/48)	Precursor type solution	91	400	20	66	Ti-rich PZT compositions
PZT (30/70)	Seeding layer	114, 157	430	36	66	Ti-rich PZT compositions Tested pyroelectric response ($\gamma \sim 1.8 \times 10^{-4} \text{ C}/\text{m}^2\text{K}$)
PZT (40/60)	Multi-annealing RTP and precursor type solution	158	450	8	47	Ti-rich PZT composition
PZT (52/48)	Low-pressure annealing	159	550	18	50	Only tested with IrO ₂ electrodes
(Pb,Ca)TiO ₃ (Pb,La)TiO ₃	PhotoChemical Solution Deposition	160	550	22	165	Tested piezoelectric response ($d_{33} \sim 30\text{-}40 \text{ pm}/\text{V}$)
(Pb,Ca)TiO ₃	PhotoChemical Solution Deposition	161	450	11	108	Tested up to Ca-contents of 50 mol% Tested pyroelectric response ($\gamma \sim 3.2 \times 10^{-4} \text{ C}/\text{m}^2\text{C}$)

Finally, Y. Fujimori et al.¹⁵⁹ reported on the low-pressure RTP to obtain PZT films onto IrO₂ electrodes at low temperatures. In this technique, the amorphous film is first treated by RTP at low temperature and low pressure to remove organics from the film. Then, the film is crystallised by normal pressure RTP, usually leading to films with homogeneous profile compositions and without dead-layers, thus improving electrical characteristics.

1.2.8. PhotoChemical Solution Deposition

PhotoChemical Solution Deposition (PCSD) is a promising technique for the fabrication of ferroelectric thin films at low temperatures. It appears collected in previous Table 1.3. The effects of the ultraviolet-light (UV) irradiation on sol-gel materials, together with the development of excimer UV lamps with narrow-band and high-density radiation have opened new ways in material processing during the last decade.¹⁶² Table 1.4 shows different UV-sources used in the literature for preparing materials. Most studies on UV-irradiation of sol-gel materials have been performed for the thin-film form, since the penetration depth of the UV photons is limited in the surface region of materials. Thus, the use of the UV-irradiation on sol-gel (or solution deposited) thin films is the main basis of the PCSD methods.

The fundamental effects induced by UV-light on sol-gel films and their applications are summarised in Figure 1.13. Energetic photons coming from UV lamps can lead to the thermal or electronic excitation of the substances present in the sol-gel film. Thermal excitation is relatively important when the local temperature at the surface is increased by irradiation with intense UV lights (phonon mode). However, UV lamps predominantly exhibit electronic rather than thermal excitation (photon mode). Therefore, the description of the main effects produced by UV-irradiation on sol-gel films will be focused basing on their electronic excitation.

Electronic excitation may lead to the activation of certain chemical bonds in the material. Structural changes, such as densification, crystallisation and reduction, can be achieved by UV-photons with energy above the bandgap of the material.

Table 1.4. *Ultraviolet light sources*

	Wavelength, nm (photon energy, eV)
<i>Incoherent</i>	
Ultrahigh-pressure mercury lamp (UHM)	270-460
High-pressure mercury lamp (HPM)	250-440
Low-pressure mercury lamp (LPM)	254 (4.9), 185 (6.7)
XeCl excimer lamp	308 (4.0)
KrCl excimer lamp	222 (5.6)
Xe ₂ excimer lamp	172 (7.2)
Synchrotron radiation	Soft X-ray ~visible
<i>Coherent</i>	
XeCl excimer laser	308 (4.0)
KrF excimer laser	248 (5.0)
ArF excimer laser	193 (6.4)

Thus, the excitation of an electron through the band gap of oxides involves the charge transfer from O^{2-} to M^{x+} . This excited state is usually deactivated through the recombination of free electrons and positive holes in the crystalline structure. However, in amorphous structures, this electronic excitation may produce the cleavage of M-O-M bonds, thus leading to the rearrangement of the gel network and consequent *densification* of the material. In 1992, the first work on UV-irradiated sol-gel films was reported by Ohisi et al.¹⁶³, in which the densification of amorphous Ta₂O₅ films by UV-irradiation was studied. UV-induced structural changes in SiO₂ gel films have also been ascribed to significant densification by dehydration.¹⁶⁴ A decrease in thickness and a variation of the refractive index of the SiO₂ film were thus produced by UV-irradiation.

The photo-induced charge transfer from O^{2-} to M^{x+} can also lead to *reduction* of the gel films. Furthermore, this phenomenon is particularly ascribed to the UV-irradiation, since reduction is not observed by regular annealing processes in air. As it was stated before, the bond cleavage by

UV-light in the gel network can result in formation of mobile oxygen atoms and in the release of oxygen, while the metallic component remains. Thus, reduction of In_2O_3 and ZnO sol-gel films by UV-light has been previously reported,¹⁶⁵ observing the formation of metal compounds in the irradiated film.

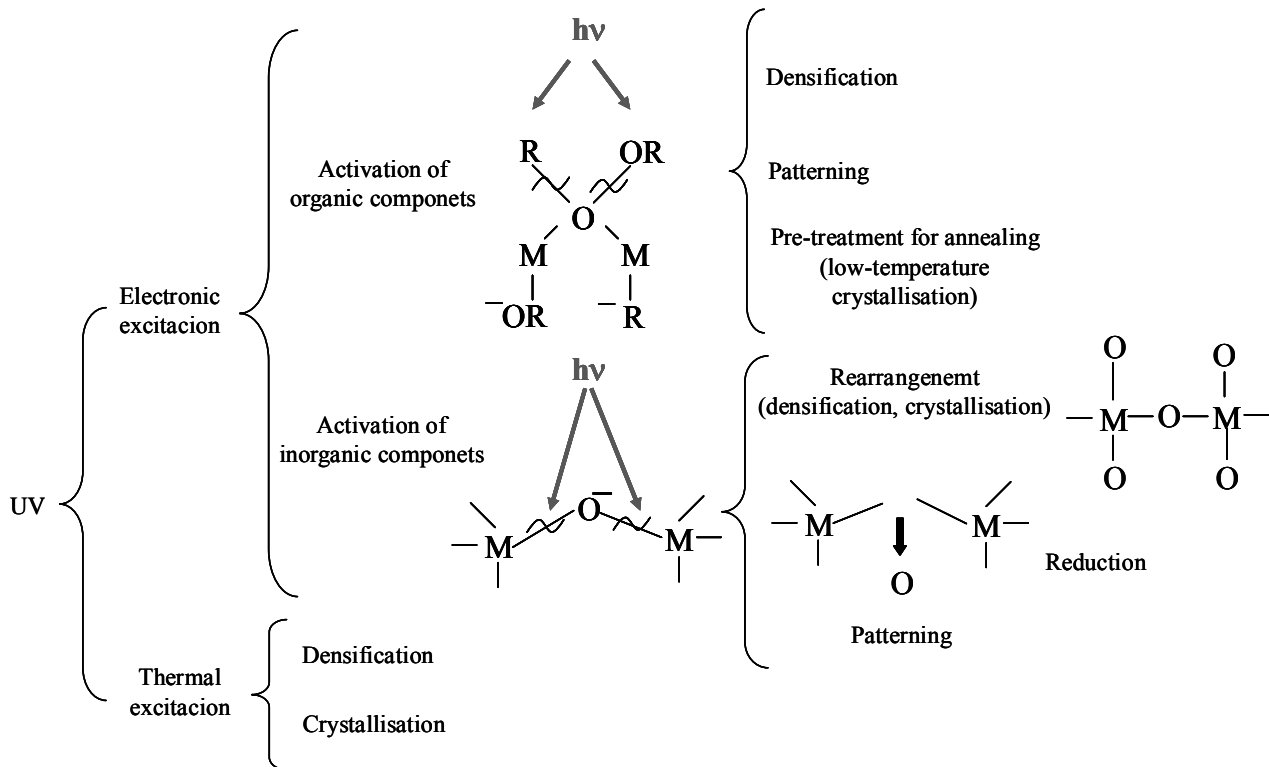


Figure 1.13. Fundamental effects induced by UV-irradiation and their applications

Photo-reduction can also produce the reaction of atmospheric water molecules (moisture) with defective sites of the material (oxygen vacancies), which results in the hydroxylation of the film surface. Highly hydrophilic surfaces have been induced by UV-irradiation in sol-gel ZnO films.¹⁶⁶

Another important application of the UV sol-gel photoannealing is the *micro-patterning* of oxide films. The method is based on the UV-irradiation of sol-gel films through a mask. Dissociated molecules are the products of reaction in the irradiated zones. These contain solvent-labile species that can be easily removed with polar solvents. By subsequent chemical etching, fine patterning on the gel film can be obtained that after its thermal treatment converts in a self-patterned oxide thin film. Ferroelectric films such as PZT ¹⁶⁷, BST ¹⁶⁸ and hybrid sol-gel materials¹⁶⁹ have been patterned by this technique.

Finally, activation of chemical bonds by UV electronic excitation can be used as a *pre-treatment for crystallisation* of sol-gel films. Although a heating process is required to obtain functional oxide films, UV-irradiation on the gel film prior to thermal treatment has been ascribed to improve the crystallinity of the annealed films, in which a lowering of the surface roughness has also been observed.¹⁶² But more important, quick decomposition and elimination of the organic species from the gel layer by the UV-irradiation may produce an advance in the crystallisation of the film. The majority of works reported on the low-temperature processing of films by this technique are focused on the fabrication of single oxide films (Ta_2O_5 , ZrO_2 or SiO_2).^{59,170,171} Until the present time, few publications are found in the literature on low-temperature UV-assisted sol-gel processing of ferroelectric films,^{160,172-174} although it would highly minimise the emission of contaminants to the atmosphere and also would promote the integration of the ferroelectric film with the Si-technology.

CHAPTER II

EXPERIMENTAL METHOD

PART 1. CALCIUM MODIFIED LEAD TITANATE (PCT) PRECURSOR SOLUTIONS

2.1.1. SYNTHESIS OF THE PRECURSOR SOLUTIONS

Calcium modified lead titanate ($\text{Pb}_{1-x}\text{Ca}_x$) TiO_3 precursor solutions with different Ca^{2+} contents ($0 \leq x \leq 0.50$) have been synthesised in this work by an aqueous solution-gel route^{92,175} and by a diol-based sol-gel route^{93,128,176}. The aqueous solution-gel route is based on the use of water as solvent, alkoxides and chelating agents such as citrates and peroxides. For the diol-based sol-gel route, compounds such as alkoxides, carboxylates and β -diketonates have been employed. Furthermore, different synthetic pathways have been developed for the preparation of the diol-based sol-gel precursor solutions.

Both synthetic methods (aqueous and diol-based) suppose a significant advance towards the field of clean technologies, since toxicity of the solvents and chemical compounds here used is relatively low when compared with other solution methods (methoxyethanol, ethoxyethanol, xylene, toluene, benzene, etc).¹³⁹⁻¹⁴⁵

2.1.1.1. Experimental setup

The experimental setup used for the synthesis of the aqueous and diol-based PCT precursor solutions is shown in Figure 2.1 (a and b, respectively).

In the case of the aqueous solution-gel method (Figure 2.1a), the synthesis of the aqueous precursor solutions involves the formation of a fresh precipitate which is filtered through a Büchner funnel with joint (A) and filter paper disc of 0.1 μm pore size. Complexation reactions and subsequent polycondensation of the reagents are developed in a round-bottom flask (B) heated by a magnetic stirrer heating bath of silicon oil equipped with an Allihn condenser column (C), cooled with water. Concerning the diol-based sol-gel processing (Figure 2.1b), reactions among the reagents are carried out in a three-neck-round-bottom flask (D) heated by a magnetic stirrer heating mantle equipped with a coil (Graham) condenser column (E), cooled with water. The reflux promotes the interchange among the groups of the reagents and the solvent, leading to the formation of a sol. Byproducts of the reaction are distilled off the solution with a distilling column (F) cooled with water.

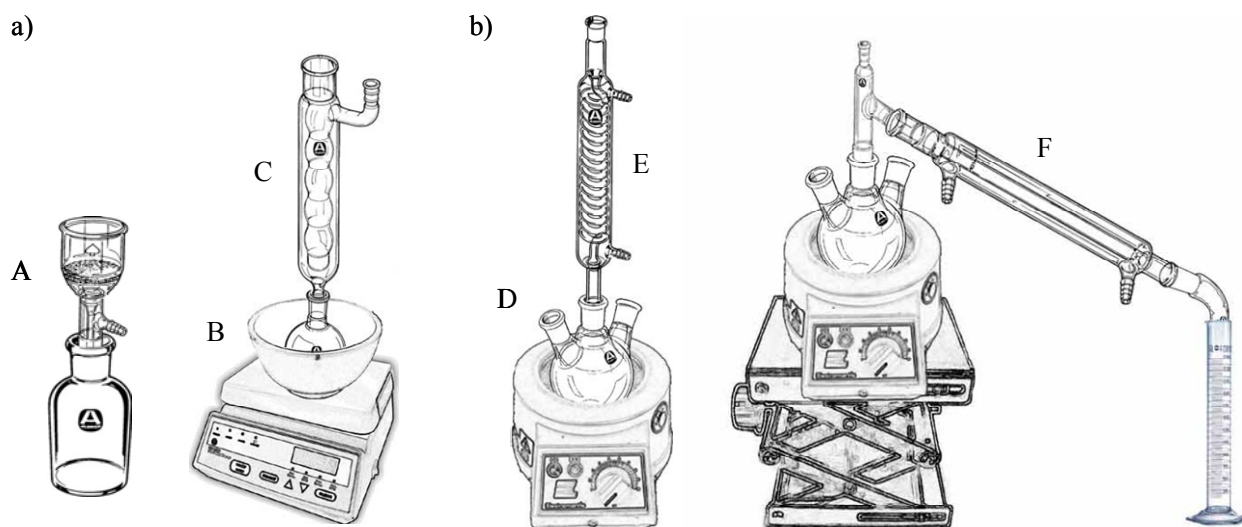


Figure 2.1. Experimental setup used in the synthesis of the aqueous (a) and diol-based (b) PCT precursor solutions

In spite of the high sensitivity towards hydrolysis of the majority of the metal alkoxides of titanium, all the processes involved in the synthesis of the PCT solutions were carried out in air and no experimental setup for dried atmosphere was necessary to put in practice. In the case of the diol-based sol-gel processing, this is because of the use of a titanium alkoxide modified with a β -diketonate (the acetylacetonate group), which presents a very low sensitivity towards moisture.¹⁷⁷ The structure of this chemical compound, as well as that corresponding to the acetylacetonone compound, is depicted in Figure 2.2.

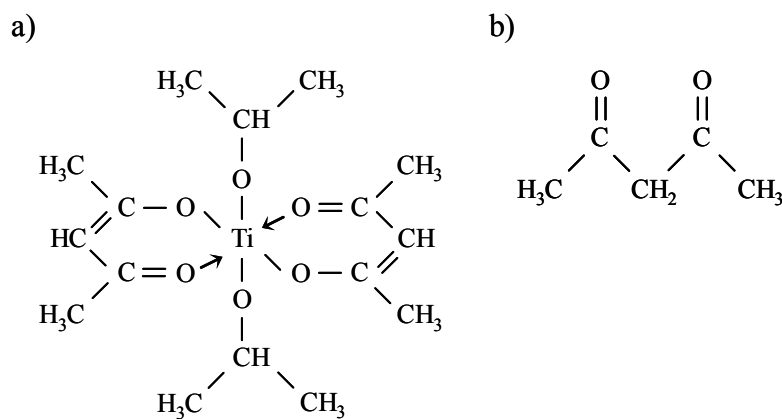


Figure 2.2. Structure of the titanium di-isopropoxide bis(acetylacetonate) (a) and acetylacetonone (b) chemical reagents

2.1.1.2. The aqueous solution-gel synthetic route

Aqueous $(\text{Pb}_{1-x}\text{Ca}_x)\text{TiO}_3$ precursor solutions were obtained by the aqueous solution-gel route shown in Figure 2.3. First, a water soluble titanium (IV) precursor was synthesised.^{92,178} Thereby, titanium (IV) tetra-isopropoxide ($\text{Ti}(\text{OCH}(\text{CH}_3)_2)_4$, Acros Organics, 98+%) was hydrolysed in water leading instantaneously to the formation of a precipitate (titanium hydroxide) that was filtered and washed with deionised water. Citric acid ($\text{HOC}(\text{COOH})(\text{CH}_2\text{COOH})_2$, Aldrich, 99%), hydrogen peroxide (35 wt% H_2O_2 solution in H_2O , Acros Organics, for analysis) both in a molar ratio of 2:1, both against Ti(IV), and water (molar ratio of water:Ti(IV) of 25:1) were added to the wet titanium precipitate. The mixture was refluxed in air at ~ 80 °C for 2 h. In this step, the citric acid and the hydrogen peroxide act as ligands in the system and coordinate the Ti(IV) cation, promoting as well complexation reactions among the species. The formed metal-chelate complexes result to be highly stable in the aqueous media and therefore a clear, red-colour peroxo-citrato Ti(IV) precursor solution was obtained. The Ti(IV) metal ion concentration measured for this solution was ~ 0.86 M.

Lead (II) and calcium (II) citrate precursors were added to the former Ti(IV) solution at room temperature to obtain a transparent $(\text{Pb}_{1-x}\text{Ca}_x)\text{TiO}_3$ precursor solution with the desired nominal composition. Calcium citrate tetrahydrate ($\text{Ca}_3(\text{O}_2\text{CCH}_2\text{C}(\text{OH})(\text{CO}_2)\text{CH}_2\text{CO}_2)_2 \cdot 4\text{H}_2\text{O}$, Aldrich, 99%) was used as the calcium reagent. In the case of lead citrate, this compound was obtained through the reaction between lead acetate (II) trihydrate ($\text{Pb}(\text{CH}_3\text{OCO})_2 \cdot 3\text{H}_2\text{O}$, Aldrich, 99%) and citric acid. Both reagents were dissolved at room temperature in a flask with plentiful deionised water in a molar ratio of lead acetate to citric acid of 1:2. The resulting reaction mixture was stirred for 5 min and settled for 15 min. The lead compound formed was filtered, washed and dried in a furnace at 60 °C for 24 h. The empirical formula of the lead (II) citrate thus synthesised correspond to $\text{C}_6\text{H}_8\text{O}_8\text{Pb}$,¹⁷⁹ deduced from the elemental analyses carried out in the product obtained.

By this method, aqueous solutions with nominal compositions of $(\text{Pb}_{0.76}\text{Ca}_{0.24})\text{TiO}_3$ and $(\text{Pb}_{0.50}\text{Ca}_{0.50})\text{TiO}_3$ (hereinafter denoted as PCT24 and PCT50, respectively) were synthesised containing a 10 mol% excess of PbO. The pH of these solutions was adjusted to ~ 8.5 by the addition of ammonia (32% NH_3 solution, Merck, extrapure), since lower pH values lead to precipitation of lead citrate.¹⁷⁹ A volume of additional water, up to a molar ratio of Ti(IV): H_2O of 1:65, was necessary to add to the PCT50 solutions to obtain a transparent and precipitate-free solution. Concentrations in the range of 0.25-0.35 M (referred as moles of PCT per litre of solution) with viscosity values near 1 cP, were measured for these PCT solutions.

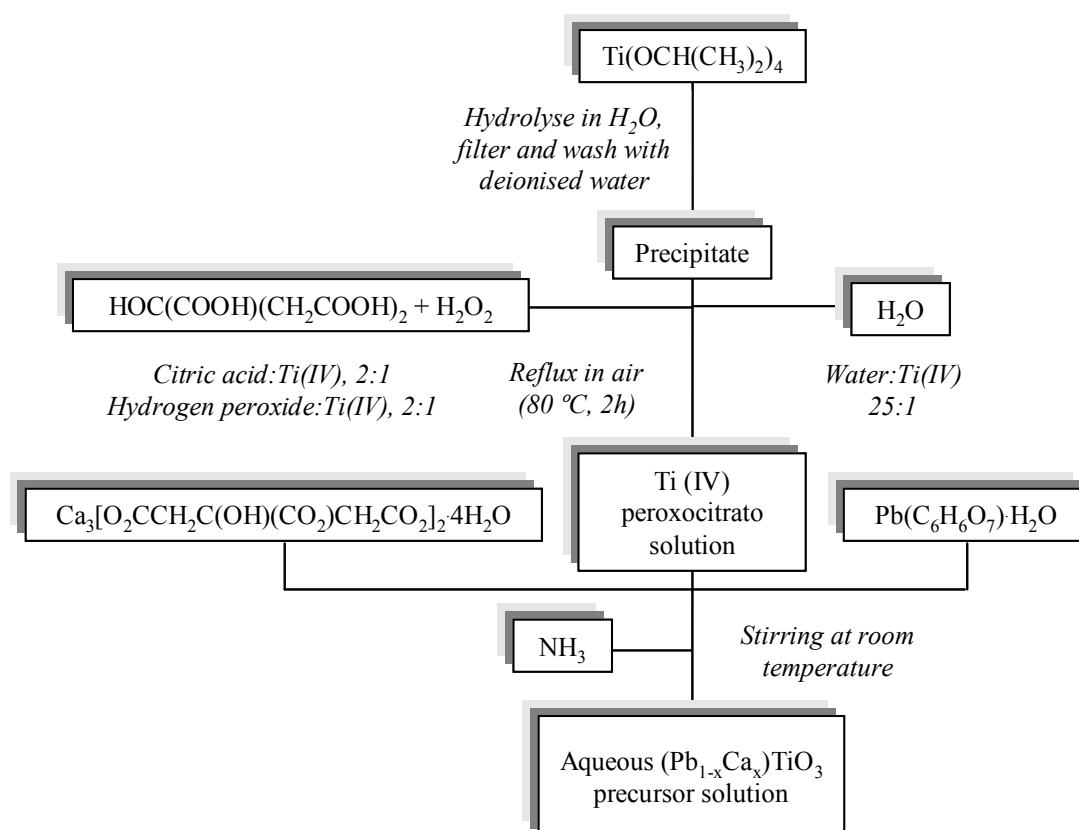


Figure 2.3. Schematic diagram of the aqueous solution-gel synthetic route

2.1.1.3. The diol-based sol-gel synthetic route

Within the polymeric systems of the sol-gel methodology, alcohols usually result one of the most appropriate solvents for dissolving and subsequent reactions (polycondensation) of the multimetal precursors. In the case of ferroelectric perovskite films, the 2-methoxyethanol solvent, $\text{CH}_3\text{OCH}_2\text{CH}_2\text{OH}$ (MOE), has been widely used in the literature for the synthesis of various systems such as those leading to $\text{Pb}(\text{Zr,Ti})\text{O}_3$ (PZT) and $\text{SrBi}_2\text{Ta}_2\text{O}_9$ (SBT) precursor solutions.^{87,180} Here, a sol-gel process based on the use of a modified titanium alkoxide and lead (II) acetate trihydrate together with a dihydroxyalcohol (also called *diol* or *glycol*) as solvent, has been used for the preparation of the PCT precursor solutions. The glycolated compounds formed after sol-gel synthesis present a higher stability against the hydrolysis than the initial metal alkoxides precursors.¹⁸¹ Furthermore, the dihydroxyalcohol here used (1,3-propanediol, $\text{HO}(\text{CH}_2)_3\text{OH}$) acts as a crosslinking agent in the process resulting in air-stable solutions and crack-free coatings, even when the film thickness is over the micrometer.^{182,183}

This route is known in the literature as the “*diol route*”¹⁰¹ and has been previously used in the synthesis of PbTiO₃ (PT), modified PT (PCT, PZT, (Pb,Sm)TiO₃ (PST), (Pb,La)TiO₃ (PLT)) or SBT precursor solutions.^{128,184-188}

In this work, the diol-based sol-gel synthetic route has been slightly modified to get the incorporation of large amounts of Ca²⁺ in free-precipitate, air-stable and low-toxic precursor solutions. Different approaches have been tested that basically differ in the way that the modifier cation (Ca²⁺) is incorporated to the chemical system. Thus, the incorporation of this cation has been carried out: through a calcium acetate (Ca(OCOCH₃)₂·xH₂O) water solution, through a calcium acetylacetonate (Ca(CH₃COCHCOCH₃)₂·xH₂O) water solution, through a calcium acetate or calcium acetylacetonate diol solution, through a calcium acetate diol-water solution or through a calcium acetylacetonate diol-water solution.

2.1.1.3.1. Incorporation of Ca²⁺ through a calcium acetate water solution

In this route, the calcium reagent was incorporated to the multicomponent system through a soluble salt of calcium acetate dissolved in water. Figure 2.4 shows the schematic diagram of this processing route.

The synthesis is based on a first preparation of a Pb(II)-Ti(IV) sol with the appropriate Pb(II):Ti(IV) molar ratio to obtain the desired (Pb_{1-x}Ca_x)TiO₃ nominal composition. To this aim, lead (II) acetate trihydrate (Pb(OCOCH₃)₂·3H₂O, Aldrich, 99%) and 1,3-propanediol (HO(CH₂)₃OH, Aldrich, 98%) were refluxed in air at ~155 °C for 1 h. Then, titanium (IV) diisopropoxide bis(acetylacetonate) (Ti(OC₃H₇)₂(CH₃COCHCOCH₃)₂, Aldrich, 75 wt% solution in 2-propanol) was added to this mixture and reflux was maintained in air at ~110 °C for 8 h. After this step, byproducts were partially distilled off the solution. The volume of the distilled liquid was the 80% vol. of the total 2-propanol (CH₃CHOHCH₃) that the synthesised solution contains.¹⁸⁵ An air-stable and precipitate-free Pb(II)-Ti(IV) sol was thus obtained. A solution of calcium acetate hydrate (Ca(OCOCH₃)₂·xH₂O, Aldrich, 99.99%) dissolved in water was added to this sol with a ratio of Ca(II):Pb(II) determined by the desired (Pb_{1-x}Ca_x)TiO₃ nominal composition,. The resulting mixture was stirred at room temperature for 12 h. After stirring, an air-stable, precipitate-free golden colour Ca(II)-Pb(II)-Ti(IV) solution was obtained.

With this procedure, $(\text{Pb}_{1-x}\text{Ca}_x)\text{TiO}_3$ precursor solutions with Ca^{2+} contents from 0 up to 50 at% ($x = 0-0.50$) were prepared. A 10 mol% of PbO excess was added to the former compositions.¹⁸⁹ Solutions contained the equivalent of 0.90-1.00 moles of $(\text{Pb}_{1-x}\text{Ca}_x)\text{TiO}_3$ per litre of solution (molar concentration), with a density of ~ 1.30 g/mL, a viscosity of ~ 40 cP and a pH near 7. Molar ratios of Ti(IV):1,3-propanediol of 1:5 and water:1,3-propanediol of 7:1 were used for the synthesis of the PCT solutions.

The chemical pathway shown in Figure 2.4 used for the synthesis of these PCT precursor solutions will be denoted *route A*.

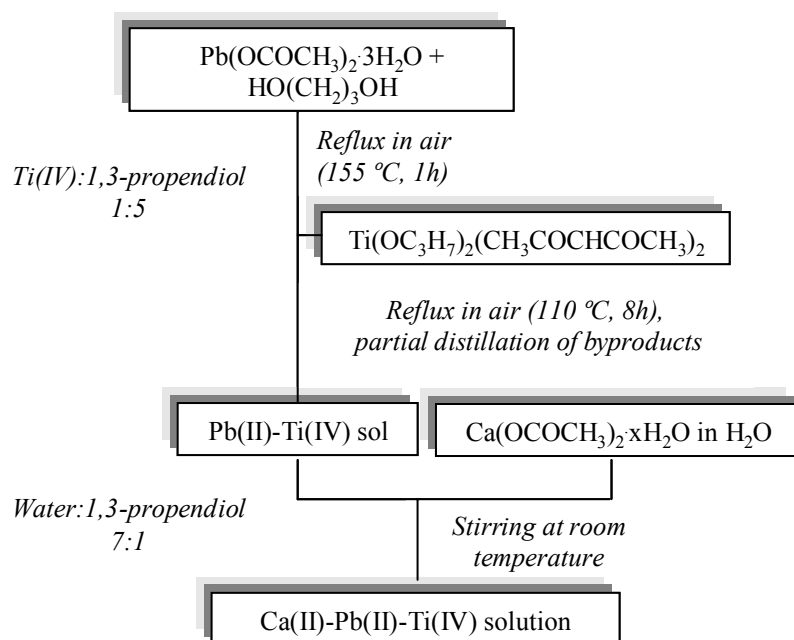


Figure 2.4. Schematic diagram of the diol-based sol-gel synthetic route A

2.1.1.3.2. Incorporation of Ca^{2+} through a calcium acetylacetonate water solution

In this case, the synthesis of the PCT precursor solutions was attempted by using a precursor of calcium consisted in a β -diketone, the calcium acetylacetonate hydrate ($\text{Ca}(\text{CH}_3\text{COCHCOCH}_3)_2 \cdot x\text{H}_2\text{O}$, Aldrich) reagent. This compound has two acetylacetonate (2,4-pentanedione) groups, whose structure is shown in Figure 2.5.

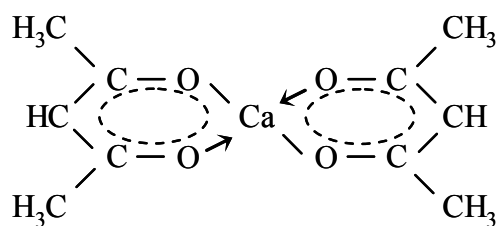


Figure 2.5. Structure of the calcium acetylacetonate chemical reagent

The preparation of the Pb(II)-Ti(IV) sol was carried out according to the methodology previously described for route A. The incorporation of the calcium reagent to this sol was tested now by a calcium acetylacetonate water solution. However, the low solubility of this reagent in water made necessary the addition of high volumes of this solvent to obtain a clear solution of calcium acetylacetonate, leading to uncontrolled hydrolysis and precipitation reactions in the system once the solution of calcium acetylacetonate was added to the Pb(II)-Ti(IV) sol. Thus, PCT precursor solutions could not be obtained by this way, and therefore it could not be explored for the preparation of films.

2.1.1.3.3. Incorporation of Ca^{2+} through a calcium acetate or calcium acetylacetonate diol solution

The calcium reagent was incorporated in this case as a starting product together with lead (II) acetate trihydrate and 1,3-propanediol. The proportion between Pb(II) and Ca(II) was adjusted to the desired $(\text{Pb}_{1-x}\text{Ca}_x)\text{TiO}_3$ composition, with a 10 mol% of PbO excess and a molar ratio of Ti(IV):1,3-propanediol of 1:5. However, neither calcium acetate nor calcium acetylacetonate could be dissolved in 1,3-propanediol, due to the insolubility of these reagents in organic solvents. Reflux of the mixture did not improve the solubility and therefore, PCT precursor solutions could not be obtained by this synthetic procedure.

2.1.1.3.4. Incorporation of Ca^{2+} through a calcium acetate diol-water solution

Figure 2.6 shows the chemical strategy followed in this route. Calcium acetate hydrate and lead (II) acetate trihydrate were refluxed together in air at $\sim 105^\circ\text{C}$ for 1 h in a mixture of 1,3-propanediol and water. Then, titanium (IV) di-isopropoxide bis(acetylacetonate) was added to the former mixture, continuing reflux in air at $\sim 90^\circ\text{C}$ for 8 h. Once reflux was completed, a partial distillation of byproducts was carried out. The volume of distilled liquid was the 80% vol. of 2-

propanol contained in the solution. Precipitate-free and air-stable PCT precursor solutions were thus obtained. Molar ratios of Pb(II):Ti(IV) and Ca(II):Ti(IV) were adjusted to the desired $(\text{Pb}_{1-x}\text{Ca}_x)\text{TiO}_3$ composition.

This synthetic route allowed us to prepare $(\text{Pb}_{1-x}\text{Ca}_x)\text{TiO}_3$ precursor solutions with $0 \leq x \leq 0.50$. All the compositions were synthesised with a 10 mol% of PbO excess and with a of 0.90-1.00 M (the equivalent of moles of PCT per litre of solution), a density of ~ 1.30 g/mL, a viscosity of ~ 14 cP and a pH ~ 7 . Molar ratios of Ti(IV):1,3-propanediol of 1:5 and water:1,3-propanediol of 7:1 were also used in this route.

The synthetic route of Fig. 2.6 will be named in this work as *route B*.

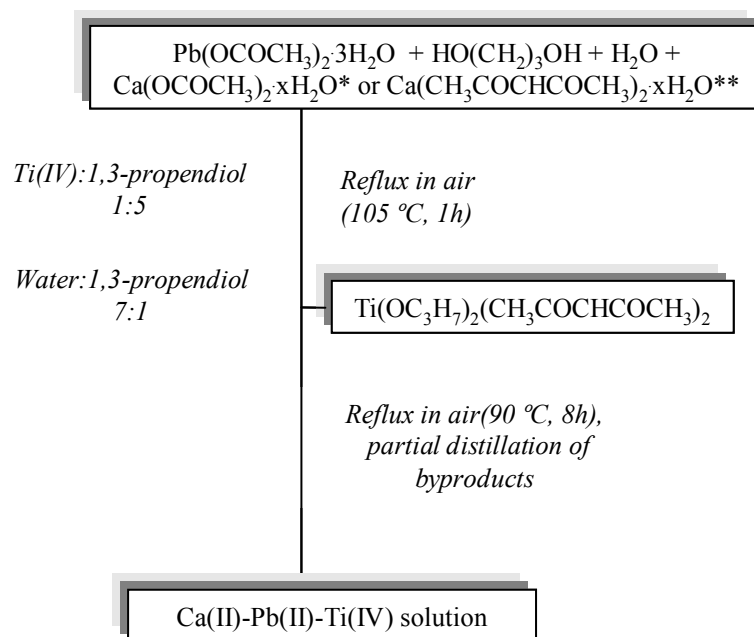


Figure 2.6. Schematic diagrams of the diol-based sol-gel synthetic routes *B** and *C***

2.1.1.3.5. Incorporation of Ca^{2+} through a calcium acetylacetonate diol-water solution

The chemical process here followed was practically the same than the previous one (route B), with the only difference that now calcium acetylacetonate hydrate was used as the calcium reagent instead of calcium acetate.

The schematic diagram of this route is shown in previous Figure 2.6. Molar ratios of Ti(IV):1,3-propanediol of 1:5 and water:1,3-propanediol of 7:1 were maintained. The volume of

distilled liquid now was the 50% vol. of 2-propanol contained in the solution, since higher volumes induced precipitation. By this procedure, only compositions with Ca^{2+} contents below 30 at% ($x < 0.30$) led to precipitate-free $(\text{Pb}_{1-x}\text{Ca}_x)\text{TiO}_3$ precursor solutions of. A concentration of ~ 0.75 M was obtained in these solutions, containing a 10 mol% of PbO excess and a density, viscosity and pH values of ~ 1.30 g/mL, ~ 12 cP and ~ 7 , respectively.

This chemical processing proposed for the synthesis of PCT precursor solutions will be named hereinafter *route C*.

2.1.2. PHYSICOCHEMICAL CHARACTERISATION OF SOL-GEL PRECURSOR SOLUTIONS

A critical issue concerning sol-gel and solution methods used in CSD is the ability to obtain homogeneous precursors with a high degree of compositional control that can be reproducible and that show optimum rheological properties for the further deposition of films onto substrates. The quality and properties of the derived films will strongly depend on the physicochemical characteristics of the precursor solutions previously synthesised. Therefore, a detailed physicochemical study of the PCT precursor solutions has been carried out in the present work. The experimental techniques used for the characterisation of these solutions are described below.

2.1.2.1. Viscosity, density and concentration

The rheological behaviour of the precursor solutions is expected to give important information on the spinnability and flow behaviour of the sols.¹⁹⁰ The viscosity measurement of the solutions can also indicate the degree of polymerization reaction in the sol and the size and shape of the particles that floccus in the sol.

The viscous properties of the PCT precursor solutions of this work were determined with a Brookfield Digital Rheometer model HBDV-III+, which consists in a cone/plate viscosimeter, as Figure 2.7 shows. These elements are arranged so that the apex of the cone is close to the plate surface. The liquid sample is filled into the space between the cone and the plate, and the measurement is carried out by rotating the cone with the plate fixed. The resistance to flow of the liquid against the cone is measured by the deflection induced in a calibrated spring attached to the cone spindle.

All the viscosity measurements were carried out at room temperature ($20 \pm 1^\circ\text{C}$) with a rotatory spindle CPE-40 model (0.5 mL sample volume), displaying values in the range of $10.5\text{--}261.6 \pm 1$ cP (mPa·s) and operating at angular velocities between 50-250 rpm.

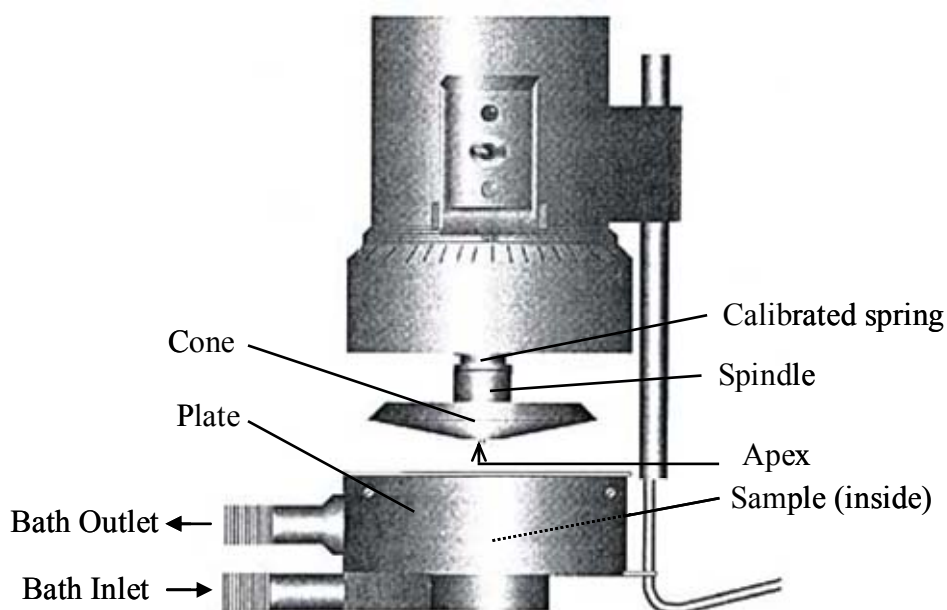


Figure 2.7. Cone/plate viscosimeter (Brookfield rheometer)

The density of the precursor solutions was calculated using Pobel pycnometers of 10 mL volume capacity. The pH of the solutions was measured by conventional pH indicator paper and more accurate measurements were carried out with a pH electrode meter.

The concentration of the PCT precursor solutions was referred as the equivalent number of moles of $(\text{Pb}_{1-x}\text{Ca}_x)\text{TiO}_3$ per litre of solution, and it was determined by conventional gravimetric analysis. Furthermore, the molar concentration of each cation present in the solution was determined by Inductively Coupled Plasma-Atomic Emission Spectroscopy (ICP-AES)¹⁹¹, obtaining similar values to those calculated by gravimetric analysis. The ICP-AES measurements of the precursor solutions were carried out at the *Chemical Analysis-Support Unit* of the ICMM-CSIC, using an ICP Perkin Elmer (Plasma 40 model) spectrometer with a Perkin Elmer (CHN 2400 model) elemental analyser and an AES Philips SP 9 spectrophotometer

2.1.2.2. Ultraviolet spectrophotometry analysis (UV)

The ultraviolet (UV) region of the electromagnetic spectrum comprises wavelengths of 200 to 380 nm (near-UV) whose associated energies are high enough to excite an electron to an orbital of higher energy of the molecule.¹⁹¹ Thus, absorption spectroscopy carried out in this region is sometimes called *electronic spectroscopy*. According to the molecular orbital theory, various types of electronic excitation may occur among the molecular orbitals of an organic compound (see Figure 2.8). However, only the low-energy transitions $n \rightarrow \pi^*$ and $\pi \rightarrow \pi^*$ are achieved by the UV radiation, giving rise to the absorption of UV light when the energy of the UV beam matches an electronic transition within the molecule. In the present work, the ultraviolet photosensitivity of the PCT solutions has been studied within the framework of the PhotoChemical Solution Deposition of ferroelectric thin films that will be discussed in detail in next *Chapter IV (Part 3)*.

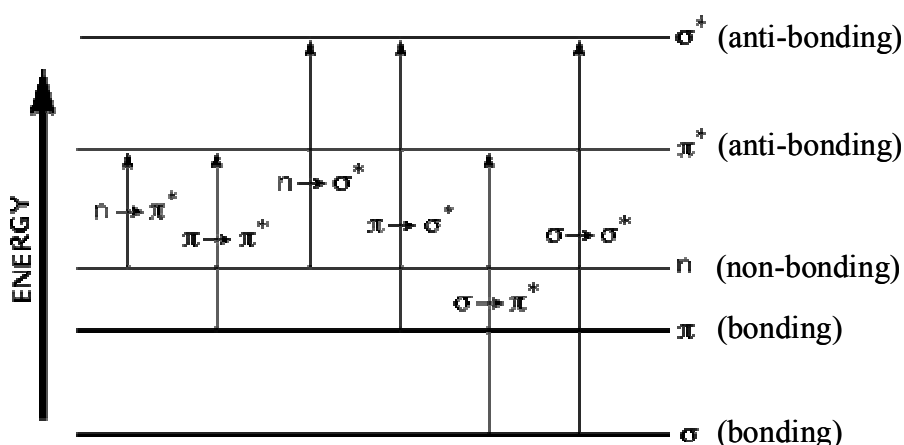


Figure 2.8. *Electronic transitions among the molecular orbitals of an organic compound*

The fundamental of the ultraviolet spectrophotometry is relatively straightforward. A beam of UV-light source is separated into monochromatic wavelengths by a prism or diffraction grating. Each single wavelength is split into two equal intensity beams by a beam splitter. One beam passes through a transparent container (cuvette) with the sample solution, while the other one passes through an identical cuvette containing only the solvent without the solute of the sample. By comparing the intensities collected by the detectors, the wavelengths at which the solute absorbs UV-light can be determined in the absorbance spectrum.

Ultraviolet absorption spectra of the PCT precursor solutions were collected with a Varian 5E spectrophotometer (200-3000 nm range). In order to not saturate the detector, solutions were previously diluted with water in a ratio of 10^5 to 1 of water to solution.

2.1.2.3. Infrared spectroscopy analysis (IR)

The infrared spectroscopy (IR) is a versatile method for the structural analysis of chemical compounds. The fundamentals of this technique lie on the vibrational motions produced in a molecule, which is not electronically excited, due to the absorption of electromagnetic radiation corresponding to the infrared region of the electromagnetic spectrum (roughly between 12800 - 10 cm^{-1}).^{192,193} The absorption of IR radiation must involve a net change in the dipole moment of the molecule. When the frequency of the radiation matches the vibrational frequency of the molecule, the IR radiation is absorbed producing a change in the amplitude of the molecular vibration. Since molecules are flexible, moving collections of atoms, the vibrations of their bonds can fall into two main categories; *stretching* (change of interatomic distance along bond axis) and *bending* (change in angle between two bonds) such as rocking, scissoring, wagging and twisting. The frequency of a determined vibration depends on the nature of the atoms involved in the bond (atomic mass) and the strength constant characteristic of that bond. Thus, every molecule or group of atoms has their own characteristic infrared spectrum.

The measurements by infrared spectroscopy contained in the present work were carried out on samples in liquid state. The analysis of the spectra led to the identification of the different functional groups present in the compound and also allowed us to monitor the reaction, due to the rupture and formation of bonds among the reagents.

The liquid samples were displayed in a cell window of cesium iodide (CsI), which does not contain bands in the mid-IR region that could overlap the spectrum of the sample. A Nicolet FT-IR 20SXC and Bruker ISS 66V-S spectrophotometers belonging to the *Infrared Spectroscopy-Support Unit* of the ICMM-CSIC were used for the measurements. The infrared spectra were collected on absorbance mode in the range of 4000 and 200 cm^{-1} .

2.1.2.4. Dynamic light scattering analysis (DLS)

Dynamic Light Scattering (DLS) is one of the most used methods to determinate the size of particles suspended in a liquid. This technique allows measuring structural parameters of the dynamic particles such as particle size, diffusion coefficient and even molecular weight of polymers in solutions.¹⁹⁴ The fundamentals of the technique lie on the interaction of a monochromatic light beam (e.g. laser) onto a solution with spherical particles in Brownian motion (random walk). According to the semi-classical light scattering theory, the electric field of the light induces an oscillating (periodic) perturbation in the electron orbits of the constituent molecules.¹⁹⁵ An induced dipole moment is thus generated which produces the emission of a secondary source of light, that is, the scattered light. The frequency shift, the angular distribution and the intensity of the scatter light are related to the size, shape and molecular interactions of the scattering particles.

Experimentally, the theory considers that particles are in Brownian motion and hence the probability density function is given by:

$$P(r,t) = (4\pi Dt)^{-3/2} \exp(-r^2/4Dt) \quad [\text{eq. 4}]$$

where P is the probability of a particle moving a certain distance (r) in any given direction during a certain time interval (t), in a medium with a diffusion constant D. If particles are assumed to be spherical, it is possible to apply the Stoke-Einstein relation as:

$$D = k_B T / 6\pi\eta a \quad [\text{eq. 5}]$$

where a is the hydrodynamic radius of the particle, k_B is the Boltzmann constant, T is the temperature and η is the viscosity of the solvent. The determination of the position of the particles from the light scattering analysis allows calculating the hydrodynamic radius of the particle through the above formulas.

DLS measurements of PCT solutions were carried out at the “*Departamento de Química y Edafología*” of the “*Universidad de Navarra*”, in Pamplona (Spain). A DynaPro-MS/X photon correlation spectrometer equipped with a 248-channel multi-tau correlator and a Peltier effect temperature unit was used for the experiments. The wavelength of the laser was 825.2 nm and a scattering angle of 90° was used. The particle size distribution in the sols was obtained from the intensity autocorrelation function by regularisation analysis, implemented in the Dynamics TM software package. The temperature of the analysis was 25 ± 0.1 °C.

2.1.2.5. Differential thermal analysis and thermogravimetric analysis (DTA-TGA)

Thermal analysis comprises a group of techniques in which a physical property of a substance is measured as a function of temperature while the substance is subjected to a controlled temperature programme.¹⁹⁶ The thermal analysis techniques used in this Thesis have been DTA, TGA and Evolved Gas Analysis (EGA), which will be described more detailed in the next.

Differential Thermal Analysis may be formally defined as a technique for recording the difference of temperature between the sample and an inert reference material (normally alumina, Al_2O_3) against either time or temperature as the two materials are subjected to identical temperature regimes in an environment heated or cooled at a controlled rate. In the recorded DTA curve, the temperature difference must be plotted with endothermic reactions downward ($dQ/dt < 0$, $T_{\text{sample}} < T_{\text{reference}}$) and exothermic reactions upward ($dQ/dt > 0$, $T_{\text{sample}} > T_{\text{reference}}$). The DTA curves provide information of transition temperatures as well as transition enthalpies.

Thermogravimetric Analysis is a technique in which the mass of a sample is measured as a function of temperature while heating or cooling the sample at some predetermined and defined rate. Phenomena that can be studied by TGA can be easily grouped into mass gain processes (absorption, adsorption or oxidation) and mass loss processes (dehydration, vaporization, decomposition or reduction).

Aliquots of the PCT stock solutions were dried at 100 °C for 12 h in a furnace. Powders thus obtained were subjected to DTA-TGA between 25 and 1000 °C, with an dried air flux of 100 mL/min and a heating rate of 10 °C/min. A Seiko TG/DTA 320U model apparatus belonging to the *Thermal Analysis-Support Unit* of the ICMM-CSIC was used for these measurements.

2.1.2.5.1. Evolved gas analysis (EGA)

The study of volatile transient species emitted during the thermal decomposition of a solid organic material can lead to elucidate the decomposition pathway followed during the thermal treatment. According to the IUPAC compendium, Evolved Gas Analysis (EGA) is a technique in which the nature and/or amount of the volatile products released by a substance subjected to a controlled temperature program are determined.¹⁹⁷ This definition involves coupled techniques such as TGA-FTIR (ThermoGravimetric Analysis-Fourier Transform Infrared Spectroscopy) and TGA-MS (Thermogravimetric Analysis-Mass spectroscopy), as more relevant.

Nowadays, both techniques result an essential addition to the thermal analysis of substances. In this work, EGA experiments have been carried out at the *Laboratory of Inorganic and Physical Chemistry* of the *University of Hasselt*, in Diepenbeek (Belgium).

2.1.2.5.1.1. *Thermogravimetric analysis-Fourier transform infrared spectroscopy (TGA-FTIR)*

In this technique, the gases emitted during the thermogravimetric experiment (TA Instruments TGA 951-2000) are detected by the use of an on-line coupled FTIR spectrophotometer (Bruker IFS 48). The use of an interferometer in the IR equipment allows the spectra in the wavelength range between 400 and 4000 cm^{-1} being scanned several times within one second. A flow gas (dried air, 100 mL/min), transparent to the IR radiation, is responsible for transporting the released species to the FTIR with no delay in time between releasing and detection.

Aliquots of the PCT precursor solutions were dried at 60 °C for 12 h in a furnace. Gel powders thus obtained were subjected to a heating treatment in air, between 20 and 1000 °C and a rate of 10 °C/min. The gases released during this process were analysed by means of FTIR.

2.1.2.5.1.2. *Thermogravimetric analysis-mass spectroscopy (TGA-MS)*

Here, thermogravimetric analysis (TA Instruments TGA 951-2000) is on-line coupled to a quadruple mass spectrometer (MS, Thermolab VG Fisons), although this time coupling requires special interface due to the different atmospheres used in both equipments (atmospheric pressure for TGA and vacuum around 10^{-6} mbar for MS). The gases released during the TGA experiment are carried to the mass spectrometer through a heated ceramic (inert) capillary that connects both apparatus. Gas molecules are ionised by electron bombardment and fragmented into positive ions that are separated as a function of their mass/charge ratio.

PCT gel powders were obtained from the precursor solutions after drying at 60 °C for 12 h in a furnace. Analyses of these powders were carried out by TGA-MS in air from 20 to 750 °C, with a heating rate of 10 °C/min and a dried air flux of 100 mL/min. The ionisation energies applied were set to values of 20 or 70 eV. The mass spectra of the evolved gas molecules were collected in the range between molecular weight/atomic number (m/z) ratios of 15-115.

PART 2. CALCIUM MODIFIED LEAD TITANATE (PCT) THIN FILMS

2.2.1. PREPARATION OF THE THIN FILMS

A technologically significant feature of CSD methods is the ability to prepare functional coatings by deposition of the fluid solutions. Thus, the thin film conformation is considered as one of the major contributions achieved in the development of microelectronic devices and integrated circuits nowadays.

In the present work, thin films have been deposited from the PCT precursor solutions described before. The PCT films obtained from the aqueous solution-gel method have been prepared at the *Interuniversity MicroElectronics Center (IMEC)* of Leuven (Belgium). Here, the cleaning of the substrates as well as the fabrication of the films was carried out in a clean room. On the other hand, the preparation of the PCT films derived from the diol-based sol-gel solutions has been carried out at the ICMM-CSIC, in a 100 class clean-room (less than 100 particles with $<0.5 \mu\text{m}$ diameter per m^3), which includes full equipment for the cleaning of the substrates (ultrasonics bath), deposition (spinner, hot-plate) and crystallisation (rapid thermal processor) of the films, and fabrication of the capacitors (sputter) under a laminar flux hood (CAM-1300-V) with a sterile air circulator unit (Telstar FFU).

All the films of this work have been crystallised by Rapid Thermal Processing (RTP), reducing the duration of the thermal treatment when compared with conventional furnace annealing.¹⁹⁸ Furthermore, a low-temperature processing of PCT films compatible with the silicon integrated circuit technology has been used, based on an ultraviolet-assisted the rapid thermal processor (UV-assisted RTP).¹⁹⁹

2.2.2.1. Substrates

PCT precursor solutions have been deposited onto silicon-based substrates, with an heterostructure of $\text{Pt/TiO}_x/\text{Ti/SiO}_2/(100)\text{Si}$ in the case of the aqueous solutions and $\text{Pt/TiO}_2/\text{SiO}_2/(100)\text{Si}$ for the diol sol-gel solutions.

$\text{Pt/TiO}_x/\text{Ti/SiO}_2/(100)\text{Si}$ wafers were provided by the *Interuniversity MicroElectronics Center (IMEC)* of Leuven (Belgium) for the deposition of the aqueous PCT solutions. Pieces of

substrates with a size of 30x30 mm² were obtained by cutting these wafers with a diamond tip. Prior to film deposition, substrates were subjected to a wet chemical cleaning using both sulphuric acid-hydrogen peroxide (SPM) and ammonia-hydrogen peroxide (APM) mixtures.⁹² Thus, substrates were first introduced in a mixture of sulphuric acid (H₂SO₄, Panreac, 96%) and hydrogen peroxide (H₂O₂ 35wt% solution in water, Aldrich, for analysis) in a ratio of H₂SO₄:H₂O₂ of 4:1 (V/V), and heated at 80 °C for 20 min on a hot plate. Thus, organic contamination set on the substrate surface was oxidised by the SPM mixture. Afterwards, the substrates were placed in a solution containing ammonia (NH₃ 32%, Merck, extrapure), hydrogen peroxide and water in a ratio of NH₃:H₂O₂:H₂O of 1:1:5 (V/V/V), and heated at 65 °C for 20 min on a hot plate. At this step, further organics oxidation and removing of metallic contaminants by complexation was carried out.

In the case of the diol sol-gel derived films, commercial (100)Si wafers of 100 mm diameter and 0.5 mm thickness were provided by the Radiant Technology or Crystal GmbH companies, with one face mirror-like polished. These substrates are spontaneously oxidised by their contact with the air, so they present a ~20 nm thick silicon oxide (SiO₂) layer onto the polished side. Titanium oxide (TiO₂) and platinum (Pt) layers were deposited by sputtering with an Alcatel SCM 450 apparatus at the “Laboratorio de Sensores” of the “Centro de Tecnologías Físicas Torres Quevedo” of CSIC, in Madrid (Spain). The TiO₂ layer (~50 nm thickness) acts as a physical barrier minimising the Si diffusion towards the Pt bottom electrode and promoting the Pt adherence.²⁰⁰ The sputtered Pt layer has a thickness between 50-100 nm and a (111) preferred orientation. Pieces of substrates of determined sizes (10x10 mm², 20x20 mm², etc) were obtained from the former wafers by cutting them with a diamond tip. Prior to the film deposition, substrates were cleaned with different organic solvents in an ultrasonics bath (Selecta). The cleaning procedure consisted in the following steps; 5 min in trichloroethylene (Cl₂CClCH, Panreac, stabilised with ethanol), 4 min in acetone (CH₃COCH₃, Panreac) and 3 min in 2-propanol (CH₃CHOHCH₃, Panreac, for analysis). Residual solvent as well as undesired particles onto the surface were finally removed from the cleaned substrates with a nitrogen flow.

2.2.1.2. Deposition, drying and pyrolysis of the thin films

The deposition of the PCT thin films of this work has been carried out by spin-coating. This process can be divided into four stages²⁰¹: deposition, spin-up, spin-off and evaporation, as shown in Figure 2.9. During the deposition stage, a liquid excess is dispensed onto the substrate surface. This liquid flows radially outward in the spin-up stage, driven by centrifugal force. In the spin-off

stage, the liquid excess flows to the perimeter of the substrate surface and leaves it as droplets. The amount of liquid excess removed decreases as the film becomes thinner, since the resistance to flow increases due to the higher concentration of non volatile components in the material. Finally, evaporation acts as the main mechanism of thinning during the last stage. As an advantage of this technique, the film thickness tends to be uniform during the spin-off stage and remains so after the deposition process, showing that the viscosity of the sol is not shear dependent and stays stable over the substrate.¹¹⁰

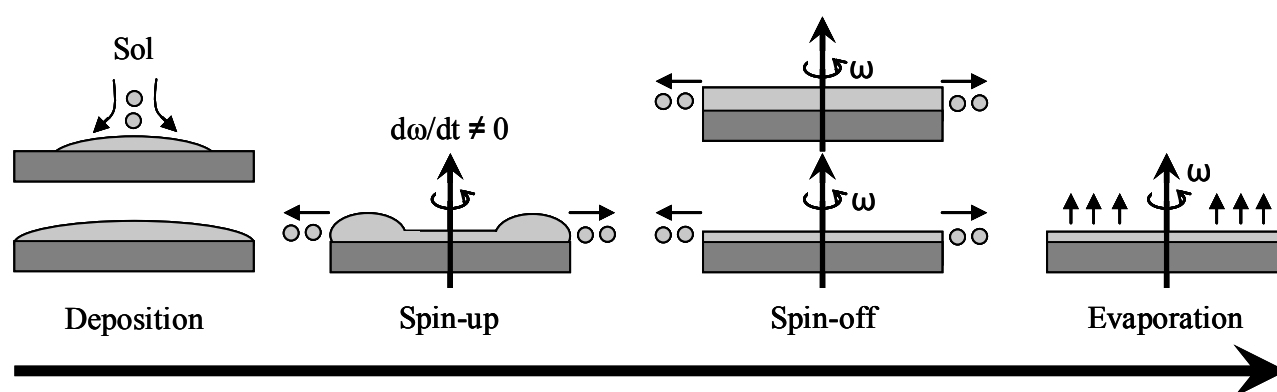


Figure 2.9. Different steps of the spin-coating deposition process

Glass syringes equipped with non-sterile plastic nozzles and coupled with filters (Millipore) of 0.2 μm pore size were used for the deposition of the PCT solutions. Coatings were obtained with a spinner (TP 6000 gyrset system of SET-Micro-Controle group model), working at 2000 rpm for 45 s.

The wet films thus obtained were dried and pyrolysed in order to remove the entrapped solvent and the majority of the organic species present within the gel network. The PCT films deposited from the aqueous solutions were subjected to a thermal treatment on three hot plates stabilised at 200, 300 and 450 $^{\circ}\text{C}$ successively, for 2 min in each hot plate. In the case of the diol sol-gel solutions, the PCT films were annealed on a hot-plate (Selecta) at 350 $^{\circ}\text{C}$ for 1 min.

Figure 2.10 shows a photograph with the equipments used at ICMM-CSIC for the deposition, drying and pyrolysis of the films.

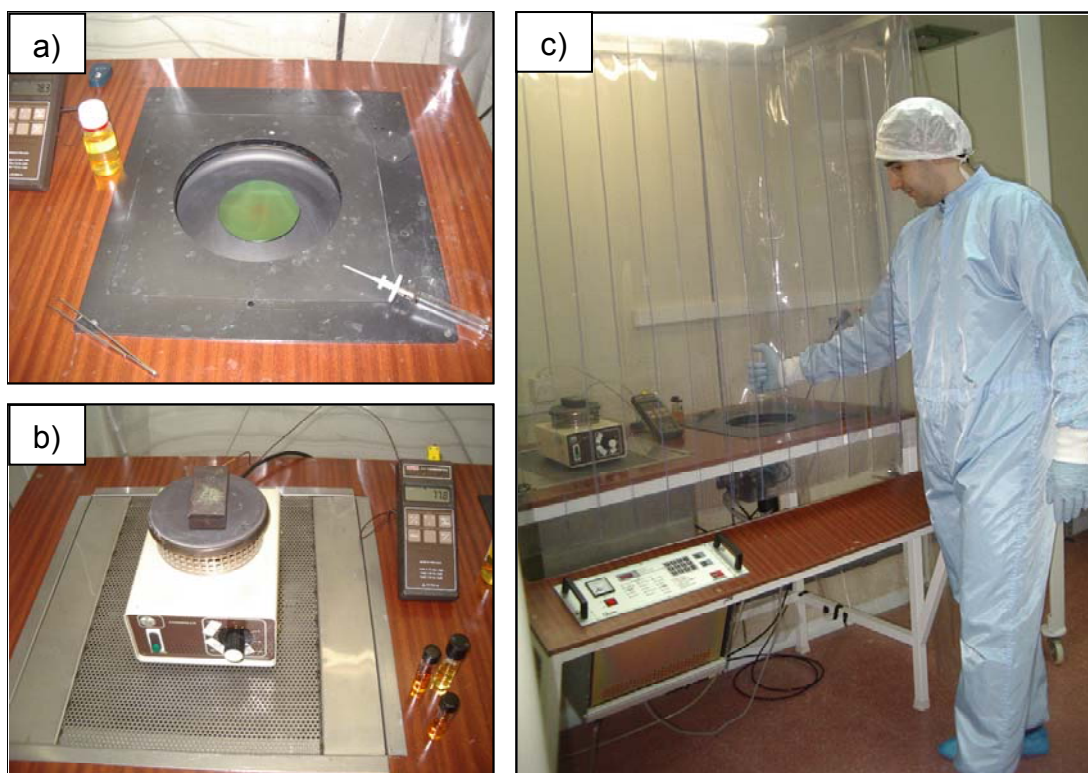


Figure 2.10. Equipments used for the deposition, drying and pyrolysis of the PCT films; spinner (a), hot-plate (b) and general view of the deposition and pyrolysis equipments (c), inside the clean-room

2.2.1.3. Crystallisation of the thin films

The as-deposited PCT films were crystallised into the desired oxide phase (i.e. perovskite) by a thermal treatment. Rapid Thermal Processing (RTP) was the technique used for the crystallisation of the thin films. The rapid heating rates (even up to 300 °C/s) registered in this process delay the removal of organic species to higher temperatures,^{111,113} where kinetics of pyrolysis reactions is greatly enhanced. Furthermore, thin film densification is also promoted by RTP, since the onset of crystallisation is also delayed to higher temperatures.

2.2.1.3.1. Rapid thermal processing (RTP)

The crystallisation of the PCT films by RTP was carried out with the Jetstar 100T JIPELEC equipment shown in Figure 2.11a. A scheme of the furnace arrangement is displayed in Fig. 2.11b. The films were placed on the sample holder plate and temperature of the process was controlled by

a pyrometer and a thermocouple in contact with the film surface. A heating rate of 30 °C/s was used for the treatments, which were carried out in air or oxygen using in both cases atmospheric pressure (1 atm). Figure 2.11c shows the thermal recipe used for the crystallisation of the films, where the films were annealed at 650 °C for 1 h.

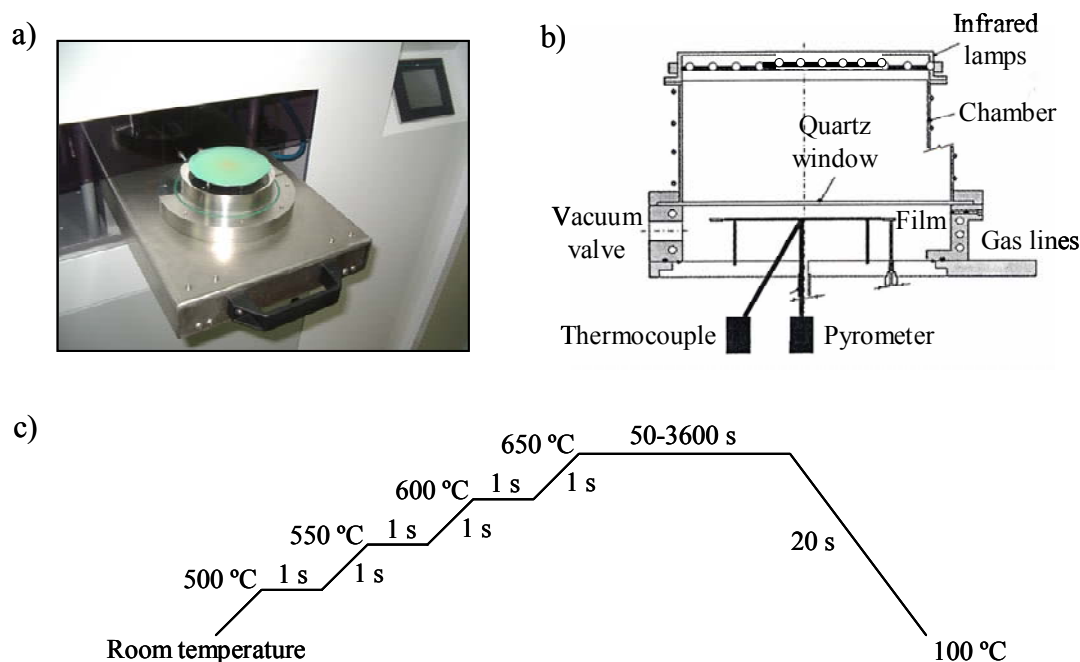


Figure 2.11. Photograph of the rapid thermal processor (a), scheme of the furnace arrangement (b) and thermal budget (c) used for the crystallisation of the films

2.2.1.3.2. Ultraviolet-assisted rapid thermal processing (UV-RTP)

The crystallisation of the films by UV-assisted RTP was carried out at the *R+D Department of the JIPELEC division (QUALIFLOW)* in Grenoble (France), within a project inside of the European Action COST528 on “*Chemical Solution Deposition of Thin Films*”. The JetClip SG, JIPELEC processor was used for these treatments. This equipment was developed in the CE European Project BRPR-CT980777, in which the ICMC-CSIC and JIPELEC participated, and it is now commercialised by JIPELEC-QUALIFLOW.¹⁹⁹ Figure 2.12 shows a photograph (a) and a scheme (b) of the UV-assisted RTP processor. It is equipped with an arrangement of high-intensity UV excimer lamps with emission set at a wavelength of 222 nm and a power of 300 W/m² (75% of the UV power was used), and with an arrangement of IR lamps for the heating of the sample. The

control and reading of the temperature of the film inside the furnace was carried out by a pyrometer and a thermocouple (in contact with the film surface) of the equipment. Furthermore, another independent thermocouple, placed on the film surface, was used for making an external reading of the film temperature during the processing. The thermal budget to which the films were subjected is shown in the recipe of Figure 2.12c. Thus, films were first irradiated with UV-light at 250 °C for 4 min, prior to the crystallisation at temperatures between 450 and 500 °C for 1 h. Treatments were carried out in air or oxygen local atmospheres (pressure of 1 atm) with a heating rate of 30 °C/s.

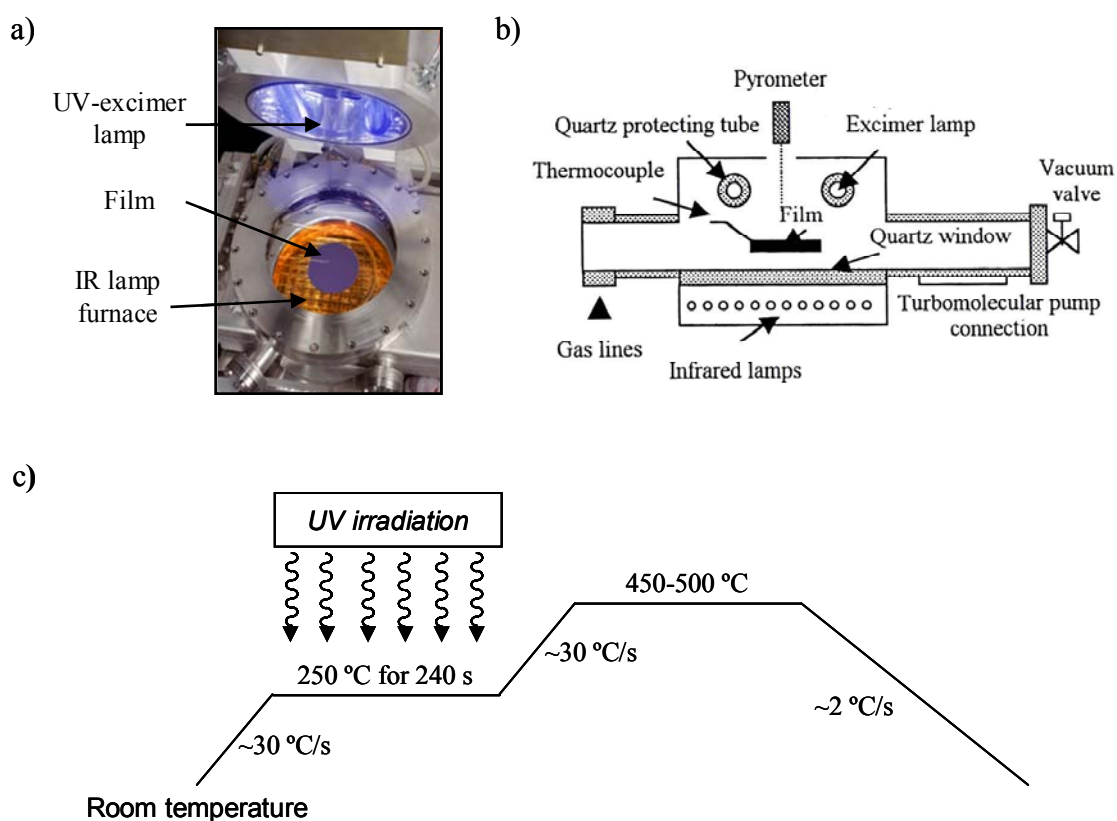


Figure 2.12. Photograph of the UV-assisted RTP processor (a), scheme of the furnace arrangement (b) and thermal budget (c) used for the crystallisation of the films

The general procedure followed for the fabrication of the PCT films of this work, together with a drawing of the heterostructure of the resulting material, is shown in Figure 2.13.

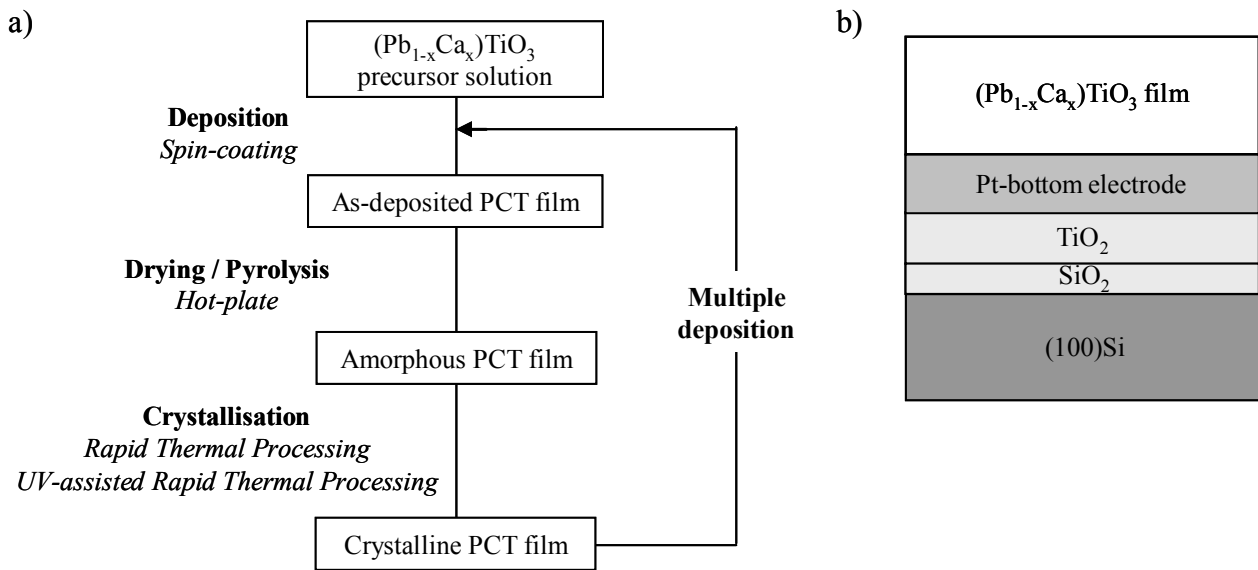


Figure 2.13. Diagram of the procedure followed for the fabrication of PCT thin films (a) and drawing (b) of the heterostructure of the resulting material

2.2.2. THIN FILMS CHARACTERISATION

(Pb_{1-x}Ca_x)TiO₃ thin films with $0 \leq x \leq 0.50$ have been studied by means of different physical techniques, thus determining their composition, crystalline structure, microstructure and heterostructure. Dielectric and ferroelectric measurements on the films have been also performed. The techniques used for the characterisation of the PCT films are described below.

2.2.2.1. Thickness measurements

The thickness of the crystalline PCT films has been determined by profilometry, and the values thus measured were compared with those obtained with other techniques that will be described in next sections, such as Scanning Electron Microscopy (SEM), Transmission Electron Microscopy (TEM) or Rutherford Backscattering Spectroscopy (RBS).

2.2.2.1.1. Profilometry

The thickness of a film can be determined by profilometry, a technique in which the height displacement induced in a tip in contact with the film surface is measured while the tip covers the length of the film. The contact between the tip and the film is maintained through a low elastic constant spring, whose deflection due to height slopes is collected by an inductive transducer and hence related with the thickness and roughness of the film.

In order to perform accurate measurements, a small surface along one or two opposite edges of the film must be peeled-off from the substrate. Thus, the thickness of the film is directly obtained by measuring the step between the film and the substrate height levels. However, after the deposition and crystallisation of the films, the substrate as well as the film results in a curved profile due to the stresses developed during the deposition process and the thermal treatment.²⁰² The curvature of the substrate can be easily subtracted from the thickness analysis if the measurement is carried out on films with two opposite sides peeled-off from the substrate, obtaining a substrate-film-substrate profile as shown in Figure 2.14.

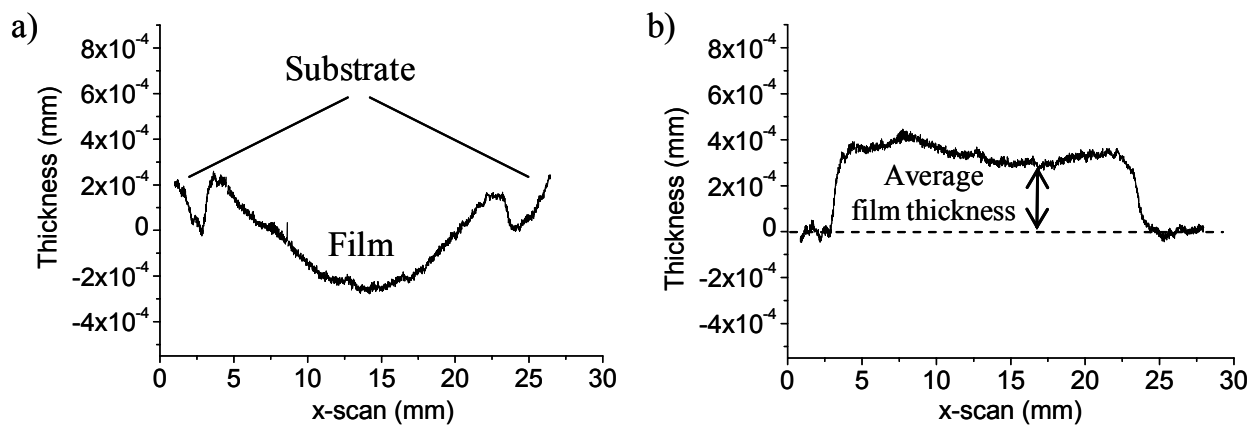


Figure 2.14. Example of a film-substrate profile obtained by profilometry (raw data) (a) and resulting profile (b) after subtraction of the substrate curvature

A Taylor-Hobson profilometer, Form Talysurf 50 model, was used to determinate the thickness of the PCT films. A carbon fiber calliper of 60 mm length, with a diamond tip at the edge of 2 μm radius and cone-shaped of 60° form, allows thickness measurements with a minimum resolution of 20 nm. The profile of the film-substrate obtained was fitted to parabolas or

circumferences through home-made software with regression coefficients near 0.99, from which values of thickness were calculated.

The edges of the film were peeled-off from the substrate by using an acidic solution that dissolves the PCT film but not the Pt bottom electrode. This solution was prepared by mixing fluorhydric acid (HF 48%, Panreac), clorhidric acid (HCl 37%, Panreac) and deionised water in a volume ratio of HF:HCl:H₂O equal to 1:1:15. An edge of the film is immersed inside the solution until the wet part of the film is peeled-off from the substrate.

2.2.2.2. Compositional and heterostructural analyses

The determination of the compositional profile of the films, as well as the characteristics of the heterostructures formed (composition and thickness of the film, bottom electrode or interfaces formed during deposition and crystallisation processes), has been carried out by means of Rutherford Backscattering Spectroscopy (RBS) and X-ray Photoelectron Spectroscopy (XPS).

2.2.2.2.1. Rutherford backscattering spectroscopy (RBS)

Rutherford Backscattering Spectroscopy (RBS) is one of most commonly applied techniques in quantitative surface analysis of. The physical fundamentals of this technique lie on the elastic collision of a high energy particles beam directed towards the atoms of a sample, and the detection of the backscattered bombarding particles as a function of the energy and/or the angle.²⁰³ The schematic configuration of this experiment is shown in Figure 2.15. The energy of the scattered ions depends on the depth of the collision and the mass of the target atom. Since the mass and the energy of the incident particles are known, from the measured energies of the scattered ions we can deduce the location of the collision and the mass (chemical identity) of the target atom.²⁰⁴

In the present work, composition and heterostructure of the PCT films were studied by means of RBS. Measurements were carried out at the “*Centro Nacional de Aceleradores (CNA)*” of Sevilla (Spain). Experimental equipment involved an ion beam source, an accelerator, a system to collimate the beam and a detector. A radiofrequency (Alphatross) plasma source and/or a sputter of Cs⁺ atoms (SNICS II) were used to obtain ions from the gases injected to the accelerator. A 3 MV Tandem-type Van der Graaff linear accelerator was used to accelerate the bombarding ions which were focused through the high-energy beam line by magnetic quadrupoles and electrostatic steerers,

obtaining a collimate ion beam of ~ 1 mm diameter. The backscattered ions were collected with a silicon surface barrier detector set at a certain Ω angle (solid angle). The RBS experimental data were analysed using the RUMP²⁰⁵ or SIMRA²⁰⁶ simulation code. Error in the calculation of the composition was $\sim 10\%$. Bulk densities of the PCT layers of 7.15 g/cm^3 (for the PCT24 composition) or 6.20 g/cm^3 (for the PCT50 composition) and of the Pt bottom electrode of 21.40 g/cm^3 were considered for the calculation of the thickness. These values are the theoretical densities of these compounds, thus considering in the calculation that the different constituent layers of the heterostructure have a bulk density of 100%.

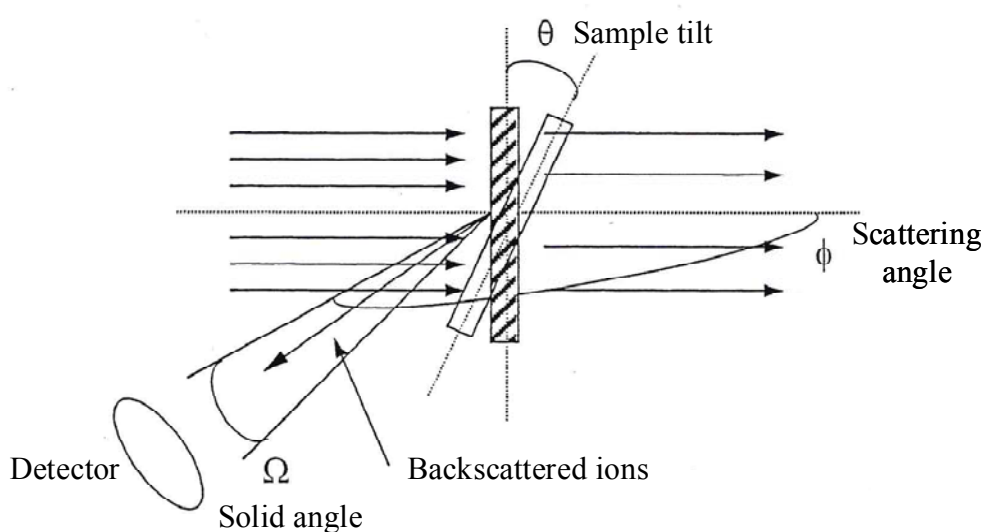


Figure 2.15. Experimental setup for the RBS measurements of the PCT films

Two different analyses were performed by RBS on the PCT films. Some of the measurements were carried out with a $2 \text{ MeV } ^4\text{He}^{2+}$ beam with the detector set at 165° (scattering angle). Since the resolution of the analysis is improved with the mass and the energy of the incident ion, more accurate measurements were carried out on the films using a $7 \text{ MeV } ^{14}\text{N}^+$ beam.

2.2.2.2.2. X-ray photoelectron spectroscopy (XPS)

X-ray Photoelectron Spectroscopy (XPS) is defined as a surface spectroscopy technique, since information provided by it only concerns a few atomic layers of the surface of the material analysed.¹⁹³ However, depth profiling in the sample can be carried out with the incorporation of an ion beam source that removes the superficial layers of the specimen. Thus, the applications of the

XPS technique are very close to those mentioned for RBS, and both techniques result complementary in the compositional and herterostructural analyses of the PCT films of this work.

The XPS technique is based on the ionisation of the atoms of the sample produced by an x-ray monochromatic incident beam (e.g. Al K_{α} , Mg K_{α}) and the subsequent analysis of the electrons emitted (also called photoelectrons) from their inner atomic orbitals (Figure 2.16). The kinetic energy (KE) at which the emitted electron leaves the sample can be measured with an electron energy analyser. Since the energy of the incident beam ($h\nu$) is determined by the x-ray generator source, the binding energy (BE) of an electron associated to a certain atom can be calculated from:

$$BE = h\nu - KE \quad [\text{eq. 6}]$$

Thus, a photoelectron spectrum with several photoelectron peaks can be recorded from the kinetic energy distribution of the emitted photoelectrons. The binding energy of the peaks is characteristic of each atom (qualitative analysis) and peaks areas can be related with the composition of the material (quantitative analysis). Furthermore, the shape of each peak and the binding energy can be slightly altered by the chemical state of the emitting atom.

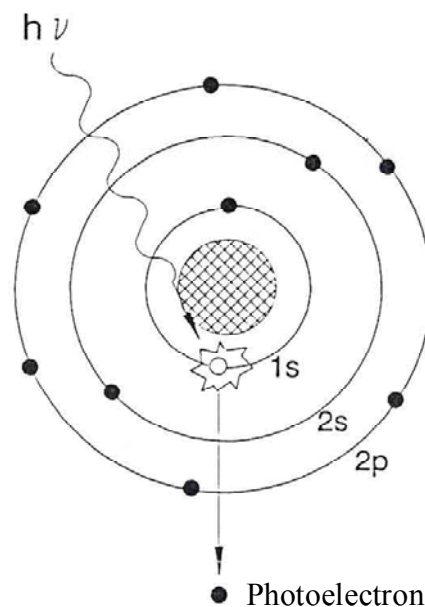


Figure 2.16. Scheme of the process of photoelectron emission

XPS measurements on the PCT films were carried out at the “*Departamento de Química Inorgánica*” of the “*Universidad de Málaga*”, in Málaga (Spain). A PHI 5700 instrument with a 4 keV Ar⁺ sputter depth profiling was used to study the composition of the films. A standard x-ray source, 15 kV, 300 W, Mg K_α (1253.6 eV) was used. The pressure in the analysis chamber was ~10⁻⁷ Pa. Survey and multiregion spectra were recorded of Ca 2p, Pb 4f, O 1s, Ti 2p, Pt 4f, Si 2p and C 1s photoelectron peaks. Binding energies were referenced to Ca 2p_{3/2} at 347.0 eV. Depth profiling was carried out using a 4 keV Ar⁺ bombardment at a current density of ~1.5 μA/cm². A crater of about 1mm diameter was studied. The in-depth scale of 3.0 nm/min was assumed to be equivalent to the sputter rate of Ta₂O₅ under the same sputter conditions.

2.2.2.3. Crystal structure

The crystalline structure of the films has been studied by X-ray Diffraction, with the Bragg-Brentano (XRD) and Grazing Incidence (GIXRD) geometries.

2.2.2.3.1. X-Ray diffraction with the Bragg-Brentano geometry (XRD)

X-Ray Diffraction (XRD) is nowadays considered as one of the most important characterisation tools used in the field of materials science and the key for many scientists to solve in a clear way the identification of crystalline structures present in the material.²⁰⁷

When an x-ray beam impinges on a crystal (i.e. a periodic ordered packing of atoms) whose interatomic distances are about the same as the wavelength (on the order of a few angstroms), part of the waves can be scattered by the atoms present in the crystal. If the scattered waves conserve the energy of the incident beam (elastic scattering) and are also able to interfere with each other (coherence), the diffraction phenomenon may occur. The diffraction arises when besides, scattered beams are combined in phase with each other producing an unmoving distribution of constructive interference and hence, a visible interference x-ray pattern. All the former conditions can be summarised in the Bragg's Law:

$$2d_{hkl} \sin \theta = n\lambda \quad [\text{eq. 7}]$$

where d_{hkl} is the distance between scattering centres (atomic hkl planes), θ is the diffraction angle, n is an integer known as the order of the diffracted beam and λ is the wavelength of the incident beam.

Each crystal presents a particular and characteristic diffraction pattern, since the different interatomic distances between the (hkl) planes are specific from its primitive unit cell. In this way, the unit cell vectors which define the structure of the crystal can be determined from the XRD patterns. For other hand, the intensity of the diffracted beams is related with the nature and arrangement of the atoms in the crystalline network. Intensity variations are indicative of preferred orientation of one or more particular crystallographic plane in the crystal.

The XRD measurements were carried out using a D500 powder diffractometer equipped with a Coolidge tube of Cu anode ($\lambda_{CuK\alpha} = 1.5418 \text{ \AA}$) working at 25 mA intensity and 40 kV voltage, and a filter of Ni. Two slits of 1° for the incident beam and other two of 1° and 0.15° for the diffracted beam were used. Counts of diffracted beams were collected by a scintillation detector. Diffraction patterns were collected in the 2θ interval between 20 and 50° , with a step of 0.05° per each 3 s. This configuration allowed us the observation of preferred orientations of the films, since the x-ray beams impinge within the bulk of the film, as difference with the GIXRD analysis where only reflections from the PCT layers next to the surface are observed. On the contrary, in the Bragg-Brentano configuration peaks reflected by the substrate can overlap the x-ray pattern of the film.

2.2.2.3.2. X-Ray diffraction with the grazing incidence geometry (GIXRD)

The conventional Bragg-Brentano geometry (θ - 2θ) may however not be the best configuration for the analysis of thin films, since reflections coming from the substrate could overlap the diffraction pattern of the film. The asymmetric Bragg geometry, also known as GIXRD, is specially used in the analysis of polycrystalline materials supported onto substrates, as the case of the PCT films of this work. In this configuration the incidence angle θ is fixed at a certain value (α) whereas the detector scans 2θ angles of the diffracted beams. Low incident angles ($1^\circ < \alpha < 5^\circ$) reduce the penetration of the incident x-rays within the bulk film and therefore, reflections coming from the substrate are avoided. In the case of films with a thin thickness and/or samples with the substrate not totally covered (a small area of the Pt bottom electrode should be free for electrical measurements), Laue peaks coming from the substrate can be detected in the diffractogram when any of the layers that form the heterostructure satisfies the Bragg conditions.²⁰⁸

For determining the appropriate incidence angle to use in the GIXRD analysis, the critical angle (α_c), which below its value the total reflection of the x-rays takes place, and the penetration depth of the x-rays for different α values were calculated for the PCT films. The critical angle was calculated from the Snell's law in total reflection conditions²⁰⁹ and from the refraction index for x-rays of a material²¹⁰, according to the following expression:

$$\sin \alpha_c = \sqrt{(2.6e^{-6} \rho \lambda^2)} \quad [\text{eq. 8}]$$

where ρ is the theoretical density of the material (7.15 g/cm³ and 6.20 g/cm³, for the PCT24 and PCT50 compositions, respectively) and λ is the wavelength of the x-ray beam ($\lambda_{\text{CuK}\alpha} = 1.540 \text{ \AA}$). An average α_c of 0.36° was thus calculated for the calcium-lead titanate system.

The penetration depth of the x-ray beams thorough the film is related to the absorption of the sample as:

$$I = I_0 e^{-\mu x} = I_0 e^{-(\mu/\rho)x\rho} = I_0 e^{-\mu_m x\rho} = I_0 e^{(-\mu x/\sin \alpha)} \quad [\text{eq. 9}]$$

where μ is the x-ray linear absorption coefficient of the material, μ_m is the masic absorption coefficient, x is the thickness of the material penetrated by the x-rays and α is incident angle of the x-rays. The equivalent penetration (Λ) is defined as the thickness that is penetrated by x-rays of I_0 intensity to decrease their intensity by 1/e ($I/I_0 = 1/e$). From eq. [9], it is obtained that:

$$\Lambda = \sin \alpha / \mu \quad [\text{eq. 10}]$$

The average μ value calculated for the PCT system is $\sim 0.059 \mu\text{m}^{-1}$, therefore the penetrations calculated for various incident angles were:

α (°)	0.5	1	2	3	4	5
Λ (μm)	0.147	0.296	0.591	0.887	1.182	1.477

According to these values, incident angles between $0.5^\circ \leq \alpha \leq 2^\circ$ were used for the majority of the GIXRD analyses of the PCT films, since higher values of α would mean that additional information from the crystal structure of the substrate would be obtained.

The GIXRD measurements were carried out in the D500 powder diffractometer previously described, but in this case a 0.4° -Soller slit and a LiF monochromator were incorporated to the detector system in order to perform analyses with the grazing incidence geometry.

A schematic illustration of both Bragg-Brentano and grazing incidence geometries is depicted in Figure 2.17.

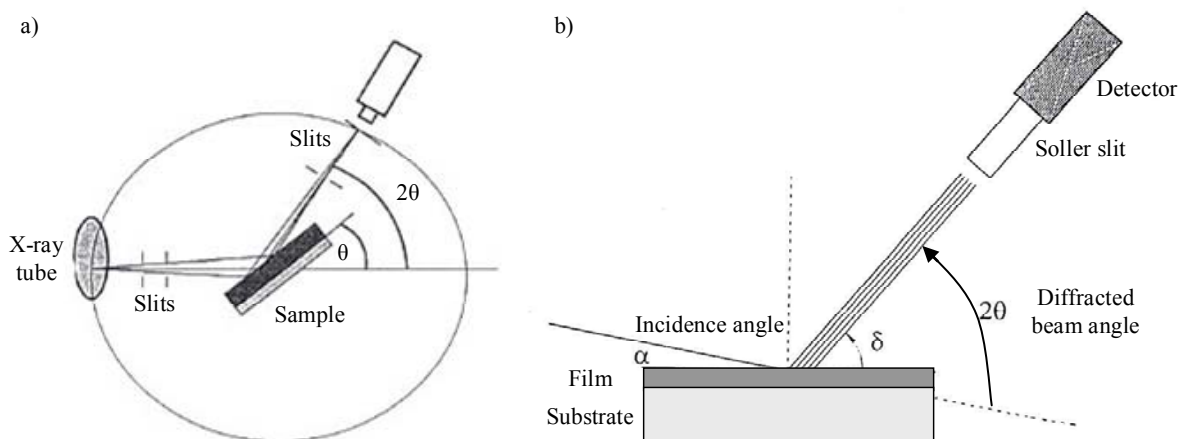


Figure 2.17. Schematic illustration of Bragg-Brentano (a) and grazing incidence (b) geometries for x-ray diffraction

2.2.2.4. Microstructural and nanoscopic studies

The microscopy is one of the most used instruments in the study of materials and involves optic, electronic (Scanning Electron Microscopy, Transmission Electron Microscopy) and scanning probe (Scanning Force Microscopy, Scanning Tunnelling Microscopy) microscopies as major derived techniques. In the present work, the microstructure of the films has been studied by Scanning Electron Microscopy (SEM), Transmission Electron Microscopy (TEM) and Scanning Force Microscopy (SFM). Further studies of the films properties at nanoscale have also been performed by Brillouin Spectroscopy (BS).

2.2.2.4.1. Scanning electron microscopy (SEM)

The electronic microscopy is based on the use of a beam of highly energetic electrons to examine objects at a very fine scale. In Scanning Electron Microscopy (SEM),²¹¹ the image is

formed by an electron beam which is focused on the specimen surface. This beam is first produced at the top of the microscope by a thermoionic electron gun. Electrons are accelerated towards the specimen using a positive electrical potential of 2-40 kV. The electron beam is confined and focused using metal apertures and magnetic lenses into a thin, monochromatic beam, directed down to the sample. The interaction between the primary electrons and the sample gives rise to various physical phenomena (backscattering, cathodoluminescence, secondary electrons formation, x-ray and Auger emission, etc). In the case of SEM, the detector collects secondary electrons and converts them into a signal that is sent to a viewing screen, producing thus an image. Secondary electrons are excited electrons of the specimen produced by the inelastic collision with the primary electron beam which result ejected from the atoms and, after undergoing additional scattering events while travelling through the sample, emerged from its surface with a low energy value (<50 eV). Due to this low energy, only secondary electrons which are near the surface can escape and be examined. Hence, the information obtained by SEM is related to the topography of the sample.

SEM images of the PCT films of this work have been obtained by three different electronic microscopes:

- Philips XL30 (SEM) microscope at the “*Univesidad Carlos III de Madrid*”, in Madrid (Spain).
- JSM 6335F NT (FEG-SEM) microscope at the “*Centro de Microscopía Electrónica Luis Bru*”, of the “*Univesidad Complutense de Madrid*”, in Madrid (Spain).
- Philips XL30FEG (FEG-SEM) microscope at the “*Instituut voor MateriaalOnderzoek (IMO-IMOMECE)*” of the *University of Hasselt*, in Diepenbeek (Belgium).

Plan-view and cross-section images of the PCT films were obtained by SEM. A fine carbon vapour coating was deposited on the samples in order to make them electrically conducting, since insulator materials can be affected by the charging phenomena produced by the electron convergence on their surface, obtaining thus distorted images.

2.2.2.4.2. Transmission electron microscopy (TEM)

A transmission electron microscope essentially works as a SEM one, with the main difference that the image formed by TEM (Transmission Electron Microscopy) is obtained from the electrons transmitted through the specimen.²¹² Since electronic absorption by the sample is much

more efficient than electronic transmission through it, TEM microscopes usually work with a high voltage electron beam of 80-400 keV. Furthermore, materials for TEM analysis must be specially thinned to get specimens which allow electrons to be transmitted through them (100-200 Å thickness).

A TEM microscope basically consists in a column, set at ultrahigh vacuum, where the illumination system is displayed along. The electron gun produces a high energy stream of monochromatic electrons which is focused into a thin, coherent beam by the use of condenser lenses. The first lens determines the spot size (general size range of the final spot that strikes the sample), whereas the second one controls its intensity (from a wide dispersed spot to a pinpoint beam). The beam is restricted by the condenser aperture until it strikes the specimen and parts of it are transmitted through. The transmitted electrons are focused by the objective lens into an intermediate image, which is enlarged by the intermediate and projector lenses until it impinges on a phosphor image screen and light is generated, allowing the user to see the image. A schematic representation of both SEM and TEM microscopes is depicted in Figure 2.18.

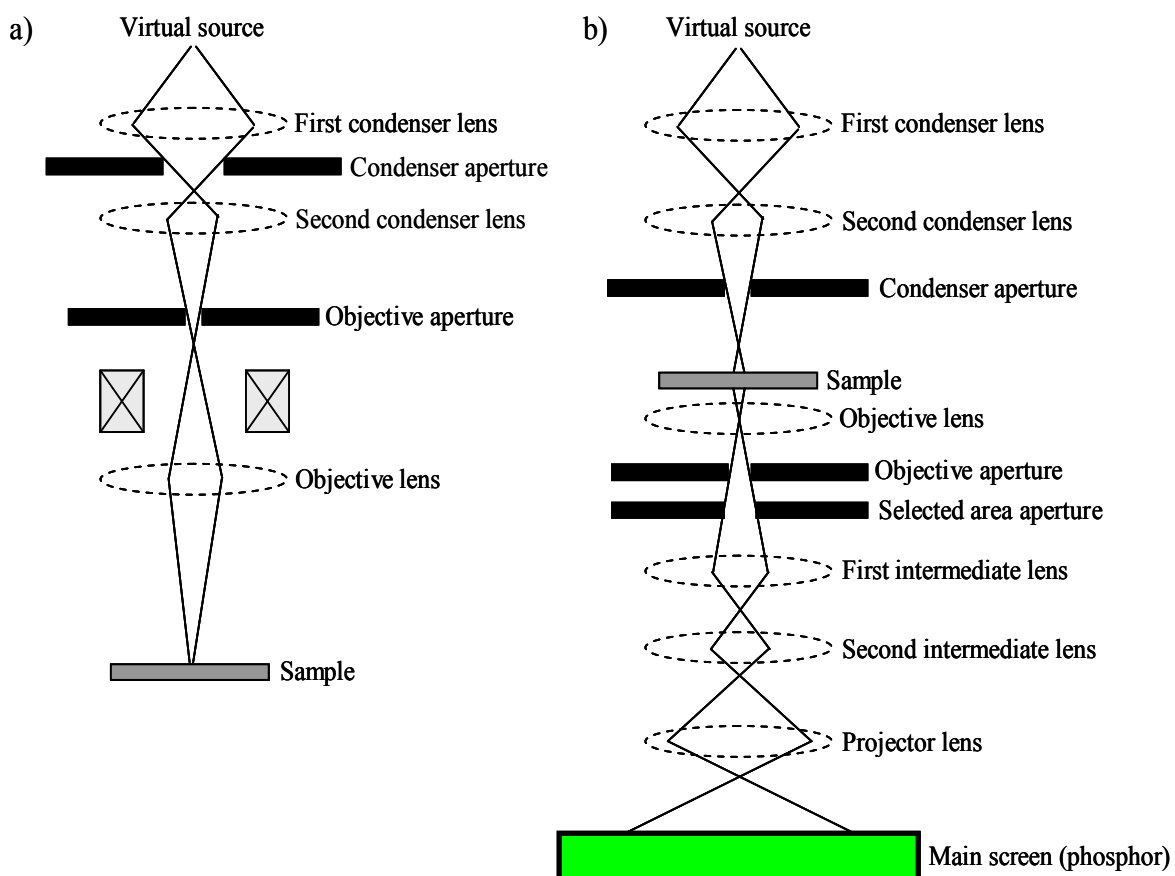


Figure 2.18. Schematic diagram of SEM (a) and TEM (b) columns

From this configuration two types of information (images) can be obtained; the direct image projected by the entire specimen (microstructure) and the electron diffraction pattern resulted when the electron beam crosses an orderly crystallographic pattern (crystallographic structure). With the objective aperture the image contrast is enhanced by blocking out high-angle diffracted electrons, whereas the selected area aperture allows collecting the diffraction patterns obtained.

From the electron diffraction patterns obtained, the interplanar distances d_{hkl} and indexation of planes $\{hkl\}$ were calculated, according to Bragg's Law and assuming low diffraction angles θ , by the following expression:

$$d_{hkl} = \lambda L / R \quad [\text{eq. 11}]$$

where L is the camera length of the microscope (specimen-screen distance), λ is the wavelength of the electron beam and R is the distance of the diffracted spot respect to the incident beam position (in the electron pattern).

TEM measurements on the PCT films have been carried out at the “*Univesidad Carlos III de Madrid*”, in Madrid (Spain), using a JEOL-200 FX II microscope operating at 200 kV. Specimens for plan-view analysis were prepared from pieces of films on substrates by mechanically polishing to $\sim 20 \mu\text{m}$ and mounting onto 7HEX (Pelco) copper grids. Further thinning to electron transparency was obtained by Ar^+ ion milling at 5 kV. For some of the PCT films, preparation of TEM specimens for plan-view observation could be carried out by an electrolytic process in solution,²¹³ in which the PCT film was peeled-off from the substrate, thus avoiding the polishing process. These films were collected on copper grids and subjected to ion milling to obtain the transparent specimens. Cross-section specimens of the films were prepared from two pieces of the film which were stacked with the films facing and glued. Lateral thickness was decreased, using a tripod polisher until a fine wedge was produced. Electron-transparent areas were obtained by the further ion milling of the polished samples.

2.2.2.4.3. Scanning force microscopy (SFM)

Another method for observing the surface topography of the materials at nanoscale, is Scanning Force Microscopy (SFM). In this technique, the presence of a conducting surface is not needed and neither special sample preparation nor vacuum is usually required.¹⁹³ The fundamentals of this microscopy lie on the interaction of a sharp probing tip with the specimen surface while a

certain area of the specimen surface is scanned.²¹⁴ In the non-contact mode (distances between the tip and the sample surface of 1-20 nm), attractive forces such as Van der Waals, electrostatic, magnetic or capillary forces produce images of topography, whereas in the contact mode ionic repulsion forces take the leading role. A third mode, called tapping or intermittent contact mode, can also be used, where the tip is oscillating above the sample surface and changes in its oscillation yield to topographic information.

In this work, the topography of the surface of the PCT films has been studied with a scanning force microscope (Nanotec® Electrónica with WSxM® software) working in contact mode with Si cantilevers (Nanosensors) of around 0.2 N/m force constant and 13 kHz resonance frequency. A schematic representation of the SFM microscope is depicted in Figure 2.19. It consists in a cantilever of a determined spring constant with a sharp tip at its end, typically composed of silicon or silicon nitride with tip sizes of the order of nanometers. The repulsive forces between the tip and the surface produce a deflection of the cantilever according to Hooke's law, which is measured using a laser spot reflected from the top of the cantilever into an array of photodiodes. The deviation on the original incident point of the laser, caused by the deflection, is corrected by the vertical displacement of the piezoelectric scanner. This scanner consists in a piezoelectric actuator (usually a ceramic) with movement in the X, Y and Z directions above which the sample is supported. Thus, as the tip scans the sample, the scanner moves the sample vertically in order to maintain constant the interaction force between the tip and the surface. From the analysis of the photodetector sign, the height profile of the sample surface is obtained and therefore the topographic image as well.

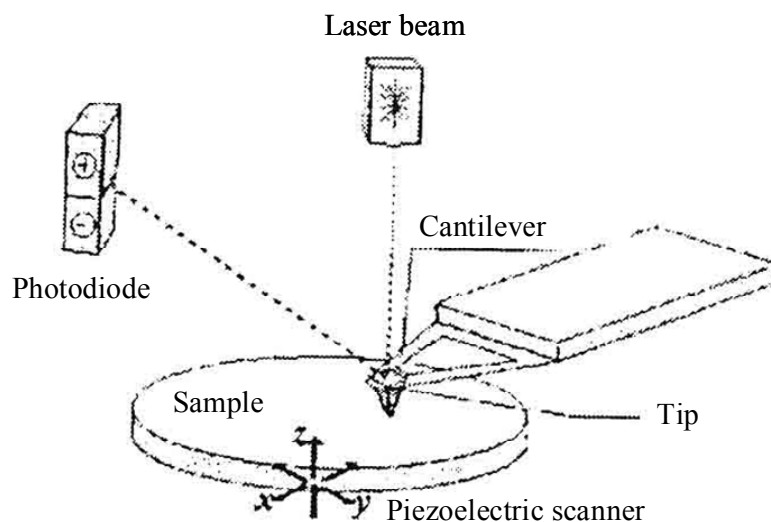


Figure 2.19. Schematic representation of a scanning force microscope

2.2.2.4.4. Brillouin spectroscopy (BS)

Brillouin Spectroscopy (BS), also known as Brillouin Light Scattering (BLS), is a powerful technique for studying the elastic and optical properties of nano-scale structures. This technique is based on the inelastic scattering of an incident optical wave field by thermally excited elastic waves (phonons) present in a sample.²¹⁵ This phenomena results in scattered photons frequency shifted (Δf) respect to the exciting incident light. A Brillouin spectrum collects the frequency shift of the thermal phonons, which is proportional to the propagation velocity of a Surface Acoustic Wave (SAW) in the material. From the sound velocities calculated, elastic properties of the material, such as the stiffness coefficient, could be also determined.

The BS technique has been specifically used before in the study of sol-gel materials,²¹⁶ since the conversion of a sol into a gel can be described as the change from a Newtonian fluid (sol) to an elastic solid (gel). This produces a change in the elastic properties of the material that is detected by the variation in the sound velocity measured by BS. Obviously, conversion of a gel or amorphous material (as-deposited amorphous film) into a crystalline material (ferroelectric film) is also accompanied by a variation in the elastic properties and thus, BS can also be useful in the study of the crystallisation process. Therefore, this technique can provide information about how crystallinity evolves in the material at nanoscale, since in the transformation from amorphous to crystalline films, intermediate states can appear such as hybrid amorphous-nanocrystalline or nanocrystalline-microcrystalline states,²¹⁷ which can result in unexpected variations of the properties of the final film that can be of interest for applications.

Brillouin Spectroscopy (BS) has been performed at room temperature on the PCT films of this work. The experimental setup²¹⁸ is schematelly shown in Figure 2.20. The light source was a 2060 Beamlok Spectra Physics Ar⁺ ion laser provided with an intracavity temperature stabilized single-mode and single-frequency z-lok etalon ($\lambda_0 = 514.5$ nm). The scattered light was analysed using a Sandercock-type 3+3 tandem Fabry-Pérot interferometer.²¹⁹ With this tandem-multipass interferometer, the contrast of the Brillouin spectra is significantly improved, since conventional Fabry-Pérot interferometers do not achieve the contrast needed to resolve the weak Brillouin doublets (10^4 - 10^5 times less intensive than the elastically scattered light). The incident polarisation direction was chosen to be in-plane (p-polarization) while no polarization analysis of the scattered light was made. The typical values for Finesse and contrast were 150 and 109, respectively. The sound propagation velocity in the films of this work was calculated with an expression that considers the effect of the reflecting substrate on which the films are supported.^{215,220}

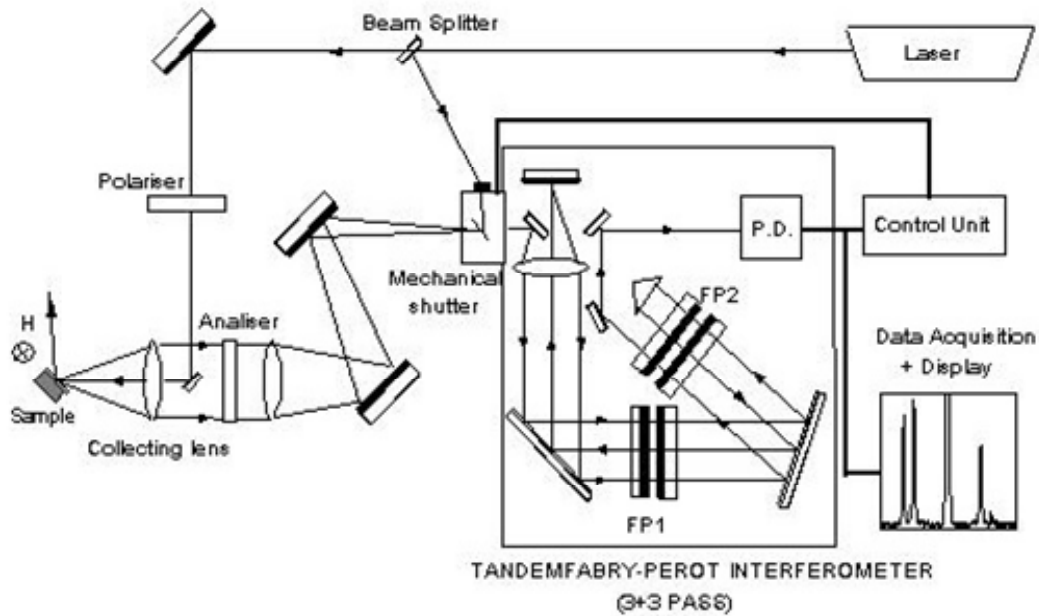


Figure 2.20. Experimental setup of the BS technique

2.2.2.5. Electrical characterisation

In order to perform electrical characterisation on the PCT films, top-dot Pt electrodes were sputtered on the films surfaces using a BAL-TEC SCD 050 sputter working at 80 mA for 300 s. A shadow mask with several dot sizes was used to obtain an array of capacitors with electrodes areas from 0.05 to 0.35 mm². The resulting Pt layer was used as bottom electrode, once a small surface along the edge of the film was peeled-off from the substrate (see previous section 2.4.1.1). Thus, parallel-plate capacitor type electrical measurements could be carried out on the films. The capacitors thus obtained were RTP-annealed in order to improve their electrical response.

2.2.2.5.1. Dielectric constant

Variation of the dielectric constant (k') and loss factor (k'') with temperature at several frequencies (100 Hz-1 MHz) has been measured on the PCT films of this work. These parameters were calculated through the expressions:

$$k' = (C_p d) / (\epsilon_0 S) \quad [\text{eq. 12}]$$

$$k'' = d / (\nu \epsilon_0 S R_p) \quad [\text{eq. 13}]$$

where C_p is the capacitance of the circuit, d is the thickness of the film, ϵ_0 is the vacuum permittivity, S is the area of the top electrode, ν is the measuring frequency and R_p is the resistance of the parallel circuit.

An impedance analyser LCR-meter HP 4284A working with a non-perturbing amplitude signal of 10 mV was used for these measurements, in the temperature range between -170 and 500 °C. Thus, the temperature at which the material evolves from a ferroelectric (polar) phase to a paraelectric (non-polar) phase could be determined from the dielectric anomaly observed. In this work, the temperature at which the dielectric constant shows a maximum value (dielectric anomaly) was defined as the transition temperature (T_m) of the system, usually determined from data collected from the paraelectric to the ferroelectric phase. A rate of 1.5 °C/s was used in both heating and cooling runs.

2.2.2.5.2. Leakage current density

One technologically significant feature in the design engineering of ferroelectric computer memories (NVFeRAMs, DRAMs) concerns the knowledge about the nature of leakages currents present in the material in order to control heating of the memory and consequent thermal breakdown.²²¹ Ferroelectric film capacitors supported onto metal electrodes exhibit several mechanisms of electronic conduction, such as thermionic Schottky currents, bulk-limited Poole-Frenkel currents and Space-Charge-Limited Currents (SCLC), among the most important ones. All of these processes contribute non-additionally to the total leakage current measured in the device. Obviously, leakage phenomena suppose an undesired effect in microelectronic devices that can produce detrimental of some properties of the film.

Leakage current densities have been measured for the PCT films of this work by the step relaxation technique,²²² using a Keithley 6512 electrometer and a HP 3325A pulse generator. Data were recorded for positive and negative dc bias, in a voltage range from ± 0.05 to ± 7 V with 30 steps on a square root scale. To prevent irreversible electrical breakdown of the capacitor and damage of the electrometer, the dc field was applied for a maximum time of 30 s, meanwhile the current measured was always lower than 100 times the initial one. The relaxation time was fixed at 90 s. The top electrode was first positively biased for each voltage, the bottom electrode acting as the cathode. Then, polarisation and relaxation currents were recorded. The value of the leakage

current was obtained as the sum of the polarisation and relaxation currents. When all data were collected for positive voltages, the capacitor was kept in short circuit for 100 min previous to the measurements at negative voltages. A schematic diagram of this measurement is shown in Figure 2.21.

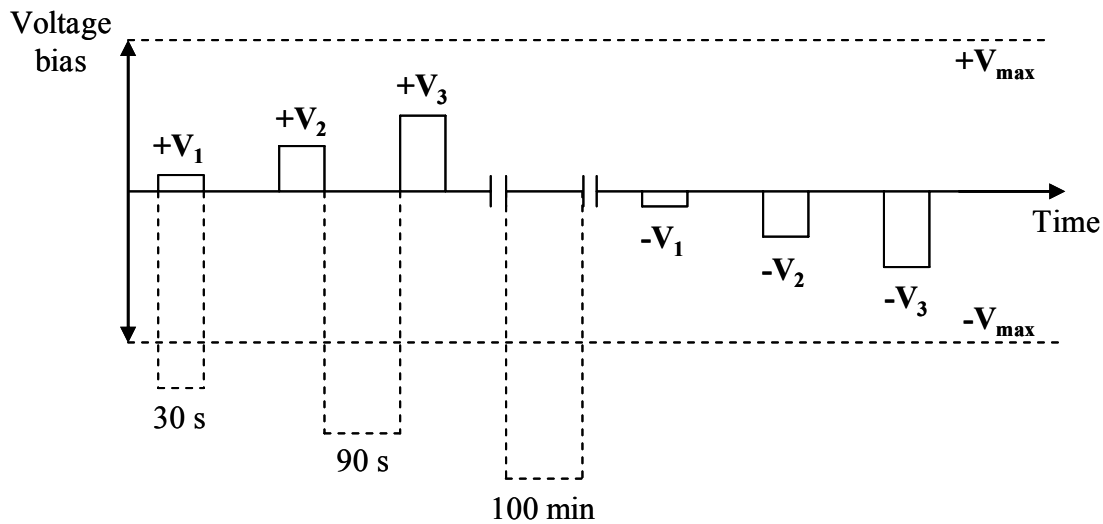


Figure 2.21. Schematic diagram of the measurement for the leakage current determination

2.2.2.5.3. Capacitance-voltage curves

The measurement of capacitance versus voltage, $C(V)$, provides information about the dielectric nature of the films, such as electric bias effects on the transition temperature, thickness dependence of nonlinearity and dielectric diffusivity of the transition. Due to the measuring technique, which performs the analysis in positive and negative changing bias, the asymmetry of the loops around zero voltage with different maximum values can indicate the existence of charge carriers at the film-electrode interfaces.

Capacitance versus bias voltage has been measured on the PCT films at different temperatures using an impedance analyser HP 4194A. A schematic representation of this measurement is shown in Figure 2.22. The $C(V)$ curves were performed by biasing the capacitor with changing bias in a staircase way, while measuring the high frequency capacitance in a stationary state with a small signal amplitude (0.01 V). Measurements were carried out by sweeping with the bias in both directions searching for hysteresis as a function of temperature.

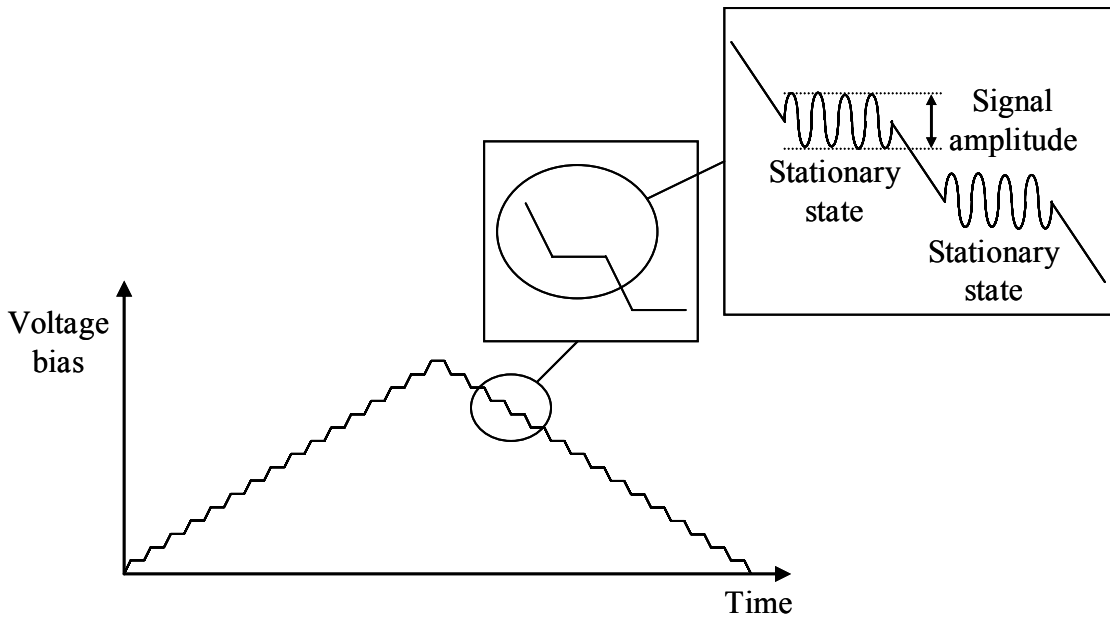


Figure 2.22. Schematic diagram of the measurement for the capacitance versus voltage curves determination

From the application point of view, the analysis of the $C(V)$ measurements allowed us to evaluate the feasibility of these films for applications in high frequency components through calculations of their tunability (the degree of variation of the dielectric constant or capacitance as a function of the applied electric field). Relative tunability, $T_{un,rel}$, is defined by:

$$T_{un,rel} = (C_{max} - C_{min}) / C_{max} \quad [\text{eq. 14}]$$

where C_{max} and C_{min} are the values of maximum and minimum of capacitance corresponding to the minimum and maximum of applied voltages, at a certain temperature. But for applications, the parameter that combines tunability with loss tangent ($\tan \delta$) results more realistic. In this work, this approach has been defined by the Figure of Merit (FOM), given by:

$$\text{FOM} = T_{un,rel} / \tan \delta \quad [\text{eq. 15}]$$

Since the capacitor must be charged from zero to V , the $C(V)$ curves can also give information about the capability of these thin films for applications in DRAMs. In order to measure the capacitor voltage drop after a writing pulse, the setup sampled the voltage level of the capacitor by a data acquisition hardware, DAQ, after applying a pulse of 3 V of amplitude for 4 ms. The measurement tasks were programmed by the commercial LabVIEW software.

2.2.2.5.4. Hysteresis loops

The existence of an electrical polarisation which its sign can be inverted by the application of an external field is the main characteristic of a ferroelectric material. Thus, the experimental measurement of the hysteresis loop consequently defines the ferroelectric behaviour of the material. Ferroelectric materials behave as non-linear dielectrics, that is, their polarisation versus applied electric field (P-E) response is not linear, giving rise to the typical hysteresis loop shown in Figure 2.23a. From this measurement, the *remanent polarisation* $P_r = (|P_r^+| + |P_r^-|) / 2$ and *coercive field* $E_c = (|E_c^+| + |E_c^-|) / 2$ parameters can be calculated. The slight asymmetry of hysteresis loops respect to the electric field axis (X axis) is usually due to the existence of polarisation internal electric fields (bias electric fields, $(|E_c^+| - |E_c^-|) / 2$) present in the sample.

Another equivalent representation of the inversion of the polarisation with electric field of a ferroelectric material is the current density versus electric field (J-E) hysteresis loops. The ac electric current represents the variation of the polarisation of the material with time ($\delta P / \delta t$). The current maxima peaks depicted in Fig. 2.23b correspond to the polarisation inversion phenomena, and remanent polarisation is calculated from the areas of those peaks whose maxima give rise to the coercive field values.

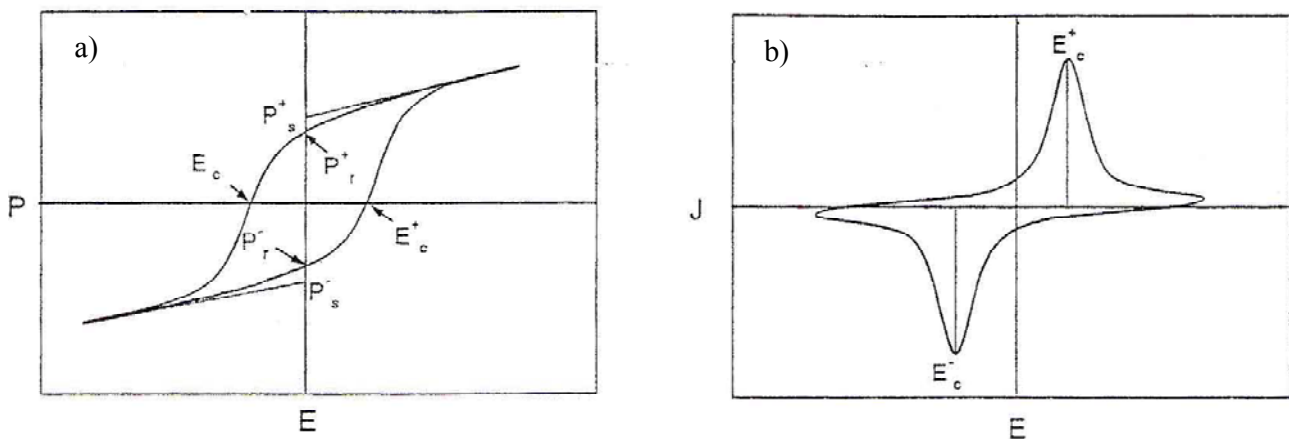


Figure 2.23. $P(E)$ hysteresis loop (a) and $J(E)$ ac current density loop (b)

Measurements of current density hysteresis loops on the PCT films have been carried out using a modified Sawyer-Tower circuit.²²³ Experimental setup consisted of a HP 8116A pulse generator that allows the application of sinusoidal waves with electrical amplitude signals between 0.01-16 V and frequencies of 1-50 MHz. Current intensity generated values, after amplification

with a Keithley 428 current amplifier, together with the voltage applied were collected with a Tektronix TDS 520 oscilloscope.

Data acquisition and further processing of files was carried out by home-made software. Thus, the integration of the current density loops obtained led to $P(E)$ calculated hysteresis loops. However, the integrated current was compensated by a non-perturbative method,²²⁴ since together with the charge generated from the polarisation inversion (ferroelectric current, i_F), contributions due to resistivity (ohmic current, i_R) and film capacity (capacity current, i_C) are also present.

2.2.2.5.4.1 Piezoresponse force microscopy (PFM)

Piezoresponse Force Microscopy (PFM) consists in an implemented scanning force microscope (see Figure 2.24) working in contact mode, in which a testing ac signal is applied between the conducting tip and the bottom electrode of a piezoelectric sample.^{225,226} Due to the reverse piezoelectric effect, local vibrations induced on the sample surface are transmitted to the cantilever, whose oscillation (deflection) is collected by the photodetection system and extracted as an electrical signal using a standard lock-in technique. This electrical signal, collected by the output of the lock-in amplifier, contains information about the deformation induced in the sample by the ac testing voltage. The amplitude of the sample vibration provides information on the magnitude of the piezoelectric coefficient, while the phase signal determines the polarisation direction in each location. Since both applied testing voltage and amplitude of the sample vibrations lie perpendicularly to the sample plane, the piezoelectric coefficient d_{33} is estimated. Thus, local hysteresis loops of d_{33} coefficient as well as the domain structure of a ferroelectric material can be obtained by PFM.

PFM measurements were carried out using the SFM microscope previously described in section 2.4.4.3 implemented with a 7265 DSP lock-in amplifier and a Agilent 33120.A function arbitrary waveform generator. Conductive commercial Pt/Ir coated tips (Nanosensors) on cantilevers with a force constant of 42 N/m and resonance frequency of 320 kHz were used to apply an ac voltage of 1 V at 50 kHz.

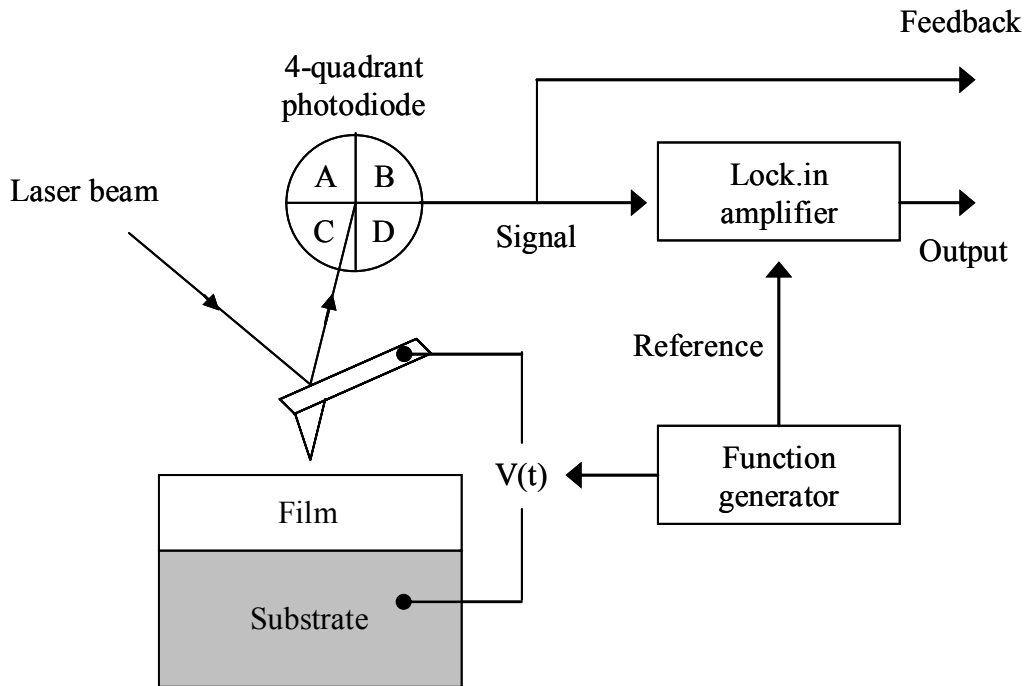


Figure 2.24. Experimental setup used for the PFM measurements on the films

2.2.2.5.5. Fatigue and retention

Fatigue and retention are considered critical issues regarding the non-volatility of memories constructed from ferroelectric materials (NVFeRAMs). Ferroelectric (polarisation) fatigue is defined as the loss of the remanent polarisation in a ferroelectric material undergoing bipolar drive, that is, the polarisation decay after several switching (read/write) cycles. Fatigue is generally agreed to be the result of charge injection and accumulation of space charge (e.g. oxygen vacancies) within the ferroelectric material that pins domain switching. Another requirement of the non-volatility of the information stored in the memory is the retention of the polarisation with time (time permanence of the electrical polarisation value). Both reduction of read/write fatigue of remanent polarisation and high endurance to the losses of the stored charge with time (retention), are main topics of interest on searching materials for NVFeRAMs applications.

Fatigue was studied in the PCT films using a Radiant Technology Inc. Testing System (RTA66A model) in the virtual ground mode, coupled to a function generator. Alternate square pulses of 8 V amplitude and 500 kHz frequency were used for the fatigue measurements of this work. After this, polarisation (writing) and (reading) pulses with the same amplitude and frequency were applied according to the schematic diagram of Figure 2.25.

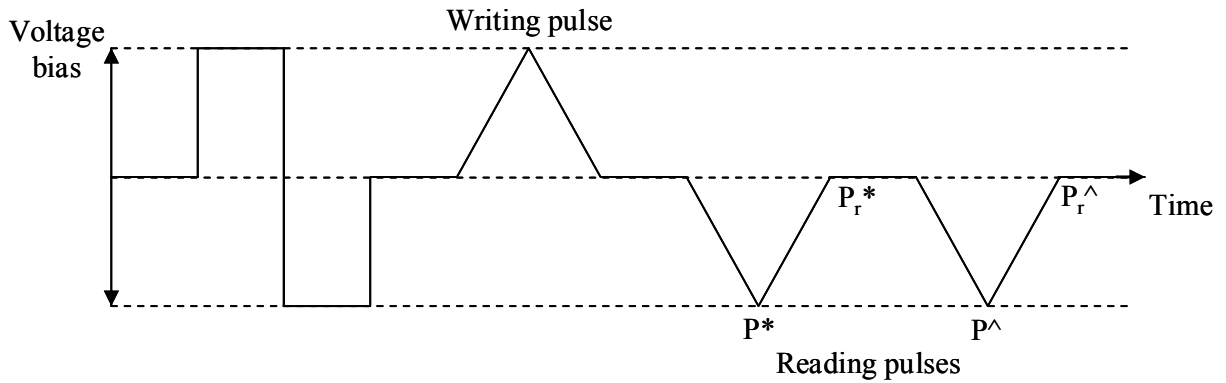


Figure 2.25. Schematic diagram of the fatigue measurement on the films

From these measurements, magnitudes of P^* , P_r^* , P^\wedge and P_r^\wedge are obtained.²²⁷ They correspond to the integrated charge measured during the increase and decrease of the voltage of the two triangular read pulses; the magnitudes with superscript (*) correspond to the first pulse and deals with the switchable polarisation, meanwhile the magnitudes with superscripts (^) measured for the second pulse, correspond to the charges relaxed or switched back during the time elapsed between both reading pulses. The differences $P^* - P^\wedge \approx P_r^* - P_r^\wedge$ are the non-volatile polarisation, P_{nv} , whose evolution with the number of switching cycles has been measured for the fatigue study of this work.

The evolution of the pyroelectric coefficient (γ) after poling with time allowed us to evaluate the polarisation retention of the PCT films through a non-perturbative method.²²⁸ Square pulses of 8 V amplitude and 50 μ s width were used for poling the films. Then, triangular pulses with an amplitude of ± 4 °C and a nominal frequency of 3 °C/min were used to estimate the γ coefficient ($\delta P/\delta T$) from the pyroelectric currents generated in the PCT films.

CHAPTER III

PCT THIN FILMS FROM THE AQUEOUS SOLUTION-GEL SYNTHETIC ROUTE

The fabrication of high performance ceramic materials usually involves environmental and economical costs related with the use of hazardous substances, energy consumption and waste generation during the whole process. In the case of the electronic industry, the environmental awareness is each time more and more demanded, as deduced from the stringent European Directives enacted in the last decades. The RoHS directive¹⁴ (“*Restriction Of the use of certain Hazardous Substances in electrical and electronic equipment*”) restricts particularly the use of lead in electrical and electronic equipment, although lead in electronic ceramic parts (e.g. piezoelectric devices) is exempt from this band at the moment. As long as viable lead-free replacement is not fully developed and lead based-on compositions (mainly represented by $\text{Pb}(\text{Zr},\text{Ti})\text{O}_3$ and PbTiO_3) continue being (and it seems to continue being in the near future) one of the most important alternatives in the fabrication of dielectric, ferroelectric or piezoelectric materials,¹⁵³ the environmental friendly trend must be also aimed at the development of low-toxic processes for the production of electronic ceramics (low-toxic solvents and reagents, low thermal budgets, etc).

For the synthesis of ceramic materials, chemical solution methods are low energy processes compared to solid and/or vapour state reactions, which is one of the keys of the soft solution processing of advanced materials.²²⁹ Furthermore, by Chemical Solution Deposition (CSD) methods, the conformation of these ceramics into the thin film form can be obtained, which nowadays is considered a significant contribution to the development of microelectronic devices and integrated circuits.

In this chapter, the development of an entirely aqueous solution-gel method for the synthesis of $(\text{Pb}_{1-x}\text{Ca}_x)\text{TiO}_3$ (PCT) precursor solutions, with $0 \leq x \leq 0.50$, is presented for the first time. Part of this work was carried out within the framework of a short-term stay in a foreign laboratory granted by the FPI (“*Formación de Personal Investigador*”) Program of the Spanish Ministry of Education and Science (MEC). This was a three months stay in the *Laboratory of Inorganic and Physical Chemistry* of the *University of Hasselt*, at Diepenbeek (Belgium).




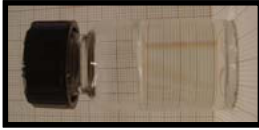
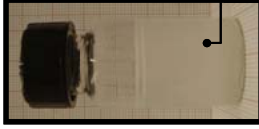

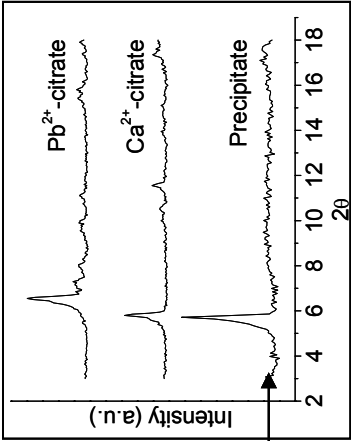
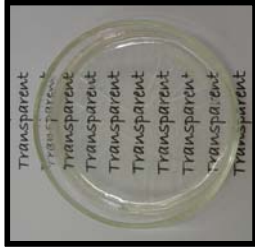
3.1. AQUEOUS PCT PRECURSOR SOLUTIONS

The calcium modified lead titanate, $(\text{Pb}_{1-x}\text{Ca}_x)\text{TiO}_3$ (PCT), precursor solutions of this work have been synthesised by the aqueous solution-gel process described in previous *Chapter II* (section 2.1.2). Thus, solutions with nominal compositions of $(\text{Pb}_{0.76}\text{Ca}_{0.24})\text{TiO}_3$ (PCT24) and $(\text{Pb}_{0.50}\text{Ca}_{0.50})\text{TiO}_3$ (PCT50) were prepared. The main physicochemical features of these solutions are detailed in Table 3.1.

Air-stable and precipitate-free PCT24 and PCT50 stock solutions are obtained by this novel aqueous solution-gel method. Although both solutions followed the same synthetic, a bigger amount of water was necessary to add to the PCT50 system in order to obtain a clear and transparent solution. This is due to the low solubility that the calcium citrate reagent exhibits in the aqueous media (solubility of ~ 0.9 g/L at room temperature for pH's above 4.5).

The properties of these solutions slightly differ concerning their physicochemical characteristics and gelation behaviour. Representative pictures of the solutions and gels are shown embedded in Table 3.1. Identical values of viscosity, density and pH were obtained in both solutions, although the more amount of water added to the PCT50 composition (as commented before) led to a solution with a lower concentration and a colorless coloration, whereas a yellowish colour was observed in the PCT24 solution. Both solutions were stored at room conditions in simple glassware. However, the PCT50 solution was stable only for a few weeks, observing the formation of precipitate (see picture). The precipitate thus formed was poured off, dried ($80^\circ\text{C}/24$ h) and subjected to x-ray diffraction. The resulting x-ray pattern is shown in the inset of Table 3.1, in comparison with the patterns of the commercial calcium citrate tetrahydrate reagent $(\text{Ca}_3(\text{O}_2\text{CCH}_2\text{C}(\text{OH})(\text{CO}_2)\text{CH}_2\text{CO}_2)_2 \cdot 4\text{H}_2\text{O}$, Aldrich, 99%) and of the lead citrate compound prepared during the synthesis procedure (see experimental section). The results reveal that the precipitate is mainly formed by a crystalline Ca^{2+} component close to calcium citrate. On the contrary, the PCT24 precursor solution remained stable even up to a year, and neither gelation (sol-gel transition) nor precipitation of the solution with time was observed (see picture).

Table 3.1. Physicochemical properties of the aqueous PCT precursor solutions

Composition	Reagents and solvents	Molar ratios	Physicochemical characteristics
			Concentration (*) Viscosity, density and pH Aspect
$(\text{Pb}_{0.76}\text{Ca}_{0.24})\text{TiO}_3$ (PCT24)	$\text{HOC}(\text{COOH})(\text{CH}_2\text{COOH})_2$ H_2O_2 , H_2O , NH_3 $\text{Ti}[\text{OCH}(\text{CH}_3)_2]_4$, $\text{Pb}(\text{C}_6\text{H}_6\text{O}_7) \cdot \text{H}_2\text{O}$ $\text{Ca}_3[\text{O}_2\text{CCH}_2\text{C}(\text{OH})(\text{CO}_2)\text{CH}_2\text{CO}_2]_2 \cdot 4\text{H}_2\text{O}$	Citric acid:Ti(IV) 2:1 H_2O_2 :Ti(IV) 2:1 H_2O :Ti(IV) 25:1	~0.35 M ~1 cP, ~1 mg/L, ~8.5 Yellowish (*) referred as the equivalent of moles of PCT per litre of solution
	Aging with time  Stable solution (up to a year)	Solution aging  Gelation (24 h) (transparent gel)	Aging with temperature (60 °C)  Gelation (24 h) (transparent gel)
$(\text{Pb}_{0.50}\text{Ca}_{0.50})\text{TiO}_3$ (PCT50)	$\text{HOC}(\text{COOH})(\text{CH}_2\text{COOH})_2$ H_2O_2 , H_2O , NH_3 $\text{Ti}[\text{OCH}(\text{CH}_3)_2]_4$, $\text{Pb}(\text{C}_6\text{H}_6\text{O}_7) \cdot \text{H}_2\text{O}$ $\text{Ca}_3[\text{O}_2\text{CCH}_2\text{C}(\text{OH})(\text{CO}_2)\text{CH}_2\text{CO}_2]_2 \cdot 4\text{H}_2\text{O}$	Citric acid:Ti(IV) 2:1 H_2O_2 :Ti(IV) 2:1 H_2O :Ti(IV) 90:1	~0.25 M ~1 cP, ~1 mg/L, ~8.5 Colorless (*) referred as the equivalent of moles of PCT per litre of solution
	Aging with time  as-synthesised  2 weeks later  Precipitation after 2 weeks	Solution aging 	Aging with temperature (60 °C)  Gelation (24 h) (transparent gel)

Small volumes of the fresh precursor solutions were dried on Petri dishes in a furnace at 60 °C for 24 h. The sol-gel transition with temperature was observed and therefore clear and transparent glassy gels were obtained for both precursor solutions (see pictures). However, if longer times of heating were applied, the PCT50 solution was prone to precipitate during gelation with temperature and a translucent although glassy gel was obtained (see picture). As more solvent is evaporated from the solution, the critical concentration for the non-solubility of calcium citrate seems to be reached. However, it seems that in the PCT24 solution the total gelation occurs before reaching the solubility point of the calcium citrate reagent in the aqueous media.

3.2. THERMAL DECOMPOSITION OF THE AQUEOUS PCT GELS

The thermal decomposition mechanism of the PCT24 and PCT50 gels obtained (60 °C/24 h) was studied by means of several coupled thermal techniques, such as Fourier Transform Infrared and Mass Spectroscopies coupled to Thermogravimetric Analysis (TGA-FTIR and TGA-MS).

Figure 3.1 shows the TGA and the corresponding derivative DTG curves measured during the thermal treatment of the PCT24 and PCT50 gels (Figs. 3.1a and 3.1b, respectively). Five steps can be distinguished in the thermal decomposition of both gels, centered at temperatures of ~75, ~210, ~345, ~460 and ~540 °C (PCT24) or 605 °C (PCT50). Respective associated weight losses to these steps are ~2.8, ~26.4, ~16.9, ~19.6 and ~1.5 wt% for the PCT24 gel and ~2.9, ~33.7, ~14.4, ~20.7 and ~1.9 wt% for the PCT50 gel. Attending to the DTG data, the broad peak attributed to the second step (210 °C) indicates that various overlapping processes may occur at this temperature interval. On the contrary, a more homogeneous decomposition process is found during the fourth step, which results in the sharp peak observed at 460 °C. Regarding the last step of the decomposition process of both gels, the temperature at which it occurs differs as a function of the PCT composition (540 °C for the PCT24 gel and 605 °C for the PCT50 gel).

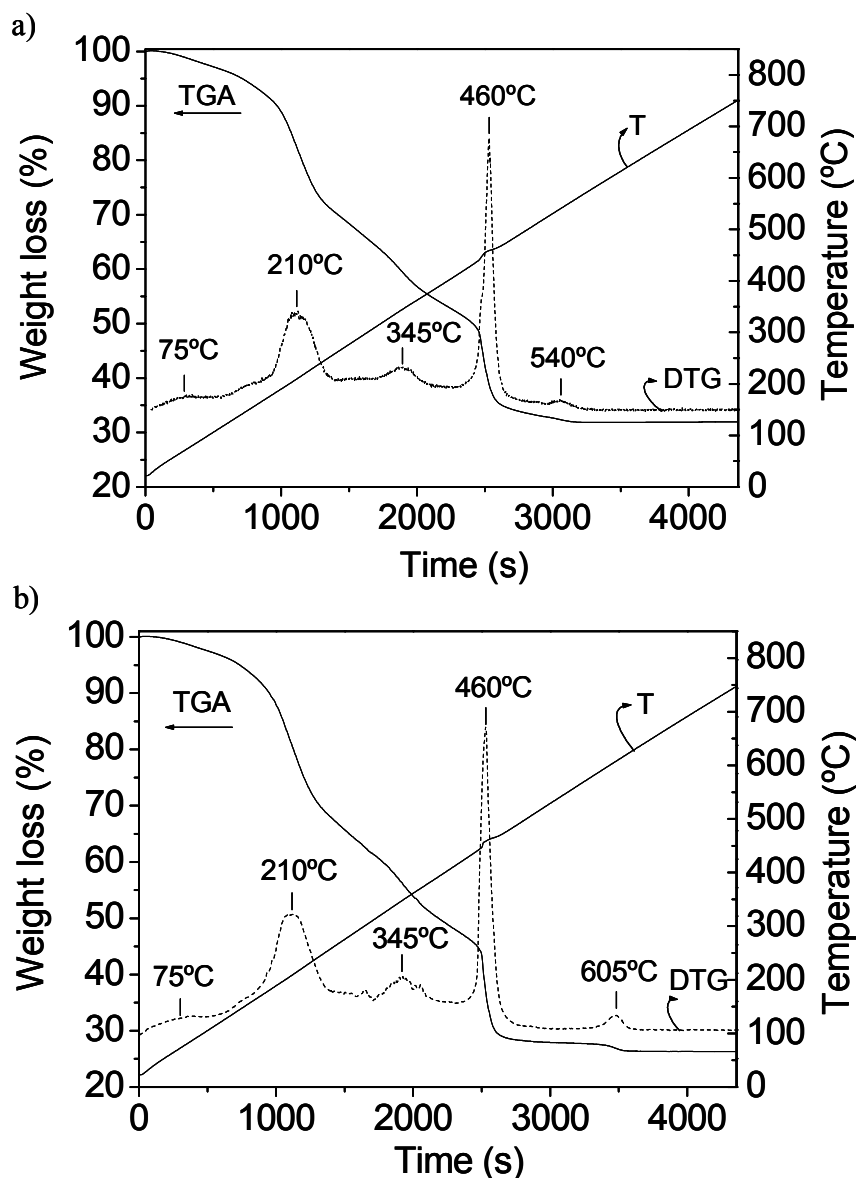


Figure 3.1. TGA-DTG of the aqueous solutions derived PCT24 (a) and PCT50 (b) gels

Analysis of the evolved gases emitted during decomposition of the gels was carried out by means of on-line coupled FTIR and MS techniques. Figure 3.2 shows the evolution with time of some characteristic IR bands analysed during the TGA-FTIR experiment of the PCT24 (Fig. 3.2a) and PCT50 (Fig. 3.2b) gels, these are; $940\text{-}913\text{ cm}^{-1}$ [$\delta(\text{NH}_3)$ of ammonia, NH_3], $2217\text{-}2137\text{ cm}^{-1}$ [$\nu(\text{C-O})$ of carbon monoxide, CO] and $2268\text{-}2395\text{ cm}^{-1}$ [$\nu(\text{C=O})$ of carbon dioxide, CO_2]. Furthermore, the total amount of the evolved gases collected in the spectrum range of $400\text{-}4000\text{ cm}^{-1}$ as a function of time is also depicted (Gram-Schmidt curve).

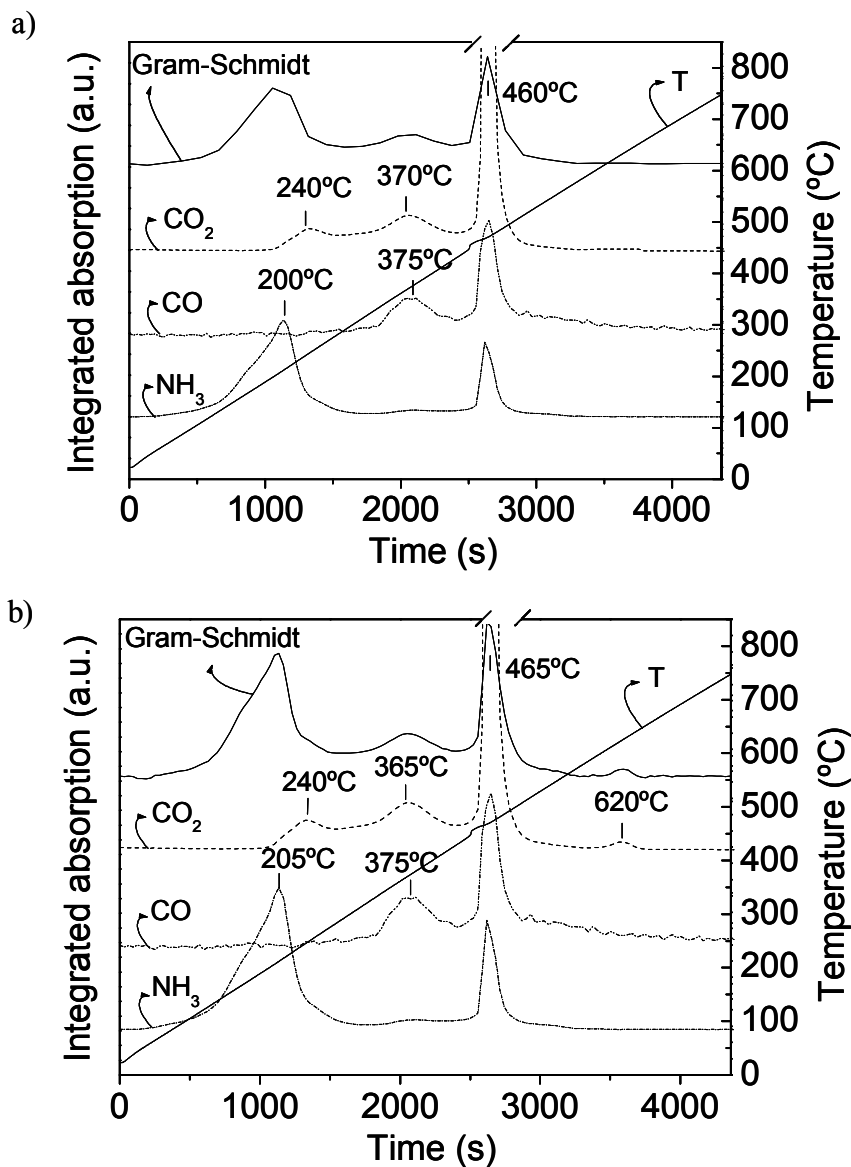


Figure 3.2. TGA-FTIR of the aqueous solutions derived PCT24 (a) and PCT50 (b) gels. Windows; $940\text{-}913\text{ cm}^{-1}$ (NH_3), $2217\text{-}2137\text{ cm}^{-1}$ (CO), $2268\text{-}2395\text{ cm}^{-1}$ (CO_2) and $4000\text{-}400\text{ cm}^{-1}$ (Gram-Schmidt)

The evolution with time of certain ion fragments as a function of their mass/charge ratio (m/z) is also depicted in Figure 3.3 for the PCT24 and PCT50 gels (Figs. 3.3a and 3.3b, respectively). Thus, m/z values of 17, 18, 30 and 44 correspond to fragments of NH_3^+ , H_2O^+ , NO^+ and CO_2^+ , respectively. Citric acid and its intermediates produce ions with m/z values of 39 (C_3H_3^+), 40 (C_3H_4^+), 41 ($^{13}\text{C}_3\text{H}_4^+$), 68 ($\text{C}_4\text{H}_4\text{O}^+$) and 112 ($\text{C}_5\text{H}_4\text{O}_3^+$).¹⁷⁸ In Fig. 3.3, the fragments of citric acid are represented by m/z values of 41 and 68.

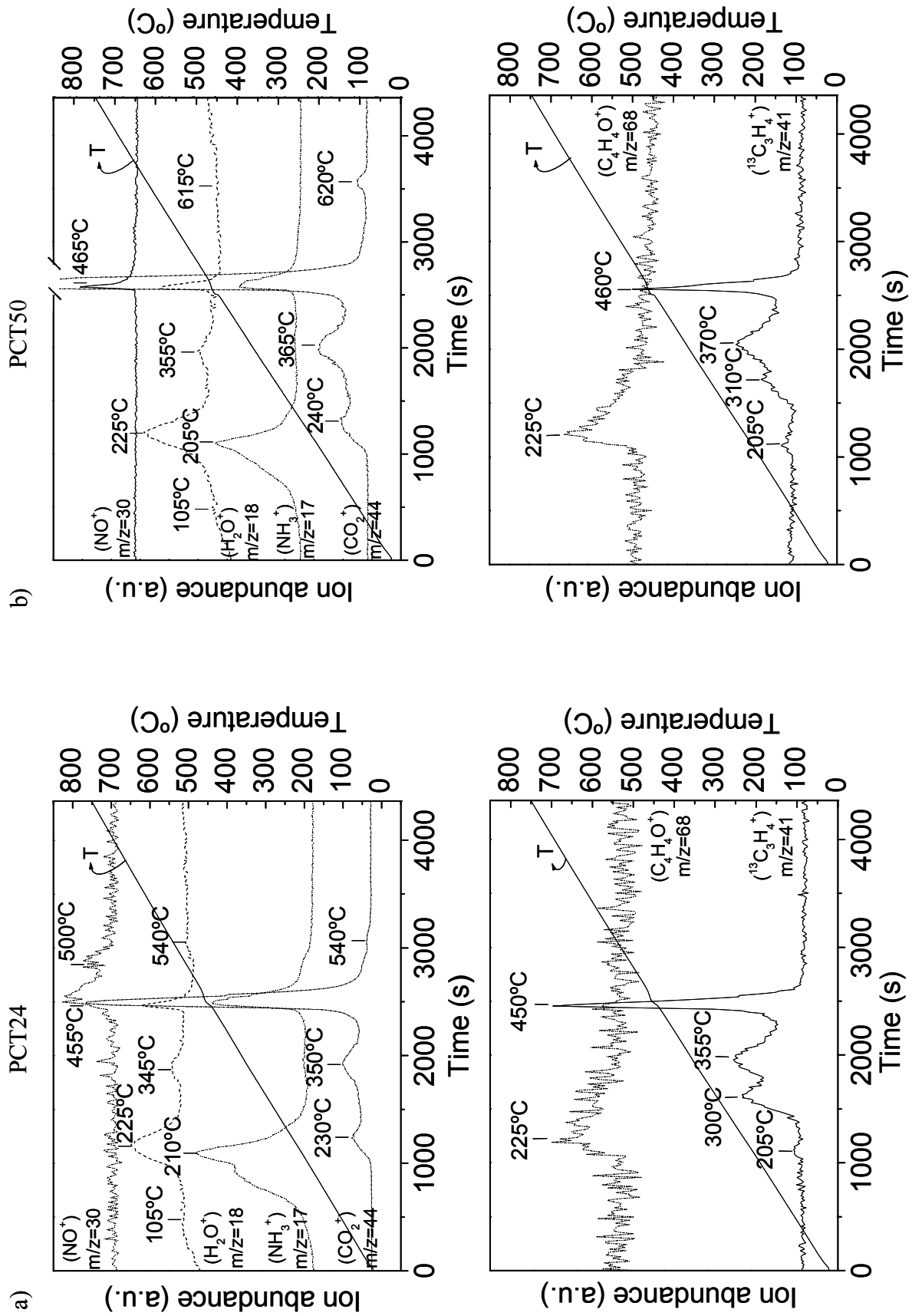


Figure 3.3. TGA-MS of the aqueous solutions derived PCT24 (a) and PCT50 (b) gels

Below 140 °C, the evaporation of residual water still entrapped within the pores of the gel takes place. A slight peak in the TGA-MS curve of this signal ($m/z = 18$) is appreciated at this temperature (Figs. 3.3a and 3.3b). Similar weight losses of ~ 2.8 - ~ 2.9 wt% are associated to this process in the TGA curves of both gels (Fig. 3.1).

In the temperature range between 140 and 250 °C, the second step of the PCT gels decomposition pathway occurs. Several processes are developed in this interval that lead to the largest weight loss measured in the TGA curves of the PCT24 and PCT50 gels (~ 26.4 and ~ 33.7 wt%, respectively). At 205-210 °C, the first peak of ammonia is observed in both TGA-FTIR and TGA-MS graphs of the gels. This signal corresponds to the decomposition of ammonium citrate, formed from the ammonia and the excess of citric acid present in the Ti(IV) solution. In the 205-225 °C interval, peaks ascribed to water ($m/z = 18$) and ions fragments of 41 ($^{13}\text{C}_3\text{H}_4^+$) and 68 ($\text{C}_4\text{H}_4\text{O}^+$) can be appreciated in Fig. 3.3 for both gels. Since the former elements correspond to fragments derived from citric acid,²³⁰ it can be concluded that at this step the decomposition of citric acid begins with its dehydration into aconitic acid and liberation of a molecule of water (see Fig. 3.4). The subsequent decarboxylation of aconitic acid into itaconic acid is produced at 230-240 °C, where the first peak in the CO_2 profile is detected in both TGA-FTIR and TGA-MS graphs of the gels. Note that the maximum of this peak does not match up with that associated to the elimination of water at ~ 225 °C, which is indicative that no combustion must be assigned to this reaction, but a decarboxylation. Itaconic acid can evolve into the cyclic itaconic anhydride and/or citraconic anhydride, as Figure 3.4 shows. However, amides can be also formed by the nucleophilic reaction of NH_3 with carboxylate groups (e.g. itaconic acid), thus leading to the formation of nitriles¹⁷⁸ ($\text{C}_2\text{H}_3\text{N}^+$) detected by the peak at 300-310 °C corresponding to a m/z value of 41 (Fig. 3.3a and 3.3b).

Further elimination of organics compounds still present in the sample is produced during the third step of the decomposition pathway of the gels, around ~ 345 °C. Here, the decomposition of coordinating ligands (citrate, peroxy) bonded to the metal atoms is carried out by the combustion and subsequent liberation of water and CO_2 , collected in both TGA-FTIR and TGA-MS analyses. At ~ 460 °C, combustion of residual species takes place with a high level of oxygen consumed (the signal at $m/z = 32$ (O_2^+) reveals a strong decrease below the background level in the TGA-MS curve, not shown). Thus, the formation of volatile species such as NH_3 , NO and CO (Figs. 3.2 and 3.3) is produced at this step.

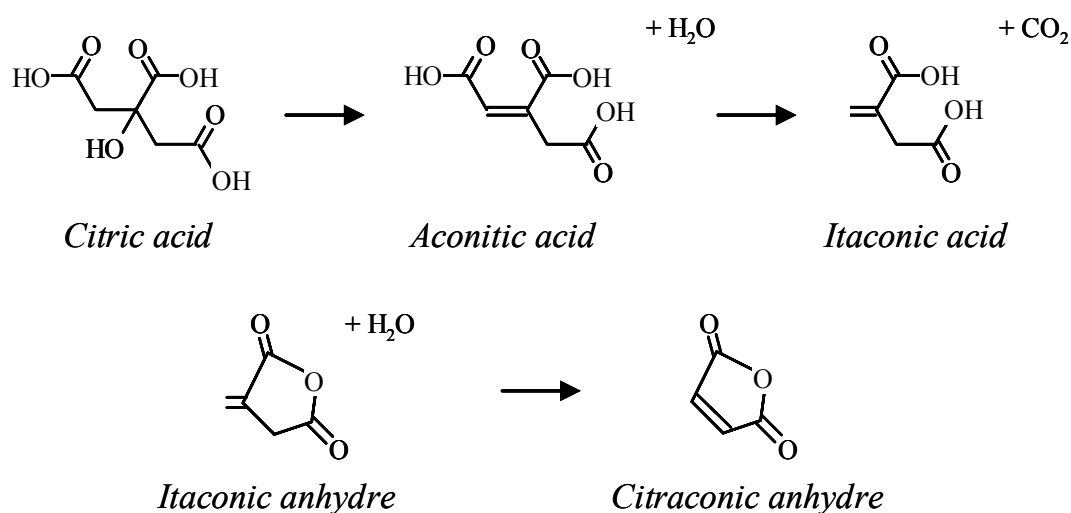


Figure 3.4. Thermal decomposition sequence of citric acid²³⁰

Finally, during the last step, a weak peak can be appreciated in the DTG curves of the PCT24 and PCT50 gels at ~ 540 and ~ 605 °C respectively, with small weight losses associated of ~ 1.5 and ~ 1.9 wt%. The low $m/z = 44$ signal collected in the TGA-MS analysis (Figs. 3.3a and 3.3b) at this temperature moreover indicates that CO_2 is released during this process. As previous studies confirmed,²³¹ this process is attributed to the decomposition of calcium carbonate ($CaCO_3$) into calcium oxide (CaO) and CO_2 that, like all the alkaline and alkaline-earth carbonates, is stable up to high temperatures. The formation of this calcium carbonate likewise could arise from the decomposition process of the calcium citrate reagent (see ref. 231). Obviously, as the concentration of Ca^{2+} in the $(Pb_{1-x}Ca_x)TiO_3$ composition of the gel is bigger, the amount of weight lost in this step is also higher, which explains the bigger weight loss of the PCT50 ($x = 0.50$) gel respect to the PCT24 ($x = 0.24$) one.

The most representative IR bands and mass fragments analysed, together with the temperatures at which corresponding peaks were detected, are summarised in Table 3.2.

Table 3.2. TGA and EGA data of the aqueous solutions derived PCT24 and PCT50 gels

Step	Temperature interval (°C)	Weight loss (%)		Peak (°C)		TGA-FTIR Bands (cm ⁻¹)	TGA-MS m/z	Fragment	Processes
		PCT24	PCT50	PCT24	PCT50				
1	< 105	~2.8	~2.9	~105	~105		18	H ₂ O	<u>Evaporation of residual solvent</u>
2	140-250	~26.4	~33.7	~210	~205	940-913	17	NH ₃	<u>Decomposition of organics entrapped within the gel network</u> Ammonium citrate → Citric acid + NH ₃ Citric acid → Aconitic acid + H ₂ O Aconitic acid → Itaconic acid + CO ₂
				~205	~205		41	¹³ C ₃ H ₄	
				~225	~225		18	H ₂ O	
				~225	~225		68	C ₄ H ₄ O	
				~230	~240	2268-2395	44	CO ₂	
3	250-400	~16.9	~14.4	~300	~310		41	C ₂ H ₃ N	<u>Decomposition/combustion of organics bonded to the metal ions (citrate/peroxo ligands)</u> *Amides → C ₃ H ₃ N C _x H _y O _z → CO + CO ₂ + H ₂ O + **CO ₃ ²⁻ Ca ²⁺ + CO ₃ ²⁻ → CaCO ₃
				~300, ~355	~310, ~370		41	¹³ C ₃ H ₄	
				~345	~355		18	H ₂ O	
				~350	~365	2268-2395	44	CO ₂	
				~375	~375	2217-2137		CO	
							41	¹³ C ₃ H ₄	
4	400-500	~19.6	~20.7	~450	~460		41	¹³ C ₃ H ₄	<u>Decomposition/combustion of remanent organics</u> Amides → NH ₃ , NO C _x H _y O _z → CO + CO ₂ + H ₂ O
				~455	~465	940-913	17	NH ₃	
				~455	~465, ~500		30	NO	
				~455	~465	2268-2395	44	CO ₂	
				~455	~465		18	H ₂ O	
				~455	~465	2217-2137		CO	
5	> 500	~1.5	~1.9	~540	~615				<u>Decomposition of calcium carbonate</u> CaCO ₃ → CaO + CO ₂
				~540	~620	2268-2395	44	CO ₂	

*coming from the reaction of NH₃ with carboxylate groups (e.g. aconitic/itaconic acid)

**coming from the pyrolysis of calcium citrate

3.3. THIN FILM PREPARATION

In order to prepare thin films, the former PCT aqueous solutions were deposited onto platinised silicon substrates. Crystal structure and microstructure of the crystalline films were studied by X-ray Diffraction and Scanning Electron Microscopy. Electrical measurements were performed on the PCT films and the feasibility for their application in microelectronic devices was thus evaluated.

3.3.1. Spinnability of the aqueous precursor solutions

The main problem related with aqueous CSD methods concerns the wetting of the substrate by the aqueous solution. The high surface tension of water hinders the wetting of the substrate (Pt/TiO_x/Ti/SiO₂/Si) by the aqueous solution and therefore, defective coatings are usually obtained. In most cases, this handicap is solved by improving the surface adhesion of the water-based solutions through the addition of surface-wetting reagents to the solution.²³² However, these organic additives can disturb the chemical system and promote the modification of the metallic precursors. Therefore, instead of modifying the characteristics of the precursor solutions, the hydrophilicity of the substrate can be enhanced by a wet chemical or dry treatment²³³. In the present work, a wet chemical process, based on the thorough cleaning of the substrate by the sulphuric acid/hydrogen peroxide (SPM, “*Piranha*” etch) and ammonia/hydrogen peroxide (APM) mixtures, has been carried out. The cleaning procedure by the SPM/APM mixtures was previously described in section 2.3.1 (*Chapter II*). The SPM mixture strongly oxidises the organic contamination present on the substrate surface whereas, in a second step, further oxidation of remanent organics together with the complexation of any metallic trace is promoted by the subsequent APM mixture.⁹² As a result, a surface without any hydrophobic impurities (organic contaminants) is obtained and therefore, the aqueous solution can spread out and a continuous film is obtained onto the substrate.

In order to emphasise the importance of the wetting enhancement, Figure 3.5 shows two photographs of the aqueous PCT solution coatings obtained onto substrates previously cleaned with the solvents trichloroethylene/acetone/2-propanol (Fig 3.5a) and/or with the SPM/APM mixture (Fig 3.5b). A single layer from the aqueous PCT solution was deposited by spin-coating onto the two Pt/TiO_x/Ti/SiO₂/Si substrates. It can be appreciated how the aqueous solution does not wet the substrate of Fig. 3.5a, leaving the practical totality of the substrate surface uncovered. On the

contrary, a smooth and uniform coating is obtained for the film of Fig 3.5b, with no appreciable defects on its surface.

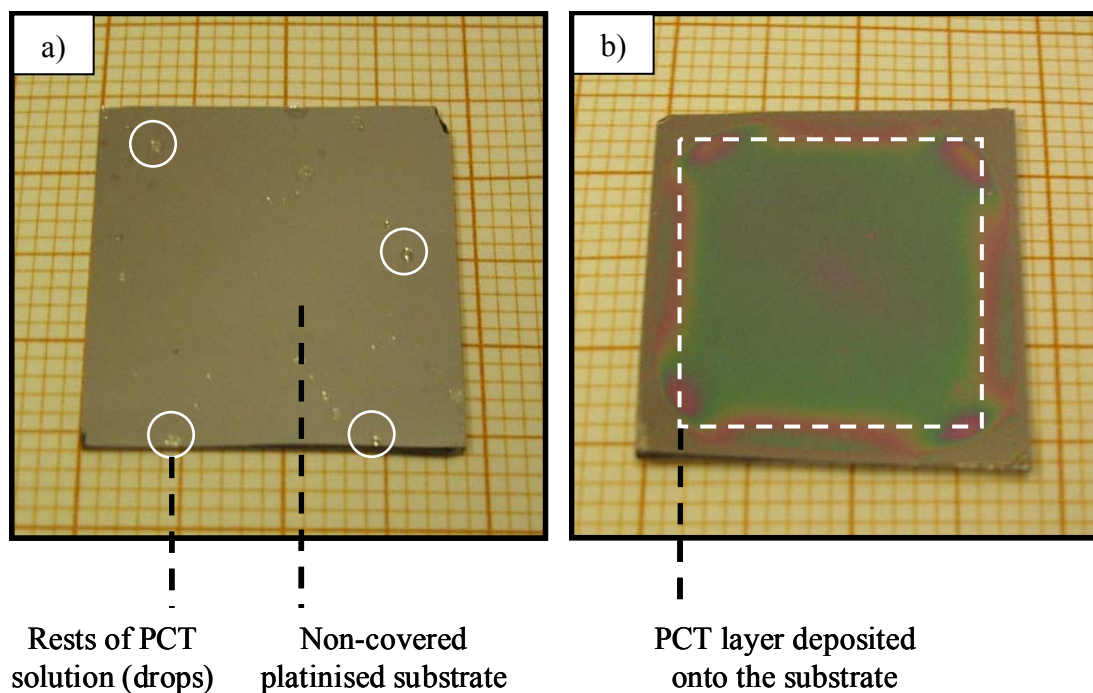


Figure 3.5. Aqueous solutions derived films deposited onto Pt-substrates previously cleaned with trichloroethylene/acetone/2-propanol (a) and SPM/APM (b) mixtures

3.3.2. Crystal structure and microstructure of the PCT films

Stock solutions were diluted with distilled water (for the PCT24 solution) or concentrated by water evaporation (for the PCT50 solution) in order to obtain solutions of ~ 0.3 M concentration. Previous to the film deposition, these solutions were refluxed at 100 °C for 1 h to decompose the excess of H_2O_2 of the solutions.²³⁴ A total of four layers were successively deposited, dried, pyrolysed and crystallised according to the experimental settings described in previous section 2.3.2. Crystallisation of the amorphous films was carried out by Rapid Thermal Processing (RTP) in air at 650 °C (recipe of Fig. 2.16c).

Several problems were found if solutions with higher or lower concentration than ~ 0.3 M were deposited. When four layers of the PCT24 stock solution (~ 0.35 M) with concentrations over 0.3 M were successively deposited, dried, pyrolysed and crystallised, films with rough surfaces were obtained. It has been tried to show the aspect of the surfaces obtained from PCT24 solutions

with different molar concentrations basing on the ability of their surfaces to reflect the visible light. Thus, Figure 3.6 shows a photograph of the crystalline films derived from PCT24 aqueous solutions with ~ 0.30 M (left) and ~ 0.35 M (right) molar concentrations. It can be observed how the shining and smooth surface of the ~ 0.30 M derived film totally reflects the object (tweezers) placed in front of it (as a mirror), whereas the surface of the ~ 0.35 M derived film scatters the light and the object consequently appear blurred in this case. Therefore, high quality PCT24 films only could be obtained from solutions with concentration ≤ 0.3 M. Higher concentrations lead to very rough films that could not be electrically characterised due to their high leakage current densities. Regarding the PCT50 stock solution (~ 0.25 M), a certain volume of this solution was put into a furnace (80 °C) and evaporated up to get a final volume with the desired molar concentration. If the evaporation continues up to reach concentrations over 0.3 M, precipitation arises in the PCT50 system. The pH of the ~ 0.3 M solution was raised again to 8.5 by the addition of few drops of ethanolamine²³⁴ ($\text{H}_2\text{NCH}_2\text{CH}_2\text{OH}$, Aldrich, 99.5+ % redistilled).

As a general conclusion, films from the PCT aqueous solutions could be only deposited from solutions with concentrations ≤ 0.3 M. A higher concentration of the solution gives rise to defective films with high rough surfaces (PCT24) or precipitation of the solution occurs (PCT50), making not possible the fabrication of the film.

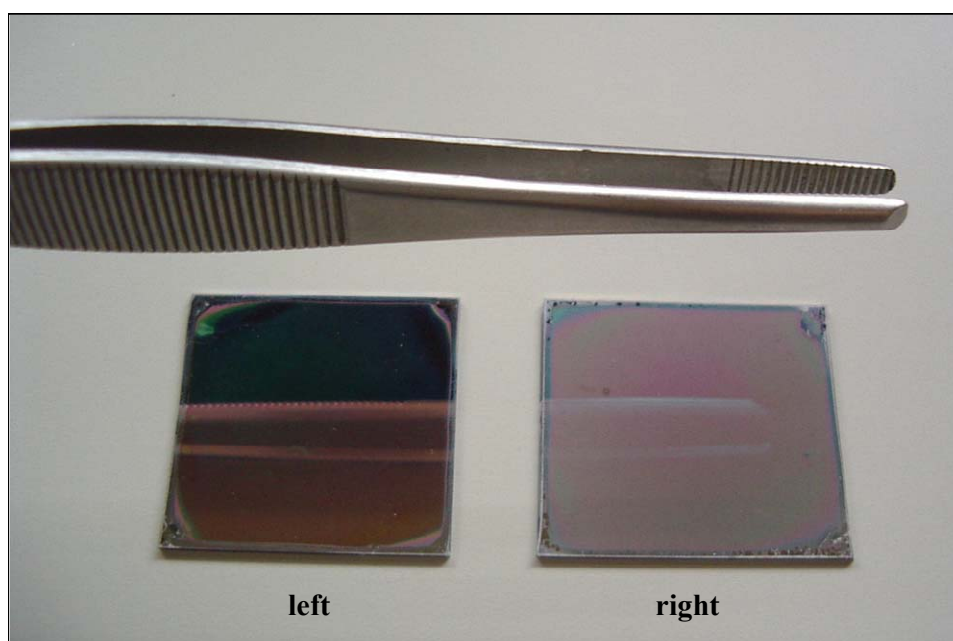


Figure 3.6. Crystalline films derived from aqueous PCT24 precursor solutions of ~ 0.30 (left) and ~ 0.35 (right) molar concentration

Figure 3.7a shows the Grazing Incidence X-Ray Diffraction (GIXRD) patterns of the PCT24 and PCT50 crystalline films. The indexation of the corresponding reflections is ascribed to the perovskite crystalline phase. The presence of a single perovskite is detected in both films, without any secondary phases observed in the patterns. In the case of the PCT24 film, a pseudocubic structure is detected where the characteristic doublets of the tetragonal structure observed in the counterpart bulk ceramics²³⁵ are here overlapped (001/100, 101/110 and 002/200). This is because of the development of tensile stresses onto the silicon-based substrates during the film processing.^{202,213} For the PCT50 film, the perovskite reflections should be adjusted to an orthorhombic structure that has been previously observed by neutron diffraction on ceramic powders of the same composition.⁴⁴ This structure is in agreement with previous studies,¹³⁷ since it has been observed how the tetragonality (c/a) of the $(\text{Pb}_{1-x}\text{Ca}_x)\text{TiO}_3$ system decreases as the substitution of Pb^{2+} by Ca^{2+} increases, and how for Ca^{2+} contents over ~ 40 at% the crystal structure changes from a tetragonal to an orthorhombic one.

The possible presence of any preferred orientation in the crystalline films was analysed by X-Ray Diffraction (XRD) with the Bragg-Brentano geometry (θ - 2θ). The XRD patterns of the PCT24 and PCT50 films are shown in Figure 3.7b. A $\langle 100 \rangle$ preferred orientation is observed for the PCT50 film, whereas the relative intensities of the perovskite peaks in the PCT24 film seems to indicate a random orientation, although information about the $\langle 111 \rangle$ direction can not be here obtained due to the overlapping between the 111 perovskite peak and the 111 Pt peak of the substrate.

Figure 3.8 present the plan-view micrographs of the films surfaces obtained by Scanning Electron Microscopy (SEM), working under field emission conditions. It can be appreciated how the substrate (Pt bottom electrode) is totally covered by the PCT film, with no areas partially uncovered. As expected from the XRD results, neither secondary phases nor phase segregation are observed in the micrographs of Fig. 3.8, denoting both films a homogeneous microstructure. The microstructure of the films consists in spherical grains which differ in their size as a function of the PCT composition. An average grain size of ~ 100 nm is measured for the PCT24 film (Fig. 3.8a), whereas a value of approximately 50 nm can be estimated from the image of the PCT50 film (Fig. 3.8b).

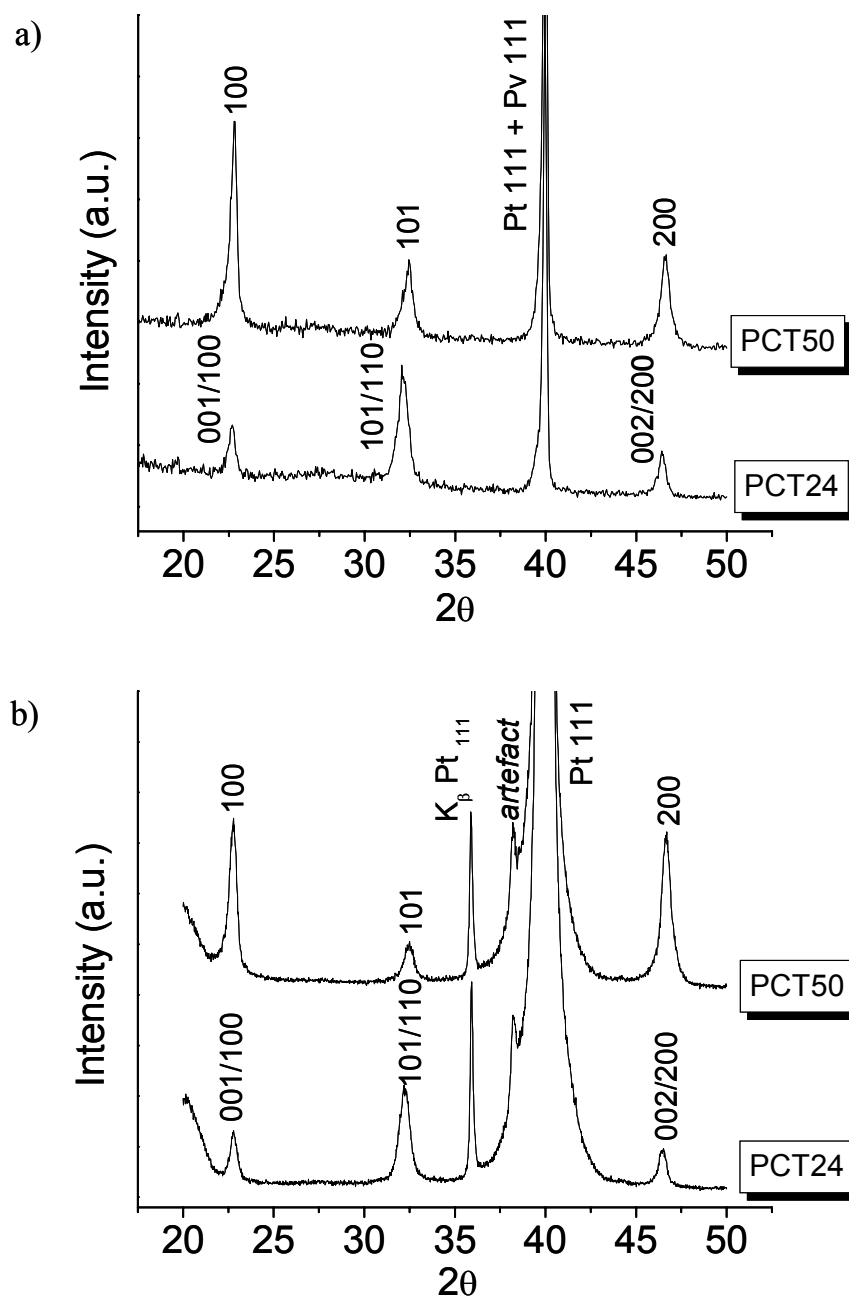


Figure 3.7. GIXRD (a) and XRD (b) patterns of the aqueous solutions derived PCT24 and PCT50 films (Pv: perovskite, Pt: platinum)

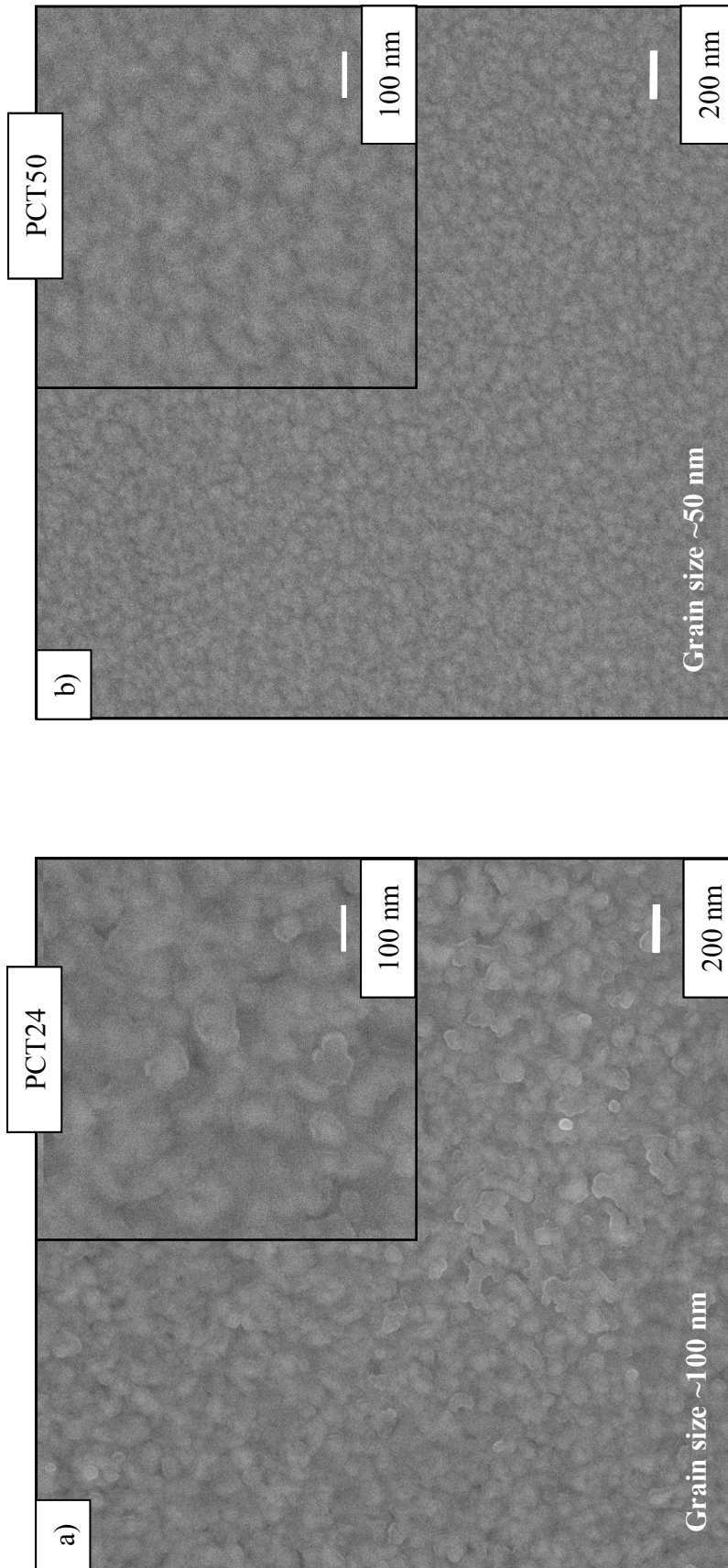


Figure 3.8. SEM micrographs (plan-view) of the aqueous solutions derived PCT24 (a) and PCT50 (b) films. Magnifications of each micrograph are embedded shown

Cross-sectional SEM images of the films were also obtained, and micrographs are shown in Figure 3.9. Thicknesses of ~ 240 nm and ~ 250 nm were calculated from these images for the PCT24 and PCT50 films (a and b, respectively).

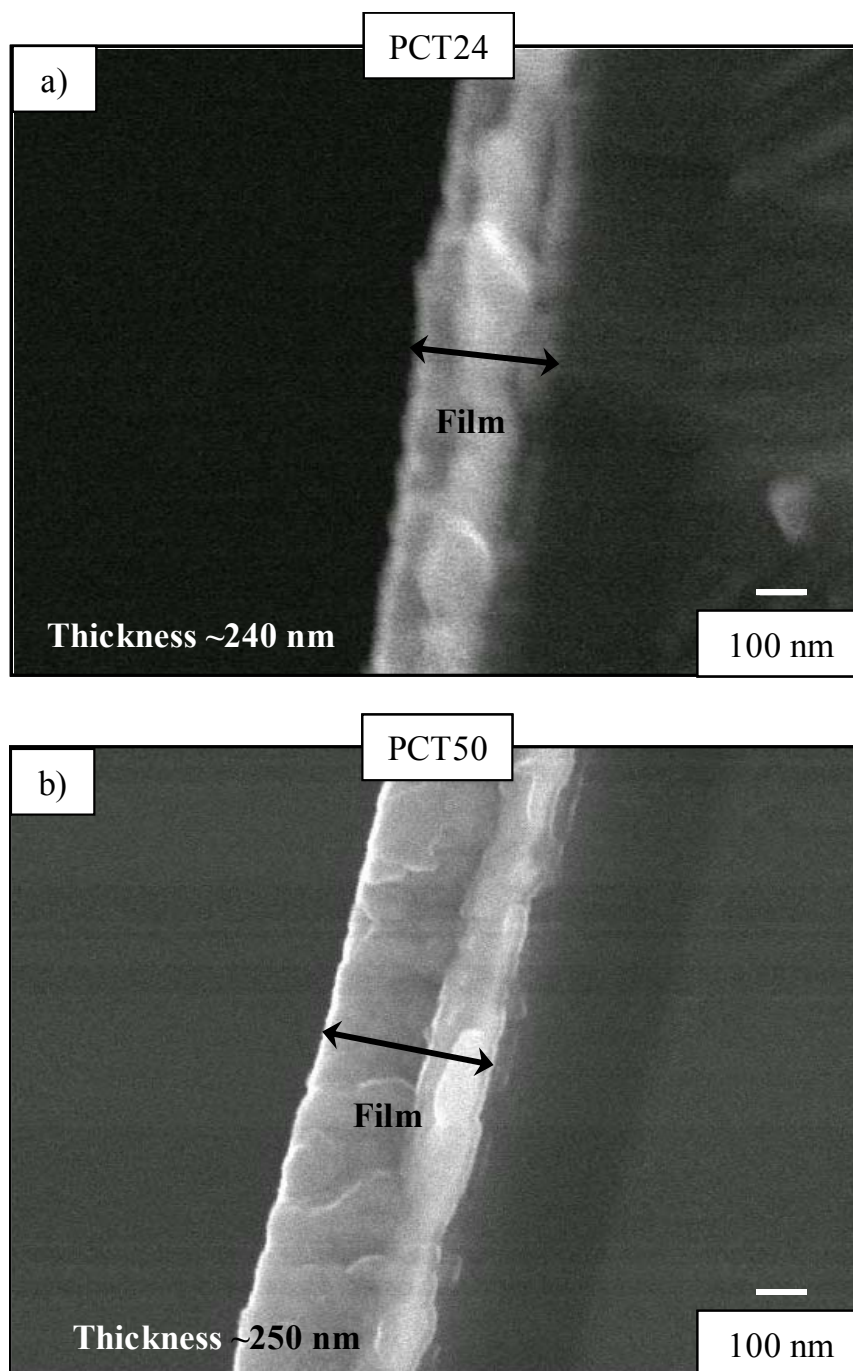


Figure 3.9. SEM micrographs (cross-section) of the aqueous solutions derived PCT24 (a) and PCT50 (b) films

3.3.3. Dielectric and ferroelectric properties of the PCT films

The dielectric and ferroelectric response of the PCT films prepared by the aqueous method was analysed through electrical measurements. Figure 3.10 shows the variation of the dielectric constant (k') with temperature of the PCT24 and PCT50 films, measured at various frequencies. Insets in the figure correspond to the variation of the loss tangent ($\tan \delta$) with temperature.

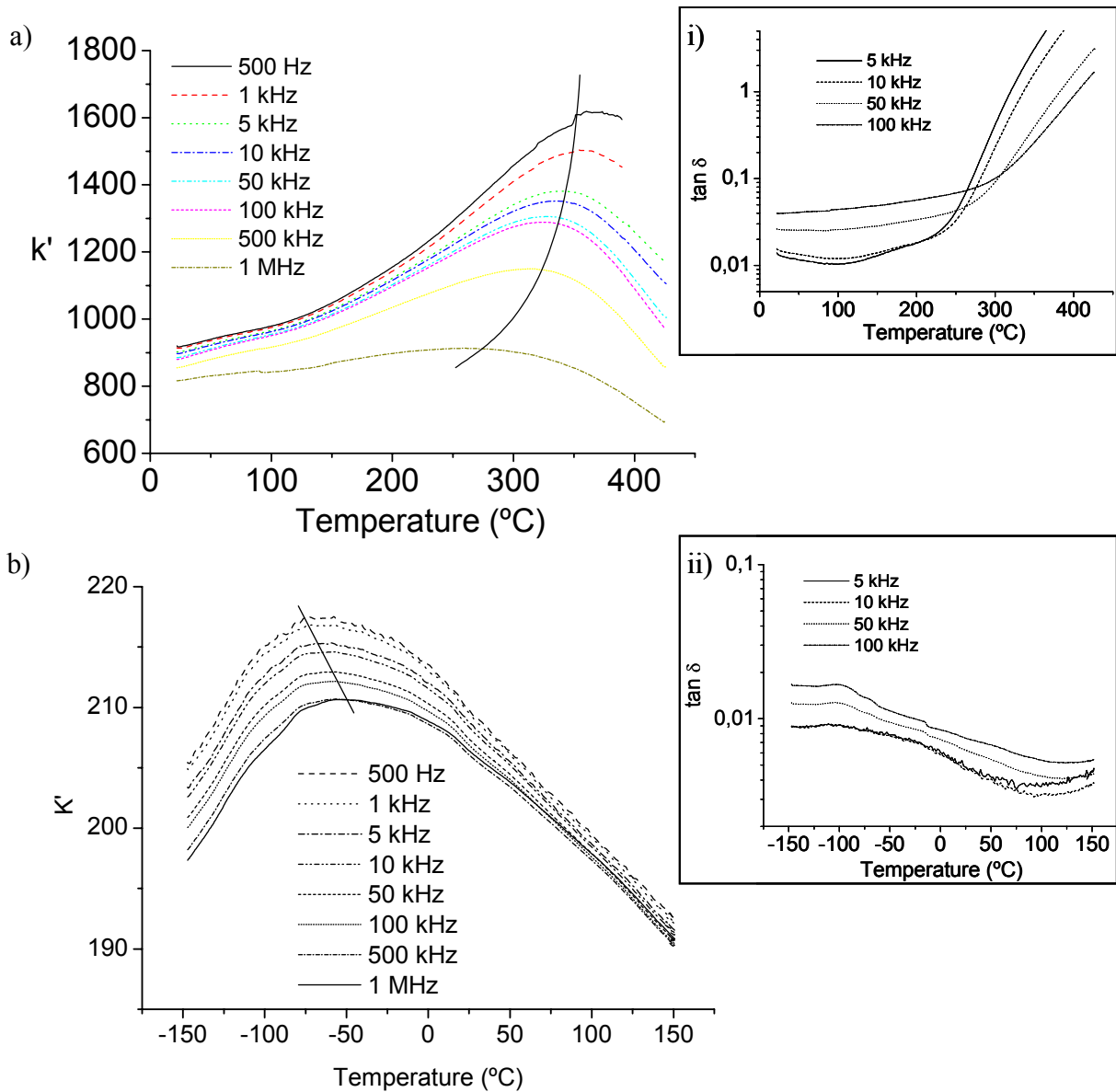


Figure 3.10. Variation of the dielectric constant (k') with temperature of the aqueous solution derived PCT24 (a) and PCT50 (b) films, measured at various frequencies. Continuous lines are depicted as a guide for the eye for the temperature maximum shift. Insets show the variation of the loss tangent ($\tan \delta$) with temperature for the PCT24 (i) and PCT50 (ii) films

A characteristic ferro-paraelectric transition can be observed in the PCT24 film (Fig. 3.10a) with values of the dielectric constant of ~ 1350 at T_m (temperature at which k' is maximum, 340°C) and of ~ 920 at room temperature, measured at 10 kHz. Loss tangent is close to 0.01 at room temperature. Acceptable values of k' and $\tan \delta$ are thus obtained for this film, similar to those corresponding to other PCT24 films prepared from non-aqueous sol-gel methods.^{126,135} A displacement of the k' maxima towards lower temperatures as the measuring frequency increases, is also appreciated in this figure (see solid line). This could suggest the presence of compositional inhomogeneities and/or extrinsic defects (e.g. low quality interfaces) in the film that would yield to the observed phenomenon, although more specific analyses should be carried out to confirm these hypotheses. Anyway, the low values of the dielectric anomaly or $\Delta k'$ (difference between the k' values measured at T_m and at room temperature), and the large diffusiveness of k' with frequency are also indicative of the heterogeneous heterostructure of this film.

In the case of the PCT50 film, a clear relaxor-like ferroelectric behaviour is observed in Fig. 3.10b. Note how the temperature of the k' maximum shifts to higher values when frequency increases, as characteristic of relaxor materials. A diffuse ferro-paraelectric transition around -55°C (T_m) is observed from data measured at 10 kHz, with an associated k' value of ~ 215 . At room temperature, this value slightly decreases down to ~ 205 . The high diffusivity of the transition is therefore corroborated by the low value of the normalised dielectric anomaly ($\Delta k'/\Delta T$) obtained. Low values of $\tan \delta$ are measured for this film at room temperature (~ 0.005 , at 10 kHz), as observed from the respective inset in the figure.

The ferroelectric character of the PCT24 film is analysed through the ferroelectric hysteresis loop of Figure 3.11. No analysis was carried out on the PCT50 film, since this perovskite composition shows a relaxor-ferroelectric behaviour (shown above for these films) with a low ferroelectric response.¹⁰ A slanted, asymmetric, low-remanent P(E) loop is obtained for the PCT24 film. Values of remanent polarisation (P_r) and coercive field (E_c) of $\sim 1.0 \mu\text{C}/\text{cm}^2$ and $\sim 40 \text{ kV}/\text{cm}$ are respectively measured at a maximum amplitude of 3.5 V. Larger voltages bias could not be applied in the measurement since high leakage conduction resulted in the film, preventing thus the obtaining of larger polarisation values. The asymmetry of the loop is corroborated by the high bias displacement obtained ($-20 \text{ kV}/\text{cm}$). The non-switching contribution to the hysteresis loop is also displayed in this figure. The high non-switching contribution observed can be associated to the presence of charged defects, such as electron holes and/or vacancies, which probably lead to large leakage conduction in the film, therefore hindering its switching.

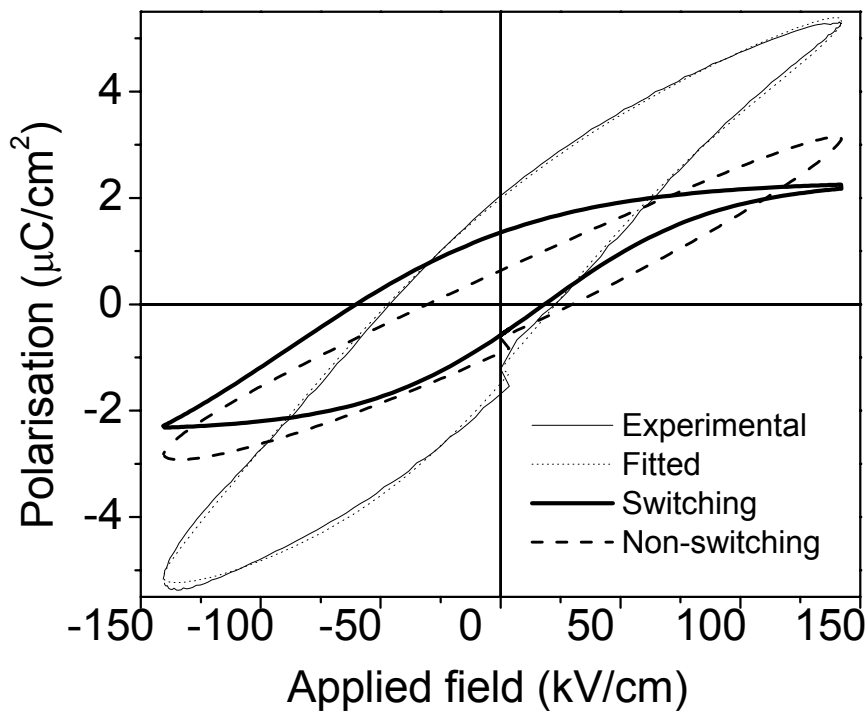


Figure 3.11. *Ferroelectric hysteresis loop of the aqueous solution derived PCT24 film. Non-switching contribution to ferroelectric domains is also depicted*

Figure 3.12 shows the field dependence dc-leakage currents at room temperature of the PCT films. As expected from the previous electrical results, large and asymmetric leakage currents are observed for the PCT24 film. The asymmetry in these data is related with differences in the nature of the top and bottom interfaces in this film (top and bottom Pt electrode-film junctions). However, this effect is not observed in the PCT50 film and low leakage current densities are here obtained (values below 10^{-9} A/cm²).

Large leakage currents can be related with charged defects, interfacial oxide phases and/or oxygen deficiency present in the sample, as major contributions. In the case of the PCT materials, even when an extra lead source is used, some PbO is always lost during annealing at high temperatures. These losses promote lead and oxygen vacancies which can be responsible of current flow in the material when an electric field is applied.²³⁷

Perhaps, the larger Pb²⁺ content in the (Pb_{0.76}Ca_{0.24})TiO₃ composition than in the (Pb_{0.5}Ca_{0.5})TiO₃ one might lead to higher amount of defects (vacancies, suboxides, interfacial oxide

phases), produced by the lead loss, that would explain the higher leakage current densities measured for the PCT24 film respect to the PCT50 film.

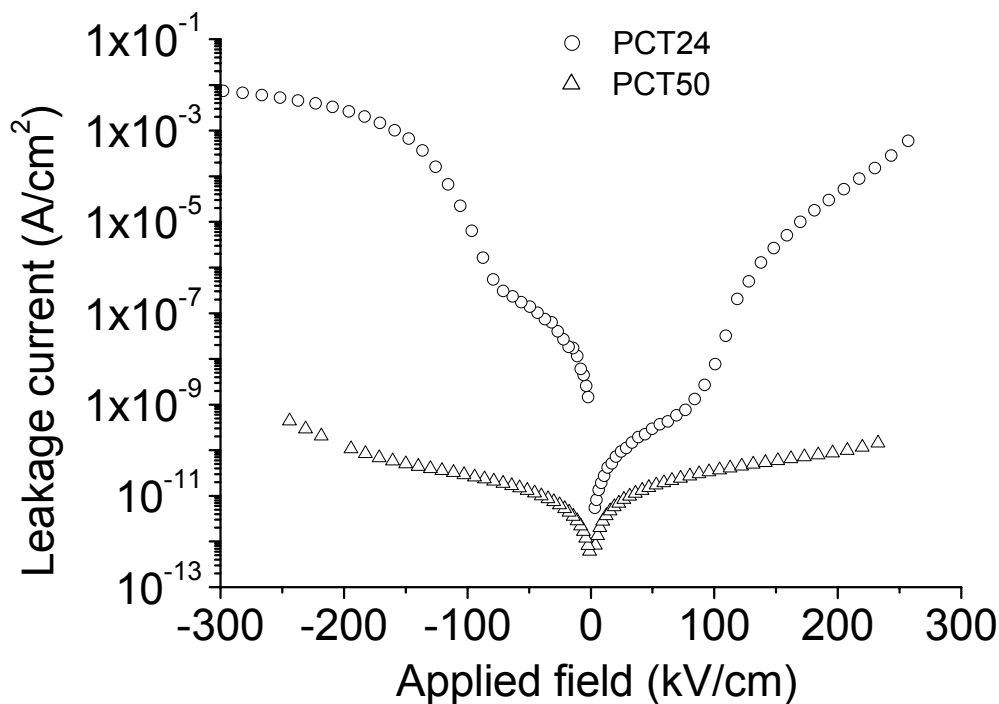


Figure 3.12. Field dependence of leakage currents for the aqueous solutions derived PCT24 and PCT50 films

The strong asymmetry of these data in the PCT24 film moreover indicates the possible presence of defective interfaces between the ferroelectric film and the top/bottom electrodes. The experimental setup of the leakage current densities measurements indicates that leakages are higher at the top electrode, which could be an indication of roughness at the top surface of the films that leads to a low quality film-top electrode junction. But, leakages are also quite high at the film-bottom electrode junction, indicating as well the presence of a defective layer here. Both asymmetry and large values of the leakage current densities of the PCT24 film prevent the correct polarisation of the film, obtaining lower values than those that would be obtained if the film could be better polarised (see Fig. 3.11).

A summary of the most important dielectric and ferroelectric parameters obtained through the electrical characterisation of the PCT24 and PCT50 films is shown in Table 3.3.

Table 3.3. Dielectric and ferroelectric parameters of the aqueous solutions derived PCT24 and PCT50 films

Film	T_m (°C)	k' (RT, 10 kHz)	k' (T_m , 10 kHz)	$\Delta k'$ (1)	$\Delta k'/\Delta T \times 10^3$ (2)	$\tan \delta$ (RT, 10 kHz)	P_r ($\mu\text{C}/\text{cm}^2$)	E_c (kV/cm)	Leakage current (A/cm ²)
(Pb _{0.76} Ca _{0.24})TiO ₃ (PCT24)	340	920	1350	430	1320	0.015	1	40	$< 10^{-7}$; $E \leq +15$ kV/cm $E \leq -40$ kV/cm
(Pb _{0.50} Ca _{0.50})TiO ₃ (PCT50)	-55	205	215	10	285	0.005	-	-	$< 10^{-9}$

(1) Difference between the dielectric constant measured at T_m and that corresponding at room temperature (RT) (*dielectric anomaly*)

(2) Normalised dielectric anomaly

3.3.4. Applications in microelectronic devices

From the electrical data obtained before, the possible applications of the PCT films obtained through the aqueous solution-gel method in the technology of functional microelectronic devices, are evaluated.

The relaxor-like ferroelectric behaviour observed in the PCT50 film, with relatively high k' values (205-210) compared with those of other high- k single oxides,²³⁸ and the low $\tan \delta$ (0.005) measured at room temperature, show the viability of these films for applications in Dynamic Random Access Memories (DRAMs)⁶¹. Furthermore, the low leakage current densities measured ($<10^{-9}$ A/cm²) prevent the thermal breakdown of the film when the capacitor is successively charge-injected/released (refreshed), making not only feasible but also effective the role of the memory.

On the other hand, the capability of a ferroelectric material to switch between two opposite polarisation states ($+P_r$, $-P_r$) and to retain the polarisation in the absence of the electric field is the main basis of a Non Volatile Ferroelectric Random Access Memories (NVFeRAMs)⁶⁵. The aqueous derived PCT24 film showed a low remanent polarisation value that at first sight discourages its application in this type of memories. Furthermore, the high leakage current density measured supposes another drawback for the integration of these films into high-density memories. Despite these undesirable effects, acceptable values of the dielectric constant and of the loss tangent were measured in the PCT24 film, which does not reject the possible application of these films in future ferro, pyro and piezoelectric applications (infrared sensors, micromechanical systems, etc), once the problems concerning the polarisation and leakage currents were solved. Further investigations are in progress to determine the presence of detrimental interfaces formed between the film and the top/bottom electrodes, responsible of the high leakage current densities of these PCT24 films and that prevent the appropriate polarisation with the electric field, resulting thus in films with a poor ferroelectric response.

3.4. REMARKS

- An environmental friendly aqueous solution-gel route for the synthesis of $(\text{Pb}_{1-x}\text{Ca}_x)\text{TiO}_3$ (PCT) precursor solutions has been developed for the first time in this work. The use of water as a non-hazardous and inexpensive solvent, together with the easy handling of the technique (no inert atmosphere is required), are the major advantages of this novel method.
- Solutions with compositions of $(\text{Pb}_{0.76}\text{Ca}_{0.24})\text{TiO}_3$ (PCT24) and $(\text{Pb}_{0.50}\text{Ca}_{0.50})\text{TiO}_3$ (PCT50) have been synthesised. The as-synthesised solutions are precipitate-free, although for large Ca^{2+} contents ($x = 0.50$) instability (precipitation) of the solution arises with a short-time aging or with the temperature-aging, as a consequence of the low solubility of calcium citrate in the aqueous media.
- These aqueous solutions do not wet the substrates here used ($\text{Pt}/\text{TiO}_x/\text{Ti}/\text{SiO}_2/\text{Si}$). Therefore, and in order to prepare thin films, the spinnability of the solutions had to be improved. For this aim, the hydrophilicity of the substrate was enhanced through a wet chemical treatment of cleaning (SPM/APM mixture). This makes possible the preparation of PCT films derived from the aqueous solutions here prepared.
- PCT films only can be prepared from aqueous solutions with concentrations ≤ 0.3 M. Higher concentrations lead to low quality PT24 films with large roughness or to the formation of precipitate in the PCT50 solutions.
- Homogeneous, crystalline and single-phase PCT films with a perovskite structure have been obtained from the aqueous precursor solutions with concentration ≤ 0.3 M, as detected by XRD and SEM. The PCT24 films show a pseudocubic structure with an apparently random orientation. The PCT50 films have a clear $\langle 100 \rangle$ preferred orientation. The microstructures of the films consist in spherical grains of ~ 100 and ~ 50 nm for $(\text{Pb}_{1-x}\text{Ca}_x)\text{TiO}_3$ compositions with $x = 0.24$ and 0.50 , respectively.
- Crystalline films of $(\text{Pb}_{0.50}\text{Ca}_{0.50})\text{TiO}_3$ composition (PCT50) show a clear relaxor-ferroelectric character with a very diffusive ferro-paraelectric transition and dielectric constant values of ~ 205 at room temperature. Both characteristics together with the low leakage currents measured (below 10^{-9} A/cm²) indicate the suitability of these PCT50 films for DRAM's. However, the crystalline films of $(\text{Pb}_{0.76}\text{Ca}_{0.24})\text{TiO}_3$ (PCT24) presents a low polarisation value (~ 1.0 $\mu\text{C}/\text{cm}^2$) and an high leakage current density that suppose critical drawbacks for their applications in ferro, pyro and piezoelectric devices.

CHAPTER IV

PCT THIN FILMS FROM THE DIOL-BASED SOL-GEL SYNTHETIC ROUTE

PART 1

*Ca²⁺ CONTENT AND CRYSTALLISATION
OF THE PCT THIN FILMS*

The degree of substitution of Pb^{2+} by Ca^{2+} in the $(\text{Pb}_{1-x}\text{Ca}_x)\text{TiO}_3$ (PCT) system plays a critical role on the structural, microstructural and electrical properties of the corresponding ceramic materials and therefore on their applications. As it was described in *Chapter I (Introduction)*, the progressive substitution of Pb^{2+} by Ca^{2+} in the PbTiO_3 perovskite leads to a decrease in the Curie temperature (T_c), spontaneous polarisation (P_s) and coercive field (E_c) compared to those of the pure PbTiO_3 , whereas the values of the dielectric constant (k') at room temperature are enhanced and the tetragonality of the system (c/a) decreases.^{11,33} These effects have been observed in ceramic powders and bulk materials (single crystals and ceramics).^{11,12,35,239} However, literature for PCT films with large Ca^{2+} contents is not too extensive. In PCT thin films, it is expected that the Ca^{2+} content may affect the crystallisation temperature of the perovskite,²⁴⁰ and therefore, alters the processing conditions of the films. This has previously been shown for lead zirconate titanate films, $\text{Pb}(\text{Zr,Ti})\text{O}_3$, where the effect of the Zr/Ti ratio on the processing temperature was reported.¹⁵⁷ Furthermore, the use of Rapid Thermal Processing (RTP) for the preparation of the films and the substrate on which the film is supported can also affect the mechanisms of nucleation and growth of the perovskite crystals. The study of these phenomena would help us to determinate not only the temperature at which the crystallisation occurs, but also to understand the structural, microstructural and electrical properties of the resulting films.

In the present section, the early stages of the crystallisation of diol-based sol-gel derived $(\text{Pb}_{1-x}\text{Ca}_x)\text{TiO}_3$ thin films in the compositional range of $0 \leq x \leq 0.5$ have been studied by means of X-Ray Diffraction (XRD) and Brillouin Spectroscopy (BS). Complementary information has been obtained from the film profiles surfaces by X-ray Photoelectron Spectroscopy (XPS), and from the observation of their surfaces by Scanning Force Microscopy (SFM) or their microstructures by Transmission Electron Microscopy (TEM). Results thus obtained have been compared with those resulting from the Thermogravimetric and Differential Thermal analysis (TGA/DTA) of powders derived from the same precursor solutions used for the deposition of the films. These studies have allowed us to determine how crystallisation evolves in the PCT films and which the influence of the Ca^{2+} content is on this evolution.

4.1.1. SOLUTIONS, GELS AND FILMS USED FOR THE CRYSTALLISATION STUDY

Films derived from solutions prepared by the diol-based sol-gel synthetic route A, described in *Chapter II* (section 2.1.3.1), were used in this study. This is a route that has been widely used in the preparation of $(\text{Pb}_{0.76}\text{Ca}_{0.24})\text{TiO}_3$ (PCT24) thin films. Processing and properties of these films have been reported in the literature.^{9,185} Here, the route A has also been tested for PCT films with progressively increased Ca^{2+} contents. Thus, substitutions of Pb^{2+} by Ca^{2+} of 0, 24, 30, 40 and 50 at% ($x = 0, 0.24, 0.30, 0.40$ and 0.50) were used leading to solutions, powders and films that are denoted as PCT0, PCT24, PCT30, PCT40 and PCT50, respectively.

4.1.2. PCT GELS

In order to determine the thermal evolution of the PCT gels with different Ca^{2+} contents, gel samples derived from the PCT solutions were subjected to Differential Thermal and Thermogravimetric Analysis (DTA-TGA).

Analyses were carried out on the PCT gel powders previously dried at 350 °C for 12 h, in order to eliminate the majority of the organic compounds and thus to decrease the effect of this process in the analysis, since it can mask the crystallisation process here studied.

4.1.2.1. Thermal evolution of the gels by Differential Thermal and Thermogravimetric Analysis (DTA-TGA)

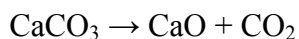
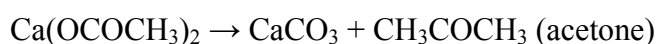
Figure 4.1.1 shows the DTA-TGA results for the PCT0, PCT24, PCT30, PCT40 and PCT50 gels.

The DTA curves during heating (i) reveal an endothermic peak at low temperatures (<100 °C) in all the systems that is associated to weight losses produced by the volatilisation of entrapped solvent.

At temperatures between 300 and 600 °C, exothermic peaks appear that can be ascribed to crystallisation and/or elimination of residual organics still present in the sample. For the PCT0 and PCT24 systems (Figs. 4.1.1 a and b), two overlapped exothermic peaks are observed in this temperature interval (peaks at ~466 and ~500 °C for the PCT0 and ~490 and ~520 °C for the PCT24), which are accompanied by a weight loss in the respective TGA curves (iii).

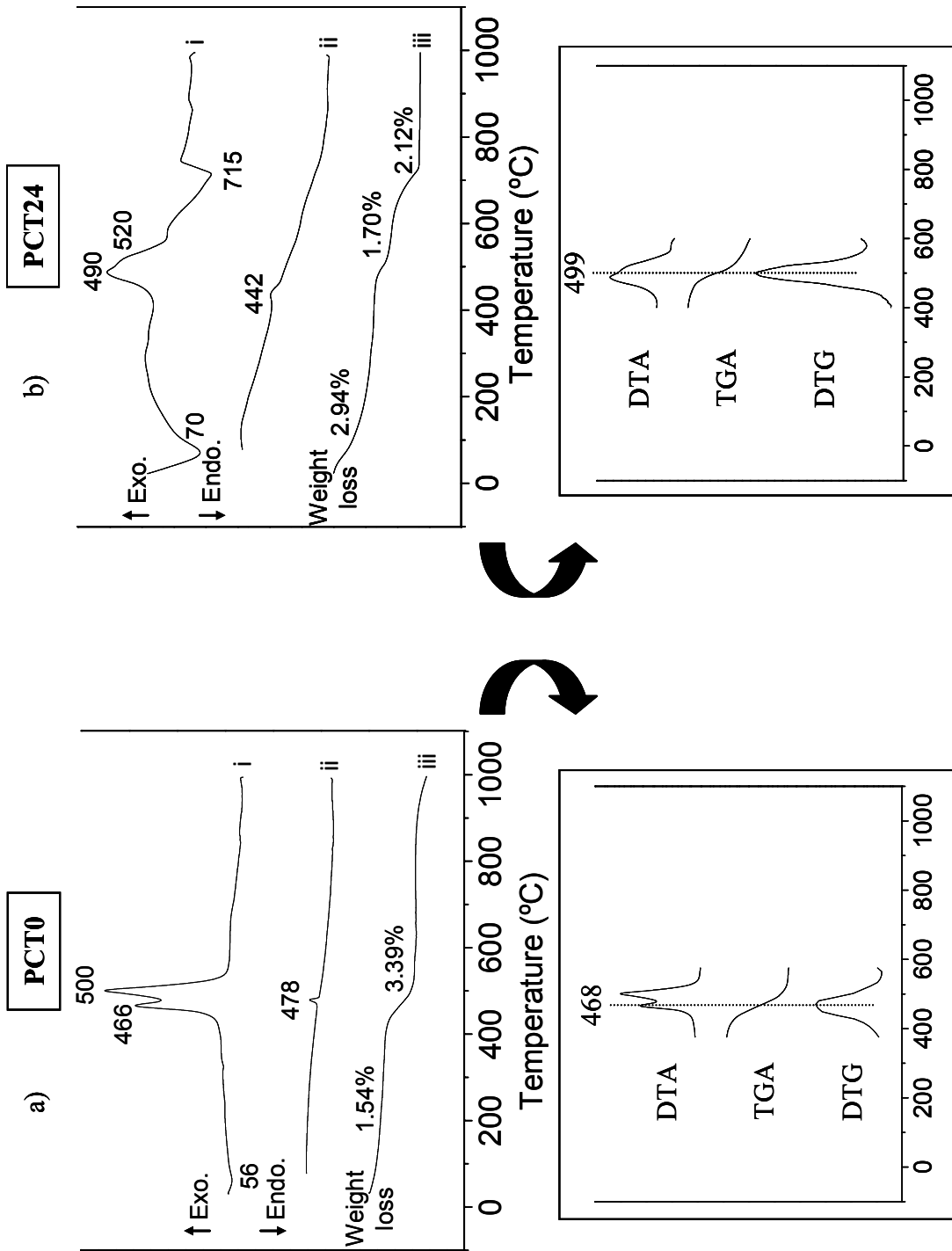
Differential thermogravimetric (DTG) curves of these powders are also shown (insets of Fig. 4.1.1) in order to clarify the types of energetic processes occurring at these temperatures. Both crystallisation and organic combustion produce exothermic anomalies, but only the latter has associated a weight loss, thus resulting in a peak in the DTG curve. From the comparison of these curves, it is concluded that the first exothermic peak for the PCT0 and PCT24 powders is produced by the elimination of organics, whereas the second one can be attributed to the crystallisation process (~ 500 and ~ 520 °C for the PCT0 and PCT24 powders, respectively). For the rest of compositions, sharp DTA exothermic peaks are recorded at ~ 558 , ~ 587 and ~ 608 °C for the respective PCT30, PCT40 and PCT50 powders, without any associated weight loss. Therefore, these peaks must be attributed to the crystallisation process. From these data, it can be concluded that crystallisation in the PCT0, PCT24, PCT30, PCT40 and PCT50 powders occurs at temperatures close to 500, 520, 558, 587 and 608 °C, respectively, indicating an increase in the crystallisation temperature of the PCT powders as the Ca^{2+} content is larger.

At higher temperatures (>600 °C), a DTA endothermic peak appears only for the powders containing calcium. Weight losses of 2.12, 2.75, 3.61 and 5.38 wt% for the PCT24, PCT30, PCT40 and PCT50 powders, respectively, are associated to these peaks. They are due to the elimination of carbon dioxide, CO_2 , coming from the decomposition of the residual calcium carbonate, CaCO_3 , derived from the acetate groups two-step decomposition (at 200-400 °C) of the calcium acetate reagent,²³¹ $\text{Ca}(\text{OCOCH}_3)_2 \cdot x\text{H}_2\text{O}$:



This fact could suggest that small amounts of Ca^{2+} may not be incorporated to the perovskite in the PCT powders at these temperatures. The molar percentage of this non-incorporated Ca^{2+} cation calculated from the corresponding weight losses would be ~ 0.05 , ~ 0.06 , ~ 0.08 and ~ 0.12 mol% for the PCT24, PCT30, PCT40 and PCT50 powders, respectively.

Finally, an exothermic peak due to the phase transition (cubic to tetragonal) can be observed in the DTA curves of the PCT0, PCT24 and PCT30 systems recorded during cooling (ii). However, this peak is not appreciated for the PCT40 and PCT50 powders, due to the low structural differences for these compositions at low and high temperatures^{10,176}. This results in a low exchange of energy for the phase transition, not observed in their corresponding DTA cooling curves. Results obtained in this study are summarised in Table 4.1.



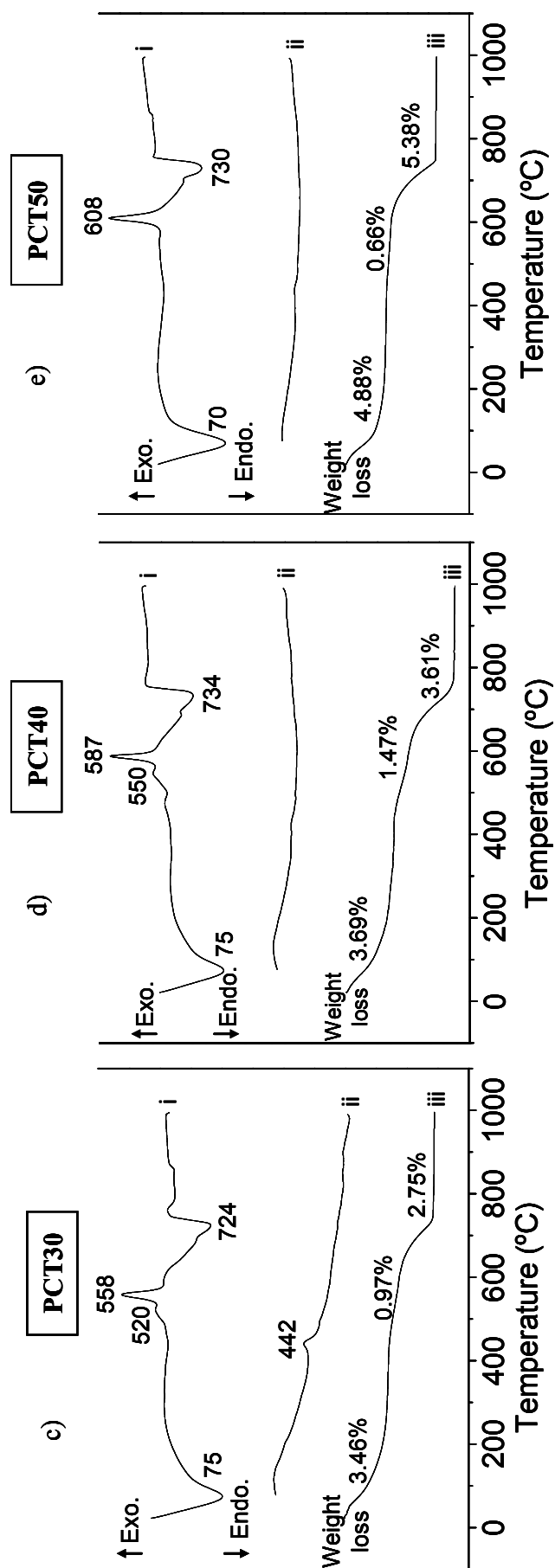


Figure 4.1.1. DTA curves for heating (i) and cooling (ii), and TGA curves (iii) of the diol sol-gel derived PCT0 (a), PCT24 (b) PCT30 (c), PCT40 (d) and PCT50 (e) powders. Insets show the DTA, TGA and DTG curves of the PCT0 and PCT24 powders

Table 4.1.1.1. Summary of the results obtained by DTA-TGA in the diol sol-gel derived PCT powders

Gel powder (nominal composition)	Temperature interval (°C)	Weight loss (iii) (%)	DTG maximum (°C)	DTA heating (i) (°C)	DTA cooling (ii) (°C)	Perovskite crystallisation temperature (°C)	Powder composition deduced from TGA weight losses	Processes
PbTiO ₃ (PCT0)	< 300	~1.54	~61	~56 (endo)	-	-	-	< 300 °C
	300-600	~3.39	~468	~466 (exo), ~500 (exo)	~478	~500	PbTiO ₃	
	> 600	-	-	-	-	-	-	Evaporation of physically absorbed water and organic solvent within the gel network
(Pb _{0.76} Ca _{0.24})TiO ₃ (PCT24)	< 300	~2.94	~71	~70 (endo)	-	-	-	300-600 °C Combustion of organic compounds, formation of calcium carbonate and crystallisation of the PCT system
	300-600	~1.70	~499	~490 (exo), ~520 (exo)	~442	~520	Pb _{0.76} Ca _{0.23} TiO ₃ + 0.01 CaO	
	> 600	~2.12	~702	~715 (endo)	-	-	-	> 600 °C Decomposition of calcium carbonate CaCO ₃ → CaO + CO ₂
(Pb _{0.70} Ca _{0.30})TiO ₃ (PCT30)	< 300	~3.46	~78	~75 (endo)	-	-	-	
	300-600	~0.97	~527	~520 (exo), ~558 (exo)	~442	~558	Pb _{0.70} Ca _{0.29} TiO ₃ + 0.01 CaO	
	> 600	~2.75	~699	~724 (endo)	-	-	-	
(Pb _{0.60} Ca _{0.40})TiO ₃ (PCT40)	< 300	~3.69	~72	~75 (endo)	-	-	-	
	300-600	~1.47	~510	~550 (exo), ~587 (exo)	-	~587	Pb _{0.60} Ca _{0.39} TiO ₃ + 0.01 CaO	
	> 600	~3.61	~719	~734 (endo)	-	-	-	
(Pb _{0.50} Ca _{0.50})TiO ₃ (PCT50)	< 300	~4.88	~68	~70 (endo)	-	-	-	
	300-600	~0.66	~487	~608 (exo)	-	~608	Pb _{0.50} Ca _{0.48} TiO ₃ + 0.02 CaO	
	> 600	~5.38	~726	~730 (endo)	-	-	-	

From these results, the thermal decomposition of these PCT gels can be divided in three different steps that occur in the same temperature intervals independent on the Ca^{2+} content. Below 300 °C, the evaporation of physically absorbed water and organic solvent within the gel network takes place. The elimination of the organic compounds is produced between 300 and 600 °C, when besides crystallisation occurs. The temperature at which this process takes place does depend on the composition of the PCT powders. Thus, the crystallisation of the PCT system moves to higher temperatures as the amount of Ca^{2+} content in the PCT powders increases. Finally, over 600 °C, the decomposition of calcium carbonate, formed in the previous step and stable up to high temperatures, is produced. The amount of calcium carbonate formed, and hence combusted, is higher as the amount of Ca^{2+} in the composition of the powder is increased.

4.1.3. PCT THIN FILMS

To study the crystallisation of the films, other techniques different from the DTA-TGA analysis should be used, since the small amount of energy and material involved in the thermal decomposition of the films would not allow us to follow easily their crystallisation by this way. Therefore, techniques such as XPS, TEM, GIXRD, XRD, SFM and BS have been used in the present work to study the crystallisation process of the PCT films as a function of the temperature and of the Ca^{2+} content.

4.1.3.1. Compositional depth profile of the films by X-ray Photoelectron Spectroscopy (XPS)

The possible presence of a small amount of Ca^{2+} (as calcium carbonate, CaCO_3) not incorporated to the PCT crystalline phase, previously observed in the DTA/TGA experiments of the powders, was investigated in the diol-based sol-gel derived PCT films by XPS. This could turn into a significant problem in the thin film form, since full crystalline PCT films with suitable ferroelectric and dielectric responses are usually obtained at temperatures of ~650 °C by RTP,¹⁸⁵ temperature at which calcium carbonate is still not decomposed in the PCT powders (see Table 4.1). Thus, the presence of calcium carbonate in the crystalline films would lead to a deviation in the composition of the $(\text{Pb}_{1-x}\text{Ca}_x)\text{TiO}_3$ perovskite, affecting their structural, microstructural and electrical properties. In order to elucidate if the crystalline PCT films contain calcium carbonate or other amorphous rests and if they have a homogeneous compositional profile, XPS analysis has been carried out on a PCT50 film. This is the most unfavourable film composition of those here

studied, since it contains the largest amount of calcium and therefore, the possibility of having a crystalline PCT film with CaCO_3 rests is higher.

Figure 4.1.2 shows the depth profiling analysis obtained by XPS in a PCT50 film crystallised onto a Pt/TiO₂/SiO₂/(100)Si substrate at 650 °C by RTP. The intensity peaks of the constituent elements of the film versus sputter time is depicted in Figure 4.1.2.

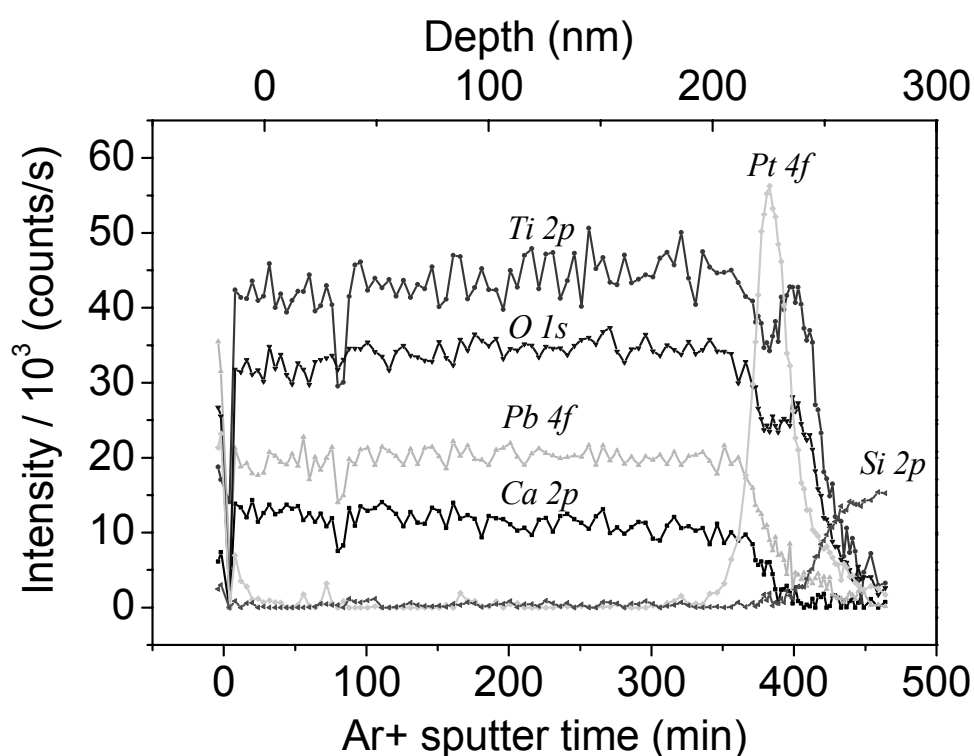


Figure 4.1.2. Photoelectron peak intensities during depth profiling of a diol sol-gel derived PCT50 film deposited on Pt/TiO₂/SiO₂/(100)Si

As it is known, prolonged Ar^+ bombardment usually leads to significant chemical changes in the film surface.²⁴¹ In the case of lead titanate (PbTiO_3) based compositions, preferential loss of Pb is ascribed to the high volatility of this element in the thermal spike on the sample surface, caused by the impinging ions.²⁴² This effect can be observed in the Pb4f core level, where a preferential loss of Pb is produced during the first minutes of Ar^+ sputtering. This fact prevents the possibility of obtaining the exact composition of the film (quantitative analysis). However, after several minutes of Ar^+ bombardment, a steady-state situation in the sample is reached from which a homogeneous profile can be deduced for the film (Fig. 4.1.2). Further depth profiling reveals the heterostructure

of the substrate; the Pt electrode, the TiO_2 layer and the (100)Si substrate. Note how the signals of the respective Ti2p and O1s core levels slightly increase after the maximum of Pt4f level appears, which is ascribed to the TiO_2 buffer layer present in the substrate (Pt/ TiO_2 / SiO_2 /(100)Si).

Figure 4.1.3 shows the binding energy spectra of C1s and O1s core levels measured at different Ar^+ sputtering times on the film.

At the beginning of the analysis, the experimental signal of the C1s level obtained in the film (Fig. 4.1.3a) is split into two Gaussian curves with peak maxima at ~ 284.7 and ~ 287.8 eV corresponding to adventitious carbon and carbon from carbonate groups, respectively.²⁴³ The presence of carbonate in the film surface is also verified from the XPS measurements of O1s core level of Fig. 4.1.3b. Once deconvoluted, two different peaks can be appreciated in the O1s spectrum before the Ar^+ sputtering, at ~ 529.9 and ~ 532.5 eV, where the former one is attributed to oxygen atoms of CO_3^{2-} groups and those of the PbO oxide²⁴⁴, that is preferentially sputtered at the beginning of the Ar^+ bombardment. Thus, both C1s and O1s signals confirm the presence of carbonates in the film surface prior to the sputter cleaning.

However, when analysing the depth profiling of the C1s signal (Fig. 4.1.3c), it is observed how it practically disappears after the first minutes of Ar^+ sputtering. In addition, the C1s peak ascribed to the carbon of carbonate groups (~ 287.8 eV) has disappeared in the spectra after 1 min of sputtering time, and also the C1s peak ascribed to adventitious carbon (~ 284.7 eV) has appreciable decreased at this sputtering time (Fig. 4.1.3a). This phenomenon, confirmed by numerous literature data,^{245,246} is attributed to the accumulation of carbon-containing contaminants of different nature (e.g. graphitic carbon, hydrocarbons, carbonates) on the sample surface when just placed it into the spectrometer, coming from the atmospheric ambient. Once the sputtering cleaning is carried out in the sample, these carbonaceous contaminants are removed from the sample surface. In the case of the O1s peak at ~ 529.9 eV, the disappearance of this signal after 1 min of sputtering time (Fig. 4.1.3b) is mainly due to the volatilisation of PbO and a minor layer of carbonate present at the film surface. It can be concluded that, after 1 min of Ar^+ sputter cleaning, the film surface appears totally free from carbon residuals, neither detecting carbon groups in the bulk film.

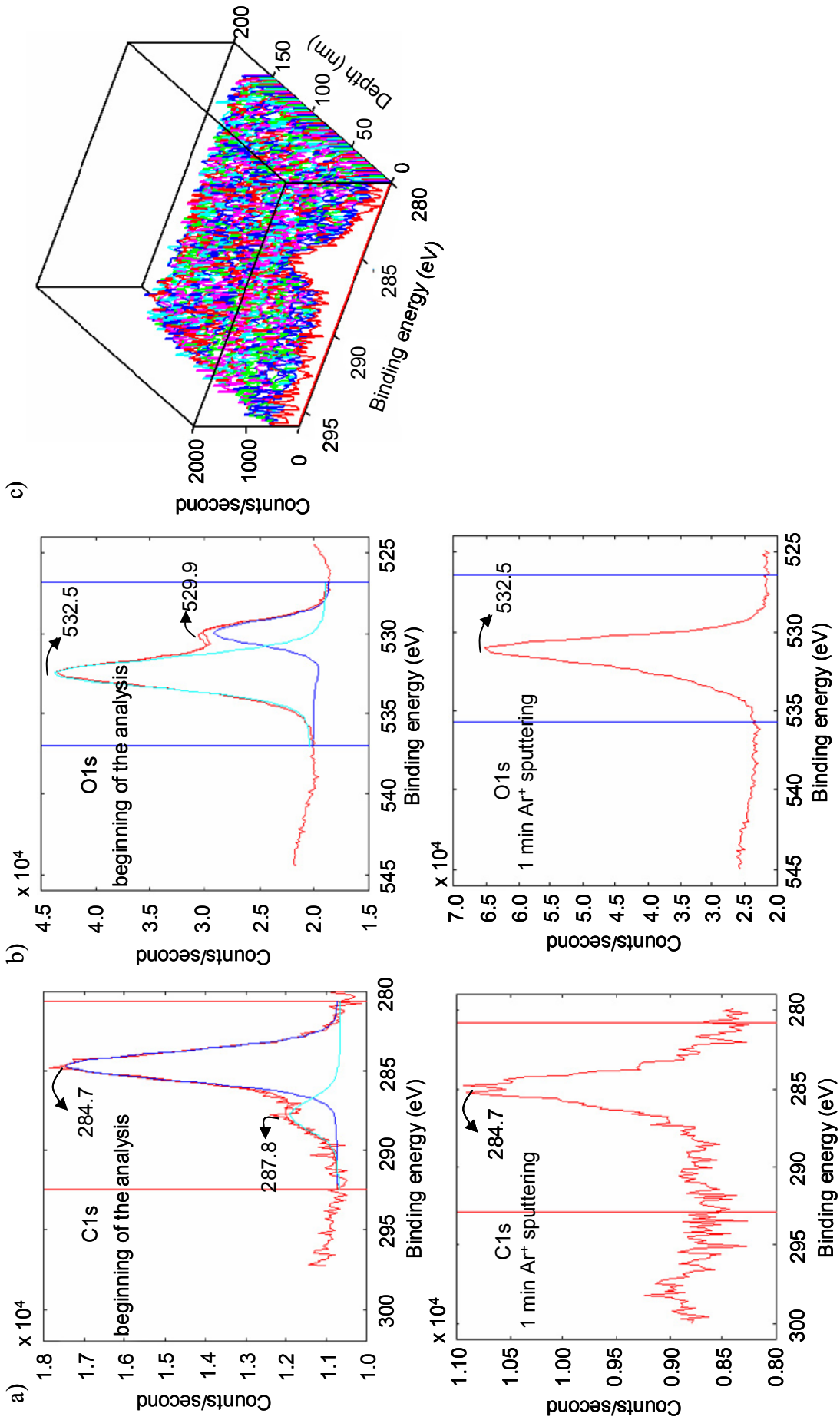


Figure 4.1.3. C1s (a) and O1s (b) core levels measured at different Ar⁺ sputtering times (beginning of the analysis and after 1 min of Ar⁺ sputtering) in the diol sol-gel derived PCT50 film. (c) Signal of C1s measured in the film as a function of depth and binding energy

Thus, the analysis of the compositional depth profile carried out by XPS does not show the presence of residual carbon (carbonates and/or other organic compounds) in the PCT50 film, which suggests the total incorporation of the Ca^{2+} cation into the crystalline structure of the film and also the absence of residual organics in the PCT films crystallised at 650 °C by RTP. Regarding the calcium carbonate previously detected in the powders, it must be taken into account that the thermal processes developed in bulk powders may slightly differ from those developed in the thin film form, mainly due to the specific conformation of the latter onto a substrate (high surface to volume ratio) and to the different thermal treatments of crystallisation carried out in both type of materials (conventional furnace or RTP).

4.1.3.2. Microstructure and crystal structure of the films by Transmission Electron Microscopy (TEM) and Selected Area Electron Diffraction (SAED)

The crystalline structure and microstructure of diol-based sol-gel derived PCT films onto Pt/TiO₂/SiO₂/(100)Si substrates with different Ca^{2+} contents (24, 35 and 50 at%) were studied by means of Transmission Electron Microscopy (TEM) combined with Selected Area Electron Diffraction (SAED) analysis. These films were crystallised by RTP at 650 °C.

Figures 4.1.4 and 4.1.5 shows the plan-view micrographs (bright-field) of the PCT24 and PCT35 films, respectively. High-magnification pictures are included for a better observation of crystal size. Cross-section micrographs (bright-field) of the PCT50 film are displayed in Fig. 4.1.6, at various magnifications. Selected area diffraction patterns of the samples are also shown in the respective figures together with indexation of major reflections observed.

In general, the microstructure of the PCT films consists in clusters or associations of grains with well-defined boundaries,²⁴⁷ as it can be observed from the surfaces images obtained by TEM (Figs. 4.1.4 and 4.1.5). Neither secondary phases nor phase segregation are observed in the micrographs of these figures. The mean size of these clusters varies from ~500 to ~370 nm for the PCT24 and PCT35 films, respectively. Magnifications of these images show grains with an average size of ~200 and ~130 nm for the respective PCT24 and PCT35 films. In the case of the PCT50 film, this study was carried out from the cross-section images obtained (Fig. 4.1.6). Here, grains of ~55 nm can be appreciated (Fig. 4.1.6d). Note that a progressive decrease in the grain size of the film is obtained as the partial substitution of Pb^{2+} by Ca^{2+} in the composition increases (~200, ~130 and ~55 nm for substitution rates of 24, 35 and 50 at%, respectively).

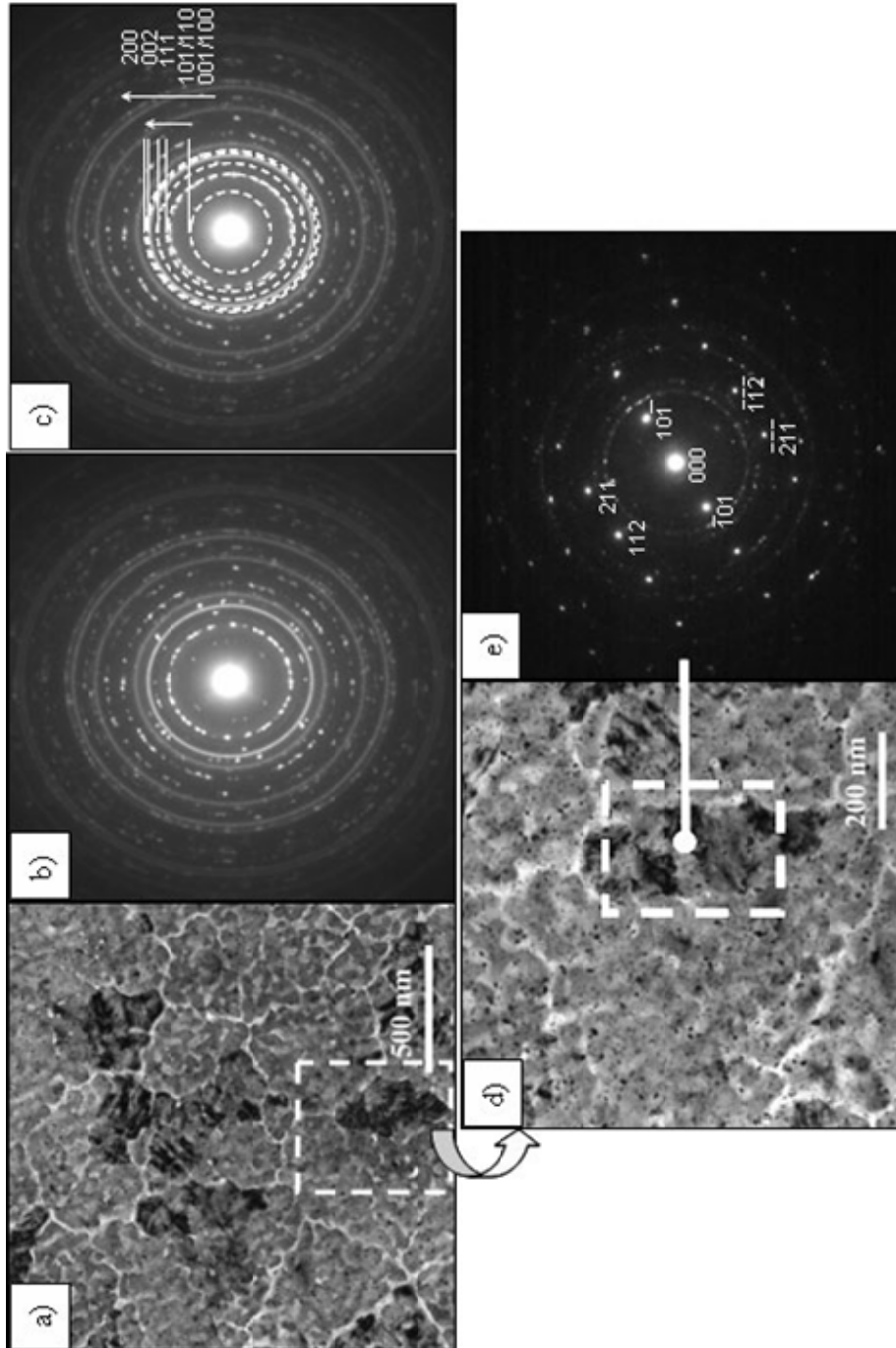


Figure 4.1.4. Bright-field TEM micrograph (a) and indexed SAED patterns (b and c) of the diol sol-gel derived PCT24 film (plan-view). Magnified micrograph to appreciate crystal size (d) and corresponding SAED pattern (e) are also shown. Continuous rings observed in the SAED patterns are ascribed to copper of the sample-holder grid

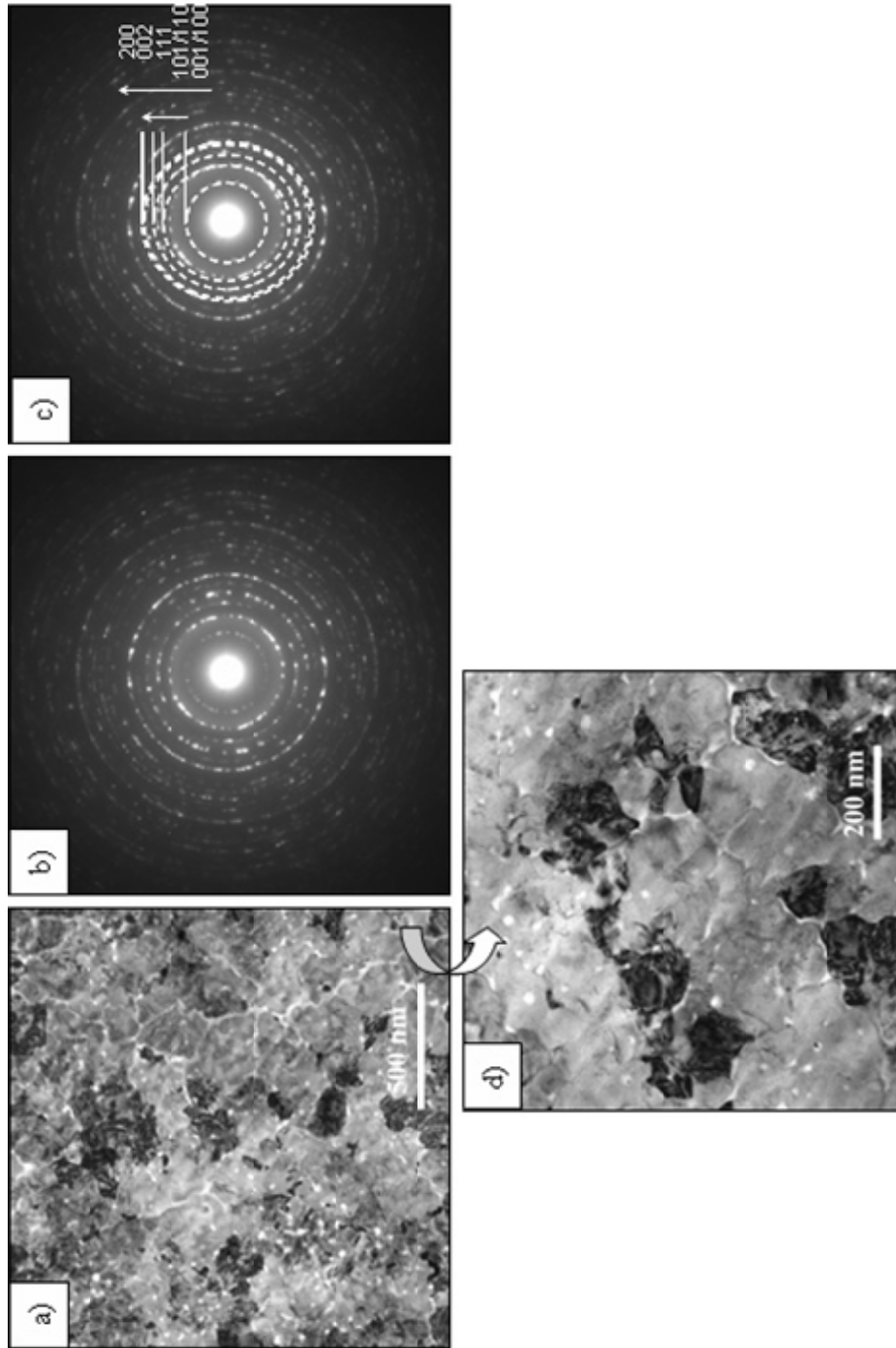


Figure 4.1.5. Bright-field TEM micrograph (a) and indexed SAED patterns (b and c) of the diol sol-gel derived PCT35 film (plan-view). Magnified crystal size (d) is also shown. Continuous rings observed in the SAED patterns are ascribed to copper of the sample-holder grid

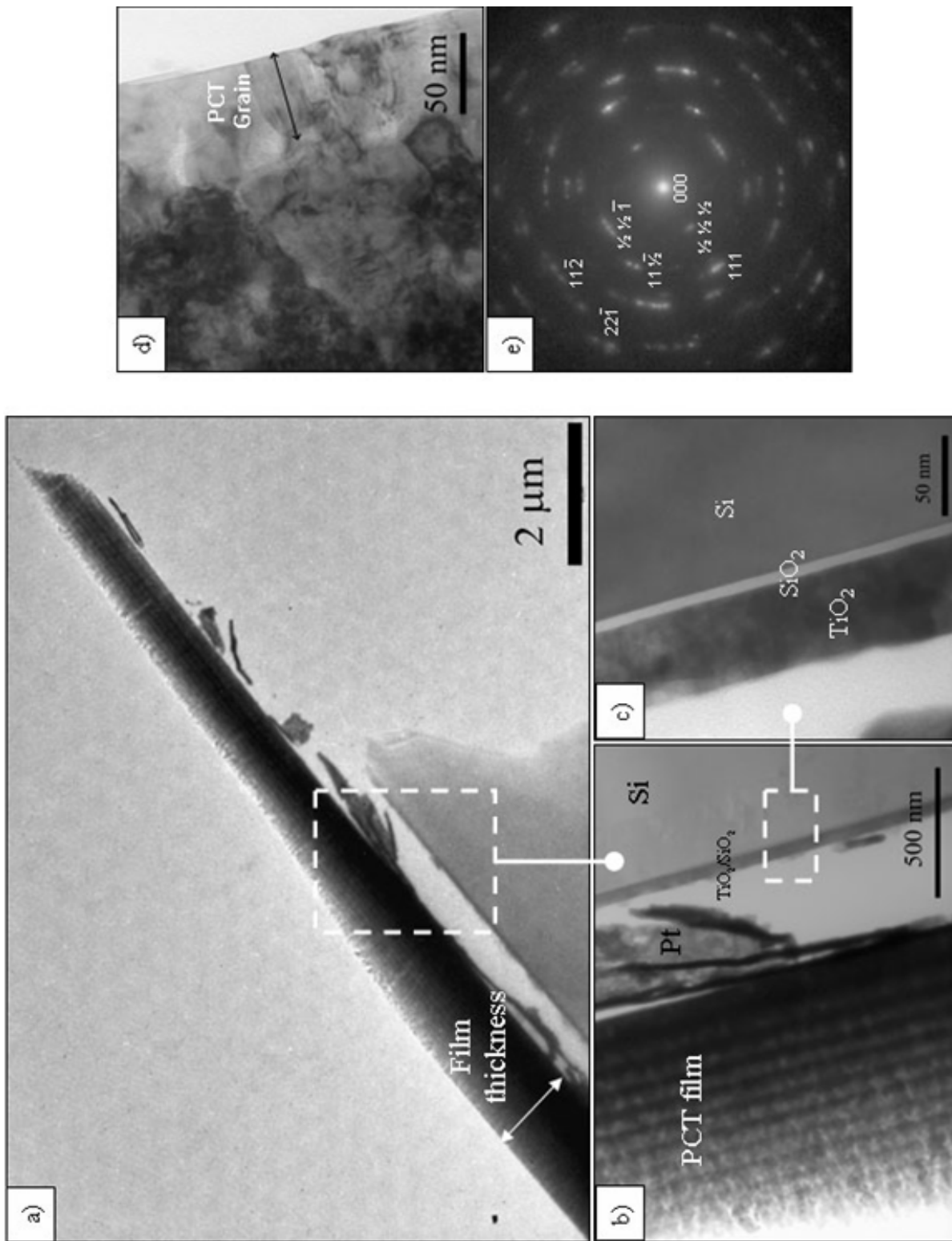


Figure 4.1.6. Bright-field TEM micrographs at different magnifications to appreciate the heterostructure (a, b and c) and the crystal size (d) of the diol sol-gel derived PCT50 film (cross-section). Corresponding indexed SAED pattern (e) is also shown

The crystal structure of the PCT films was also studied from the SAED patterns of the figures. A tetragonal elementary perovskite unit cell for the PCT24 (Fig 4.1.4b and c) and PCT35 (Fig 4.1.5b and c) films is deduced from the indexation of the corresponding polycrystalline electron diffraction patterns (Fig 4.1.4e moreover shows the electron diffraction pattern of a single crystal of PCT24 for the $[\bar{1}31]$ zone axis). A tetragonality (c/a) of ~ 1.04 is calculated for the PCT24 and PCT35 films that agree with values reported in the literature.⁴⁰

While there is general unanimity that the structure of the PCT perovskite is tetragonal for Ca^{2+} contents below 40 at%, there are conflicting reports about the correct structure for PCT perovskite compositions with Ca^{2+} contents over 40 at%. Earlier works carried out on single crystals³⁶ and bulk ceramics^{43,44} of the same composition report on the orthorhombic structure for this perovskite composition. For the PCT50 film of this work, only a pseudocubic crystal structure is deduced from the reflections observed in the electron diffraction pattern of Fig. 4.1.6e. Furthermore, extra reflections appear in the pattern that can be indexed to the $(\frac{1}{2}\frac{1}{2}\frac{1}{2})$ and $(\frac{1}{2}\frac{1}{2}1)$ superlattice reflections. Some authors point that these type of reflections only appear in electron-diffraction patterns, and not in neutron powder diffraction, due to surface effects.^{248,249} An ordered structure is proposed for $(\text{Pb}_{1-x}\text{Ca}_x)\text{TiO}_3$ ceramic powders with $0.4 \leq x \leq 0.7$ that leads to the appearance of superlattice reflections in the corresponding electron diffraction patterns.⁴² Other authors have also observed the presence of this ordered structure for ceramic powders with $x \geq 0.42$ and $x = 0.50$ by neutron⁴³ and x-ray⁴⁴ diffraction experiments, respectively. The formation of this superstructure can arise due to i) 1:1 chemical ordering of Pb^{2+} and Ca^{2+} ions,⁴¹ ii) antiphase-inphase tilting of oxygen octahedra (TiO_6)^{39,45} and/or iii) off center location (atomic shuffles) of $\text{Pb}^{2+}/\text{Ca}^{2+}$ ions^{39,45}. From the results obtained in this work, however, it cannot be deduced the main force (cation displacements and/or octahedral rotations and/or distortions) responsible of the superlattice reflections detected in the perovskite elementary cell of the PCT50 film. It has to be noted that this ordered structure has been previously observed in high-Ca PCT powders and bulk ceramics. To the author's knowledge, this is the first time that these superlattice reflections are detected in PCT thin films.

The heterostructure of the PCT50 film can also be observed in the micrographs of Figs. 4.1.6a to c. Note how the multiple layers that constitute the film (15 layers, in this case) can be distinguished. An average thickness of ~ 80 nm is measured for each single layer, whereas a total thickness value of ~ 1300 nm is calculated for this PCT50 film. Thicknesses of the SiO_2 and TiO_2

layers of the substrate are around ~ 6 and ~ 55 nm, respectively. The Pt layer resulted damaged during the specimen preparation and no thickness could be estimated from the images.

Homogeneous surface microstructures are deduced from these TEM investigations on the diol-based sol-gel PCT films treated at $650\text{ }^{\circ}\text{C}$ by RTP. A decrease in grain size is obtained in the crystalline films as increasing the Ca^{2+} content of the PCT composition. Furthermore, the tetragonality of the PCT perovskite system is lowered as high Ca^{2+} doping is introduced in the system. Thus, a tetragonal structure is observed in the PCT films with low Ca^{2+} content (PCT24 and PCT35), whereas films with higher Ca^{2+} concentration (PCT50) present a distorted orthorhombic structure, as deduced from the SAED patterns obtained in these films.

4.1.3.3. Crystal phases in the films by Grazing Incidence X-Ray Diffraction (GIXRD) analysis

For the crystallisation study of the films described hereinafter, a single coating of the diol-based sol-gel PCT solutions (concentration of ~ 1 M) was deposited onto oxidised silicon substrates ($\text{SiO}_2/(\text{100})\text{Si}$) without Pt bottom electrodes, to avoid overlapping of the 111 perovskite peak and the 111 Pt peak. The deposited layers were RTP treated in air at temperatures between 400 and $650\text{ }^{\circ}\text{C}$, for 50 s.

The PCT films treated at different temperatures were analysed by GIXRD, thus minimising any reflection coming from the substrate. Figure 4.1.7 shows the GIXRD ($\alpha = 1^{\circ}$) patterns of the PCT films treated at different temperatures.²⁴⁰

At $400\text{ }^{\circ}\text{C}$ (Fig. 4.1.7a), none of the films show reflections of crystalline phases except the PCT0 film, which presents broad peaks corresponding to a pyrochlore (Py) structure with a composition close to that of the $\text{Pb}_2\text{Ti}_2\text{O}_6$ phase (JCPDS#26-142)^{250,251}. Reflections corresponding to the perovskite appear in the PCT films with low Ca^{2+} contents (PCT0, PCT24 and PCT30) treated at $425\text{ }^{\circ}\text{C}$ (Fig. 4.1.7b), although a large background characteristic of amorphous or low-crystalline phases is also observed. At this temperature, films with high Ca^{2+} contents (PCT40 and PCT50) are amorphous according to the x-ray diffraction results obtained. Over $450\text{ }^{\circ}\text{C}$ (Figs. 4.1.7c and d), all the films show the existence of the perovskite phase, even though the background mentioned before is still present in some films (see inset of this figure).

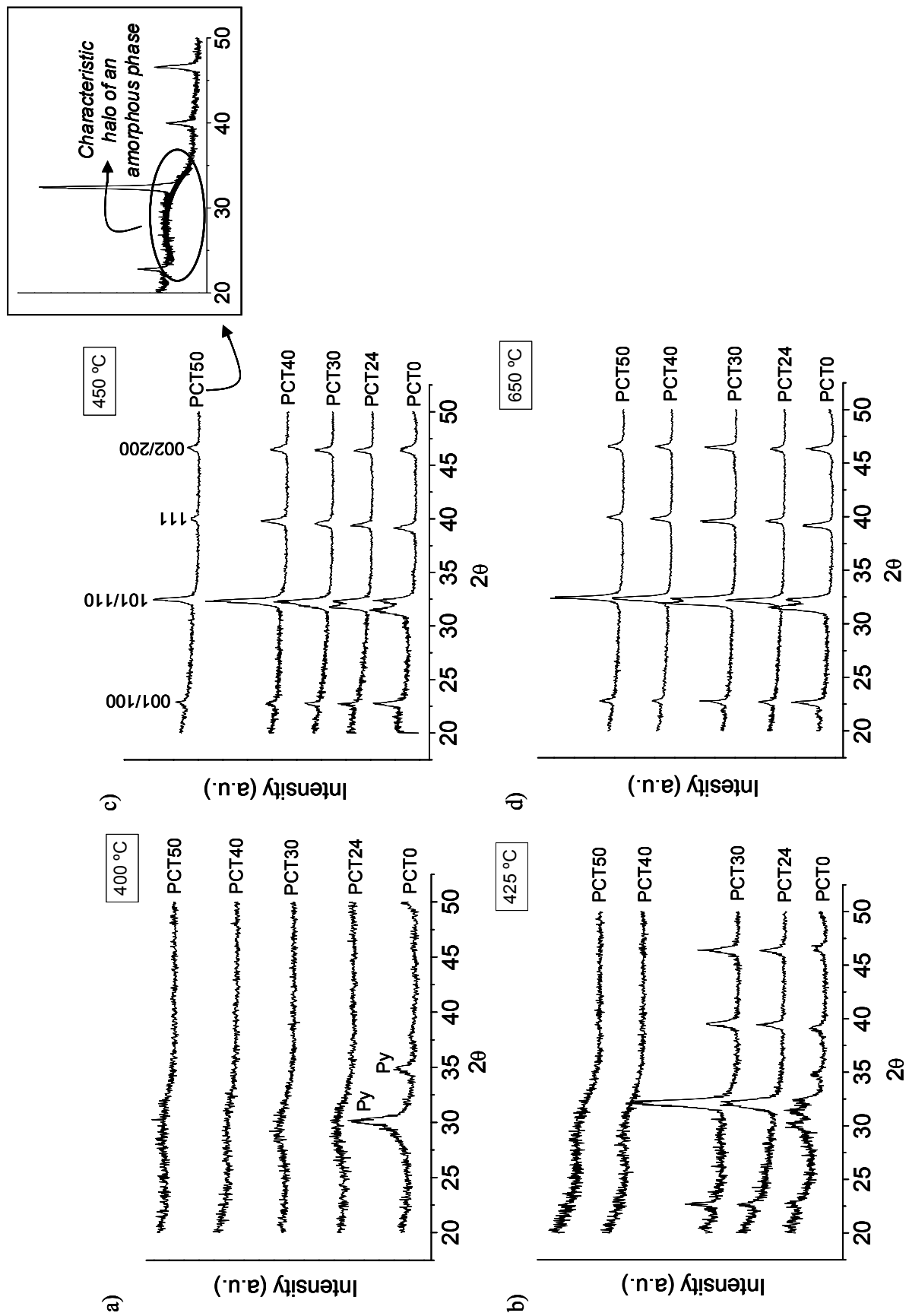


Figure 4.1.7. GIXRD patterns of the diol sol-gel derived PCT films treated at 400 °C (a), 425 °C (b), 450 °C (c) and 650 °C (d) by RTP (Py: pyrochlore). Indexed peaks correspond to the perovskite. Inset shows the GIXRD pattern of the PCT50 film treated at 450 °C

From the appearance of crystalline phases in the films observed in the GIXRD patterns of Fig. 4.1.7, differences in the crystallisation behaviour of the PCT films can be deduced. For films without Ca^{2+} in the composition (PCT0), a pyrochlore second phase coexists with the perovskite during its initial development at ~ 425 °C, disappearing with the increase of the processing temperature. However, for films with low Ca^{2+} contents (PCT24 and PCT30), the perovskite reflections are the only ones observed at 425 °C, whereas the films with large Ca^{2+} contents (PCT40 and PCT50) remain amorphous by GIXRD at this temperature. A slight increase in temperature, 450 °C, produces also the formation of the perovskite in these high-Ca films, although residual amorphous or low-crystallinity phases are still present in them (see inset).

These results indicate that PCT films with low Ca^{2+} concentration require lower energy (via temperature) to active the nucleation of the PCT perovskite. This is in agreement with the previous DTA results of the PCT powders, where the crystallisation of the perovskite also takes place at higher temperatures as the Ca^{2+} content increases. Although the crystallisation temperatures of the PCT powders determined by DTA/TGA do not have to match up exactly with those measured in the films (due to the reasons previously stated), the trend towards an increase on the crystallisation temperature of the PCT perovskite as the substitution of Pb^{2+} by Ca^{2+} in the system is larger, is also confirmed by the GIXRD results of the films.

4.1.3.4. Crystallinity of the perovskite films by X-Ray Diffraction (XRD) analysis

Coupled θ -2 θ measurements (XRD) were also carried out on the PCT films, but analyses were limited to the 111 reflection of the perovskite, because it is a single reflection and is not affected by contributions of other reflections coming from the substrate.

The 111 perovskite peaks measured for the PCT films treated at different temperatures were fitted by Pseudo-Voigt functions and resulting curves are shown in Figure 4.1.8. For clarity in the figure, only 111 peaks corresponding to three different temperatures are shown. From the fitted 111 peaks, the full-width at half maximum values (FWHM) were calculated. Figure 4.1.9 shows the variation with temperature of the FWHM values calculated from these peaks for different Ca^{2+} contents.

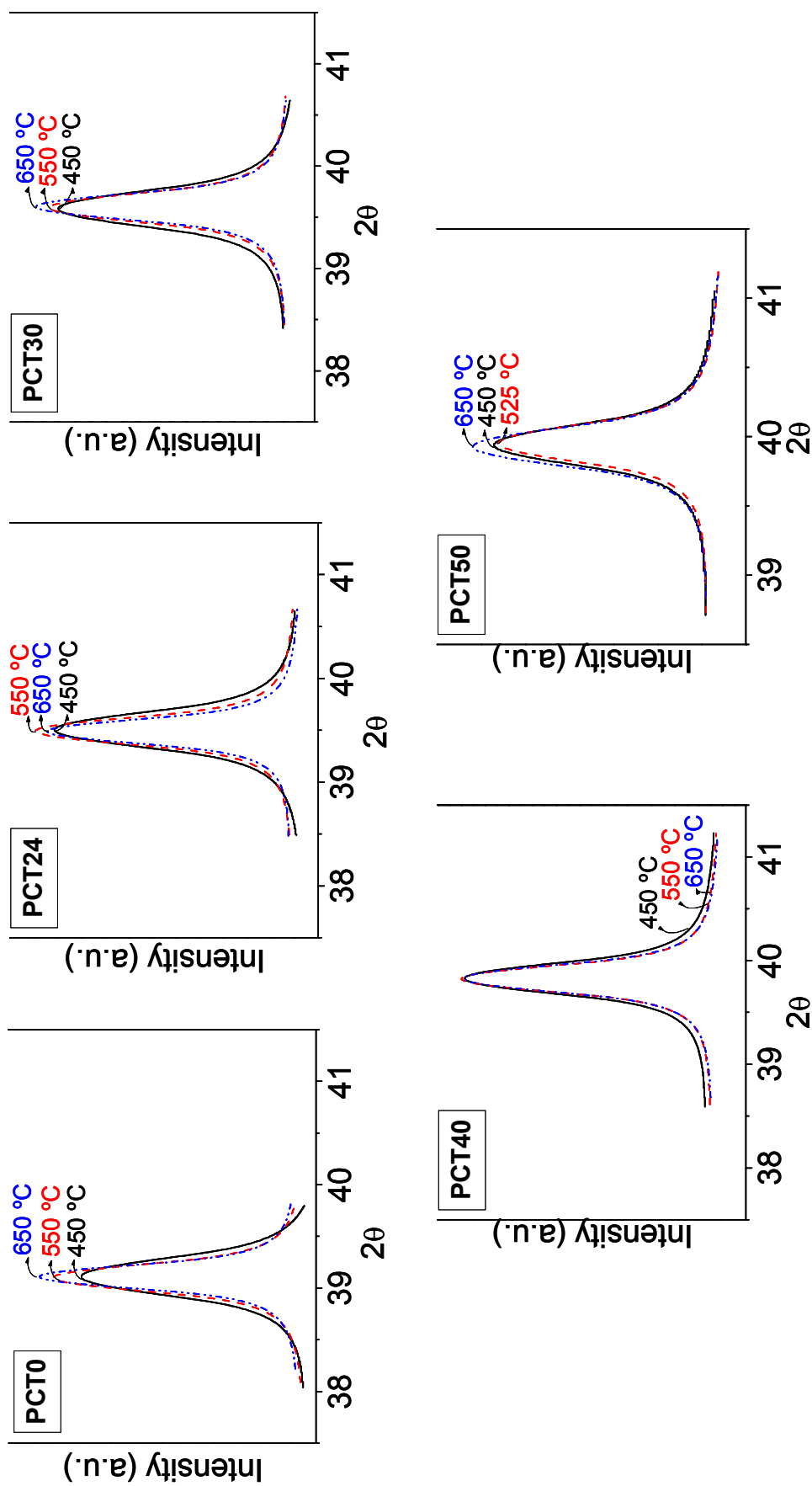


Figure 4.1.8. Pseudo-Voigt curves corresponding to the 111 perovskite peaks of the diol sol-gel derived PCT films treated at different temperatures

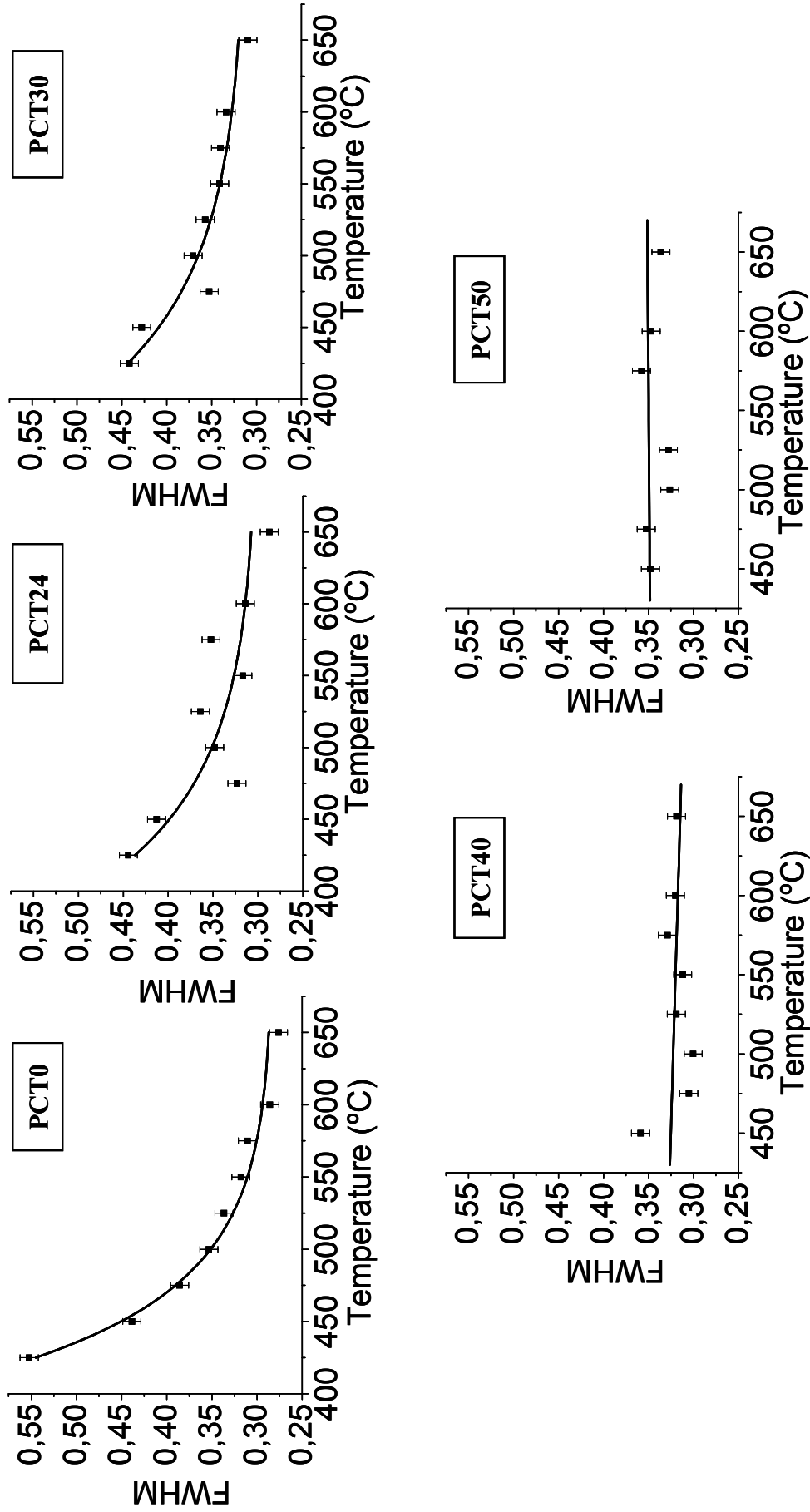


Figure 4.1.9. Variation with temperature of FWHM values of the 111 perovskite peak measured by XRD with the Bragg-Brentano geometry of the diol sol-gel derived PCT films

An exponential decay with increasing temperature is observed for films with low Ca^{2+} doping (PCT0, PCT24 and PCT30), whereas films with Ca^{2+} contents over 40 at% (PCT40 and PCT50) show almost constant values of FWHM. The broadening of the 111 peak is related to crystallite size and micro-strain of the PCT perovskite, both parameters indicative of the degree of crystallinity in the material. The decrease with temperature of the FWHM values of the PCT films with low Ca^{2+} content (Figs 4.1.9a-c) can be associated to an increase in crystallite size (as the crystallite is bigger, it diffracts more coherently) and also to changes in micro-strains with temperature (the paraelectric (cubic)–ferroelectric (tetragonal) transition during cooling after the crystallisation of the films can contribute to the development of micro-strains in the cell). However, PCT films with large Ca^{2+} contents crystallise into the paraelectric phase that here is also the stable phase at room temperature. Then, not too much change in micro-strains should be expected. Thus, the steady FWHM values with temperature (Figs. 4.1.9d and e) would indicate that both micro-strains and crystallite size maintain practically constant with temperature in the PCT films with a Ca^{2+} content over 40 at%.

To corroborate the former hypotheses, the partial contribution of both crystallite size and micro-strains to the FWHM value of the 111 reflection of the films was calculated from the XRD data using the variance method proposed by Langford et al.²⁵². Thus, crystallite size and micro-strains for the PCT films were studied as a function of the processing temperature and of the Ca^{2+} content, as Figure 4.1.10 shows.

The variation of these parameters with temperature for the two extreme PCT compositions, PCT0 and PCT50, are depicted in Figs. 4.1.10a and b, respectively. For the PCT0 film, the crystallite size becomes larger and the micro-strains are reduced as the annealing temperature increases. However, in the film PCT50, crystallite size and micro-strains only increase and decrease slightly, respectively.

When crystallisation occurs from an amorphous material, small crystals start to nucleate inside the amorphous matrix as the temperature increases. The crystal size should increase as crystallisation evolves with the processing temperature. This crystallisation evolution has also associated a reduction in crystal defects due to the correct rearrangement of the ions in the perovskite structure. This results in a decrease in the micro-strains of the crystals. Crystal growth and micro-strains reduction are clearly observed for the films with low Ca^{2+} content (PCT0 in Fig. 4.1.10a).

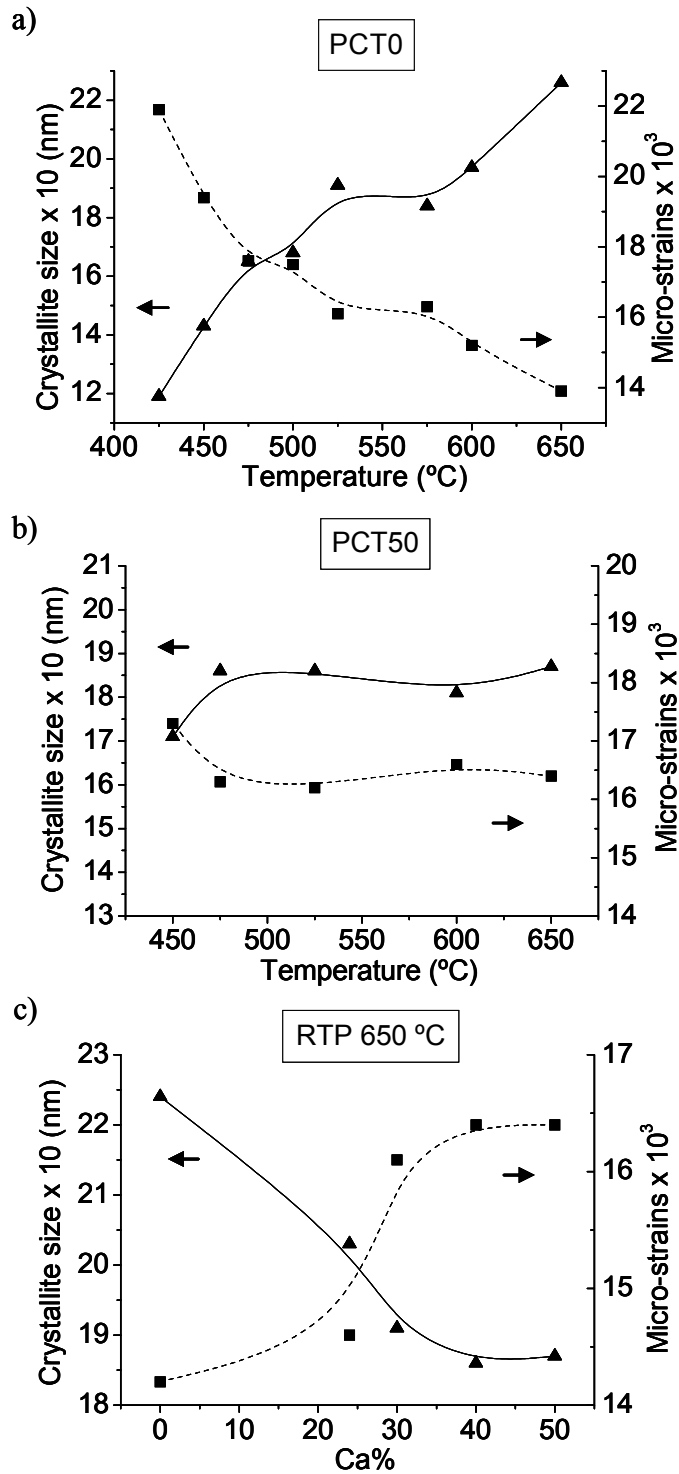


Figure 4.1.10. Crystallite size and micro-strains calculated with the variance method²⁵² from the XRD diffraction data of the 111 perovskite reflection for the diol sol-gel derived PCT0 (a) and PCT50 (b) films treated at different temperatures by RTP. Graph (c) shows both values for PCT films treated at 650 °C by RTP as a function of the Ca²⁺ content

However, for the films with large Ca^{2+} contents, the perovskite crystallisation starts at slightly higher temperatures, in agreement with the GIXRD results. Thus, note that the first perovskite reflections for the PCT50 film are recorded at 450 °C (Figs. 4.1.7c and 4.1.10b), whereas for the film PCT0 is 425 °C (Figs. 4.1.7b and 4.1.10a), and moreover the kinetic with temperature of the crystallisation process is slower; only a slight increase and decrease in crystal size and micro-strains, respectively, are observed for the PCT50 film in the Fig. 4.1.10b. Figure 4.1.10c shows the calculated values of crystallite size and micro-strains for the PCT films with different Ca^{2+} contents, processed by RTP at 650 °C. Here, it is observed how the crystallite size and micro-strains abruptly decrease and increase, respectively, as the Ca^{2+} content in the films is larger, until an almost constant value seems to be reached.

Therefore, both GIXRD and XRD results show a considerable effect of the Ca^{2+} content on the crystallisation process of the PCT films. Perovskite crystals start to nucleate at lower temperatures in the films with low Ca^{2+} than in those with high Ca^{2+} . Besides, the kinetic of crystals growth is much faster with temperature in the former. In the latter films, the crystal growth and the micro-strain relaxation seem to be inhibited, compared with the films with low Ca^{2+} contents.

4.1.3.5. Surface morphology of the films by Scanning Force Microscopy (SFM)

Although the concept of crystallite size (coherent diffraction domain) is not the same as grain size (in polycrystalline ferroelectrics), both values are correlated and allow us to establish a relation between grain size of the films, measured by Scanning Force Microscopy (SFM), and crystal size, deduced from the XRD results of the previous section.

Surface images of the films obtained by SFM are shown in Figure 4.1.11, where the grain size values measured from these images are also indicated in the photographs. SFM images of Fig. 4.1.11a and b correspond to PCT0 films processed by RTP at 450 and 650 °C. Grain sizes of ~35 and ~150 nm were measured for these films at 450 and 650 °C, respectively. On the other hand, the SFM images of the PCT50 films processed at these temperatures, shown in Fig. 4.1.11c and d, indicate that the increase in grain size from the films processed at low and high temperatures (~25 nm at 450 °C and ~55 nm at 650 °C) is much smaller than that of films with low Ca^{2+} content.

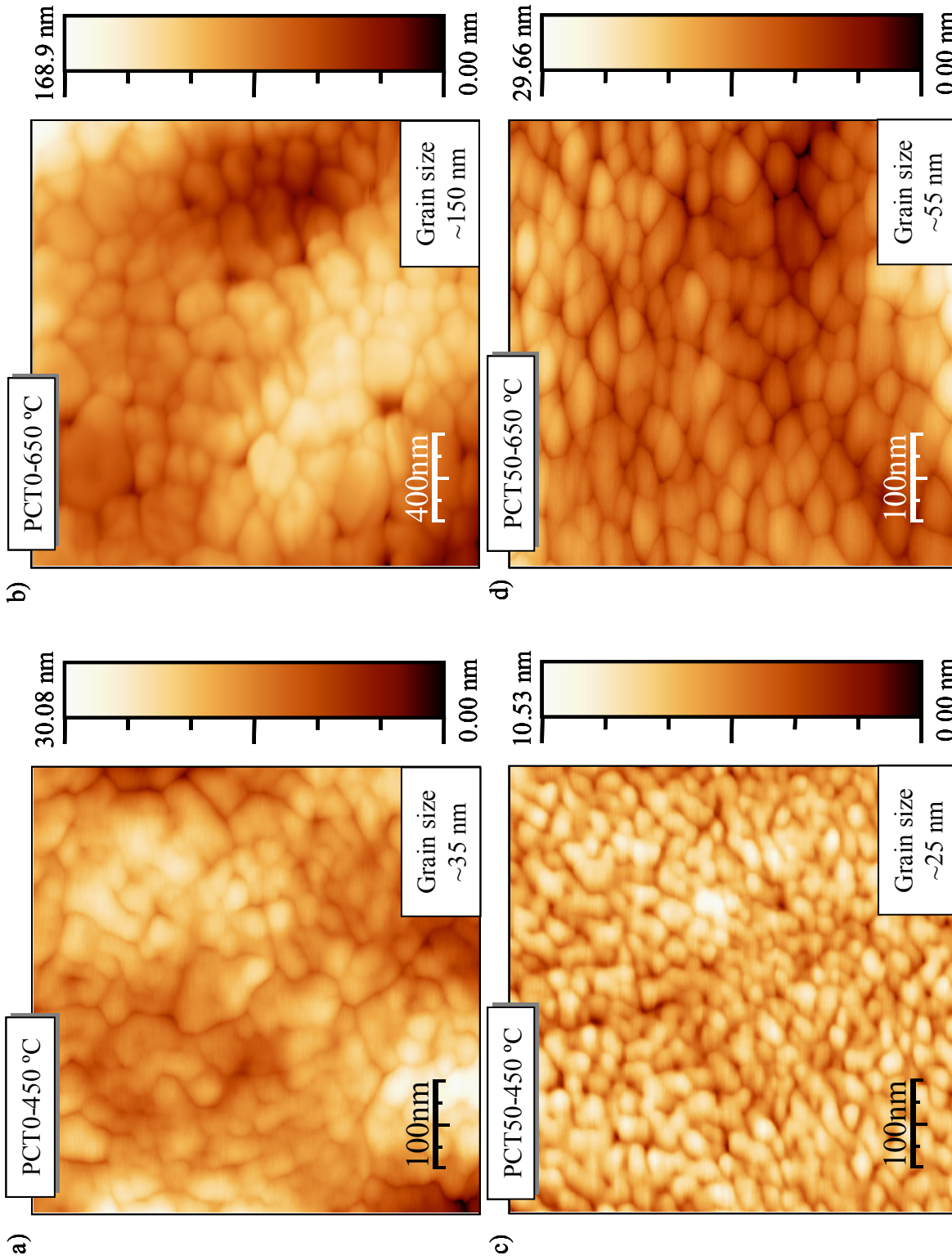


Figure 4.1.11. SFM images of the surfaces of the diol sol-gel derived PCT0 (a) and PCT50 (b) films, treated at 450 and 650 °C. Note the lower magnification used in the photograph of the PCT0 film at 650 °C than that of the other photographs

Thus, a clear increase in grain size with temperature is observed in the PCT0 films (from ~35 nm at 450 °C to ~150 nm at 650 °C), which is related with the respective increase in crystallite size shown in the graph of Fig. 4.1.8a. But, for the PCT50 films, the increase in grain size is much smaller (from ~25 nm at 450 °C to ~55 nm at 650 °C), which is in agreement with the slight increase in the crystallite size from 450 °C to 650 °C, deduced from the graph of Fig. 4.1.8b. From the comparison between the grain size values obtained for the PCT0 and PCT50 films annealed at 650 °C (~150 and ~55 nm, respectively), it can be concluded that films microstructures are formed by smaller grains as the Ca^{2+} content in the system is higher, which is in accordance with the results of the crystallite sizes shown in Fig. 4.1.10c and the previously shown grain size measurements obtained by TEM in these PCT films (Figs. from 4.1.4 to 4.1.6).

4.1.3.6. Crystallisation of the films at nano-scale by Brillouin Spectroscopy (BS)

To obtain additional information about the crystallisation process of the PCT films, this phenomenon has been studied at the nano-scale by means of BS, which would permit us to determine those temperatures at which the first stages of the crystallisation occur. An elastic instability between the amorphous and the micro-crystalline state has been previously reported for PCT24 thin films by BS,²¹⁷ which was associated with an intermediate nano-crystalline state of the films. Therefore, this anomaly has been used in this work to determine the temperature range where the first nano-crystals appear in the films. Brillouin Spectroscopy was carried out on the PCT0 and PCT50 films (low and high Ca^{2+} content).

The variation of the sound velocity of acoustic waves travelling through these films treated at different temperatures is shown in Fig. 4.1.12. The dash lines drawn on the graphs mark a similar tendency in both types of films, although processes occur at different temperatures. A general behaviour divided in three different parts (A, B and C) can be distinguished. In part A, the sound velocity decreases until it reaches the minimum B, where after then, the sound velocity values along C become to increase. Inset i of Fig. 4.1.12 shows the BS spectrum of the PCT0 film treated at 400 °C. Here, modes corresponding to two different crystal phases are detected.

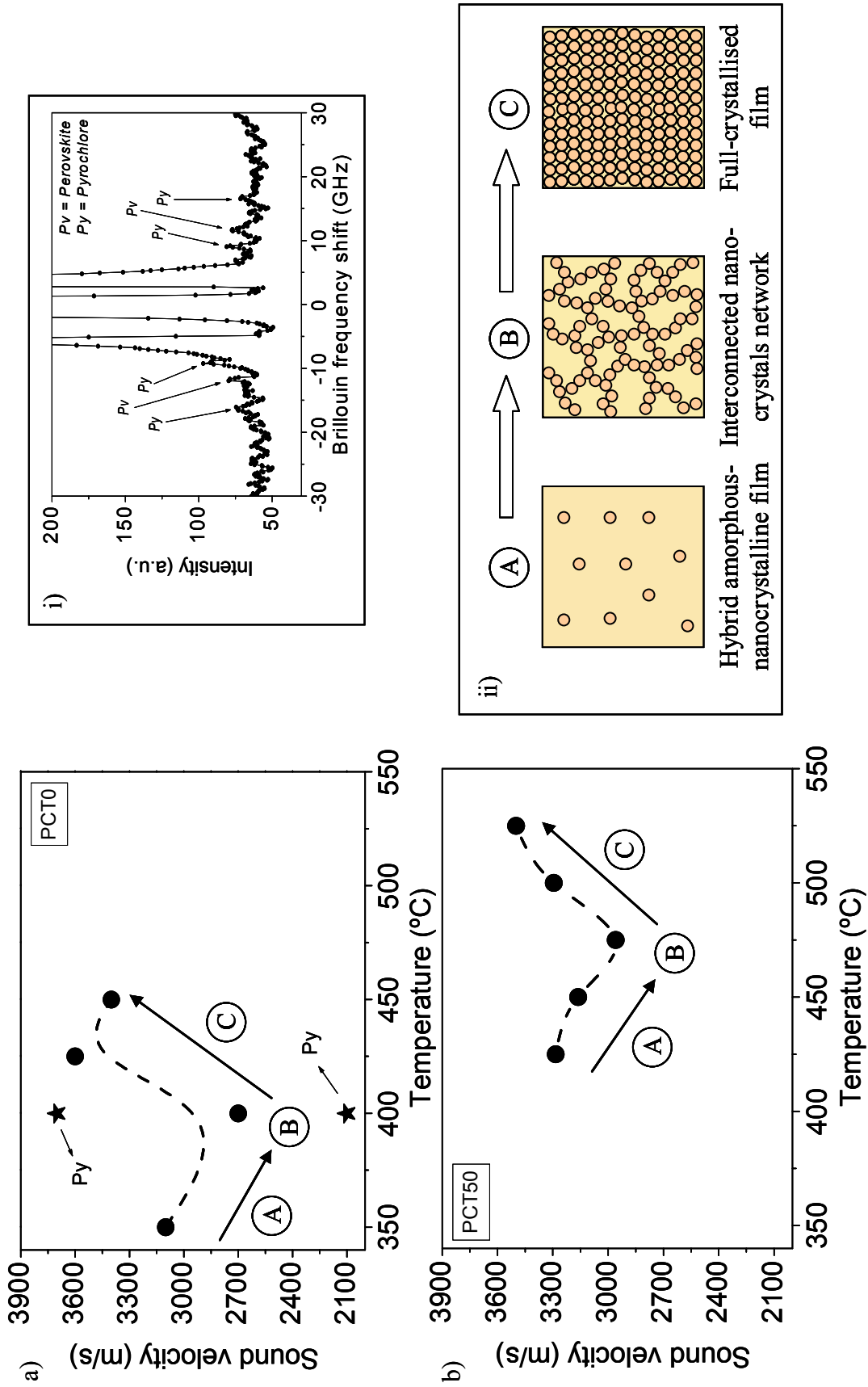


Figure 4.1.12. Variation of the sound velocity of acoustic waves travelling through the diol sol-gel derived PCT0 (a) and PCT50 (b) films, as a function of the processing temperature. Inset i shows the BS spectrum of the PCT0 film at 400 °C. Inset ii shows a schematic graph of the crystallisation process with temperature of the PCT films

The initial decrease of the sound velocity observed in the part A of the graphs is an indication of the softening of the material. This can be attributed to the formation of nano-crystals that start to nucleate inside an amorphous matrix (the as-deposited film). The elastic instability B is reached when the nano-crystals form an inter-connected network. Note that the second pyrochlore crystalline phase detected by GIXRD in the PCT0 films at 400 °C is also observed by BS. The BS spectrum of this film contains three peaks instead of only one (see inset i of this figure). This fact is due to the coexistence of two nano-crystalline phases at this point for the PCT0 films. From the position of the peaks, we infer that the two extreme peaks should correspond to the longitudinal and transverse modes of the pyrochlore nano-crystalline phase. The zone C of the graphs of Fig. 4.1.12 shows a hardening of the samples as the temperature increases. Here, the full-crystallisation of the films and the subsequent crystal growth with temperature occur. A schematic diagram of the different stages (A, B and C) of the crystallisation process with temperature of the PCT films is depicted in inset ii of Fig. 4.1.12.

Therefore, the BS results indicate that the crystallisation of the diol-based sol-gel derived PCT thin films follows a similar pathway for low and high calcium contents. Hybrid amorphous-nano-crystalline films are initially formed and progress with temperature to form, first, an inter-connected nano-crystal network and, finally, a full-crystallised film. From this BS study it is also inferred that the crystallisation of the films starts at higher temperatures as the Ca^{2+} content increases (note how the BS curves of Fig. 4.1.12, although showing a similar behaviour, are displaced towards higher temperatures for the PCT50 films), as was also observed by GIXRD and XRD.

4.1.4. REMARKS

- The crystallisation with temperature of diol-based sol-gel derived $(\text{Pb}_{1-x}\text{Ca}_x)\text{TiO}_3$ (PCT) powders and films has shown to be dependent on the Ca^{2+} content.
- During crystallisation of these powders and films, organic species are eliminated from the system at temperatures between 300-600 °C, where formation of calcium carbonate (CaCO_3) is also produced. This calcium carbonate decomposes in the powders at temperatures over those of the crystallisation temperature of the PCT system (>600 °C). However, rest of CaCO_3 or other organics compounds are not detected in the PCT films crystallised by RTP at 650 °C. The analysis of these films by XPS shows homogeneous compositional profiles without carbon rests in the bulk film.
- Neither secondary phases are detected by TEM analysis in these films, observing a decrease in grain size with the Ca^{2+} content. The crystal structure of the PCT films is tetragonal for compositions with low Ca^{2+} contents and orthorhombic for those with high Ca^{2+} contents. Furthermore, a superlattice has been detected by SAED in the PCT50 films.
- The increase of the Ca^{2+} content in the PCT system produces the movement of the crystallisation of the perovskite phase towards higher temperatures, in both powders and thin film materials. Crystallisation of the perovskite in the PCT thin films treated by RTP occurs at lower temperatures than in the PCT powders treated by conventional thermal processes.
- In the PCT films, the perovskite crystallisation is carried out by an initial nucleation of perovskite nano-crystals in an amorphous matrix. As a consequence a softening of the film is observed by Brillouin spectroscopy. This hybrid amorphous nanocrystalline film evolves towards the formation of an inter-connected nanocrystalline network into the film. After this, the full-crystallisation of the film is produced that is accompanied by a progressive hardening of the film as a result of the crystal growth.
- In the case of pure PbTiO_3 films, the first crystalline phases developed into the film have two different crystal structures: perovskite and pyrochlore. The pyrochlore-type phase disappears with the increase of temperature. This secondary phase is not detected in the films of this work when Ca^{2+} is incorporated into the PbTiO_3 composition.

- The crystal growth in the PCT films, which occurs with the increase of the processing temperature, is accompanied by a decrease in the micro-strains of the films. These phenomena are clearly observed in PCT films with low Ca^{2+} contents, whereas they seem to be inhibited in the films as the Ca^{2+} content increases. Here a slow crystal and grain growth, and a slow micro-strain reduction are observed with increasing processing temperature. Thus, the crystallisation phenomena of the PCT films seems to be hindered as the Ca^{2+} content in the system is higher.

CHAPTER IV

PART 2

SOL-GEL PROCESSING AND PROPERTIES OF THE PCT THIN FILMS

Generally speaking in the sol-gel technique, metal precursors are dissolved in organic solvents with water as hydrolysis agent and some acid or base catalyst.²⁵³ Reactions of hydrolysis and polycondensation among the reagents lead to a sol in which polymers or particles floccus in the suspension. Then, the particles link together until they form a continuous network with the solvent trapped inside, that is, a gel.

There are many parameters which can influence the sol-gel processing such as (i) the starting chemical compounds, (ii) the type of solvent, (iii) the role of catalysis or (iv) the chemical pathway followed in the synthesis. As example, the implications of using an aqueous solution-gel method, in which the organic solvent is totally replaced by water, have been described in previous *Chapter III*. Thus, the choice of starting chemicals, solvent type and solution chemistry, as well as handling conditions and annealing procedures, can determine the performance and properties of the final ceramic material. In addition, in the sol-gel methods that use metal precursors dissolved in organic solvents chemical reactions can continue after the synthesis of the sol and change the structure and properties of the solutions and gels in a phenomenon known as “aging”. In some cases, the change in precursor characteristics over time (weeks to months) may result in a degradation of the properties and hence in the applications of the functional materials prepared from these aged sols and gels (e.g. thin films).

In the present section, it has been studied how the use of different chemical reagents (calcium acetate or calcium acetylacetonate) and/or synthetic strategies (route A, B or C) can strongly affect the characteristics of the diol-based synthesised sol-gel ($\text{Pb}_{1-x}\text{Ca}_x$) TiO_3 (PCT) solutions and derived films. Furthermore, the effects of the sol aging on the physicochemical features of the PCT solutions have been also investigated. The results will allow us to understand the underlying chemistry involved in the different diol-based routes used for the synthesis of PCT solutions and the critical role that it plays on the properties of the derived films.

4.2.1. PCT PRECURSOR SOLUTIONS

Precursor solutions of calcium modified lead titanate, $(\text{Pb}_{1-x}\text{Ca}_x)\text{TiO}_3$ (PCT), were synthesised according to the different diol-based sol-gel processing routes described in the experimental section. Small and large substitutions of Pb^{2+} by Ca^{2+} were introduced in the PCT system ($x = 0.24, 0.50$). A detailed description of the different processing routes tested will be stated below. The major physicochemical features of the PCT solutions obtained will be also shown in this section.

4.2.1.1. Synthetic routes

Table 4.2.1 summarises the main characteristics of the different diol-based sol-gel synthetic routes tested for the preparation of the PCT precursor solutions of this work.

Stable PCT *sols* or *solutions* are obtained by the routes A, B and C. The introduction of the calcium precursor (calcium acetate or calcium acetylacetonate) at the same time than the other metal reagents and solvents in the routes B and C leads, after reflux, to the formation of a real Ca(II)-Pb(II)-Ti(IV) *sol*. On the other hand, a PCT *solution* is obtained when a water solution of the calcium reagent (calcium acetate) is simply added to the previous synthesised Pb(II)-Ti(IV) *sol* in the synthetic route A. Note that substitutions of Pb^{2+} by Ca^{2+} up to 50 at% can be introduced in the PCT system through the routes A and B, whereas only PCT compositions with Ca^{2+} contents below 30 at% can be prepared from the synthetic route C. In the case of the routes named D and E, the low solubility of the calcium reagent (calcium acetate or calcium acetylacetonate) in water or diol makes not possible the preparation of PCT precursor solutions.

Here, solutions, gels and films derived from the synthetic routes A and C, and with a nominal composition of $(\text{Pb}_{0.76}\text{Ca}_{0.24})\text{TiO}_3$ (PCT24) will be denoted hereinafter as PCT24-A and PCT24-C, respectively. Solutions, gels and films derived from the synthetic routes A and B, and with a nominal composition of $(\text{Pb}_{0.5}\text{Ca}_{0.5})\text{TiO}_3$ (PCT50) will be named PCT50-A and PCT50-B, respectively. The main physicochemical features of the PCT *sols* and *solutions* thus obtained are shown in Table 4.2.2.

Table 4.2.1.1. Physicochemical characteristics of the different diol-based sol-gel synthetic routes tested for the preparation of PCT solutions

Synthetic route	Processing procedure	Type of precursor	Stability of the precursor as a function of the Ca ²⁺ content
A	Synthesis of a Pb(II)-Ti(IV) sol to which a <i>calcium acetate</i> water solution is added	Pb(II)-Ti(IV) sol + calcium acetate water solution	Stable <i>solution</i> for all Ca ²⁺ contents (from PCT24 to PCT50)
B	Synthesis of a Ca(II)-Pb(II)-Ti(IV) sol using <i>calcium acetate</i> as starting reagent	Ca(II)-Pb(II)-Ti(IV) sol	Stable <i>sol</i> for all Ca ²⁺ contents (from PCT24 to PCT50)
C	Synthesis of a Ca(II)-Pb(II)-Ti(IV) sol using <i>calcium acetylacetonate</i> as starting reagent	Ca(II)-Pb(II)-Ti(IV) sol	Stable <i>sol</i> for Ca ²⁺ contents ≤30 at% (PCT24)
D	Synthesis of a Pb(II)-Ti(IV) sol to which a <i>calcium acetylacetonate</i> water solution is added	Not applicable	(Low solubility of calcium acetylacetonate in water)
E	Synthesis of a Pb(II)-Ti(IV) sol to which a <i>calcium acetate</i> or <i>calcium acetylacetonate</i> diol solution is added	Not applicable	(Low solubility of calcium acetate and/or calcium acetylacetonate in diol)

Table 4.2.2. Physicochemical characteristics of the PCT precursor solutions prepared from the diol-based sol-gel synthetic routes A, B and C

Nominal composition	Synthetic route	Type of precursor	Reagents and solvents	Incorporation of Ca ²⁺	Molar ratios	Concentration, density, viscosity
(Pb _{0.76} Ca _{0.24})TiO ₃	A	Solution (PCT24-A)	Pb(OCOCH ₃) ₂ ·3H ₂ O Ti(OC ₃ H ₇) ₂ (CH ₃ COCHCOCH ₃) ₂ OH(CH ₂) ₃ OH	Water solution of Ca(OCOCH ₃) ₂ ·xH ₂ O	Ti(IV):diol 1:5 H ₂ O:diol 7:1	~0.80 M, ~1.30 g/mL, ~13 cP
	C	Sol (PCT24-C)	H ₂ O	Diol-water solution of Ca(CH ₃ COCHCOCH ₃) ₂ ·xH ₂ O	Ti(IV):diol 1:5 H ₂ O:diol 7:1	~0.80 M, ~1.30 g/mL, ~12 cP
(Pb _{0.50} Ca _{0.50})TiO ₃	A	Solution (PCT50-A)	Pb(OCOCH ₃) ₂ ·3H ₂ O Ti(OC ₃ H ₇) ₂ (CH ₃ COCHCOCH ₃) ₂ OH(CH ₂) ₃ OH	Water solution of Ca(OCOCH ₃) ₂ ·xH ₂ O	Ti(IV):diol 1:5 H ₂ O:diol 7:1	~0.90 M, ~1.30 g/mL, ~40 cP
	B	Sol (PCT50-B)	H ₂ O	Diol-water solution of Ca(OCOCH ₃) ₂ ·xH ₂ O	Ti(IV):diol 1:5 H ₂ O:diol 7:1	~0.90 M, ~1.30 g/mL, ~14 cP

4.2.1.2. Precursor solutions studied by Infrared spectroscopy (IR) analysis

The Infrared spectroscopy (IR) technique was used to study the nature of the PCT sols and solutions (both indicated as “solutions” in this chapter) synthesised by the different routes described above and to determine the reaction mechanisms that take place during their synthesis. According to Table 4.2.2, the study is presented here for the PCT24 solutions obtained by the synthetic routes A and C, and for the PCT50 solutions synthesised through the routes A and B.

Figure 4.2.1 shows the IR spectra of the distilled liquids (Fig. 4.2.1a) and of the solutions (Fig. 4.2.1b) obtained in the synthesis of the PCT24-A and PCT24-C precursor solutions. On the other hand, Figure 4.2.2 presents the IR spectra of the distilled liquids (Fig. 4.2.2a) and of the solutions (Fig. 4.2.2b) obtained in the synthesis of the PCT50-A and PCT50-B precursor solutions. In the case of the route A, the distilled liquid corresponds to that collected from the distillation after reflux of a Pb(II)-Ti(IV) sol, whereas in the routes B and C the distilled liquid is that collected from the distillation after reflux of a Ca(II)-Pb(II)-Ti(IV) sol (see Tables 4.2.1 and 4.2.2).

The IR spectra of the distilled liquids (Figs. 4.2.1a and 4.2.2a) indicate that, for both compositions, byproducts of the reactions are water (H_2O), 2-propanol ($(\text{CH}_3)_2\text{CHOH}$), acetic acid (CH_3COOH) and isopropylacetate^{185,254} ($\text{CH}_3\text{COOCH}(\text{CH}_3)_2$), independently of the synthetic route followed. Water is observed through the broad band at $\sim 3400\text{ cm}^{-1}$ ascribed to the $\nu(\text{O-H})$ stretching vibrations and the $\delta(\text{O-H-O})$ bending mode detected at $\sim 1622\text{ cm}^{-1}$. The mode $\nu(\text{O-H})$ at $\sim 3400\text{ cm}^{-1}$ is also characteristic of alcohols ($(\text{CH}_3)_2\text{CHOH}$). The presence of 2-propanol is confirmed by the $\nu(\text{C-H})$ and $\nu(\text{C-O(H)})$ vibrations observed in the region between ~ 2975 and $\sim 2926\text{ cm}^{-1}$, and $\sim 945\text{ cm}^{-1}$, respectively, and the $\delta(-\text{CH}_3)$ bending mode at 1375 cm^{-1} . The band at $\sim 1710\text{ cm}^{-1}$ can be assigned to the $\nu(\text{C=O})$ stretching vibrations of acetic acid. Furthermore, during the course of the synthesis reactions, isopropylacetate can be formed between the acetate ligands of the lead (routes A, B and C) and/or calcium (routes A and B) reagents, and the isopropyl ligand of the titanium reagent.²⁵⁵ The $\nu(\text{C=O})$ stretching vibration that appears between ~ 1740 and $\sim 1730\text{ cm}^{-1}$ can be ascribed to this ester (see insets of Figs. 4.2.1a and 4.2.1b).

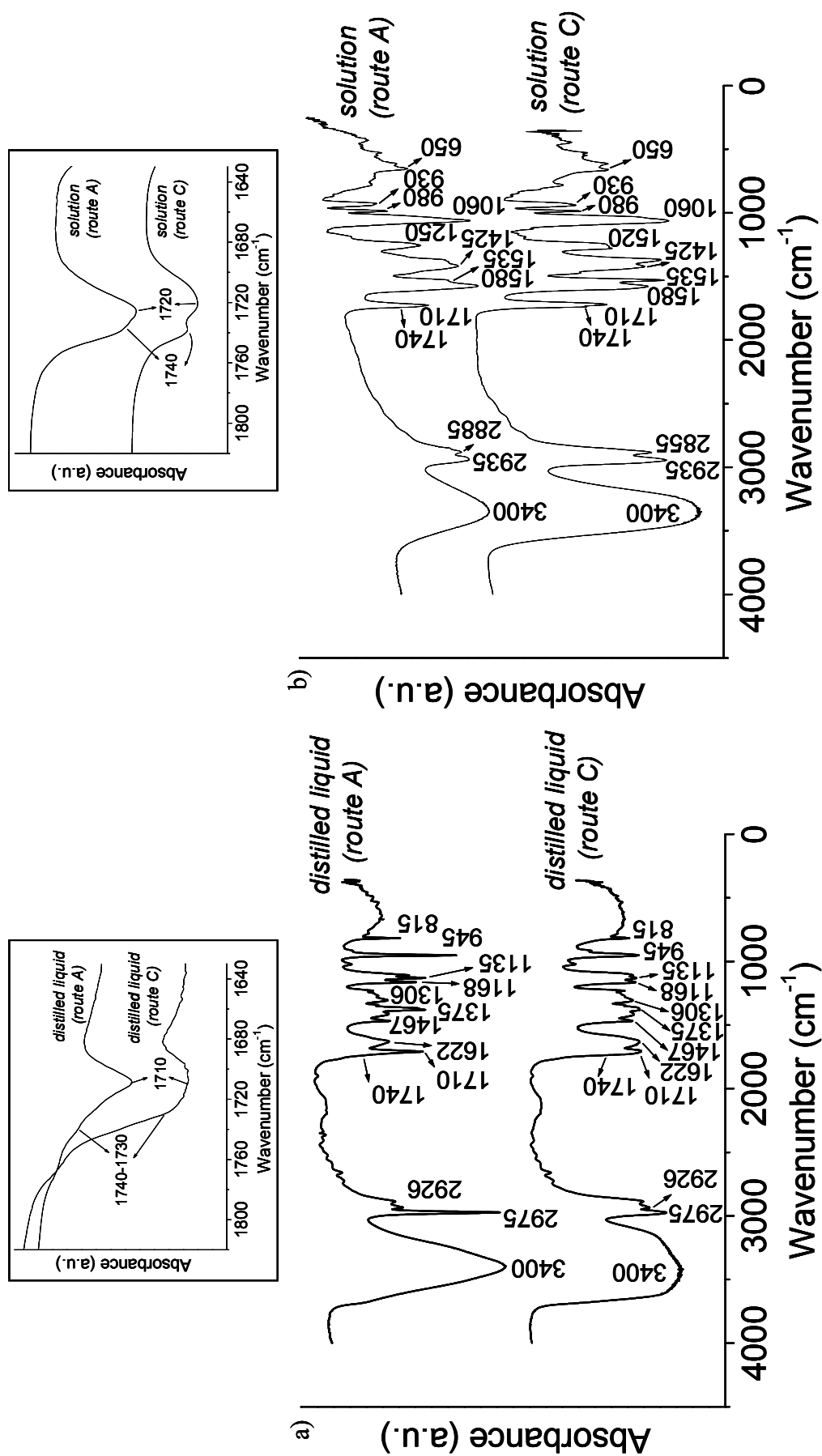


Figure 4.2.1. IR spectra of the distilled liquids (a) and of the precursor solutions (b) corresponding to the diol sol-gel synthesis of the PCT24 solution following the routes A and C. Insets correspond to the wavenumber interval where the $\nu(\text{C}=\text{O})$ stretching vibrations of acetic acid (1720-1710 cm^{-1}) and isopropylacetate ester (1740-1730 cm^{-1}) are observed

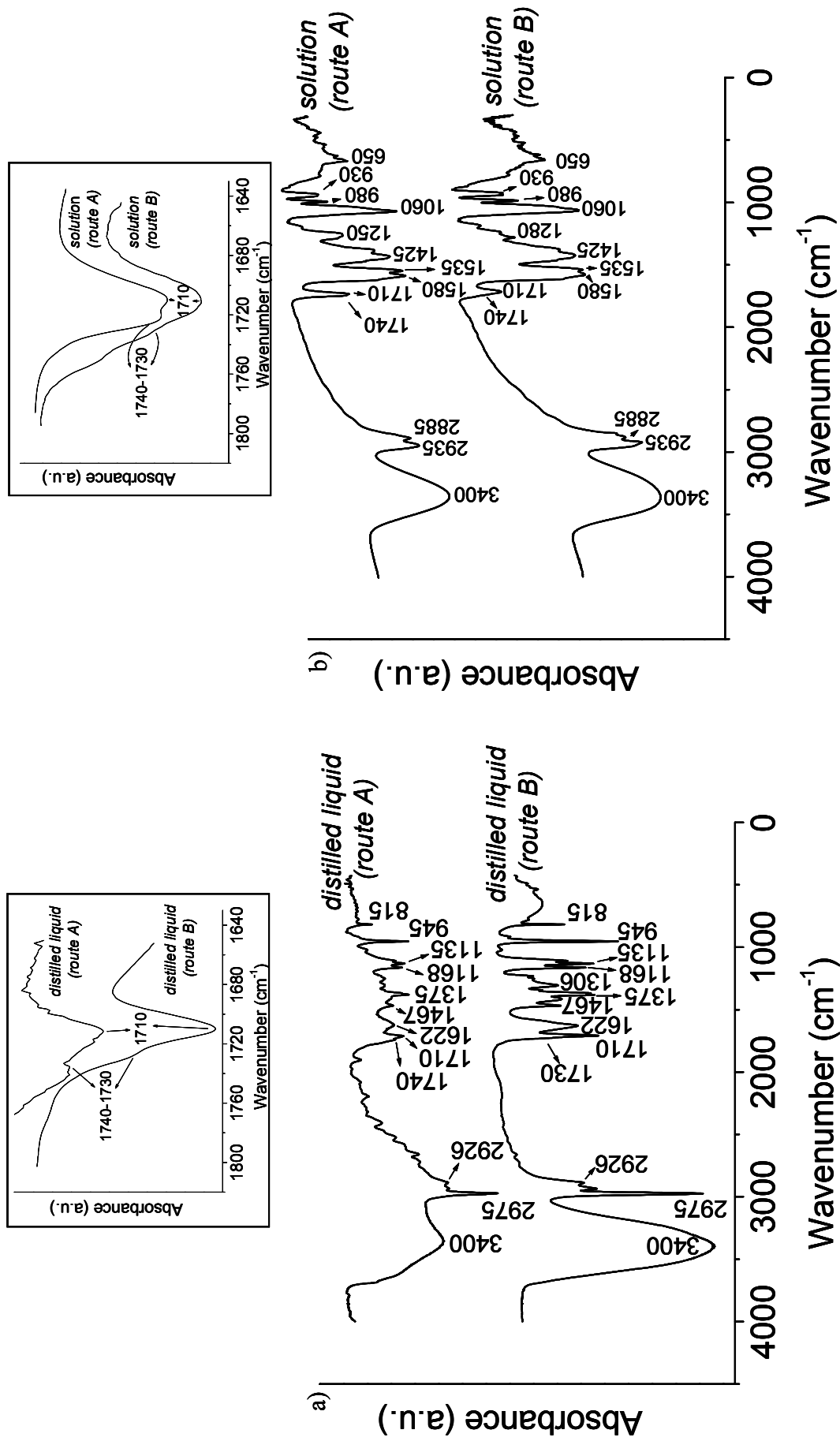


Figure 4.2.2. IR spectra of the distilled liquids (a) and of the precursor solutions (b) corresponding to the diol sol-gel synthesis of the PCT50 solution following the routes A and B. Insets correspond to the wavenumber interval where the $\nu(\text{C}=\text{O})$ stretching vibrations of acetic acid ($1720\text{--}1710\text{ cm}^{-1}$) and isopropylacetate ester ($1740\text{--}1730\text{ cm}^{-1}$) are observed

The IR spectra of the synthesised PCT24 and PCT50 precursor solutions (Figs. 4.2.1b and 4.2.2b) show the absorbance of the acetylacetonate groups, as shown by the combined bands $\nu(\text{C}=\text{C}) + \nu(\text{C}=\text{O})$ at $\sim 1580 \text{ cm}^{-1}$ and $\nu(\text{C}=\text{O}) + \nu(\text{C}=\text{C})$ at $\sim 1535 \text{ cm}^{-1}$,²⁵⁶ and the mode $\delta(-\text{CH}_3) + \nu(\text{C}-\text{C})$ at $\sim 1425 \text{ cm}^{-1}$. Note that these vibrations do not appear in the distilled liquids, which could indicate that titanium remains bonded to the acetylacetonate ligands in the solutions (and also calcium would remain bonded to these ligands in the PCT24-C solution). However, if the rupture of these bonds would occur, giving rise to acetylacetone, this last compound could not be distilled from the solutions in any case, since its boiling point ($\sim 140 \text{ }^\circ\text{C}$) is higher than the temperatures here used for the distillation of byproducts during the synthesis reactions. The $\nu(\text{C}-\text{H})$ vibrations at $\sim 2935 \text{ cm}^{-1}$ and $\sim 2885 \text{ cm}^{-1}$, and the $\nu(\text{C}-\text{O}(\text{H}))$ ones at $\sim 930 \text{ cm}^{-1}$ corresponding to the isopropyl ligand, are here lower than those of 2-propanol detected in the IR spectra of the distilled liquids. This indicates the rupture of the bonds between titanium and isopropyl groups of the $\text{Ti}(\text{OC}_3\text{H}_7)_2(\text{CH}_3\text{COCHCOCH}_3)_2$ reagent, and elimination of 2-propanol in the distilled liquid. The appearance in the IR spectra of the precursor solutions of the $\nu(\text{C}=\text{O})$ stretching vibrations at $\sim 1740 \text{ cm}^{-1}$ (see insets of Figs. 4.2.1b and 4.2.2b) and at $1720\text{-}1710 \text{ cm}^{-1}$ corresponding to the isopropylacetate ester and acetic acid, respectively, confirms again the rupture of some of the bonds between lead or calcium and the acetate groups of the $\text{Pb}(\text{OCOCH}_3)_2 \cdot 3\text{H}_2\text{O}$ (routes A, B and C) and $\text{Ca}(\text{OCOCH}_3)_2 \cdot x\text{H}_2\text{O}$ (routes A and B), and the formation of the isopropylacetate ester. Here, these bands show that neither free acetic acid nor isopropylacetate are totally distilled from the solutions. This could lead to the presence of residual acetate ligands in the gel structure.²⁵⁷ The no total elimination of the esters formed during the sol-gel synthesis of PZT solutions has been proposed as one of the causes that can deteriorate the ferroelectric properties of the derived films.²⁵⁸ Modes corresponding to the 1,3-propanediol and water solvents ($\nu(\text{O}-\text{H})$ at $\sim 3400 \text{ cm}^{-1}$ of both, $\nu(\text{C}-\text{O}(\text{H}))$ at $\sim 1060 \text{ cm}^{-1}$ of 1,3-propanediol) are also observed in the spectra of the synthesised solutions (Figs. 4.2.1b and 4.2.2b). Here, the low frequency absorption between 500 and 750 cm^{-1} , not observed in the distilled liquids spectra, is comprised of various contributions indicating the presence of multiple M-O (metal–oxygen) environments.

Infrared spectroscopy has been used to monitor and characterise the PCT solutions used in the subsequent preparation of gels, powders and thin films of this chapter. From the IR results obtained, it is deduced that water, 2-propanol, acetic acid and isopropylacetate are the main byproducts of reaction in the three synthetic routes (A, B and C). From this study, however, it is not

possible to know if the acetylacetonate groups remain bonded to the metal precursor or if acetylacetone is formed.

Therefore, it is expected that the isopropyl groups of the titanium reagent and the acetate groups of the lead acetate and/or calcium acetate reagents could be partially exchanged by diol groups coming from the solvent,^{95,183} thus giving us an approximation to the chemical reactions that occur during the synthesis of the solutions. However, significant properties such as the extent of oligomerization of the reactions, the homogeneity of the sols and their respective particle size cannot be inferred from the infrared spectroscopy analysis here shown. In order to obtain reliable information about these parameters, Dynamic Light Scattering measurements were carried out on the PCT solutions.

4.2.1.3. Particle size distributions by Dynamic Light Scattering (DLS) and viscosity measurements of the solutions

Figure 4.2.3 shows the particle size distributions of the PCT solutions obtained by DLS at room temperature. The results of the PCT24-A and PCT24-C solutions are depicted in Fig. 4.2.3a, whereas those obtained for the PCT50-A and PCT50-B solutions are shown in Fig. 4.2.3b.

Considering the PCT solutions processed by the synthetic route A (PCT24-A and PCT50-A), the PCT24-A solution is formed by two differentiated groups of particles with average sizes of ~4 and ~15 nm (Fig. 4.2.3a). For the PCT50-A solution, a broad and asymmetrical distribution of particle size is obtained that can be separated in two Gaussian curves (Fig. 4.2.3b). The peaks maxima of these curves correspond to average particle sizes of ~15 and ~50 nm (see inset of this figure). On the contrary, an almost symmetrical distribution with a mean particle size of ~3 and ~15 nm is measured for the respective PCT24-C and PCT50-B solutions (Figs. 4.2.3a and b, respectively).

In practical terms, solutions synthesised from the route A are mainly constituted by two types of particles, with well-differentiated hydrodynamic radii, whereas single and uniform particles form the more homogeneous network of the respective PCT24-C and PCT50-B sols. This can be related with the fact that solutions derived from the route A consist in a mixture of a Pb(II)-Ti(IV) sol and a water solution of calcium acetate, whereas the routes B and C lead to Ca(II)-Pb(II)-Ti(IV) sols that should be more homogeneous than the former mixture (see Table 4.2.1).

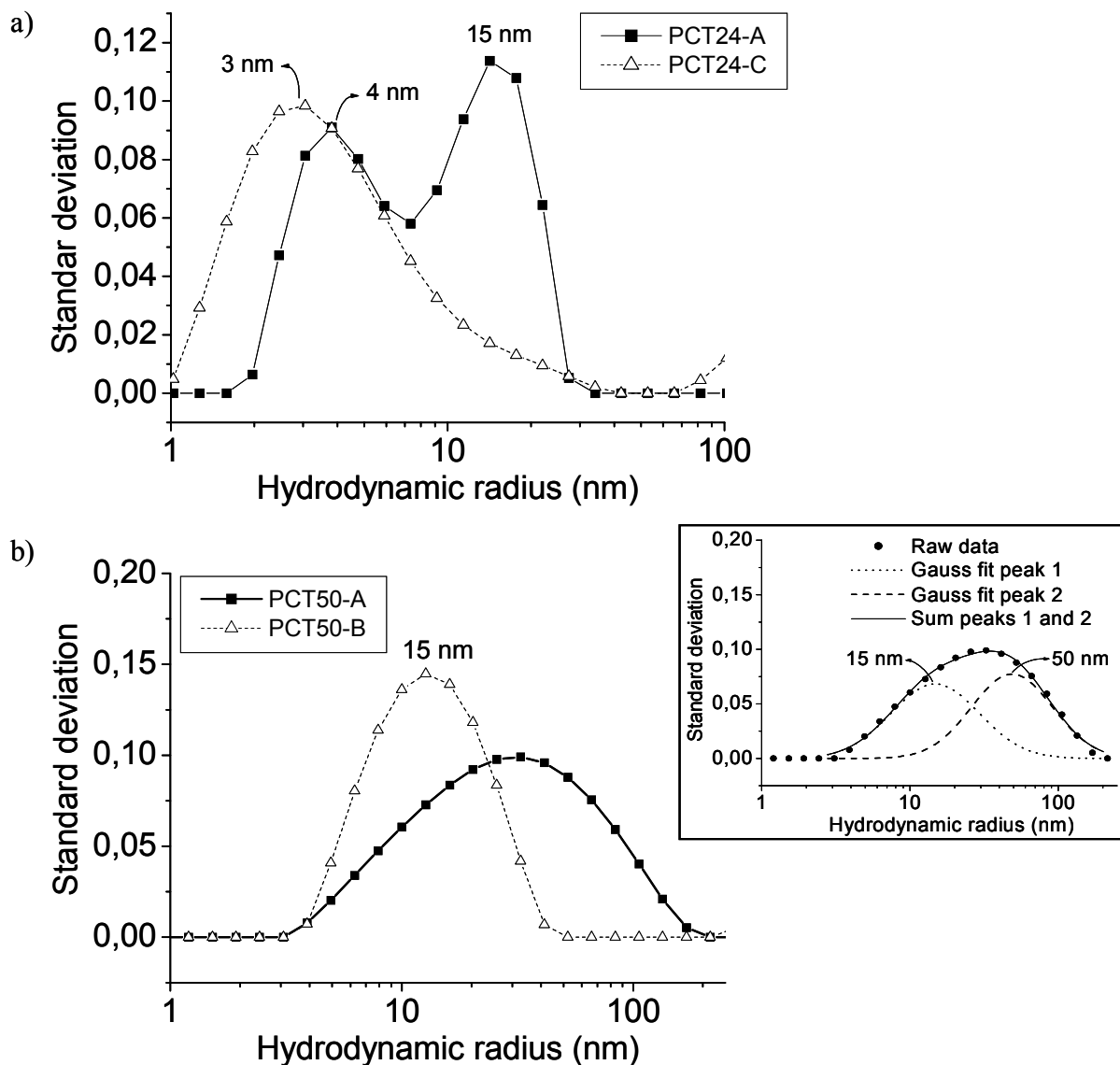


Figure 4.2.3. Particle size distributions in a lognormal representation of the diol sol-gel PCT24-A and PCT24-C solutions (a) and of the diol sol-gel PCT50-A and PCT50-B solutions (b) determined by DLS. Inset shows the two Gaussian curves separated from the asymmetrical particle size distribution measured by DLS in the PCT50-A solution

Comparing the particle sizes, it seems that PCT solutions with high Ca^{2+} contents (PCT50) are constituted by larger particles than solutions with lower Ca^{2+} concentration (PCT24). In order to elucidate if the heterogeneity in particle size of the solutions derived from the route A is produced by particle aggregation or not, rheological measurements were carried on all the solutions to study their flow behaviour.

Figure 4.2.4 shows the viscosity values of the PCT solutions as a function of the shear rate, measured at room temperature.

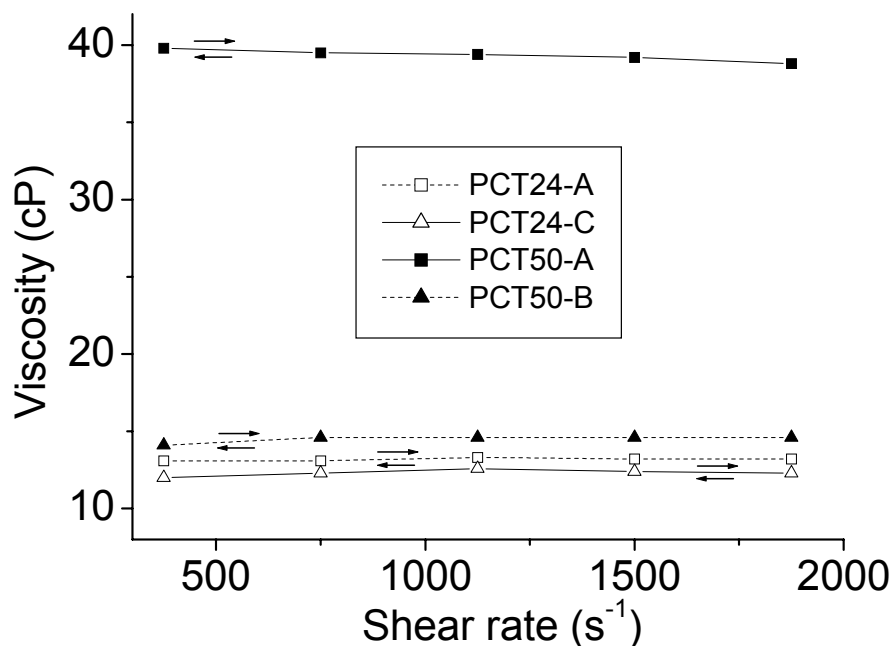


Figure 4.2.4. Viscosity of the diol sol-gel PCT24-A, PCT24-C, PCT50-A and PCT50-B solutions, as a function of shear rate

The no dependence of the viscosity values of the solutions with the shear rate (e.g. shear thinning, shear thickening) observed in the graphs indicates the Newtonian nature of these fluids.¹⁹⁰ Therefore, it can be concluded that the heterogeneity in particle size of the PCT24-A and PCT50-A solutions is not due to particle aggregation, since this would produce a decrease in viscosity as the shear rate increases.²⁵⁹ Thus, molecular level heterogeneity, rather than homogeneity, is the most significant structural feature of the route A-derived PCT precursor solutions, showing by DLS two particle size distributions which differ in nature (not particle aggregation) and particle size (hydrodynamic radii). The large difference in viscosity of the PCT50-A solution (~40 cP) respect to the PCT24-A, PCT24-C and PCT50-B solutions (~13, ~12 and ~14 cP, respectively) can be related with the presence of particles of much bigger size (~50 nm) in the former than in the latter ones (<15 nm), as measured by DLS.

From the diverse studies carried out here on the PCT solutions synthesised by the different diol-based sol-gel routes here shown, differences are found if the calcium reagent is simply mixed with the synthesised Pb(II)-Ti(IV) sol (route A) or if it is reacted with the lead (II) and titanium (IV) compounds to form a Ca(II)-Pb(II)-Ti(IV) sol (routes B and C). In the latter, the three cations participate in the sol network giving rise to a more homogeneous precursor solution than in the first case, where a mixture is obtained and not a real sol. Here, the calcium acetate compound would occupy random positions within the Pb(II)-Ti(IV) sol network. This may cause a modification of the precursor structure²⁶⁰ which would preclude the formation of a uniform network of particles. A proposed sol structure for this case is presented in Figure 4.2.5, based on the studies carried out by Hennings et al.²⁶¹

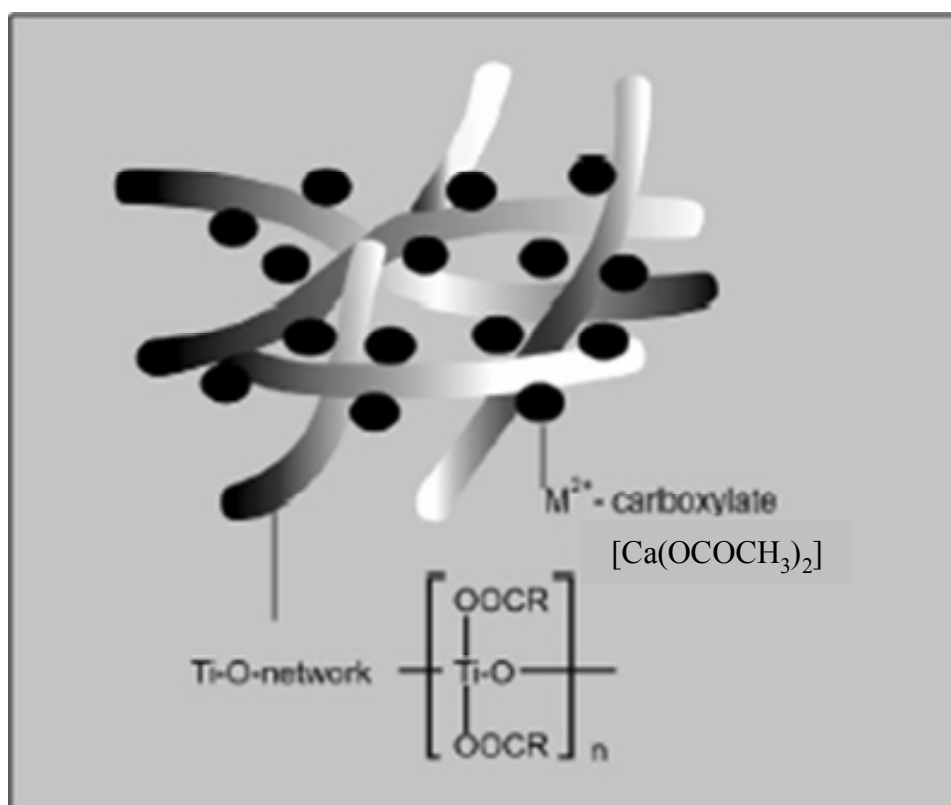


Figure 4.2.5. A proposed Pb(II)-Ti(IV) sol network with occluded calcium acetate molecules for the diol sol-gel PCT solutions derived from the synthetic route A (proposed for barium or strontium titanate precursors²⁶¹)

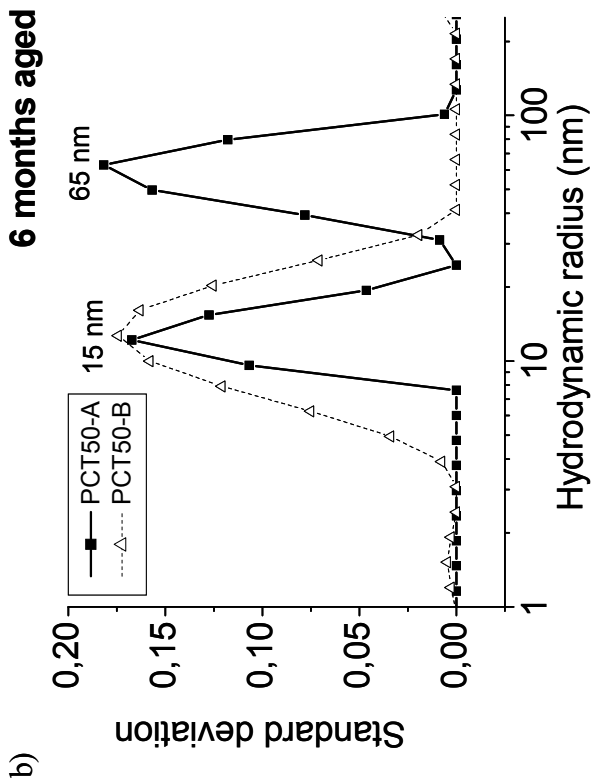
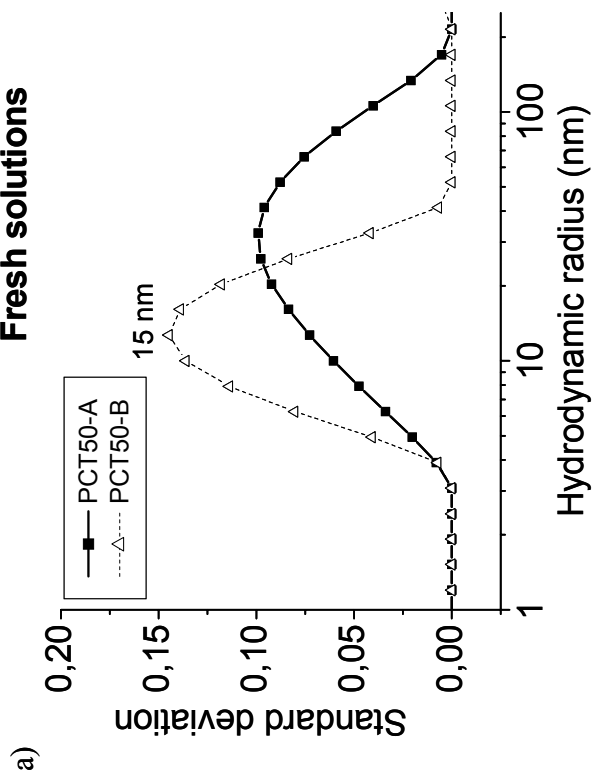
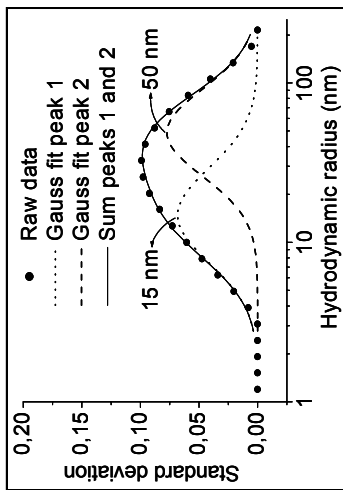
The no incorporation of A-site precursors into the oligomeric structure of the sol has also been observed in hybrid sol-gel processing of solutions of ABO_3 perovskite compositions, such as $BaTiO_3$ (BT)²⁶¹ and $Pb(Zr,Ti)O_3$ (PZT)²⁶². Thus, Sengupta et al.²⁶² reported on the non-contribution of the A-site cation to the polymeric M-O-M framework of hybrid sol-gel derived PZT solutions, as deduced by EXAFS (Extended X-Ray Absorption Fine Structure) analysis. Instead, the A-site species are proposed to be adsorbed or occluded on the surface of the B-site oligomers,²⁶¹ and hence not intimately involved in the formation of the gel network.²⁵⁷

4.2.1.4. Aging of the solutions with time

The phenomenon of sol aging with time was studied on the PCT50-A and PCT50-B solutions. According to previous results, the latter consists in a real sol, whereas the former is constituted by a mixture of a sol and a calcium acetate water solution (see Table 4.2.1). Both solutions were prepared at the same time and with the same physicochemical features (~0.9 molar concentration, 1.30 g/mL density and pH ~7, see Table 4.2.2). Once synthesised, the solutions were stored in closed beakers at room temperature and thus, subjected to the regular fluctuations of temperature and humidity during their aging in the laboratory.

Particle size distributions obtained by DLS in the solutions and their evolution with the aging time are shown in Figure 4.2.6. The results for the PCT50-A and PCT50-B solutions just synthesised and at 6, 14 and 20 months after their synthesis are depicted in this figure.

As it was stated before, the broad and asymmetrical distribution of particle size that initially presents the PCT50-A solution (Fig. 4.2.6a) can be separated using two Gaussian curves (see inset) into size distributions with peaks maxima at ~15 and ~50 nm. After six months of aging, two particle size distributions with average sizes of ~15 and ~65 nm are clearly observed in Fig. 4.2.6b. After 8 months of aging, this solution precipitated. The DLS analysis of the remanent liquid after 14 months of aging continues showing two particle distributions, but with average sizes of ~15 and ~120 nm. No more measurements were carried out at further aging times (i.e. 20 months of Fig. 4.2.6d) in this solution due to its degradation. Probably, the growth of the larger particles (from ~50 nm in the fresh solution to ~120 nm in the solution aged 14 months) gives rise to the formation of precipitate.



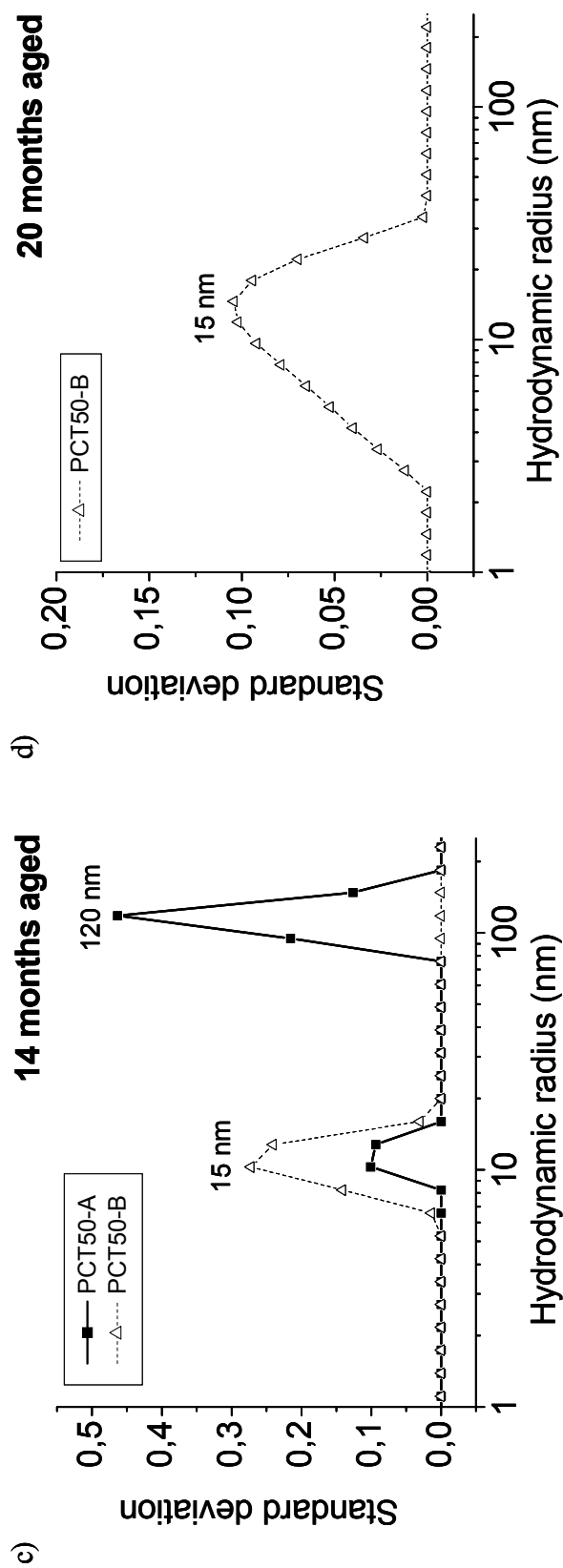


Figure 4.2.6. Lognormal representation of the particle size distributions of the diol sol-gel PCT50-A and PCT50-B solutions determined by DLS on the fresh solutions (a) and after 6 (b), 14 (c) and 20 (d) months of aging

On the contrary, the particle size distribution measured by DLS for the PCT50-B solution remains almost constant along the time, as it can be observed in Fig. 4.2.6a to d. A narrow and symmetrical distribution with a mean particle size of ~ 15 nm is measured initially and after 6 and 14 months of aging. The solution aged for 20 months has the same average particle size, although the distribution shows a slight asymmetry indicating a slight increase in the heterogeneity of this sol with long aging times.

Figure 4.2.7 shows the viscosity values of the PCT50-A and PCT50-B solutions measured at different aging times. The thickness of a single layer derived from these solutions after crystallisation by RTP at 650°C is also shown.

As the sol is formed by particles of bigger size, their resistance to flow is higher and hence the viscosity values measured must be higher too. For this reason, the PCT50-A solution has larger values of viscosity than the PCT50-B solution at any time of aging. The presence of particles with sizes of ~ 65 nm in the PCT50-A solution after 6 months of aging (Fig 4.2.16b) produces an increase in the viscosity value up to ~ 50 mPa's, before a clear precipitate can be observed in this solution. No variation of the particle size of the PCT50-B solution takes place along the aging time, which explains the maintenance of the viscosity (near 14 mPa's) of this sol with the time. Regarding the thickness values of the derived films, the more viscous the solution is, the thicker the film will be. Thus, crystalline films prepared from the PCT50-A solution have a thickness value that clearly increases (from ~ 705 to ~ 1200 nm) after 6 months of aging. However, the thickness of the crystalline PCT50 films derived from solution B remains almost constant (average thickness of ~ 500 nm) after 20 months of solution aging.

Some authors propose a continual esterification mechanism among the different compounds present in the solution as a major aspect of hybrid sol-gel aging.^{104,260} The formation of these esters yields larger precursor species resulting in thicker films. Although the same effect is observed here for the PCT50-A solution aging (i.e. thicker films are obtained as solution ages), it can be not confirmed whether the key mechanism for this effect is related to esterification or not. The presence of secondary esters (i.e. isopropylacetate) in the diol-based sol-gel solutions of PCT was detected by IR analysis (see section 4.2.1.1) even at the initial time of synthesis (fresh solutions). Despite this fact, a single distribution of particles was observed for the PCT50-B fresh solution. Thus, the presence of a second particle size distribution of bigger size in the PCT50-A solution must be ascribed to the heterogeneous mixture of components that constitute this solution (a Pb(II)-Ti(IV) sol and a calcium acetate solution) and not to the presence of esters.

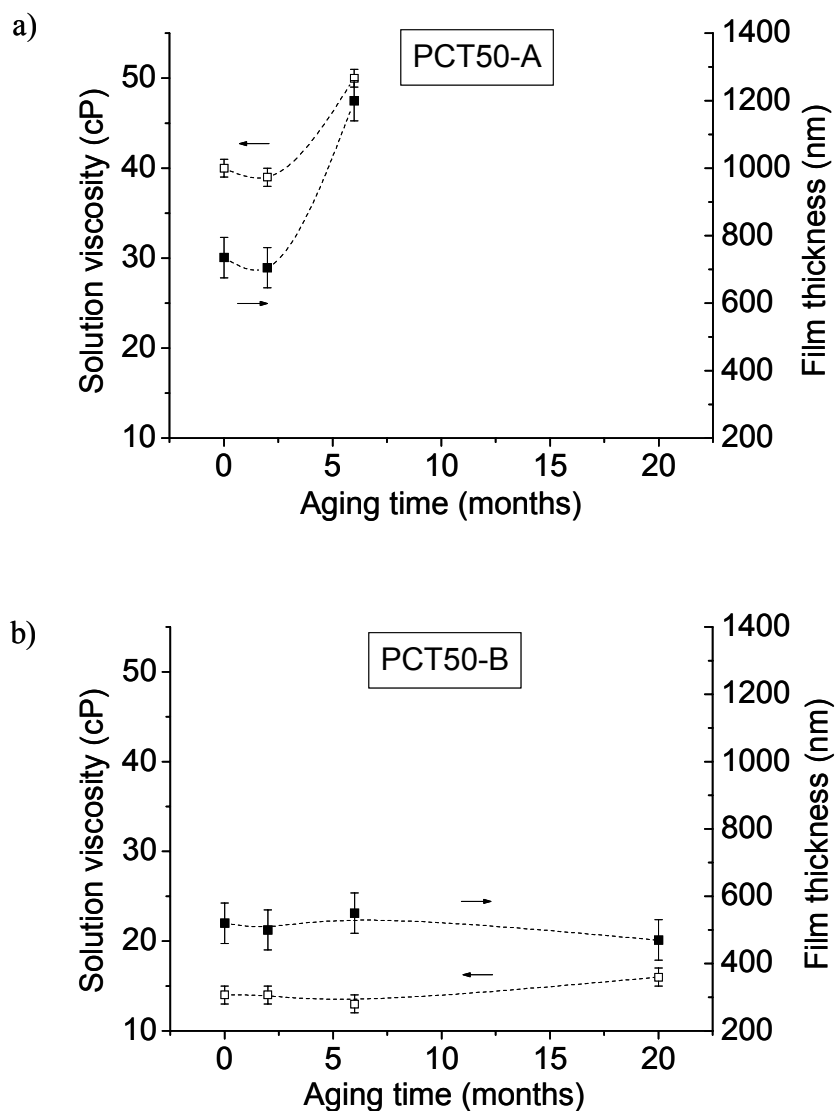


Figure 4.2.7. Variation of the viscosity and of the thickness of the derived crystallised film with the aging time of the diol sol-gel PCT50-A (a) and PCT50-B (b) solutions

From the above DLS results, it can be inferred how the growth of these bigger particles with the time is the main responsible of the aging phenomenon of the PCT solutions processed through the synthetic route A, leading thereby to films with higher values of thickness. Summarising, the heterogeneity of the PCT-A solutions increases with time resulting in the formation of precipitate with long aging times. However, the PCT-B sols remain stable and with a high degree of homogeneity for long times.

4.2.2. PCT GELS

Aliquots of the PCT precursor solutions were dried in a furnace (100 °C/24 h) and the thermal decomposition of the derived gel powders was studied by means of Thermogravimetric and Differential Thermal Analysis (TGA-DTA).

4.2.2.1. Thermal evolution of the gels by Differential Thermal and Thermogravimetric Analysis (DTA-TGA)

Figure 4.2.8 shows the DTA-TGA curves of the PCT24-A and PCT24-C gels, whereas DTA-TGA data of the PCT50-A and PCT50-B gels are shown in Figure 4.2.9.

Three different thermal intervals can be distinguished in the decomposition process of the PCT gels. Below 200 °C, the evaporation of water and alcohol (solvents) still entrapped within the gel network takes place, which is ascribed to the weak endothermic peak of the DTA curves below 80 °C and the small weight loss associated in the TGA data.

The largest weight loss measured in the decomposition of the gels is produced in the temperature range between 200 and 500 °C. Here, the elimination of organic compounds, mainly through various exothermic processes, occurs in all the chemical systems. Thus, it can be appreciated that the pyrolysis of organic species is carried out through a two-step process in the gels derived from the solutions processed by the synthetic route A (PCT24-A and PCT50-A). Two clearly differentiated exothermic peaks are recorded in DTA curves of these gels, at ~300 and ~487 °C for the PCT24-A gel (Fig. 4.2.8a) and at ~290 and ~375 °C for the PCT50-A gel (Fig. 4.2.9a). On the other hand, the gels derived from the solutions synthesised through the routes B and C (PCT50-B and PCT24-C) seem to have a simpler decomposition path in this temperature interval.

Elimination of organics in the PCT24-C gel is ascribed to the exothermic peak centered at ~320 °C in the DTA curve of Fig. 4.2.8b. The broadness of this peak, with a shoulder at ~346 °C, indicates that various processes occur at this interval, as in the PCT24-A and PCT50-A gels, but with the difference that here these processes are focused around this certain temperature with an associated single weight loss of ~23.6 %. A small exothermic peak is also observed in this system at ~490 °C that occurs without any weight loss. This can indicate that this exothermic is due to crystallisation. In the case of the PCT50-B gel, a sharp and single exothermic peak at ~340 °C is recorded, in which an small shoulder at ~300 °C can be distinguished (Fig. 4.1.9b).

Over 500 °C, small weight losses are observed in the TGA curves of the PCT24-A, PCT50-A and PCT50-B gels with associated endothermic peaks at ~650 °C, attributed to the elimination of organic residuals that are stable up to high temperatures. Here, the decomposition of calcium carbonate (CaCO_3), formed during the pyrolysis of the calcium acetate reagent occurs.²³¹ Weight losses of ~6.2 and ~4.5 wt% are measured for the PCT50-A and PCT50-B gels (Fig. 4.2.9), respectively, against the ~2.6 wt% of the PCT24-A gel (Fig. 4.2.8a). The larger weight losses observed in the former gels are attributed to the higher Ca^{2+} concentration of the PCT50 composition respect to the PCT24 one.

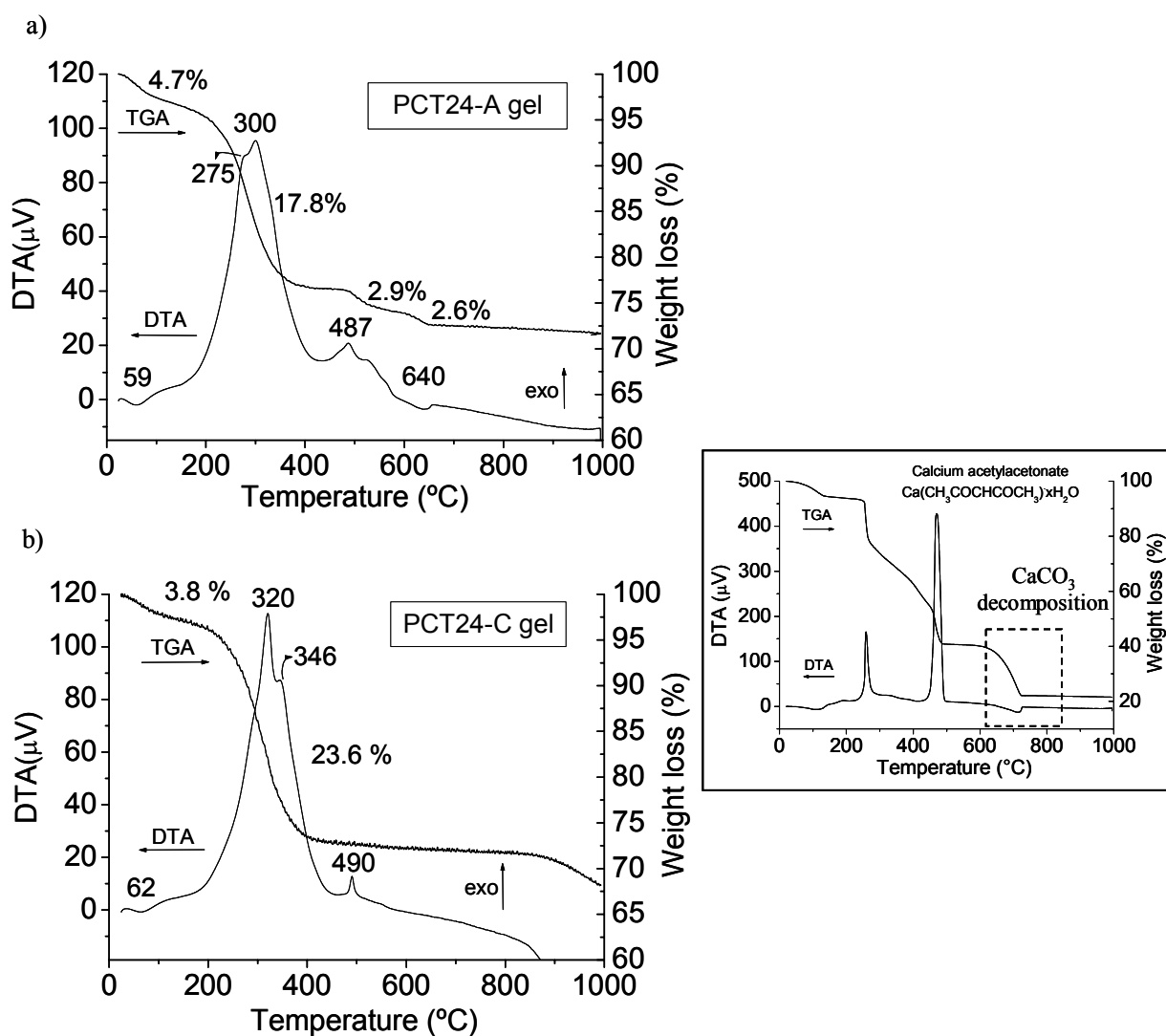


Figure 4.2.8. DTA-TGA of the diol sol-gel derived PCT24-A (a) and PCT24-C (b) gels. Inset shows the DTA-TGA curves of the calcium acetylacetonate chemical reagent

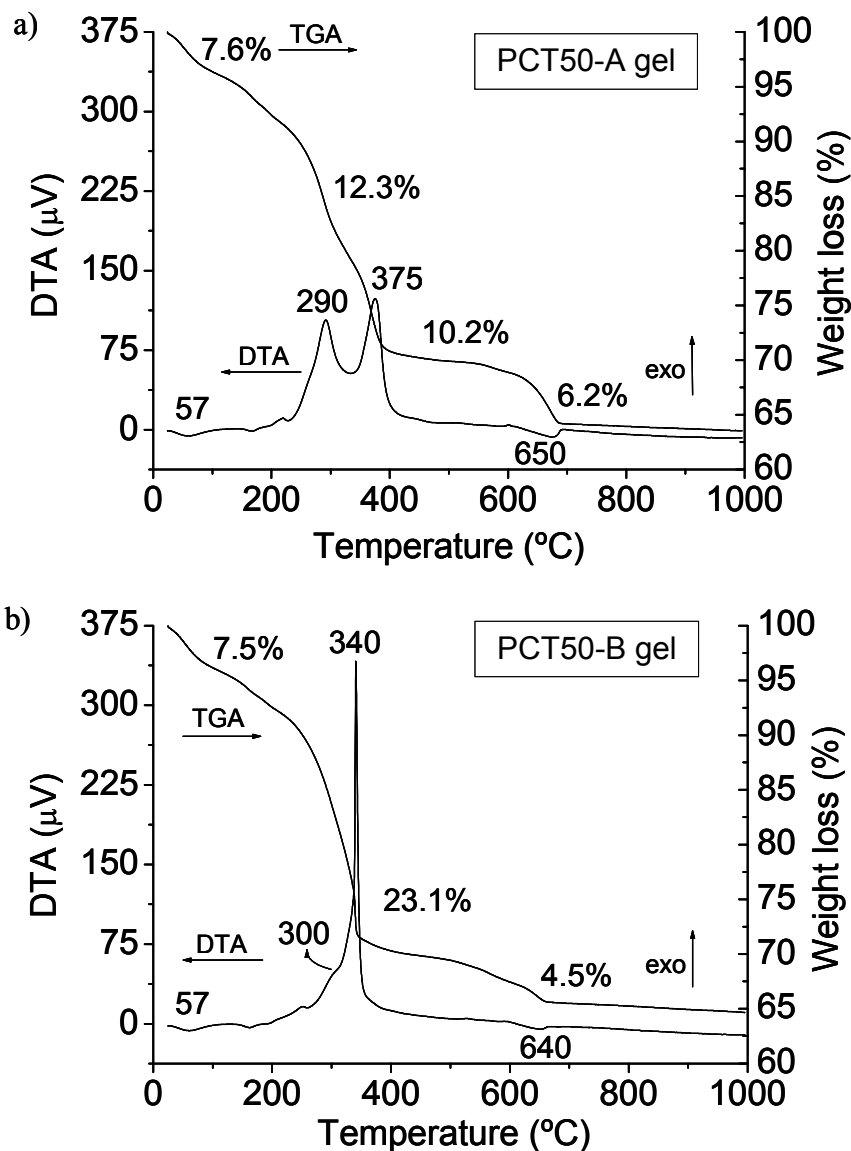


Figure 4.2.9. DTA-TGA of the diol sol-gel derived PCT50-A (a) and PCT50-B (b) gels

However, any weight loss or energetic process are detected in this temperature interval (>500 °C) for the PCT24-C gel. The decomposition of CaCO_3 at these temperatures is therefore not observed for the PCT24-C gel (Fig. 4.2.8b), which may be ascribed to the use of the calcium acetylacetonate reagent in the synthetic route C. The main products of the thermal decomposition of calcium acetylacetonate are acetone (CH_3COCH_3) and calcium carbonate (CaCO_3),²⁶³ which is indicated in inset of Fig. 4.2.8b, where the thermal decomposition of the calcium acetylacetonate chemical reagent is shown. The absence of calcium carbonate in the PCT24-C gel indicates the

possible rupture of the calcium-acetylacetonate bonds during the synthesis reactions (reflux) of the Ca(II)-Pb(II)-Ti(IV) sol, since if this compound (calcium acetylacetonate) would remain in the solution after the sol synthesis, the decomposition at high temperatures of CaCO_3 should be detected in the DTA-TGA of the derived PCT24-C gel. Acetylacetonate groups are not detected by IR analysis in the distilled liquid (byproducts of reaction, see Fig. 4.2.1a), which indicates that probably remain in the synthesised sol and that are eliminated during the thermal decomposition at low temperatures (boiling point of acetylacetone is ~ 140 °C; see in the experiment section that reflux and distillation temperatures used in the synthesis of the PCT24-C sol are always lower).

Differences can be deduced from the thermal decomposition pathway of the PCT gels as a function of the chemical processing followed in the synthesis of their respective precursor solutions. Thus, the thermal decomposition of the PCT gels is simpler in the gels obtained through the routes B and C (PCT24-C and PCT50-B) than in those derived from the route A (PCT24-A and PCT50-A). Elimination of organic compounds in the latter ones is produced at various temperatures, denoting a decomposition pathway in several steps, whereas organic species are pyrolysed in a close temperature range in the former. Therefore, organics removal of the PCT gels of this work seems to be dependent on the solution chemistry used. The more homogeneous sol network proposed for the PCT24-C and PCT50-B gels, is probably responsible of the simpler decomposition of these gels than those of the PCT24-A and PCT50-A gels derived from a mixture solution of a Pb(II)-Ti(IV) sol and a calcium acetate just dissolved in water.

The use of the calcium acetate reagent in the synthesis of the PCT precursor solutions by the routes A and B gives rise to calcium carbonate during the thermal decomposition of the derived gels (PCT24-A, PCT50-A and PCT50-B). A higher amount of calcium carbonate is formed in the PCT50-A gel than in the PCT50-B one, when comparing both respective weigh losses associated (6.2 and 4.5 wt%). This could denote the more presence of calcium acetate not incorporated to the gel network, and therefore a potential source of carbonate formation, in gels obtained through the route A respect to the route B. However, this intermediate compound is not formed in the gels obtained by the synthetic route C (PCT24-C), where calcium acetylacetonate is used as the Ca^{2+} source,¹³¹ and where the practically total elimination of the organic species in the PCT24-C gel is produced at temperatures below 500 °C (Fig. 4.2.8b).

A comparative description of the most significant data of the thermal decomposition of these gels is shown in Table 4.2.3.

Table 4.2.3. DTA-TGA data of the diol sol-gel derived PCT gels

Gel powder (nominal composition)	Temperature interval (°C)	Weight loss (%)	DTA peaks (°C)	Processes
PCT24-A (Pb _{0.76} Ca _{0.24})TiO ₃	< 200	~4.7	~59 (endo)	< 200 °C
	200-500	~20.7	~275 (exo), ~300 (exo), ~487 (exo)	<u>Evaporation of physically absorbed water and organic solvent within the gel network</u>
	> 500	~2.6	~640 (endo)	
PCT24-C (Pb _{0.76} Ca _{0.24})TiO ₃	< 200	~3.8	~62 (endo)	200-500 °C
	200-500	~23.6	~320 (exo), ~346 (exo), ~490 (exo)	<u>Combustion of organic compounds, formation of calcium carbonate and crystallisation of the PCT system</u>
	> 500	-	-	
PCT50-A (Pb _{0.50} Ca _{0.50})TiO ₃	< 200	~7.6	~57 (endo)	> 500 °C
	200-500	~22.5	~290 (exo), ~375 (exo)	<u>Decomposition of calcium carbonate</u>
	> 500	~6.2	~650 (endo)	CaCO ₃ → CaO + CO ₂
PCT50-B (Pb _{0.50} Ca _{0.50})TiO ₃	< 200	~7.5	~57 (endo)	
	200-500	~23.1	~300 (exo), ~340 (exo)	
	> 500	~4.5	~640 (endo)	

4.2.3. PCT THIN FILMS

The characterisation of the films derived from the diol-based PCT solutions previously studied has been carried out using different techniques that provided us information about the crystal structure, microstructure and heterostructure of the films. The dielectric and ferroelectric properties of these films have made possible the evaluation of their applications in microelectronic devices.

4.2.3.1. Crystalline phases in the films as a function of temperature

Grazing Incidence X-Ray Diffraction (GIXRD) was used to study the crystalline phases formed in the PCT films with temperature. A single layer of the PCT solutions was deposited by spin-coating onto oxidised silicon substrates ($\text{SiO}_2/(100)\text{Si}$). The films were dried on a hot plate at 350 °C for 60 s and annealed by Rapid Thermal Processing (RTP) at various temperatures for 60 s. According to the previous nomenclature assigned to the PCT precursor solutions, the films will be named PCT24-A, PCT24-C, PCT50-A and PCT50-B.

Fig. 4.2.10 shows the GIXRD patterns of these films, processed by RTP at various temperatures.

After drying at 350 °C, all the PCT films are amorphous by x-ray diffraction. For the PCT24-A and PCT24-C films, the first reflections corresponding to crystalline phases are observed in their respective patterns after crystallisation at 425 and 375 °C, respectively. A single perovskite phase is detected in both cases, with no secondary phases observed. In the case of the PCT50-A and PCT50-B films, the appearance of a single perovskite phase occurs after crystallisation at 450 °C. Once the perovskite is formed, higher temperatures only improve the crystallinity of the films

The effect of the Ca^{2+} content on the crystallisation of the PCT films was previously studied in *Part I* of this chapter. As it was concluded, the increase of the Ca^{2+} content in the PCT system produces a displacement of the crystallisation of the perovskite towards higher temperatures. This is confirmed from the results shown in Figure 4.2.10, where the crystallisation of the PCT50 films occurs at higher temperatures (450 °C) than that of the PCT24 films (375 and 425 °C for the PCT24-C and PCT24-A films, respectively).

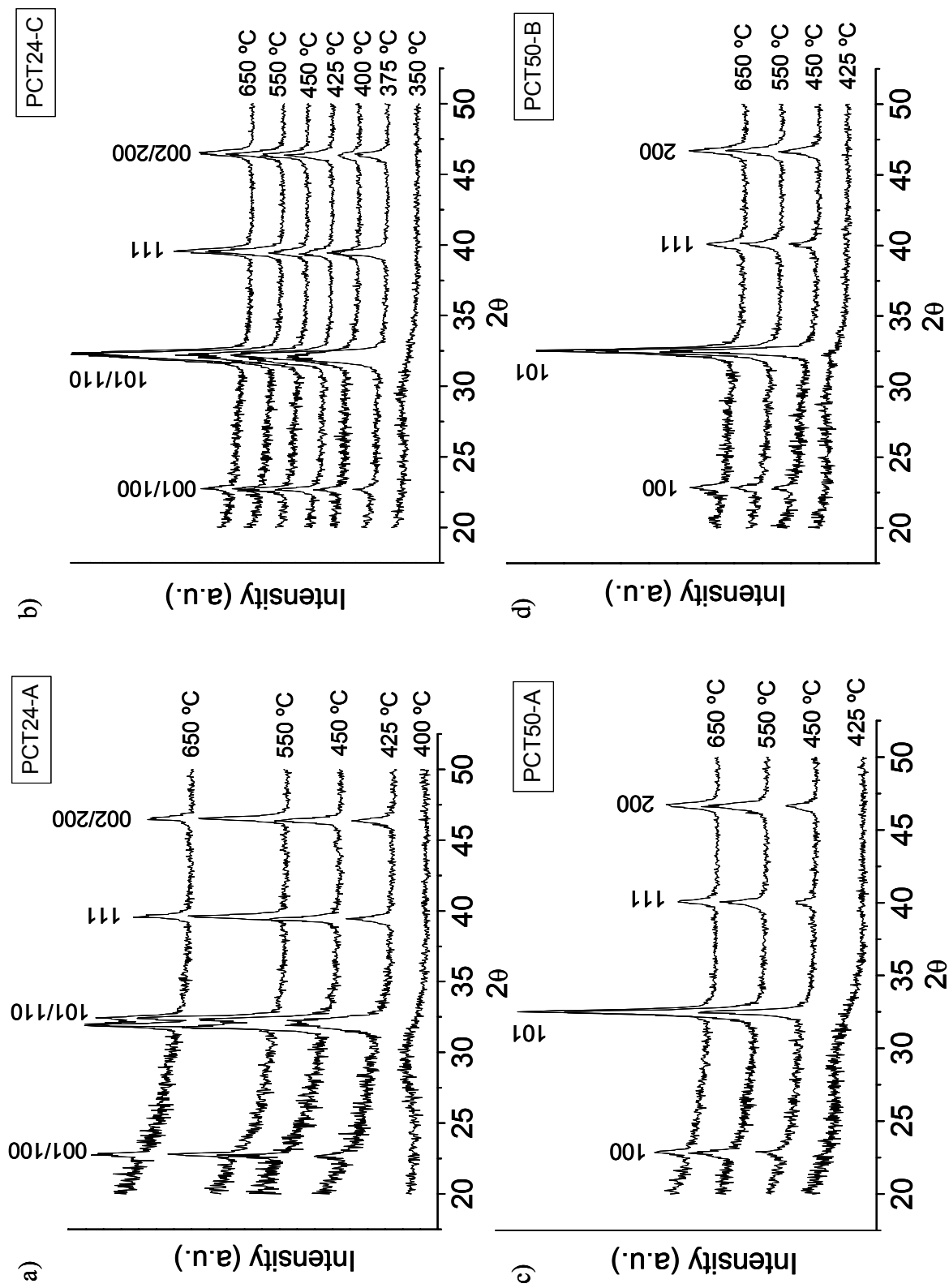


Figure 4.2.10. GIXRD patterns of the diol sol-gel derived PCT24-A (a), PCT24-C (b), PCT50-A (c) and PCT50-B (d) films RTP-treated at different temperatures

The chemical processing used in the synthesis of the PCT solutions also seems to affect the crystallisation of the derived films. Note that the presence of the perovskite phase is detected at rather lower temperatures in the PCT24-C film (~ 375 °C) than in the PCT24-A film (~ 425 °C). This can be attributed to the different decomposition mechanisms that both films suffer during their thermal treatment from the as-deposited state to the crystalline ceramic state. According to the thermal decomposition processes previously studied in the PCT24 gels (section 4.2.2.1), all the organic species are eliminated from the PCT24-C gel powder at temperatures below 500 °C, whereas the formation of calcium carbonate in the PCT24-A gel delays the total elimination of organics from this gel up to higher temperatures (see Fig. 4.2.8). A similar thermal decomposition pathway is expected in the films, although probably occurring at lower temperatures in RTP-treated thin films, as discussed in *Part 1* of this chapter. In practical terms, during pyrolysis of the films, M-O-C and M-O-H bonds are broken, with removal of associated volatile species, and formation of an amorphous M-O-M network, which subsequently evolves towards the crystalline oxide phase.⁹⁶ The lower pyrolysis temperature of the PCT24-C film promotes its earlier crystallisation (375 °C) respect to the PCT24-A film (425 °C). In the latter, organic compounds are totally removed from the system at higher temperatures (mainly due to calcium carbonate decomposition), delaying the onset of the perovskite crystallisation towards higher temperatures. Calcium carbonate is not formed in the PCT24-C system which probably makes possible the advance of the perovskite crystallisation in the derived films.

4.2.3.2. Crystalline structure of the films by X-Ray Diffraction with the Grazing Incidence (GIXRD) and with the Bragg-Brentano (XRD) geometry

Here, PCT films were deposited onto (111)Pt/TiO₂/SiO₂/(100)Si substrates from the precursor solutions (with a concentration of ~ 0.3 M). After drying, the films were crystallised by Rapid Thermal Processing (RTP) in air at 650 °C for 50 s. A total of 15 layers were successively deposited, dried and crystallised. The last deposited layer was RTP treated at 650 °C, but for a time of 3600 s.

The crystalline structure of these films was studied by means of X-Ray Diffraction, with the Grazing Incidence (GIXRD) and with the Bragg-Brentano (XRD) geometry. Figure 4.2.11a shows the GIXRD patterns ($\alpha = 1^\circ$) of the PCT films, whereas the possible presence of preferred orientations in the films was analysed from the XRD patterns of Figure 4.2.11b.

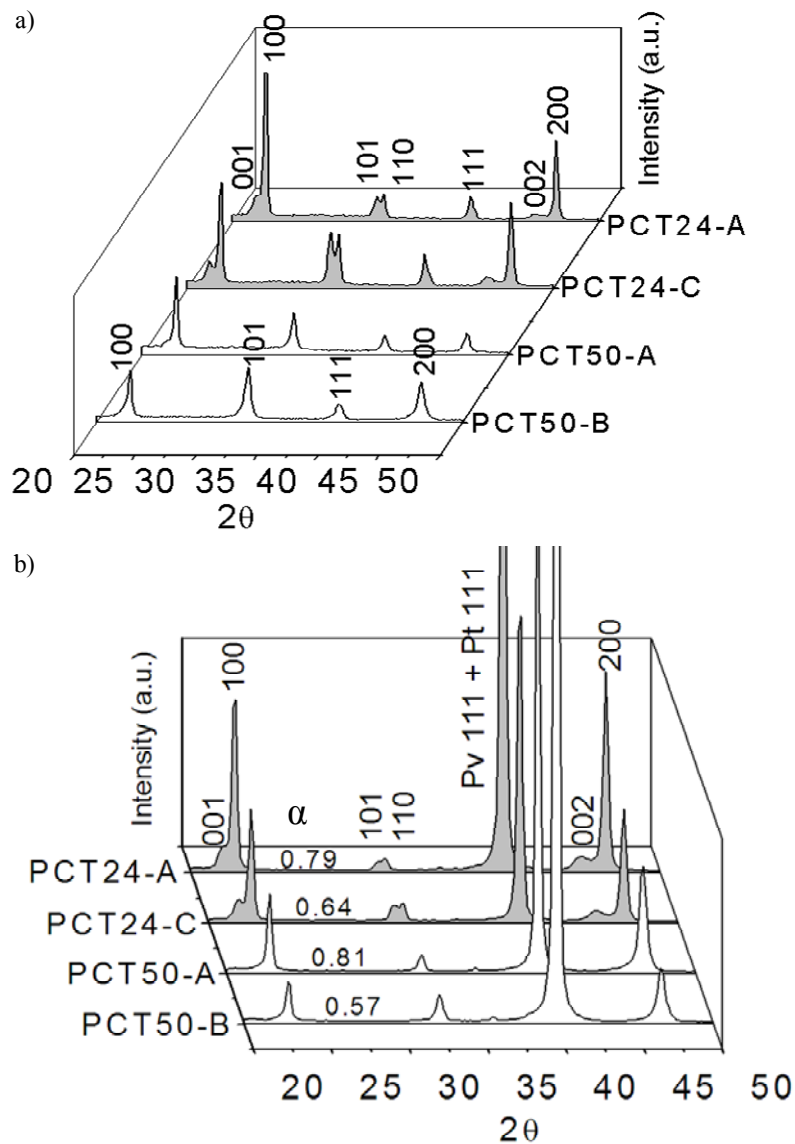


Figure 4.2.11. GIXRD (a) and XRD (b) patterns of the diol sol-gel derived PCT films

All the PCT films show the presence of a single perovskite phase, with non-noticeable second crystalline phases observed (Fig. 4.2.11a). In the case of the PCT24 films (PCT24-A and PCT24-C), a tetragonal structure is deduced from the patterns, in which the characteristic doublets of this perovskite structure (001/100, 101/110 and 002/200) can be distinguished. On the other hand, the distorted orthorhombic structure proposed⁴³ for ceramic powders of the PCT50 composition cannot be inferred by the x-ray diffraction data of the PCT50 films of this work, and only a pseudocubic structure can be deduced from the patterns.

The crystal structure of the films used to be distorted due to stresses induced by the substrate, which can also affect the film texture. A <100> preferred orientation is observed in the PCT films that is a result of the tensile stress produced by the silicon-based substrate during the annealing.^{202,213} In order to evaluate the degree of <100> orientation of the films, a semiquantitative preferred <100> orientation rate α is defined for each PCT24 and PCT50 films as:

$$\alpha_{\text{(PCT24)}} = I_{100} / (I_{001} + I_{100} + I_{101} + I_{110}) \quad [\text{eq. 16}]$$

$$\alpha_{\text{(PCT50)}} = I_{100} / (I_{100} + I_{110}) \quad [\text{eq. 17}]$$

The intensity values were taken at the peak maximum of the respective reflections in the XRD patterns of Fig. 4.2.11b. Values thus obtained have to be compared with those corresponding to a random PCT24 (JCPDS 39-1336) and PCT50 bulk ceramic²⁶⁴, that is, 0.12 in both cases. The α values calculated in the films are shown embedded in their respective XRD patterns (Fig. 4.2.11b). Note that all the α values of the films are above 0.12, denoting a clear <100> preferred orientation. However, a stronger <100> orientation is present in the PCT films derived from solutions processed by the route A than from the routes B and C (α values of 0.79 and 0.81 for the PCT24-A and PCT50-A films, respectively, and 0.64 and 0.57 for the respective PCT24-C and PCT50-B films).

From these results, it can also be observed how the tetragonality of the PCT films decreases as the amount of partial substitution of Pb^{2+} by Ca^{2+} is higher (from the PCT24 films to the PCT50-films), as it was stated in the previous *Part 1* of this chapter. Furthermore, the solution chemistry and the chemical precursors seem to influence the degree of orientation of the derived crystalline PCT films. It has been frequently observed how the orientation of sol-gel derived films is dependent on the processing conditions employed.²⁶⁵⁻²⁶⁹ Although some authors ascribed the changes in film orientation to variations in precursor organic nature (e.g. hydrolysis conditions,²⁶⁸ chelating agents,²⁶⁹ etc), other authors point that the key mechanism that indeed promote these changes may lie in the pyrolysis behaviour of the films.²⁷⁰ Thus, for films that exhibit low pyrolysis temperatures, the thermal input during thermal treatment would lead to surmount the energy barriers for more than one nucleation events. On the contrary, for precursor systems with high pyrolysis temperatures, nucleation events other than the most energetically favourable one become less attractive.

In the case of the PCT films, the “natural” growth of the perovskite film leads to the mixed <100> and <001> orientations,²⁷¹ although the stress state present during the film processing onto Si-based substrates promote the <100> preferred orientation²⁰² as observed in the patters of Fig.

4.2.11b. However, in the PCT24-C and PCT50-B films this preferred orientation is not as stronger as in the PCT24-A and PCT50-A films. Perhaps, the lower pyrolysis temperature observed in the PCT24-C system (all the organic species are pyrolysed below 500 °C, as deduced from Fig. 4.2.8b) respect to the PCT24-A system, may induce the nucleation along other crystallographic directions in addition to the energetically most favourable $\langle 100 \rangle$ one.²⁷⁰ As a result, the texture along this axis is slightly lower in the PCT24-C film. In the case of the PCT50 system, although remanent organics (calcium carbonate) are decomposed at high temperatures in both PCT50-A and PCT50-B gels (see Fig. 4.2.9), pyrolysis of the majority of the organic species is developed more homogeneously in the PCT50-B gel, which could enhance the driving force for diverse nucleation events in the film, also resulting in a lower $\langle 100 \rangle$ preferred orientation when compared with the PCT50-A film.

4.2.3.3. Films microstructure by Scanning Force Microscopy (SFM) and Scanning Electron Microscopy (SEM)

The microstructure of the films surfaces was observed by Scanning Force Microscopy (SFM). Figure 4.2.12 shows the SFM images of the PCT24-A and PCT24-C films (Fig. 4.2.12a and b) and of the PCT50-A and PCT50-B films (Fig. 4.2.12c and d). Average grain size values calculated for each film are also shown in the images. Thus, mean grain sizes of ~150 and ~190 nm are measured from the surfaces images of the PCT24-A and PCT24-C films, respectively. On the other hand, grains of an average size of ~50 nm constitute the microstructure of both PCT50-A and PCT50-B films, as observed from their respective surface images.

Micrographs of the films surfaces were also obtained by Scanning Electron Microscopy working under field emission conditions (FEGSEM). Figure 4.2.13 shows the plan-view micrographs of the PCT24-A and PCT24-C films (Fig. 4.2.13a and b) and of the PCT50-A and PCT50-B films (Fig. 4.2.13c and d). Magnifications of these images are shown embedded in order to appreciate grain size. Cross-section images of these films are also shown in Figure 4.2.14.

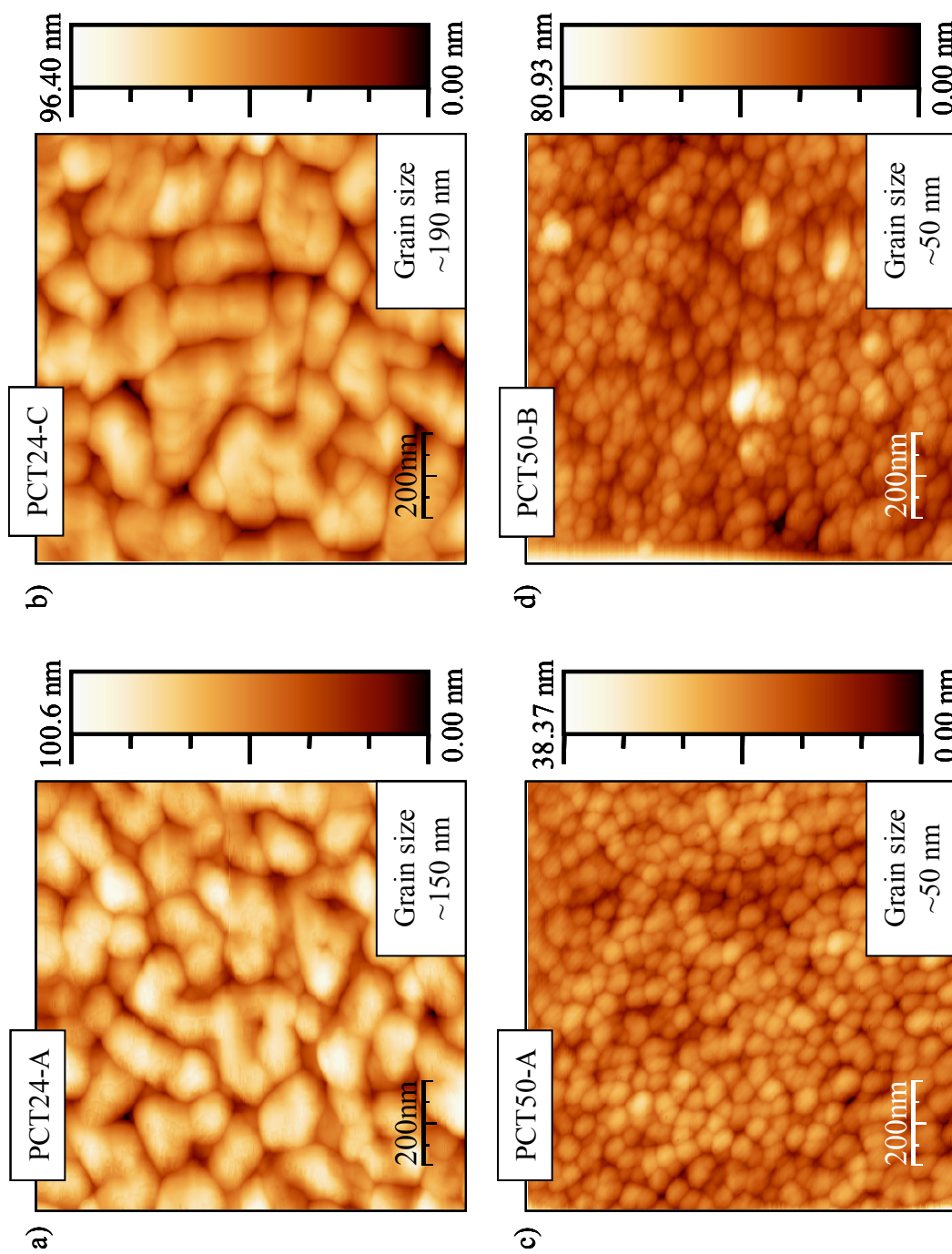


Figure 4.2.12. SFM images of the diol sol-gel derived PCT24-A (a) and PCT24-C (b) films, and PCT50-A (c) and PCT50-B (d) films. Calculated grain sizes are shown in the images

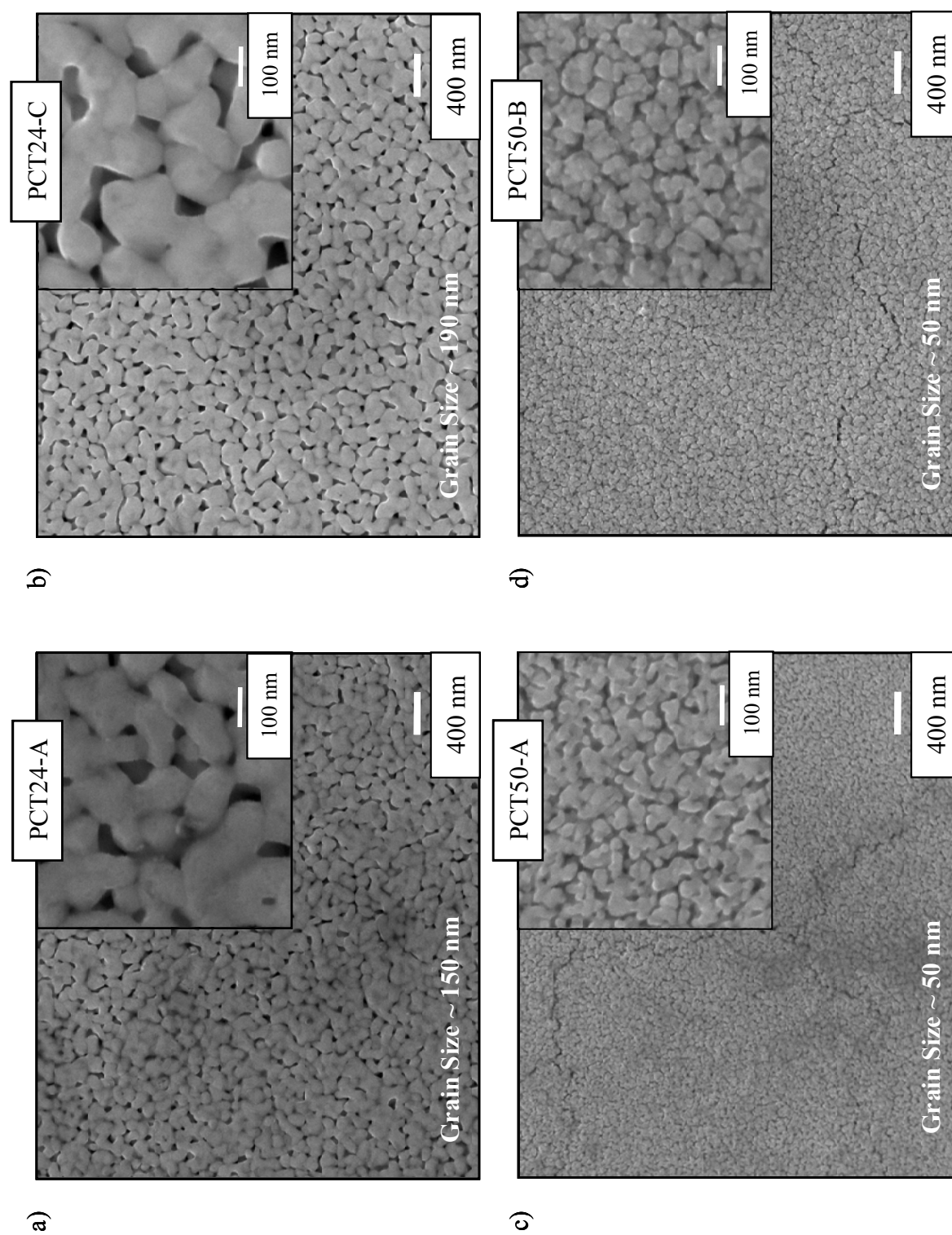


Figure 4.2.13. SEM micrographs (plan-view) obtained in the diol sol-gel derived PCT24-A (a) and PCT24-C (b) films, and PCT50-A (c) and PCT50-B (d) films. Magnifications of each micrograph are embedded shown

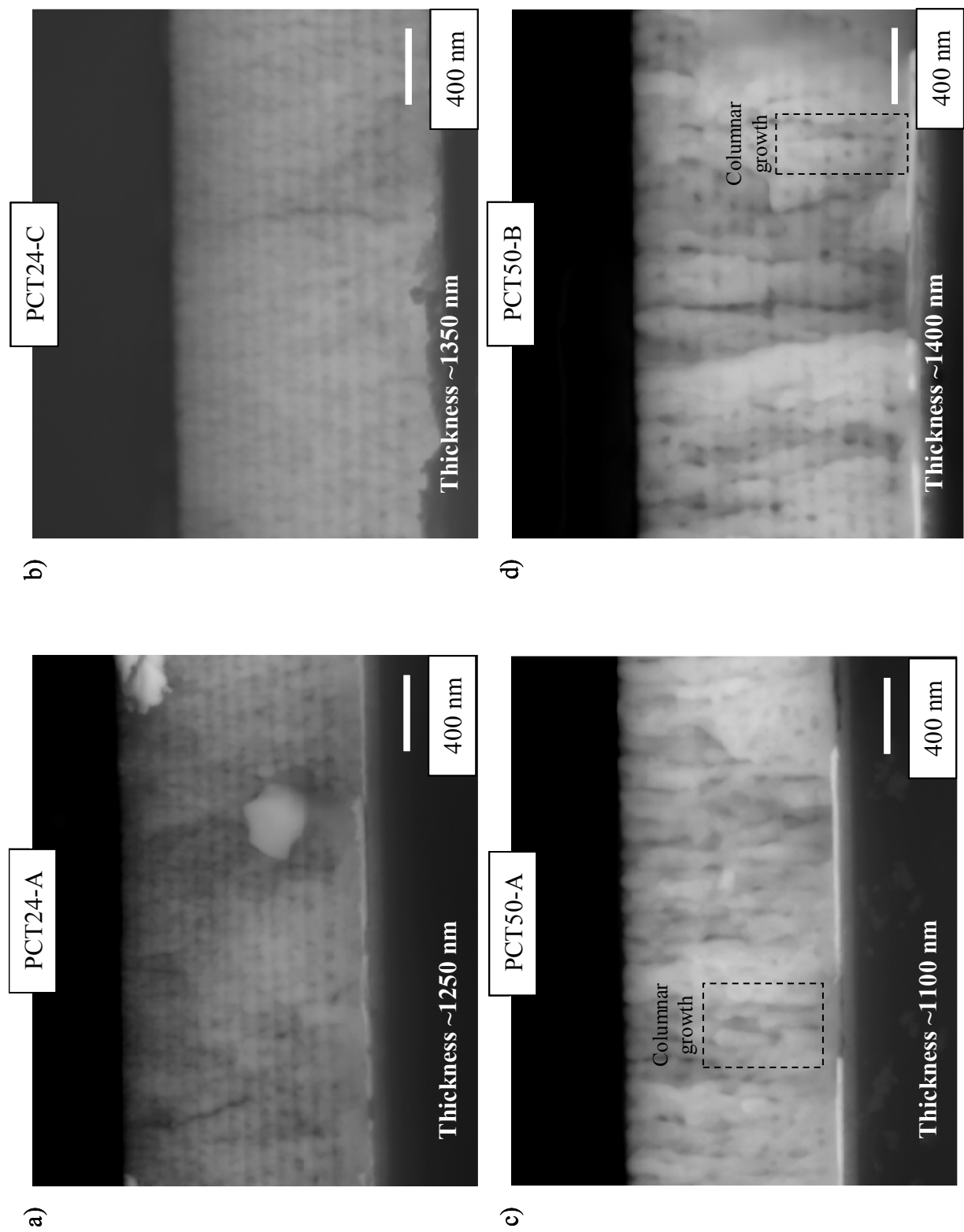


Figure 4.2.14. SEM micrographs (cross-section) obtained in the diol sol-gel derived PCT24-A (a) and PCT24-C (b) films, and PCT50-A (c) and PCT50-B (d) films

All the films show homogeneous microstructures, without any morphological differentiated secondary phases. However, differences in grain size are deduced from the images of Fig. 4.2.13. Thus, average grain sizes of ~ 150 and ~ 190 nm are measured for the PCT24-A and PCT24-C films, respectively, whereas a value of ~ 50 nm is calculated for both PCT50-A and PCT50-B films. These results are in accordance with those calculated by Scanning Force Microscopy. The influence of the Ca^{2+} content of the PCT system on the grain size of the crystalline films was studied in the previous *Part 1* of this chapter. As it was concluded there, crystallite growth seems to be hindered in high-Ca PCT perovskite films compositions and therefore, these films are formed by smaller grains (~ 50 nm) when compared with films with lower Ca^{2+} contents (~ 150 - 190 nm).

From the cross-section images of Fig. 4.2.14, thicknesses of ~ 1250 , ~ 1350 , ~ 1100 and ~ 1400 nm are calculated for the PCT24-A, PCT24-C, PCT50-A and PCT50-B films, respectively, that are close to those obtained by profilometry (~ 1220 , ~ 1390 , ~ 1250 and ~ 1420 nm, respectively). The multiple layers that constitute the PCT films (15 layers) can be distinguished in the cross-section images, where microstructures mainly formed by equiaxed grains can be observed, although a columnar grain growth also seems to be present in the PCT50 films (indicated in their respective figures). Note that a larger amount of porosity within the bulk film is observed in the PCT24-A, PCT50-A and PCT50-B films respect to the PCT24-C film. As discussed before, calcium carbonate is formed during the annealing of the former films that decomposes into CaO and CO_2 at a temperature close to that of the perovskite crystallisation. The release of CO_2 at these high temperatures probably yields to the formation of pores in these films.

The results obtained by SFM and SEM indicate that the chemical precursors and solution chemistry also play an important role on the microstructural features of the derived films. The characteristics of the pyrolysis process of the films will again serve to explain the microstructures observed. Thus, PCT24 solutions prepared from the synthetic route C lead to crystalline films with microstructures formed by bigger grains (~ 190 nm) than those obtained when followed the synthetic route A (~ 150 nm). This effect could be explained by the different decomposition process that both films suffer during their annealing. Although these processes may occur at different temperatures in the films, the thermal decomposition pathway of the PCT gel powders gives us an idea about the differences observed in the film microstructures. As it was observed in Fig. 4.2.6, all the organics are removed below 500 °C in the PCT24-C gel. Accompanying the elimination of the organic compounds, the rearrangement of the gel network to form an inorganic amorphous film is also produced, which then evolves to the ceramic crystalline state by nucleation and growth

mechanisms. However, in the PCT24-A gel, remanent organics are still present up to high temperatures, at which calcium carbonate decomposes. The formation of this carbonate delays the complete pyrolysis of the film and therefore prevents the structural reorganization of the network and the subsequent nucleation and growth of the PCT grains. As a result, lower grain sizes are developed in the PCT24-A film. On the contrary, the solution chemistry seems not to affect the microstructure of the PCT50 films obtained, since both PCT50-A and PCT50-B films are constituted by grains of the same size (~50 nm), independently of the synthetic procedure followed to prepare the respective solutions (route A and B). The use of the calcium acetate reagent in both routes derives in the formation at high temperatures of calcium carbonate that is responsible of delaying the onset of the pyrolysis and crystallisation processes towards higher temperatures and of the formation of pores within the bulk film.

4.2.3.4. Films heterostructure by Rutherford Backscattering Spectroscopy (RBS)

The Rutherford Backscattering Spectroscopy (RBS) experimental spectra (2 MeV $^4\text{He}^{2+}$) of the films and their corresponding simulations are depicted in Figures 4.2.15 and 4.2.16 for the PCT24 and PCT50 films, respectively. A good fit between the experimental and simulated curves is obtained for all the films. Regions of the spectra from which the main information can be inferred are indicated in the graphs. The respective heterostructures of the films deduced from these analyses are also shown in the figures.

A heterogeneous compositional profile is simulated for the PCT films obtained from the solutions processed by the route A (PCT24-A and PCT50-A), where an interface between the PCT layer and the Pt bottom electrode is detected. The elemental composition of this interface is $0.76\text{Pb} + 0.24\text{Ca} + 1.00\text{Ti} + 3.00\text{O} + 0.10\text{Pt}$ (error ~10%) for the PCT24-A film (Fig. 4.2.15a) and $0.50\text{Pb} + 0.50\text{Ca} + 1.00\text{Ti} + 3.00\text{O} + 0.10\text{Pt}$ (error ~10%) for the PCT50-A film (Fig. 4.2.16a). The thickness of these interfaces is in both cases around 13 % of the respective total films thickness. In addition, the more superficial layers of these films present lead deficiency respect to the bulk film, which can be attributed to the PbO volatilisation during firing. A more homogeneous compositional profile is obtained for the PCT24-C (Fig. 4.2.15b) and PCT50-B (Fig. 4.2.16b) films, with a slightly lower content of lead (II) than the films derived from the route A.

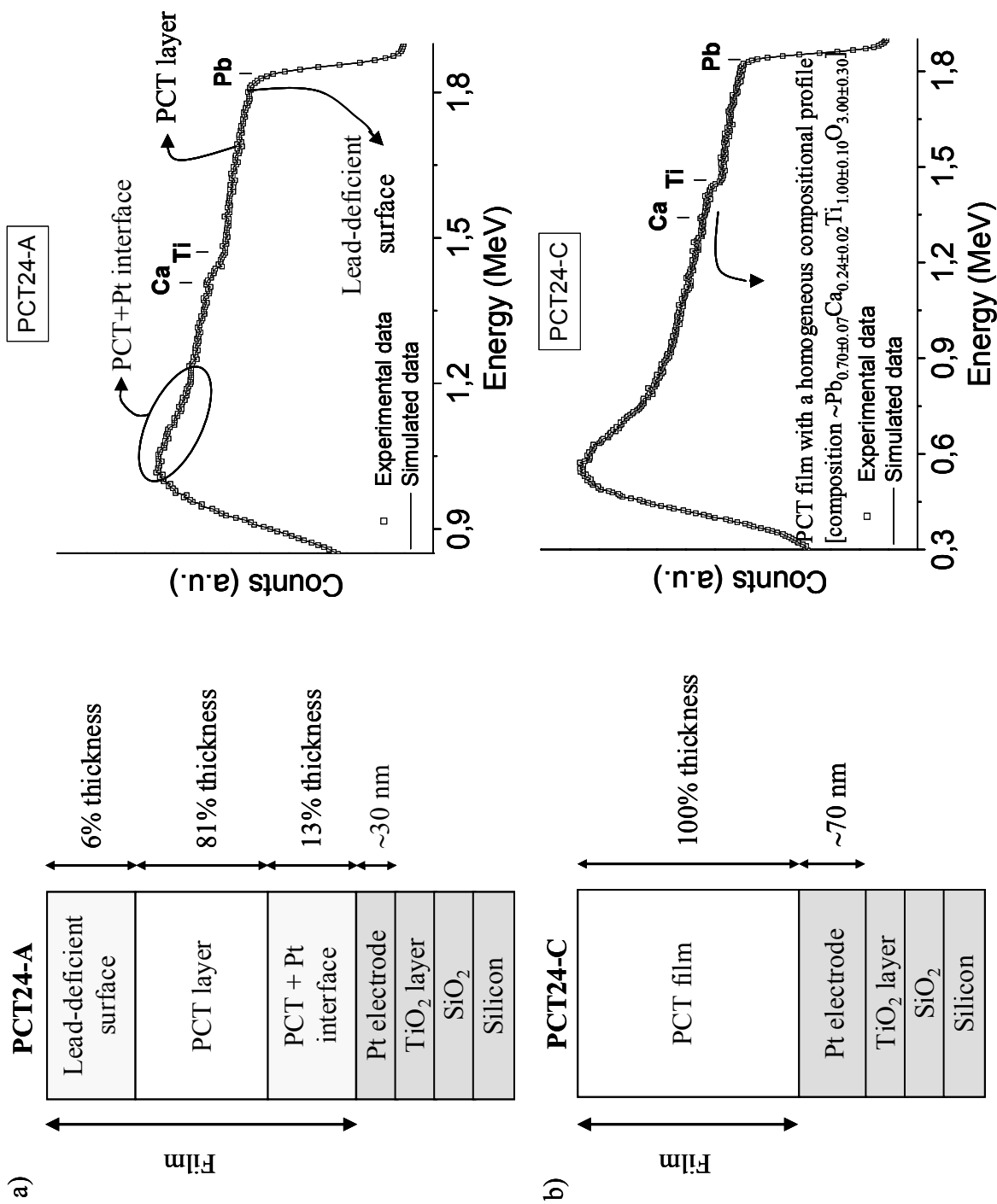


Figure 4.2.15. RBS spectra and heterostructure deduced from RBS data for the diol sol-gel derived PCT24-A (a) and PCT24-C (b) films

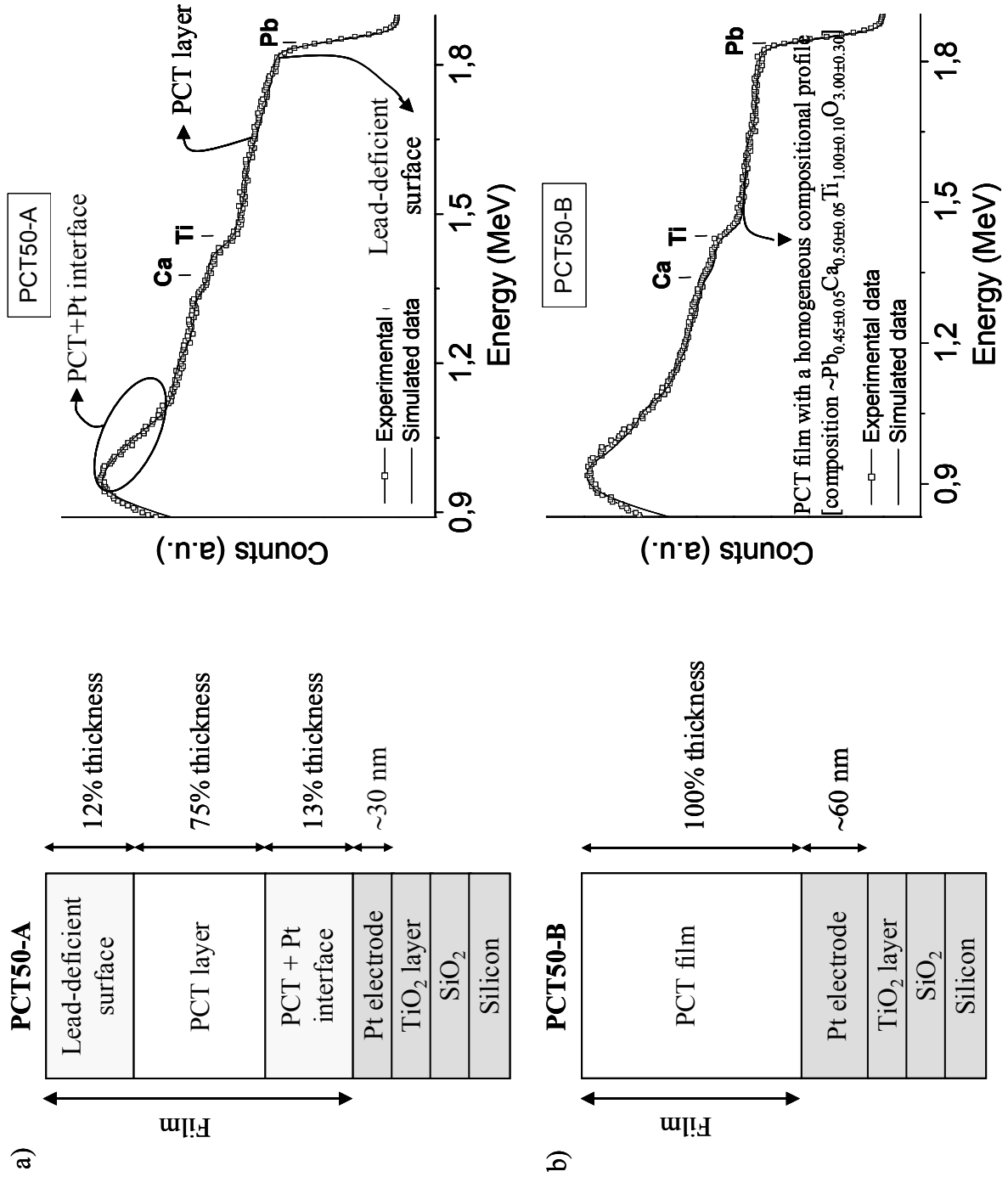


Figure 4.2.16. RBS spectra and heterostructure deduced from RBS data for the diol sol-gel derived PCT50-A (a) and PCT50-B (b) films

Thus, an average elemental composition close to the nominal one is deduced from the RBS data as $\text{Pb}_{0.70\pm 0.07}\text{Ca}_{0.24\pm 0.02}\text{Ti}_{1.00\pm 0.10}\text{O}_{3.00\pm 0.30}$ for the PCT24-C film, and $\text{Pb}_{0.45\pm 0.05}\text{Ca}_{0.50\pm 0.05}\text{Ti}_{1.00\pm 0.10}\text{O}_{3.00\pm 0.30}$ for the PCT50-B film, always assuming that a single perovskite phase is formed. Furthermore, no appreciable interface between the PCT layer and the Pt bottom substrate is detected in both films.

Thicknesses of ~ 844 and ~ 1270 nm are calculated from the RBS data for the PCT24-A and PCT24-C films, whereas a thickness of ~ 880 and ~ 895 nm is determined by RBS for the PCT50-A and PCT50-B films. The thickness of the Pt bottom electrode has been also calculated (see figures).

A summary of the most important heterostructural features of the PCT films deduced from these RBS analyses is shown in Table 4.2.4.

It has to be noted that for the PCT24-A, PCT50-A and PCT50-B films, considerable differences in thickness are found between the value calculated by RBS and the average one obtained by SEM and profilometry (see Table 4.2.4). This is explained by the film composition and bulk density taken into account in the calculation of the RBS thicknesses. Theoretical densities of 6.20 g/cm^3 (for the PCT24 composition) or 7.15 g/cm^3 (for the PCT50 composition) have been used, thus always considering in the calculation that the different constituent layers of the film heterostructure have the nominal composition of the perovskite and bulk density of 100 %. However, these assumptions are not accurate when the film has porosity and the film heterostructure is formed by compositionally differentiated layers (lead-deficient surface layers or Pt-film bottom interfaces). The PCT24-A, PCT50-A and PCT50-B films contains porosity as observed by SEM. Furthermore, the two first films also have lead-deficient surface layers and Pt bottom electrode-PCT film interfaces (see Figs. 4.2.15 and 4.2.16). These effects are enough to introduce an appreciable error in the calculation of the RBS thickness. On the contrary, the thickness calculated by RBS in the PCT24-C film is quite close to those measured by SEM and profilometry (see Table 4.2.4). This is due its low porosity and to the absence of surface layers or interfaces.

Therefore, the RBS results indicate that the film heterostructure of these PCT films is related with their processing. First, a relationship between solution homogeneity and film homogeneity can be established. Homogeneity of sols and gels is a critical goal in sol-gel processing of ceramic materials, since in a dried homogeneous gel the atoms can be arranged in a manner close to that expected in the desired final crystalline phase.^{272,273} In other words, the local atomic arrangement in the sols can be controlled during their synthesis to resemble that of the final crystalline phase.²⁷⁴

Table 4.2.4. RBS data obtained in the diol sol-gel derived PCT films

Nominal composition (Film)	PCT film				Thickness (nm) calculated by		Thickness deviation ³
	Lead-deficient surface %thickness	Composition ¹	Bottom interface		SEM Profilmometry (Average)	RBS ²	
			Composition	%thickness			
PCT24-A (Pb _{0.76} Ca _{0.24})TiO ₃	7%	(Pb _{0.73} Ca _{0.24})TiO ₃	80%	PCT + Pt	13%	~1250 (1235)	~844
PCT24-C (Pb _{0.70} Ca _{0.24})TiO ₃	-	(Pb _{0.70} Ca _{0.24})TiO ₃	100%	PCT + Pt	-	~1350 (1370)	~1270
PCT50-A (Pb _{0.50} Ca _{0.50})TiO ₃	12%	(Pb _{0.49} Ca _{0.50})TiO ₃	75%	PCT + Pt	13%	~1100 (1175)	~880
PCT50-B (Pb _{0.45} Ca _{0.50})TiO ₃	-	(Pb _{0.45} Ca _{0.50})TiO ₃	100%	PCT + Pt	-	~1400 (1410)	~895

(1) Error of ~10 %. The formation of films with perovskite structure is assumed

(2) Thickness was calculated considering the nominal composition of the perovskite and its theoretical density

(3) Deviation of the thickness measured by RBS from the average thickness calculated by SEM and profilometry

The high homogeneity of the PCT24-C and PCT50-B solutions previously shown by DLS, provides a better compositional control of the derived films. As a result, the crystalline films show a homogeneous depth profile and a composition quite close to that of the respective stoichiometric perovskites. However, the solutions derived from the route A are formed by two distributions of particle sizes (see DLS results of section 4.2.1.2), which can be responsible of the heterogeneous compositional profile observed by RBS in the PCT24-A and PCT50-A films (lead-deficient surface, PCT layer and bottom interface). Second, the pyrolysis and crystallisation of the films during their thermal treatment also affect the film heterostructure. The simpler pyrolysis of the PCT24-C system, where calcium carbonate is not formed and the total elimination of the organics is produced below 500 °C, leads to films with a high bulk density and a composition close to that of the expected perovskite.

4.2.3.5. Dielectric and ferroelectric properties of the PCT films. Applications in microelectronic devices

The feasibility of the diol-based sol-gel method to produce PCT films with optimum and interesting properties within the technology of multifunctional microelectronic devices, is evaluated in this section.

4.2.3.5.1. PCT24 thin films

In order to evaluate the dielectric properties of the PCT24 films here prepared, the variation of the dielectric constant (k') with temperature was measured for the films at various frequencies. Figure 4.2.17 shows the results obtained for the PCT24-A and PCT24-C films.

A clear ferro-paraelectric transition, characteristic of this perovskite composition, is observed in both PCT24-A and PCT24-C films, with a transition temperature (defined as the temperature at which the dielectric constant is maximum, T_m) near ~375 °C. This temperature is lower in bulk ceramics of the same composition (~260 °C),¹² since in ferroelectric thin films supported onto silicon substrates a shift of T_m towards higher temperatures is normally produced due to the presence of tensile stresses. Note that the PCT24-C film has larger k' values than those measured in the PCT24-A film.

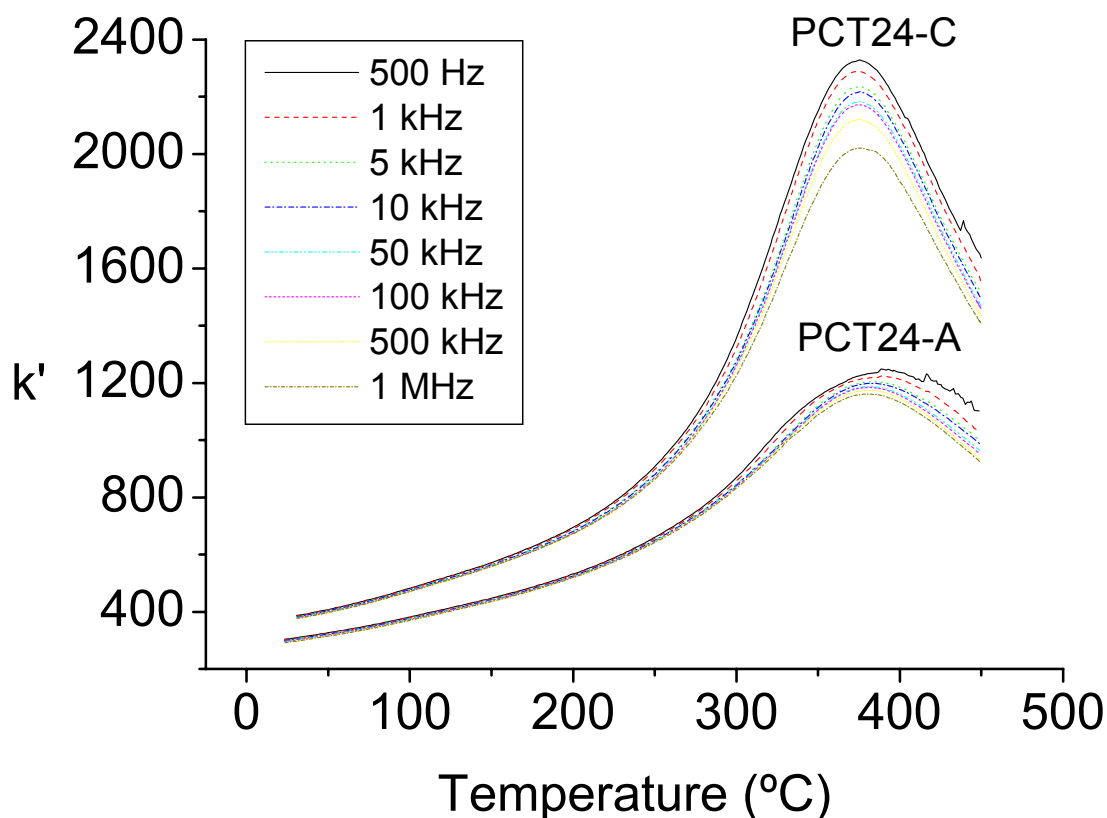


Figure 4.2.17. Variation of the dielectric constant (k') with temperature of the diol sol-gel derived PCT24 films, measured at various frequencies

Dielectric constants of ~ 1190 and ~ 2210 are obtained at T_m in the PCT24-A and PCT24-C films, respectively, measured at 10 kHz. At room temperature, these values decrease down to ~ 300 (PCT24-A) and ~ 380 (PCT24-C). Values of the dielectric anomaly, $\Delta k'$, (difference between the k' values at T_m and at room temperature) of 890 and 1830 are also calculated for the PCT24-A and PCT24-C films, respectively.

The different dielectric response of these films is related with the differences in the films discussed in the previous sections and that are dependent on the processing route. Thus, the lower values of the dielectric constant of the PCT24-A film respect to the PCT24-C film are mainly related with the development of a heterogeneous heterostructure in the former. A film heterostructure formed by different layers makes the k' values much lower for this film than for the PCT24-C film, according to the approximation of several in-series capacitors (bulk film, lead-deficient surface layer and interface). The homogeneous film heterostructure of the PCT24-C film

together with a larger grain size (~ 190 nm against ~ 150 nm in the PCT24-A film), make that this film has higher dielectric constant than the PCT24-A film.

The compensated $P(E)$ hysteresis loops of the PCT24 films, measured by the method of pulses²³⁷ that eliminates the contribution of possible non-ferroelectric charges to the hysteresis loop, are shown in Figure 4.2.18.

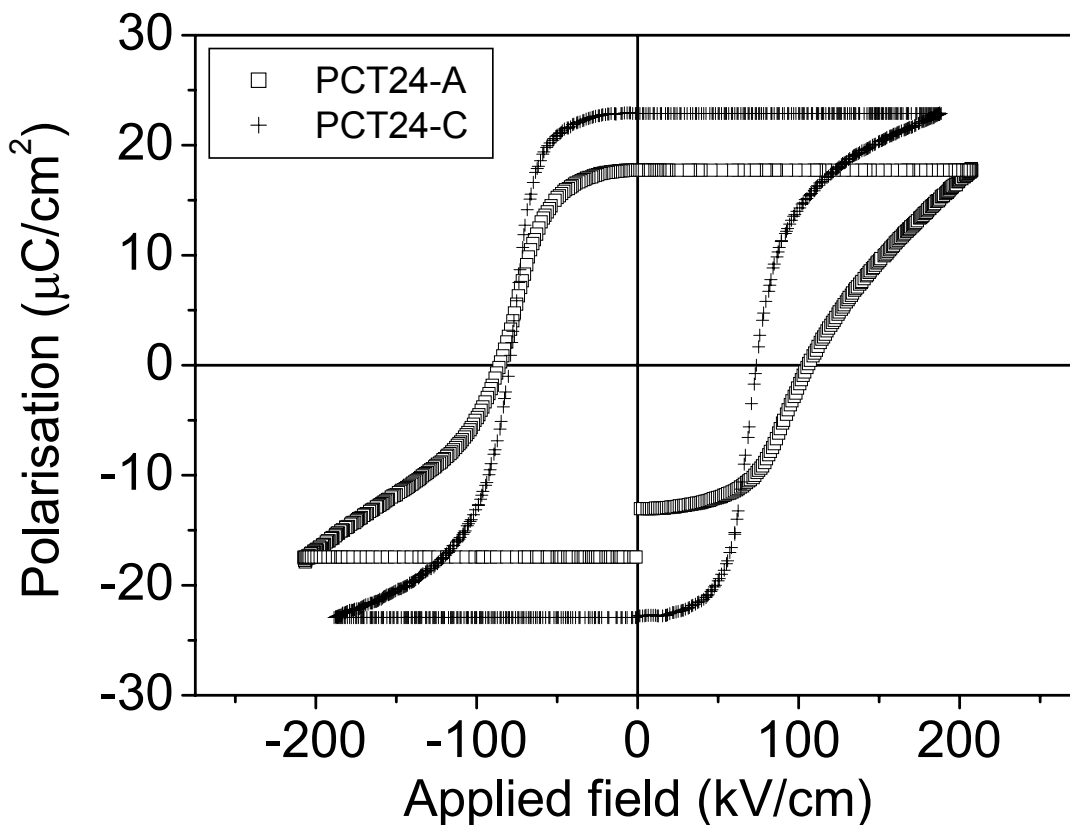


Figure 4.2.18. Pulsed hysteresis loops of the diol sol-gel derived PCT24 films

The incomplete closing of the loop in the PCT24-A film is due to a small effect of leakage contribution present, while the PCT24-C shows a close and well-defined ferroelectric loop. Values of remanent polarisation (P_r) of ~ 16.5 and ~ 22.9 $\mu\text{C}/\text{cm}^2$ are obtained for the PCT24-A and PCT24-C films, respectively, with coercive fields (E_c) of ~ 96 and ~ 77 kV/cm , respectively. These P_r values are indicative of a larger amount of commutable ferroelectric phase present in the PCT24-C film than in the PCT24-A film, as expected from the previous values of the dielectric anomalies ($\Delta k'$) calculated in both films (1830 and 890, respectively).

The different ferroelectric response measured in these films is ascribed to the lower porosity, the more homogeneous film heterostructure and the larger grain size of the PCT24-C film respect to the PCT24-A film. It is well-known that the polarisation of polycrystalline ferroelectric films decreases as the grain size is lower,²⁷² and that the surface layers or electrode-film interfaces also contribute to lowering the ferroelectric response of the films.^{22,121}

4.2.3.5.1.1. Evaluation of the PCT24 films for applications in multifunctional microelectronic devices

The better ferroelectric behaviour (larger k' and P_r values) of the PCT24 film processed through the route C respect to that derived from the route A, makes the former a better candidate for its use in multifunctional microelectronic devices such as Non-Volatile Ferroelectric Random Access Memories (NVFeRAMs) or pyroelectric sensors. Thus, a PCT24-C film with a thickness of ~ 300 nm was prepared and characterised as described below.

Figure 4.2.19 depicts the ferroelectric hysteresis loop of this film. Values of remanent polarisation (P_r) and coercive field (E_c) of $10.1 \mu\text{C}/\text{cm}^2$ and $92 \text{ kV}/\text{cm}$ are respectively obtained.

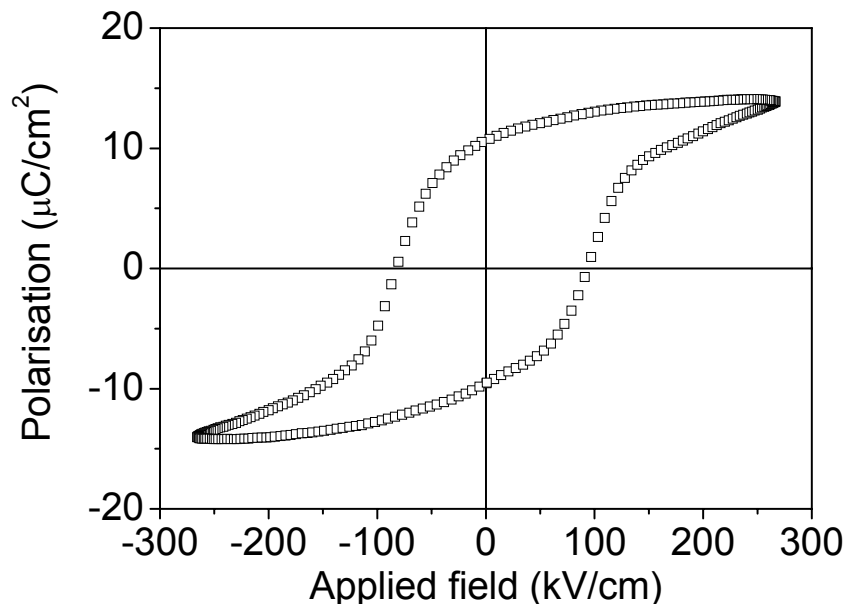


Figure 4.2.19. Compensated hysteresis loop of the ~ 300 nm thick diol sol-gel derived PCT24-C film

A key feature in memory devices (NVFeRAMs) is that they are typically read destructively, which leads to the requirement that the ferroelectric materials endure large numbers of switching cycles. Thus, the decrease of switching charge due to repeated polarisation reversal, known as fatigue, was analysed in Figure 4.2.20 for the PCT24-C film.

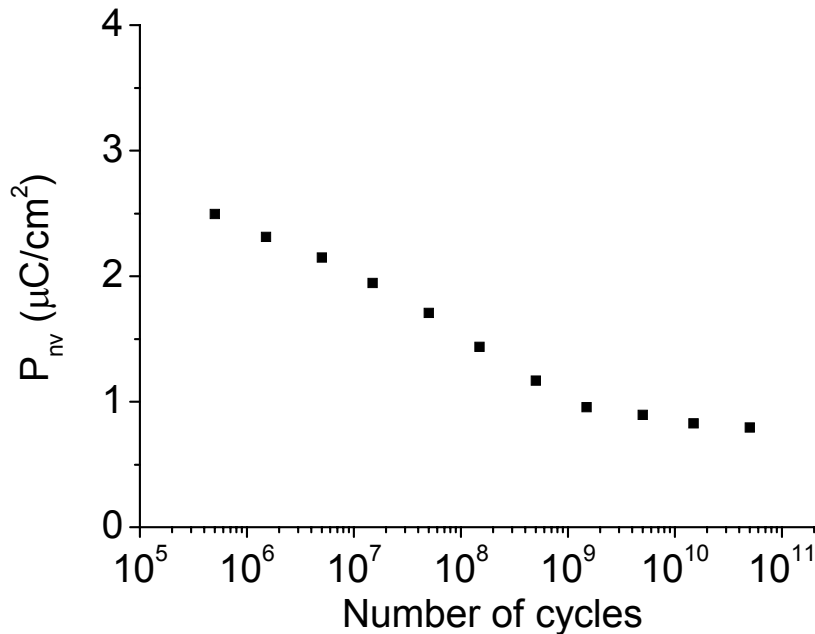


Figure 4.2.20. *Fatigue of the ~300 nm thick diol sol-gel derived PCT24-C film*

The film showed an initial non-volatile polarisation value (P_{nv}) of $\sim 3.1 \mu\text{C}/\text{cm}^2$. The 80% of this value is retained up to 5×10^5 cycles. Similar fatigue values have been measured in other sol-gel PCT24 films deposited onto platinised substrates.⁵ However, fatigue of this film is much lower than that reported for other compositions proposed for non-volatile memories applications.²⁷⁵

The retention of the polarisation with time was also performed in the PCT24-C film. Thus, the evolution of the pyroelectric coefficient (γ) of the film after poling with time is depicted in Figure 4.2.21.

After poling, the pyroelectric coefficient (γ) measured in this film resulted to be $\sim 1.2 \times 10^{-8} \text{ C}/\text{cm}^2\text{C}$, which is in the range of the high γ values obtained for multiple deposited and crystallised sol-gel PCT films.⁷⁵ Furthermore, the 90% of the γ value is retained up to ~ 10 years, which indicates the viability of this film for possible applications in infrared sensors.

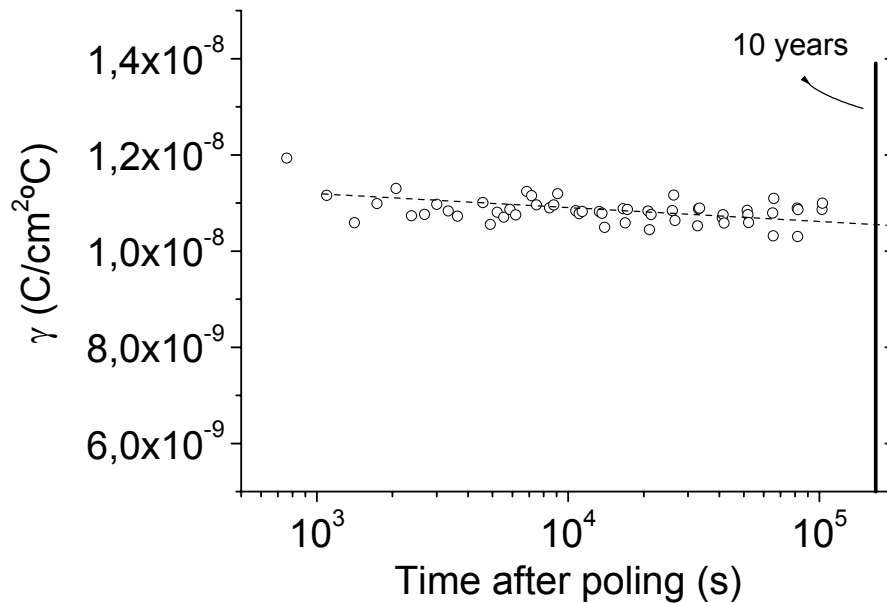


Figure 4.2.21. Evolution of the pyroelectric coefficient (γ) of the ~ 300 nm thick diol sol-gel derived PCT24-C film after poling (retention)

Summarising, the PCT24-C film here evaluated shows high values of remanent polarisation and low coercive fields, which proves its large ferroelectric response. However, low fatigue values are obtained as compared with other type of films prepared onto Si-based substrates.⁴ At first sight, this discourages its use in switching applications such as NVFeRAMs. This result was expected from previous works reported about the fatigue characteristics of thin films based on lead titanate perovskite compositions deposited onto platinised silicon substrates.²⁷⁶ In spite of this, acceptable values of pyroelectric coefficient are obtained for this film with a high retention of this value after a long period of time. This would suggest the successful applicability of these films in pyroelectric devices (infrared sensors).

The high retention of these films can be related to the processing method followed for their fabrication (route C). Crystalline PCT24 films derived from the route C develop homogeneous compositional profiles with an adjusted stoichiometry and perovskite structure. No secondary phases, bottom interfaces or lead-deficient surface layers are formed in them, which highly justify the optimum dielectric-ferroelectric characteristics of these films.

4.2.3.5.2. PCT50 thin films

The variation of the dielectric constant (k') with temperature of the PCT50 films, measured at various frequencies, is shown in Figure 4.2.22.

A relaxor-like ferroelectric behaviour is observed for both PCT50-A and PCT50-B films. The T_m shifts towards higher values when the measuring frequency increases, as characteristic of a relaxor material. A diffuse transition with a T_m near -10 and -5 °C is observed for the PCT50-A and PCT50-B films, respectively. Values of k' of ~380 (PCT50-A) and ~545 (PCT50-B) are measured at room temperature and 10 kHz frequency. As in the case of the PCT24 films, lower k' values are obtained for the PCT films derived from the route A (PCT50-A), which is explained by its heterogeneous heterostructure deduced by RBS. The PCT50-B film has a more homogeneous heterostructure and hence higher k' values are obtained. These values, as expected, are lower than those of bulk ceramics (800-1500, at room temperature)³³, but are larger than those reported for PCT films with Ca^{2+} contents of 40 at% (~400)^{132,133} and close to those measured at room temperature in dielectric films of other compositions.²⁷⁷

The ferroelectric response of these films has not been tested, since this perovskite composition has a poor ferroelectric activity.¹⁷⁶

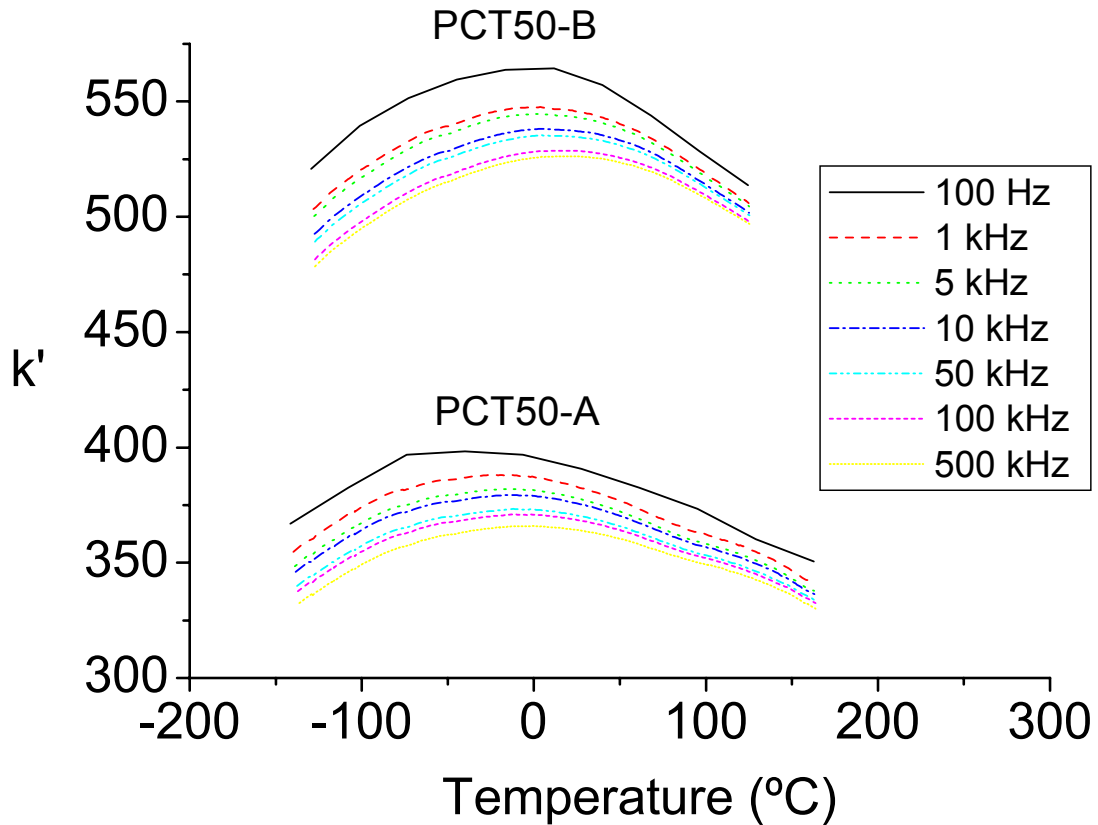


Figure 4.2.22. Variation of the dielectric constant (k') with temperature of the diol sol-gel derived PCT50 films, measured at various frequencies

4.2.3.5.2.1. Evaluation of the PCT50 films for applications in DRAMs and high-frequency components

As the PCT50-B film looks more promising for applications in Dynamic Random Access Memories (DRAMs) and voltage-tunable devices (mainly due to the high k' values at room temperature and the low ferroelectric hysteresis), a further and more complete dielectric characterisation was carried out on this film and results are stated below.

In memory devices, films with a low thickness are usually required because of the low voltages at which they work. Furthermore, the storage of charge in DRAM devices improves with the decrease of the film thickness. Thus, a PCT50-B ultra-thin film (thickness of ~ 100 nm) has been used for the results discussed below.

Figure 4.2.23 shows the field dependence dc-leakage currents at room temperature of this film.

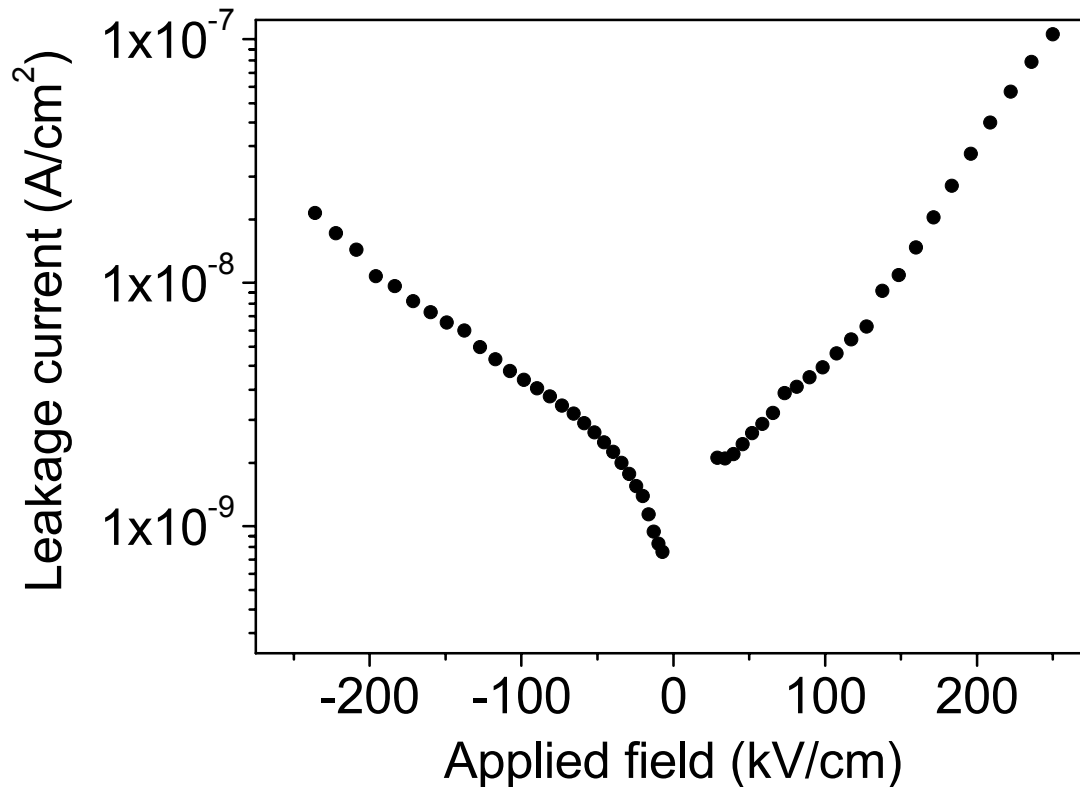


Figure 4.2.23. Leakage current behaviour of an ~80 nm thick PCT50-B film

Leakages currents below 10^{-8} A/cm² are obtained for the range of applied electric fields used in the measurements. Values below 10^{-7} A/cm² are required for computer charge storages devices (DRAMs), which prove the feasibility of this film for these applications. Furthermore, a relatively high dielectric constant was measured in this film at room temperature ($k' \sim 225$).

Since the capacitor of a DRAM must be successively charged-released between zero and V (refreshment of a DRAM), the testing of voltage drop of the film after a writing pulse was also performed by means of a homemade data acquisition set up.

Figure 4.2.24 shows the results obtained in the PCT50-B ultra-thin film.

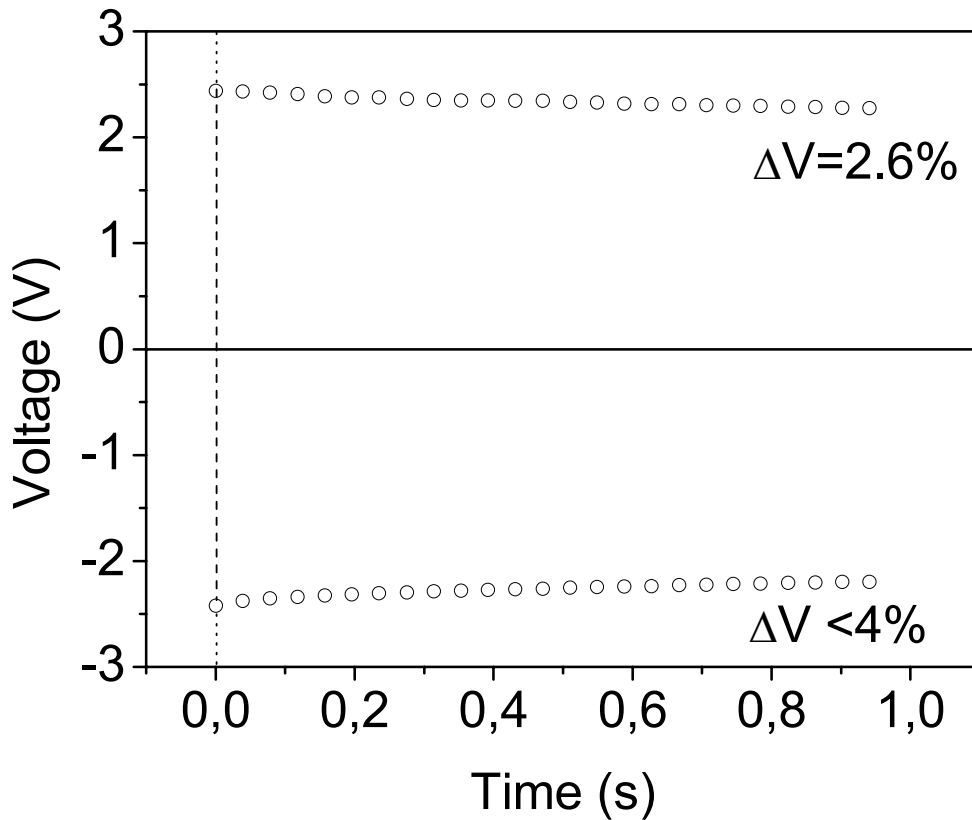


Figure 4.2.24. Time voltage drop after the writing pulse in a ~ 100 nm thick PCT50-B capacitor, for the two signs of voltage charge

In accordance with current recommendations,²⁷⁸ a capacitor for DRAMs applications should retain more than the 90 % of its charge after 200 ms (the usual refreshment time in a DRAM). The voltage drop of this film is less than 5 %, which fulfils these recommendations.

Therefore, the relatively high dielectric constant at room temperature of the PCT50-B ultra-thin film here evaluated, with the low leakage current densities measured and the ability to retain above the 95% of the written voltage after 200 ms, are indications of the reliable chance of these films for DRAMs applications.

On the other hand, the variation of the capacitance with voltage allows us to evaluate the feasibility of these films for voltage-tunable devices (varactors). In this case, a PCT50-B film of ~ 1200 nm was analysed. The $C(V)$ curves of this film are shown in Fig. 4.2.25 for different temperatures: -20 °C (below the transition temperature, T_m) and 20 , 70 and 100 °C (above the transition temperature).

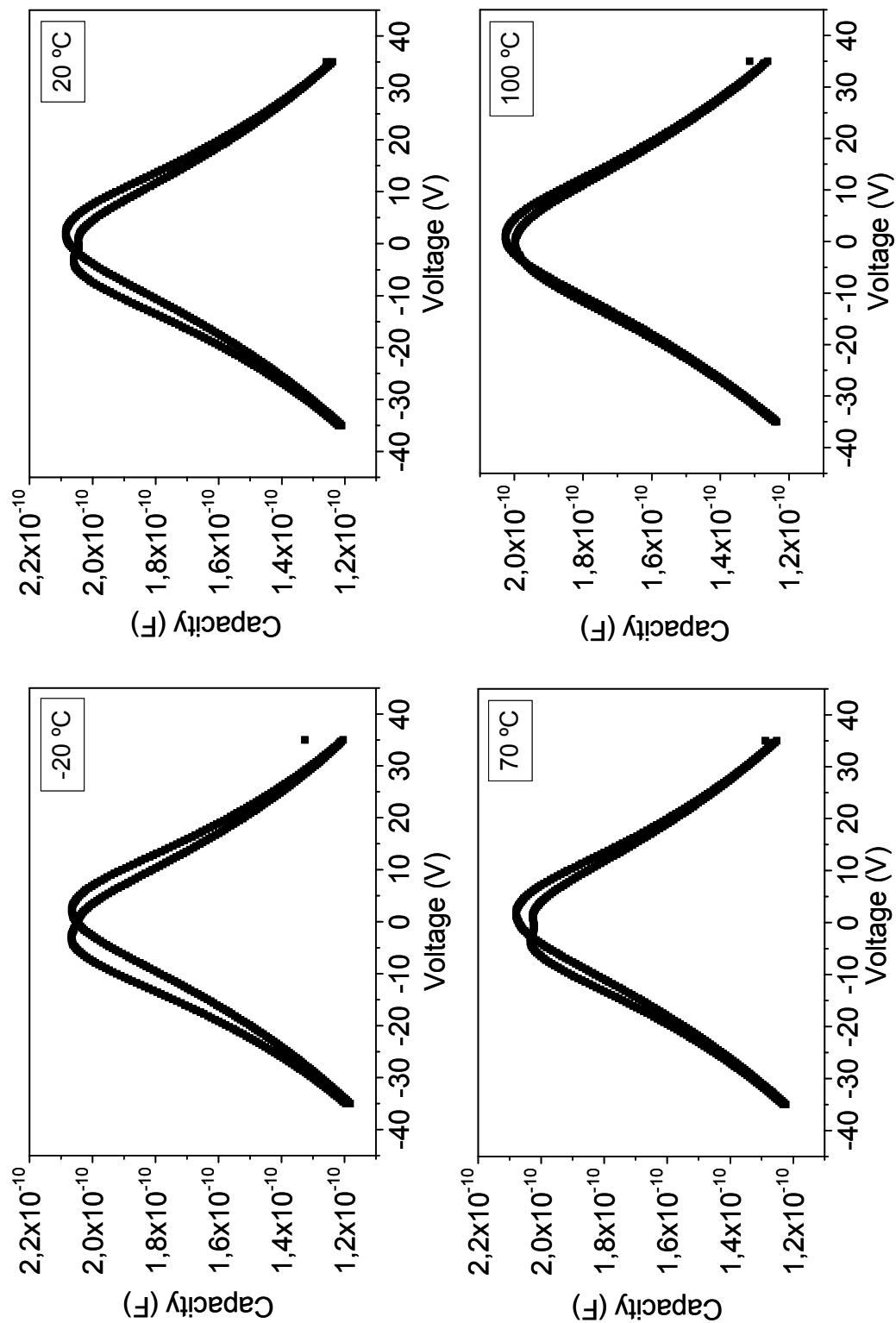


Figure 4.2.25. Capacitance-voltage (C-V) curves for a ~1200 nm thick diol sol-gel derived PCT50-B film measured at various temperatures (-20, 20, 70 and 100 °C)

From these results, the relative tunability ($T_{un,rel}$) of the film was calculated according to eq. [14] (see *Chapter II*). Also, the figure of merit (FOM) of the film, which combines both relative tunability and loss tangent ($\tan \delta$) parameters, was calculated (eq. [15] of *Chapter II*). Fig. 4.2.26 depicts the temperature dependence of tunability, figure of merit and $\tan \delta$ of this film.

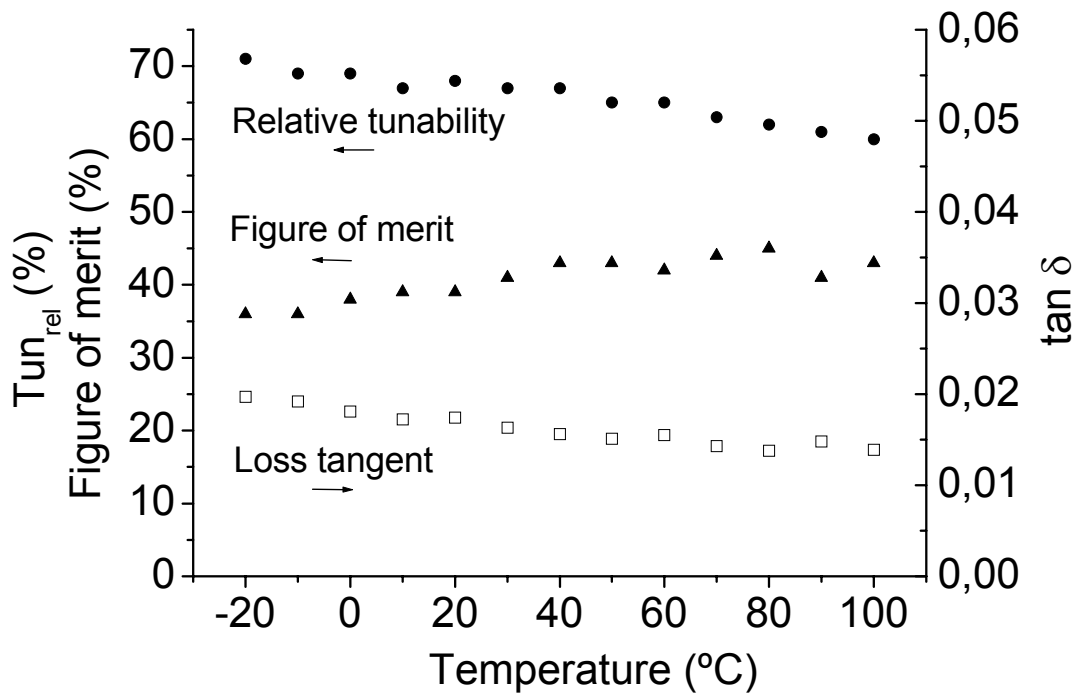


Figure 4.2.26. Relative tunability, figure of merit and $\tan \delta$ of the diol sol-gel derived PCT50-B film at different temperatures, measured at 1 kHz

From the C(V) curves of Fig. 4.2.25 it can be appreciated how the ferroelectric relaxor-like character of the PCT50-B film persists up to 100 °C, well above the transition temperature. Values of tunability shown in Fig. 4.2.26 are around 60-70 % and do not change more than 10 % with temperature. Figure of merit is close to 40 % and increases with temperature. This effect is due to the relaxor-like behaviour of these films, in which the dielectric loss tangent ($\tan \delta$) decreases with the increase of temperature. Both tunability and figure of merit values of the PCT50-B film are comparable to those reported for other alternative materials^{56,279} used in these applications, showing thus the potential use of these films in voltage-tunable components such as varactors.

4.2.4. REMARKS

- Three different diol-based sol-gel synthetic routes (A, B and C) have been successfully used in the preparation of stable PCT precursor solutions. The chemical processing followed for the solution synthesis determines the homogeneity of the solution and the pyrolysis and crystallisation of the derived films. Solution homogeneity and pyrolysis process affect the crystal structure, microstructure, heterostructure and electrical properties of the derived films. PCT24 and PCT50 films can be prepared from solutions derived from the route A. However, the route B has only been tested in the fabrication of the PCT50 films, whereas the route C does not allow the incorporation of high calcium contents and only PCT24 films could be prepared from it.
- Diol-based sol-gel PCT solutions derived from the synthetic route A are constituted by two differentiated distributions of particle size which correspond with the heterogeneous mixture of components (a Pb(II)-Ti(IV) sol and a water solution of calcium acetate) that form this solution. On the other hand, homogeneous sols with an uniform and single distribution of particle size are obtained from the routes B and C (real Ca(II)-Pb(II)-Ti(IV) sol). The particle size of these solutions and sols increases with the calcium content.
- The heterogeneity of the PCT solutions derived from the route A increases with time (aging effect) leading to the formation of precipitate around 8 months after the synthesis. The sols derived from the routes B and/or C are very stable with time, showing a low aging effect.
- The thermal decomposition of the PCT gels derived from these solutions is more homogeneous in those obtained from the routes B and C than in those derived from the route A, where the elimination of organics is produced in a wider temperature range. Calcium carbonate rests, which decompose at high temperatures, are comparatively lower in the gels derived from the route B than from the route A. Furthermore, this carbonate is not formed in the gels derived from the route C.
- Crystalline PCT films with a single perovskite phase are obtained in all the cases after a RTP treatment at 650 °C, as observed by XRD. A tetragonal structure is detected for the PCT24 films, whereas a pseudocubic structure is observed for the PCT50 films. A <100> preferred orientation is obtained in the films, although this orientation is lower in the films derived from the routes B and C.

-
- The microstructure of the PCT films is influenced by both the Ca^{2+} content and the solution chemistry. PCT24-A films are formed by grains with a mean size of ~ 150 nm, whereas average grain sizes of ~ 190 nm constitute the microstructure of the PCT24-C films. In the case of the PCT50-A and PCT50-B films, microstructures formed by grains of ~ 50 nm and columnar growth are obtained. Furthermore, porosity is observed in the cross-section SEM images of the films, which is significantly lower in the PCT24-C film.
 - PCT films derived from the route A (PCT24-A and PCT50-A) have a heterogeneous compositional profile, in which bottom interfaces and lead-deficient surfaces are formed. However, a homogeneous film heterostructure is deduced by the RBS analyses for the PCT films derived from the routes B and C (PCT24-C and PCT50-B), with a composition close to that of the expected PCT perovskite.
 - These PCT films with homogeneous microstructures have better dielectric and ferroelectric responses than the films derived from the route A. Higher values of remanent polarisation and lower coercive fields are measured in the hysteresis loops of the PCT24-C film ($\sim 22.9 \mu\text{C}/\text{cm}^2$ and ~ 77 kV/cm) respect to the PCT24-A film ($\sim 16.5 \mu\text{C}/\text{cm}^2$ and ~ 96 kV/cm). Furthermore, the values of dielectric constant are much higher in the former than in the latter one (~ 2210 and ~ 1190 respectively, at T_m). The PCT50 films have a clear relaxor-like ferroelectric character with higher values of the dielectric constant at room temperature for the PCT50-B film (~ 545) than for the PCT50-A film (~ 380).

CHAPTER IV

PART 3

LOW-TEMPERATURE PROCESSING OF PCT THIN FILMS BY PHOTOCHEMICAL SOLUTION DEPOSITION

One of the major challenges for the integration of ferroelectric materials into the silicon semiconductor industry is the reduction of the processing temperature of the active ferroelectric thin film.¹⁵ This should not exceed ~ 550 °C, since the silicon based substrates and other elements of the microelectronic device would be seriously damaged over this temperature. However, crystallisation of ferroelectric perovskites occurs at higher temperatures (over 600 °C).

With this aim, particular attention has been paid to the low-temperature sol-gel processing of ferroelectric thin films, since sol-gel enables the easy preparation of precursors with a high stoichiometric control and tailored physicochemical properties.^{106,108,114} One of the successful approaches in the low-temperature sol-gel processing of films is the so-called UV sol-gel photoannealing¹⁶² (PhotoChemical Solution Deposition, PCSD), which has resulted in the preparation of high-k single oxide thin films at low temperatures.^{163,280,281}

In general, low-temperature ceramic sintering techniques are also effective to reduce hazards volatilisation and exhaust gas emission during the processing, in addition to lower the energy consumption (via thermal heating) of the whole process.¹⁵³ In the case of the PCT films here presented, it is expected that the decrease of the processing temperature may avoid the lead volatilisation during firing.

In this work, ferroelectric PCT thin films supported onto silicon substrates have been prepared at low temperatures by means of PCSD.^{161,282} The thermal treatment of crystallisation of the films was carried out in a UV-assisted RTP equipment at the *R+ D Department of the JIPELEC division (QUALIFLOW)*¹⁹⁹ in Grenoble (France). This equipment was used for the crystallisation of the films during a two-week short-term scientific mission supported by the European Action COST528 on “*Chemical Solution Deposition of Thin Films*”. The functionality of the resulting films and the feasibility for their use in silicon integrated microelectronic devices is here evaluated.

4.3.1. PHOTO-ACTIVATION OF THE PCT SOLUTIONS AND UV-ASSISTED LOW-TEMPERATURE PROCESSING OF THE PCT FILMS

Diol-based sol-gel PCT precursor solutions were prepared according to the synthetic route A. Solutions with nominal compositions of $(\text{Pb}_{0.76}\text{Ca}_{0.24})\text{TiO}_3$ (PCT24) and $(\text{Pb}_{0.50}\text{Ca}_{0.50})\text{TiO}_3$ (PCT50) were synthesised. The photosensitivity of sol-gel solutions depends on the chemical nature of their components. Photo-reactive generators can be added to the sol to achieve photo-activation or, as here tested, solutions can be synthesised from metal precursors containing ligands that absorb UV-light.^{160,283,284} The PCT solutions derived from the synthetic route A (PCT-A solutions) use a modified titanium alkoxide (titanium di-isopropoxide bis-acetylacetonate, $\text{Ti}(\text{OC}_3\text{H}_7)_2(\text{CH}_3\text{COCHCOCH}_3)_2$) that has two acetylacetonate groups. These β -diketonate complexes have characteristic absorption bands in the near-ultraviolet region of the electromagnetic spectrum (200-380 nm) due to $\pi \rightarrow \pi^*$ electronic transitions.²⁸⁵ The photo-excitation of this transition produces the dissociation of the chelating bonds.²⁸¹ Thus, an appreciable photosensitivity of these solutions is expected.

The molecular structure of the β -diketonate titanium alkoxide reagent used in the synthesis of the PCT precursor solutions is shown in Figure 4.3.1, together with the UV-absorption spectrum of the solutions.

A maximum in the UV-absorption of the solution at $\lambda < 275$ nm is observed (Fig. 4.3.1b), which is in the range where the acetylacetonate groups absorb UV-light. Thus, the use of this titanium reagent in the synthesis procedure provides PCT solutions which are inherently photosensitive under ultraviolet (UV) light.¹⁶⁰

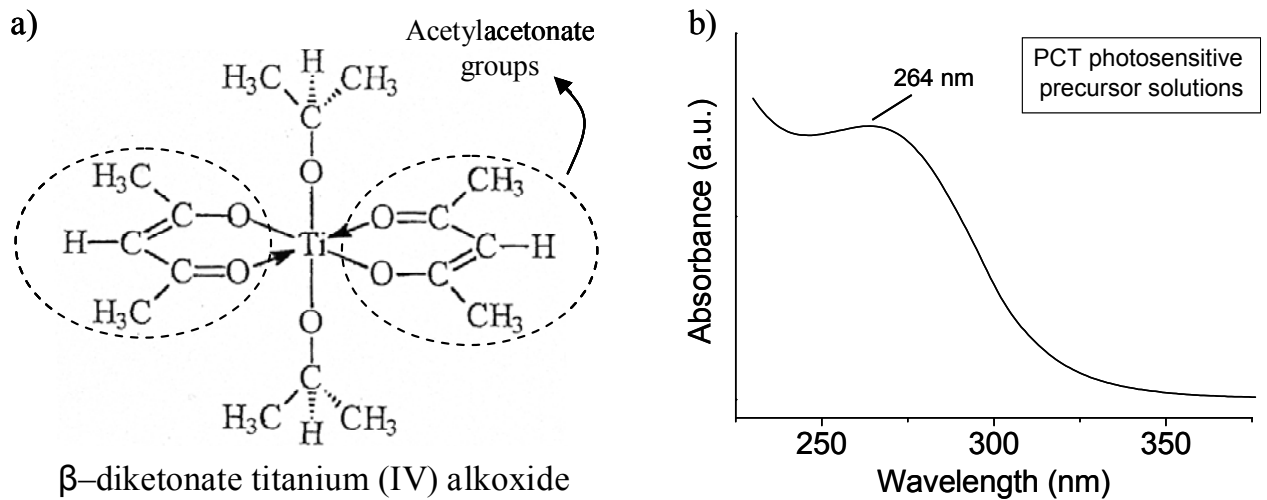


Figure 4.3.1. Molecular structure of the titanium di-isopropoxide bis-acetylacetonate chemical reagent (a) and UV absorption spectrum of the PCT solutions (b)

However, as the β -diketonate ligands are responsible of this absorption, the UV-irradiation of the derived sol-gel films should be carried out at a temperature at which this compound would still be inside the chemical system. In order to set the optimum temperature for the UV-irradiation, the thermal decomposition of the PCT gel powders was studied by Differential Thermal and Thermogravimetric Analysis (DTA-TGA).

Figure 4.3.2 shows the DTA-TGA curves obtained in the PCT24 and PCT50 gel powders derived from the respective photosensitive PCT solutions.

As it was described in previous *Part 2* of this chapter, the elimination of organic compounds in the PCT gels occurs at temperatures between 200 and 500 °C. Thus, 250 °C was selected in the present work as the temperature at which the sol-gel films could be irradiated (see solid lines in the graphs). At this temperature, the acetylacetonate groups responsible of UV-absorption are still present in the gel film and therefore, their electronic excitation and the subsequent activation of the organic compounds of the system would be produced by the UV-light.

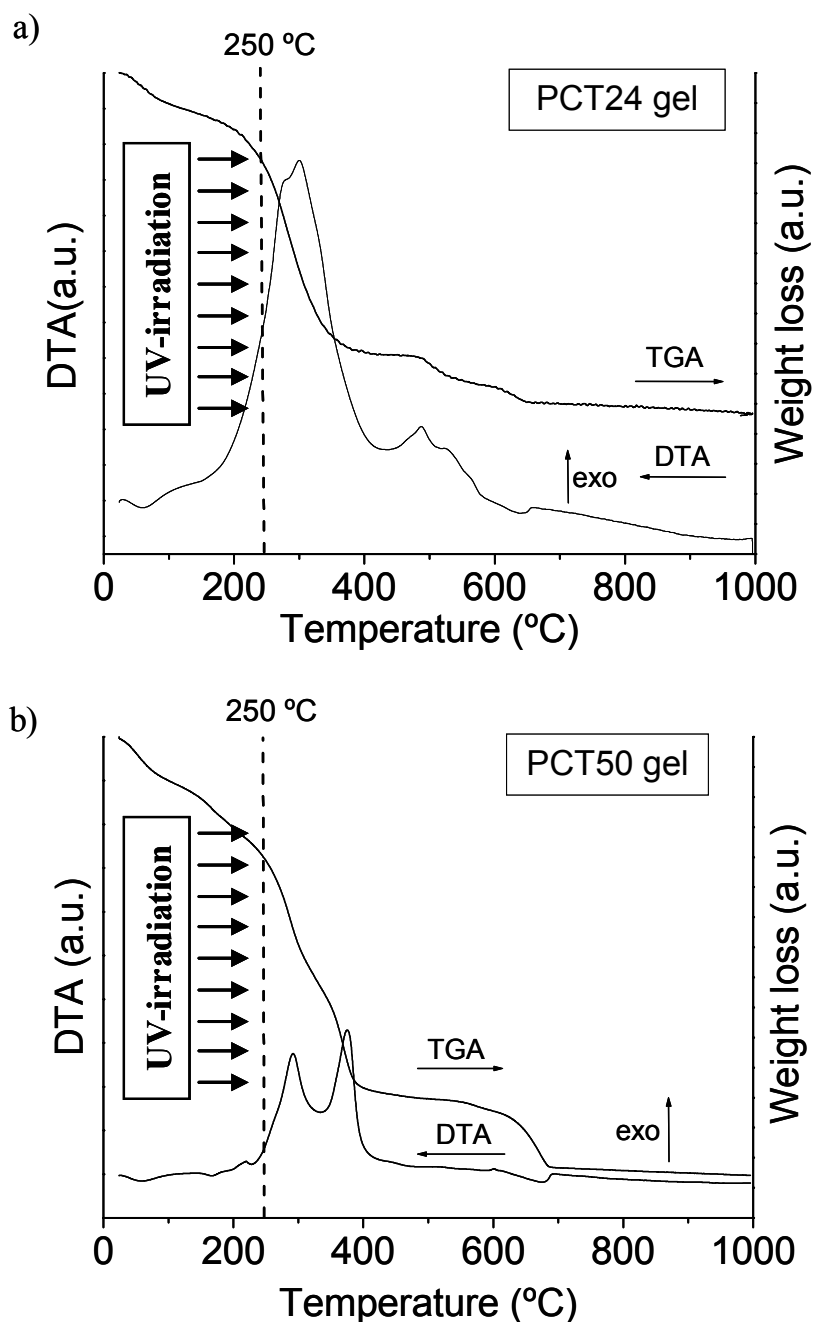


Figure 4.3.2. DTA-TGA of the diol sol-gel derived PCT24 (a) and PCT50 (b) gels, showing the optimum temperatures for the UV-irradiation of the gel films.

The effectiveness of the UV-irradiation on the photo-excitation and subsequent dissociation of the alkyl group-oxygen bonds of the organic components of the gel was analysed. Figure 4.3.3 shows the infrared (IR) spectra of two PCT films deposited onto sapphire substrates and treated in air at 250 °C for 240 s, with and without UV-irradiation.

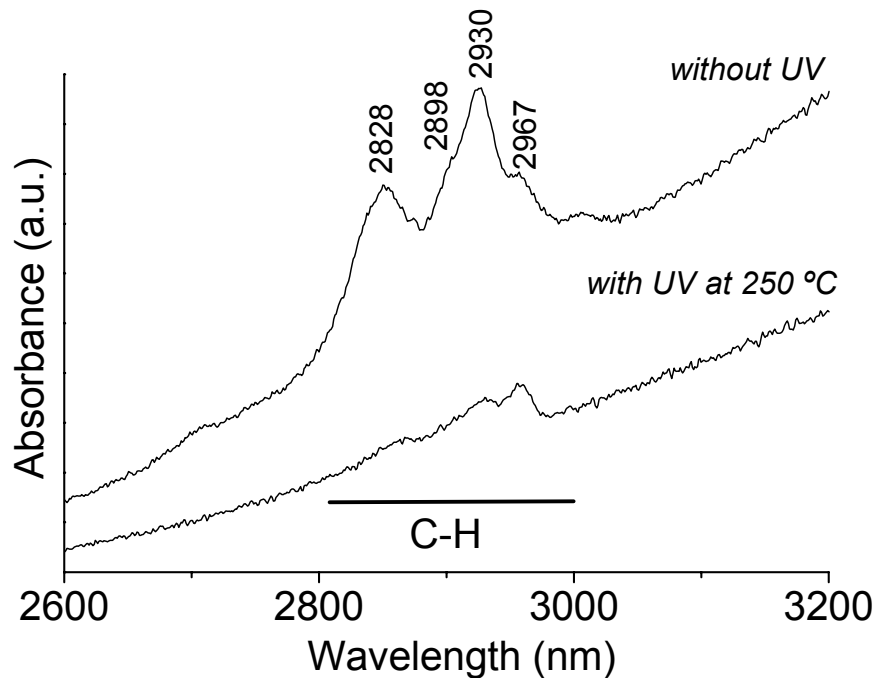


Figure 4.3.3. FTIR spectra of the gel layers derived from the photosensitive diol sol-gel solutions and treated at 250 °C for 240 s with and without UV-irradiation

The spectrum of the non-irradiated gel film shows the stretching vibrations of the CH₂ groups ($\nu_{\text{asym}} \sim 2930 \text{ cm}^{-1}$ and $\nu_{\text{sym}} \sim 2828 \text{ cm}^{-1}$) and of the CH₃ groups ($\nu_{\text{asym}} \sim 2967 \text{ cm}^{-1}$ and $\nu_{\text{sym}} \sim 2898 \text{ cm}^{-1}$), indicating the presence of C-H bonds of residual organics. However, these bands have almost disappeared in the irradiated film. Here, UV-irradiation has produced the cleavage of the C-H bonds enhancing the elimination of the organics from the film at a relatively low temperature of 250 °C, the temperature selected for the UV-irradiation of the films.

After irradiation, the fabrication of the PCT perovskite films was tested at temperatures $\leq 500 \text{ °C}$. Multi-oxide ferroelectric perovskite films have been previously prepared in the literature at these low temperatures, observing the formation of the perovskite phase at $\sim 500 \text{ °C}$.¹⁷²⁻¹⁷⁴ However, these films only showed a clear ferroelectric response when processed at higher temperatures, over 550 °C.¹⁶⁰ From the application point of view, it is not only important to decrease the crystallisation temperature of the PCT films of this work, but also the preservation of their properties. In the next, this point will be discussed, showing the competitiveness of the PCSD technique for the integration of multi-functional perovskite thin films with the Si-technology.

4.3.2. LOW-TEMPERATURE PCT THIN FILMS

PCT24 and PCT50 films onto Pt/TiO₂/SiO₂/Si(100) substrates were deposited from the former photosensitive solutions and subjected to UV-irradiation at 250 °C for 240 s and further crystallisation at temperatures \leq 500 °C. Irradiation and crystallisation of the films were carried out in a UV-assisted processor¹⁹⁹ (see previous section 2.3.3.2). This equipment was developed by JIPELEC-QUALIFLOW²⁸² and it was used in this work during a short stay of the author at the R+D Department of the JIPELEC division in Grenoble (France).

Air or oxygen atmospheres were used to promote the *photo-excitation* of the organics¹⁶² or the *ozonolysis*²⁸⁶ in the films. The *photo-excitation* of the organics contained in a sol-gel derived film consists in their electronic excitation by the photons of the UV-light and their subsequent elimination from the film. *Ozonolysis* is produced when the film is irradiated in an oxygen atmosphere; oxygen (O₂) is readily dissociated under UV-light, forming ozone (O₃) and active oxygen species O(¹D). O₃ is a strong oxidant agent that produces the rapid combustion of the organic compounds and the active oxygen species can react with suboxides, improving stoichiometry and decreasing the density of defects and oxygen vacancies.²⁸⁶⁻²⁸⁸

Structural, microstructural and heterostructural characterisation of the films thus obtained has been carried out by means of different techniques. Furthermore, the electrical properties of these films are discussed and related to the ferroelectric behaviour in the case of the PCT24 films and the relaxor-ferroelectric characteristics of the PCT50 films, which make them attractive for their use in a wide range of applications.

4.3.2.1. Crystalline structure of the films by X-Ray Diffraction with the Grazing Incidence (GIXRD) and with the Bragg-Brentano (XRD) geometry

Figure 4.3.4 shows the GIXRD patterns of the PCT films prepared by PCSD at different temperatures and using air or oxygen firing atmospheres.

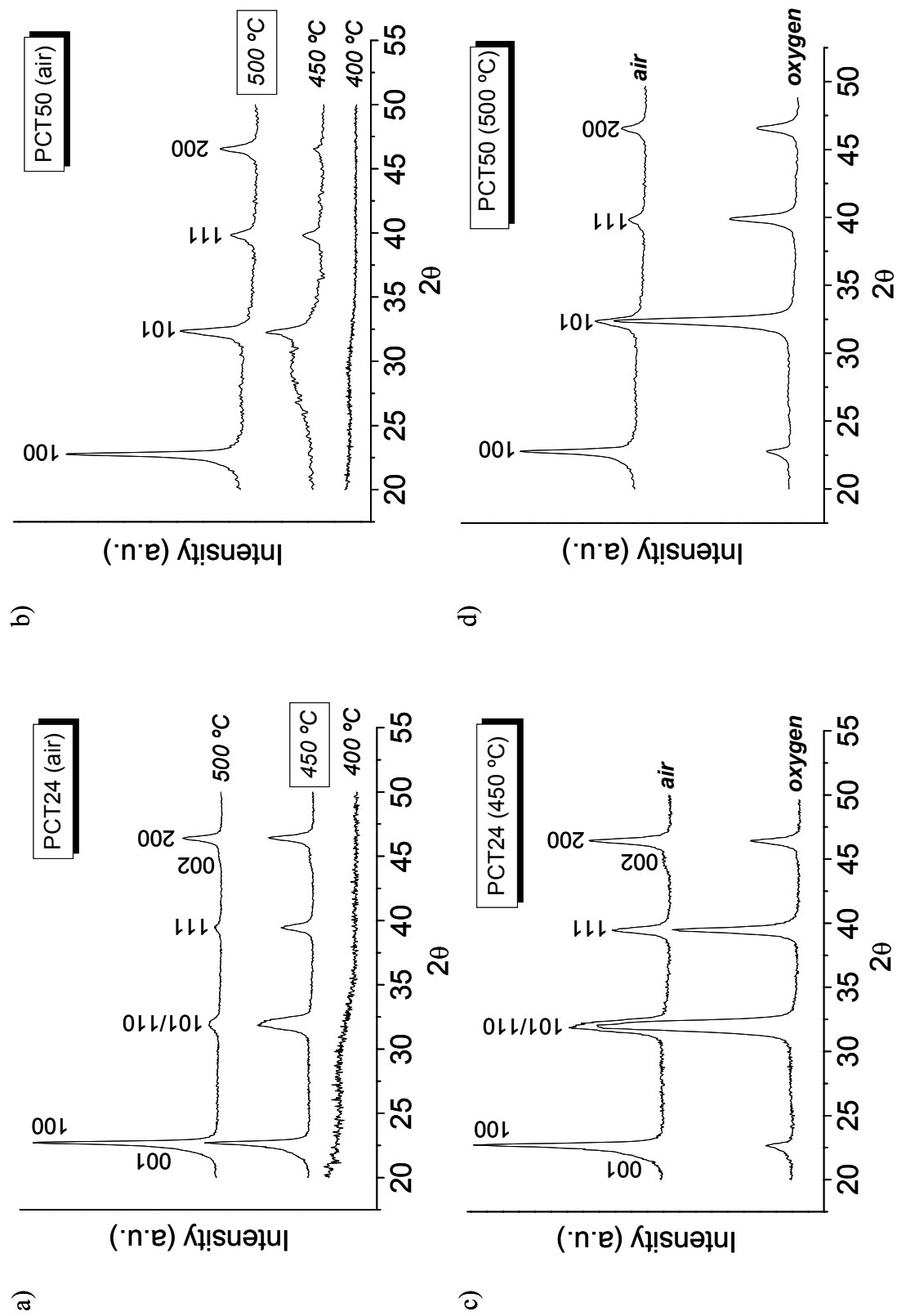


Figure 4.3.4. GIXRD patterns of the UV-irradiated PCT24 (a) and PCT50 (b) films processed in air at different temperatures, and of the UV-irradiated PCT24 films at 450 °C (c) and PCT50 films at 500 °C (d) processed in air or oxygen atmosphere

A single perovskite phase appears at 450 °C in the PCT24 films, whereas for the PCT50 films this phase is formed at higher temperatures (500 °C). This is in agreement with the studies shown in previous sections. The films show a pseudocubic structure without any noticeable secondary phases or rests of amorphous phases detected. The temperature at which the crystallisation of the perovskite occurs seems not to be affected by the environment of air or oxygen used during the irradiation and thermal treatment of the films.

However, the use of air or oxygen during the irradiation and heating does seem to influence the texture obtained in the films, as deduced from the XRD patterns of Figure 4.3.5. This figure shows the XRD patterns of the PCT24 and PCT50 films processed at 450 and 500 °C, respectively, in air or oxygen atmosphere.

In these patterns, the 111 reflections of the Pt bottom electrode and of the PCT films are overlapped. This does not make possible to detect possible preferred orientations of the perovskite film along the $\langle 111 \rangle$ axis. From the XRD analysis of this work it can be only deduced that the films processed in air have a $\langle 100 \rangle$ preferred orientation, whereas in oxygen this perovskite orientation does not appear as a preferred one.

Although the first perovskite peaks also appear at low temperatures (see section 4.2.3.1) in the GIXRD patterns of the PCT24 and PCT50 films processed without irradiation (conventional RTP heating), these films contained a considerable amount of secondary amorphous and nanocrystalline phases that spoiled their dielectric and ferroelectric responses. Now, PCT24 and PCT50 perovskite films are formed at 450 and 500 °C, respectively by PCSD, temperatures lower than the maxima recommended in the semiconductor industry to not damage the silicon-based microelectronic device (~ 500 °C). But, their properties have to be tested in order to prove their ferroelectric and/or dielectric character, in spite of the low-temperature processing, and to evaluate the reliability of these films in devices.

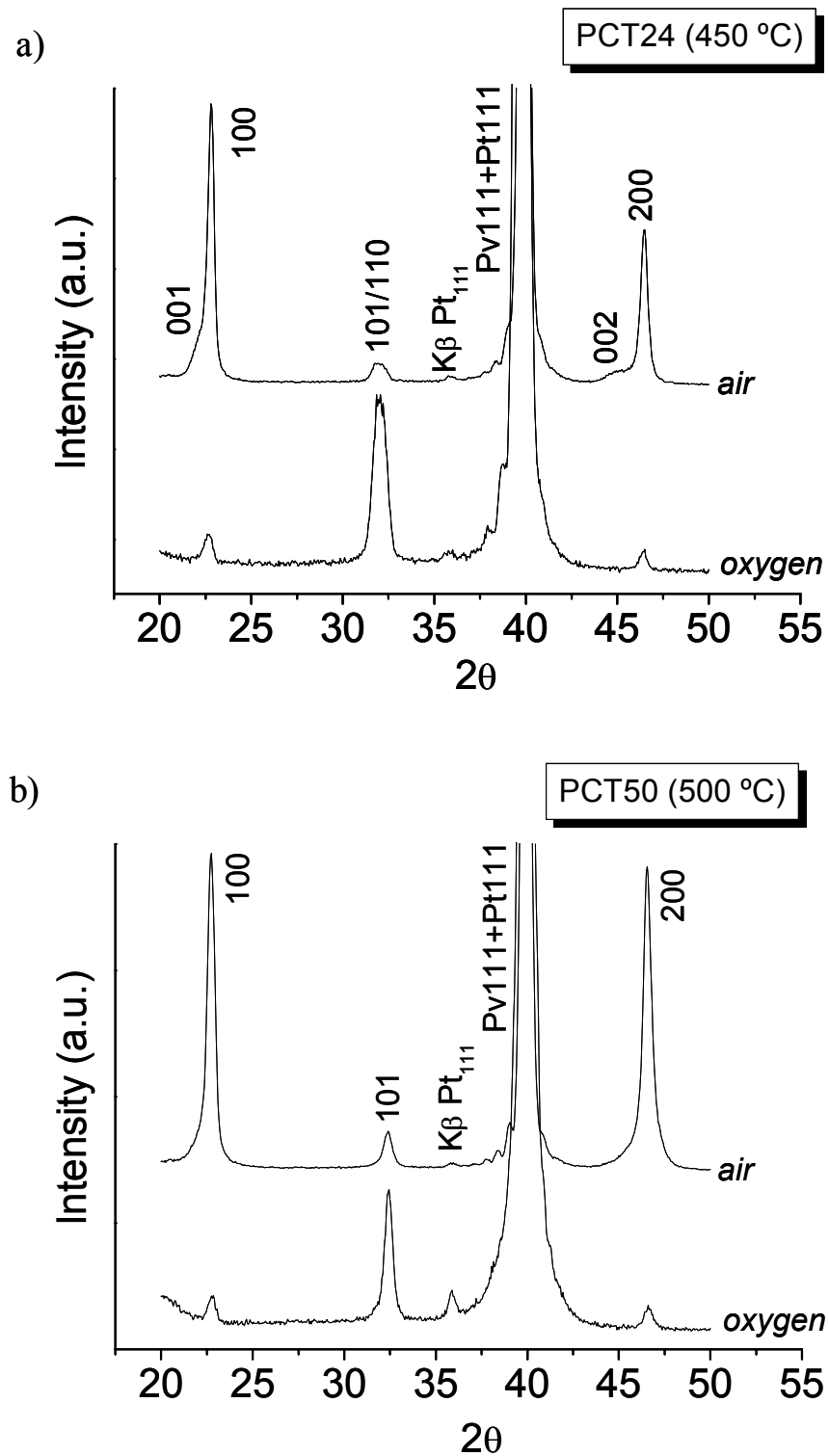


Figure 4.3.5. XRD patterns of the UV-irradiated PCT24 films crystallised at 450 °C (a) and of the UV-irradiated PCT50 films crystallised at 500 °C (b), using air or oxygen atmosphere

4.3.2.2. Microstructure of the films by Scanning Electron Microscopy (SEM) and Scanning Force Microscopy (SFM)

The microstructure of the films surface was observed by Scanning Electron Microscopy operating under field emission conditions (FEGSEM). Figure 4.3.6 shows the plan-view micrographs obtained in the PCT24 and PCT50 films processed in air or oxygen. Cross-section images of these films are also shown in Figure 4.3.7.

Regions with different contrast are shown in the micrographs of the films surfaces (Fig. 4.3.6) which may be associated to differentiated phases present in the film (phases of different grain size, different amount of porosity, different composition, etc.). However, these differences in contrast are not seen in the cross-section images of Fig. 4.3.7. Here, films sections with homogeneous microstructures and with a similar grain size of ~30 nm are observed for all the PCT films. The thicknesses of the PCT films calculated from these images are between 250-300 nm.

The topography of the PCT24 films was also analysed by SFM (Figure 4.3.8). Amplified regions of the films surfaces are shown inserted in the images in order to appreciate grain size.

The line profile obtained along the films surfaces reveals areas with variations in height up to around 15 nm (insets of Fig. 4.3.8). Furthermore, note that the aspect of these images is rather similar to the SEM images obtained on the same surfaces (Fig. 4.3.6), which suggest that the main contribution to the contrast in the latter images is due to the irregular topography of the samples and not to the presence of secondary phases. This is in agreement with the GIXRD patterns of Fig. 4.3.4, where second crystalline phases are not detected. From the amplified images, an average grain size of ~30 nm is measured for both PCT24 films, in agreement with those sizes obtained by SEM.

These SEM and SFM results combined with the GIXRD and XRD data seem to indicate that the films are mainly formed by a perovskite phase, not observing secondary phases or phase segregation. These PCT films are nanostructured, formed by grains with an average size of ~30 nm, which is much lower than that measured in PCT24 and PCT50 films processed at higher temperatures (650 °C) without irradiation, ~150 and ~50 nm, respectively (see previous section 4.2.3.3). In the latter films, hereinafter named “conventional films”, the grain size obtained is strongly affected by the Ca²⁺ content of the PCT composition, obtaining lower grain sizes as the Ca²⁺ content in the PCT system is higher.²⁴⁰ The low temperature at which the films are now processed by PCSD is responsible of the low grain size of these films.⁹⁶

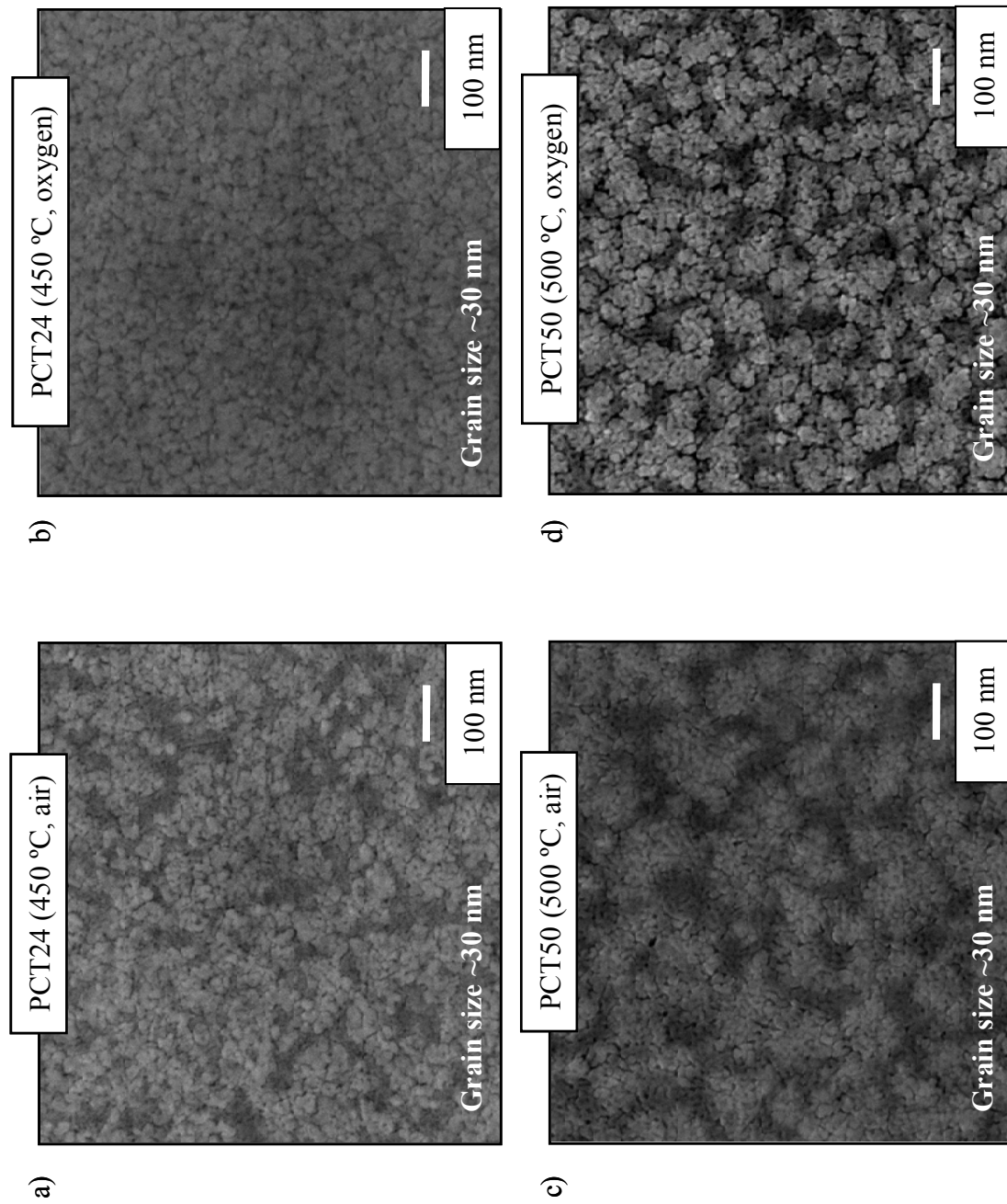


Figure 4.3.6. SEM micrographs (plan-view) obtained in the; PCT24 film processed by UV-assisted RTP at 450 °C in air (a), PCT24 film processed by UV-assisted RTP at 450 °C in oxygen (b), PCT50 film processed by UV-assisted RTP at 500 °C in air (c) and PCT50 film processed by UV-assisted RTP at 500 °C in oxygen (d)

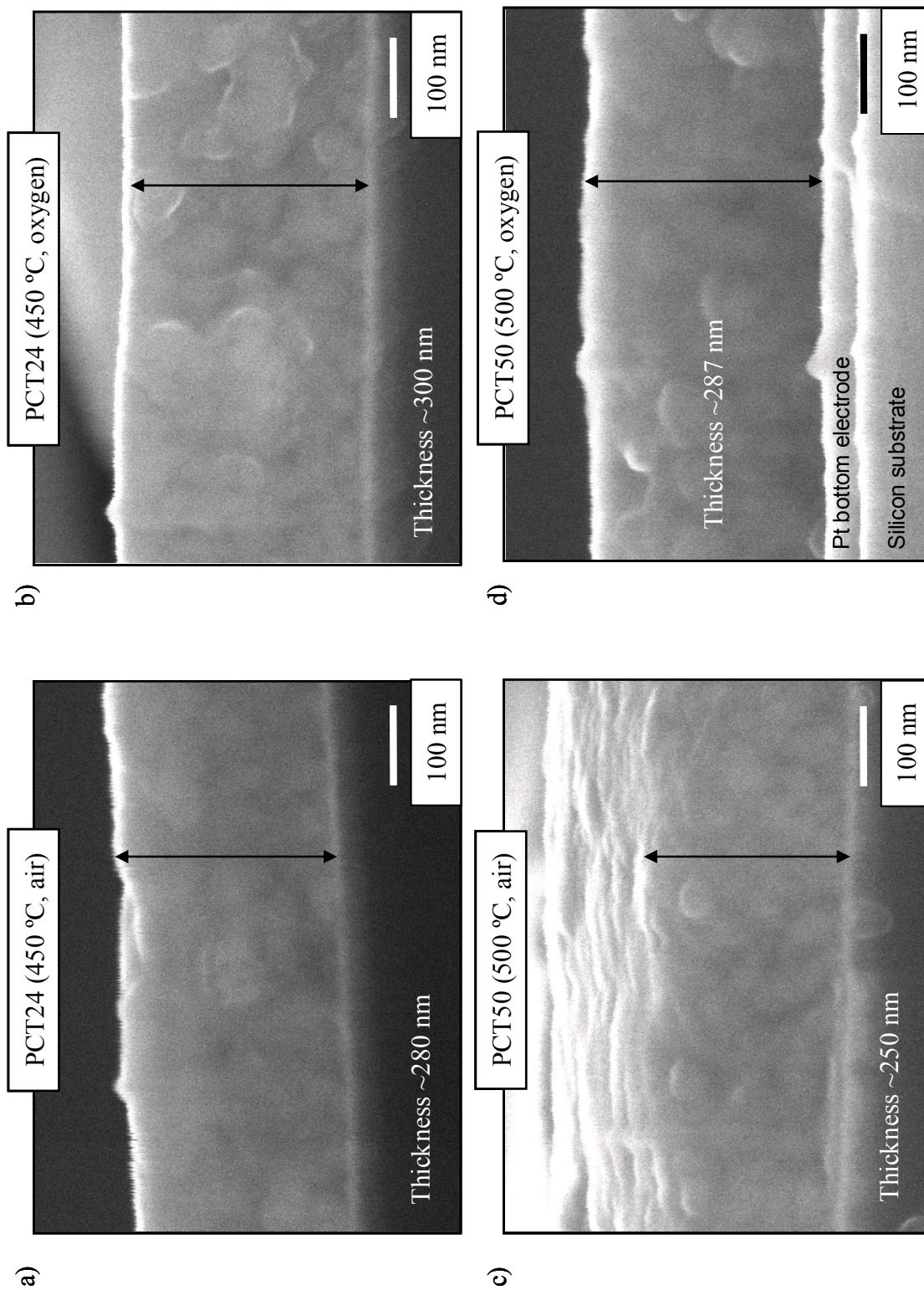


Figure 4.3.7. SEM micrographs (cross-section) obtained in the; PCT24 film processed by UV-assisted RTP at 450 °C in air (a), PCT24 film processed by UV-assisted RTP at 450 °C in oxygen (b), PCT50 film processed by UV-assisted RTP at 500 °C in air (c) and PCT50 film processed by UV-assisted RTP at 500 °C in oxygen (d)

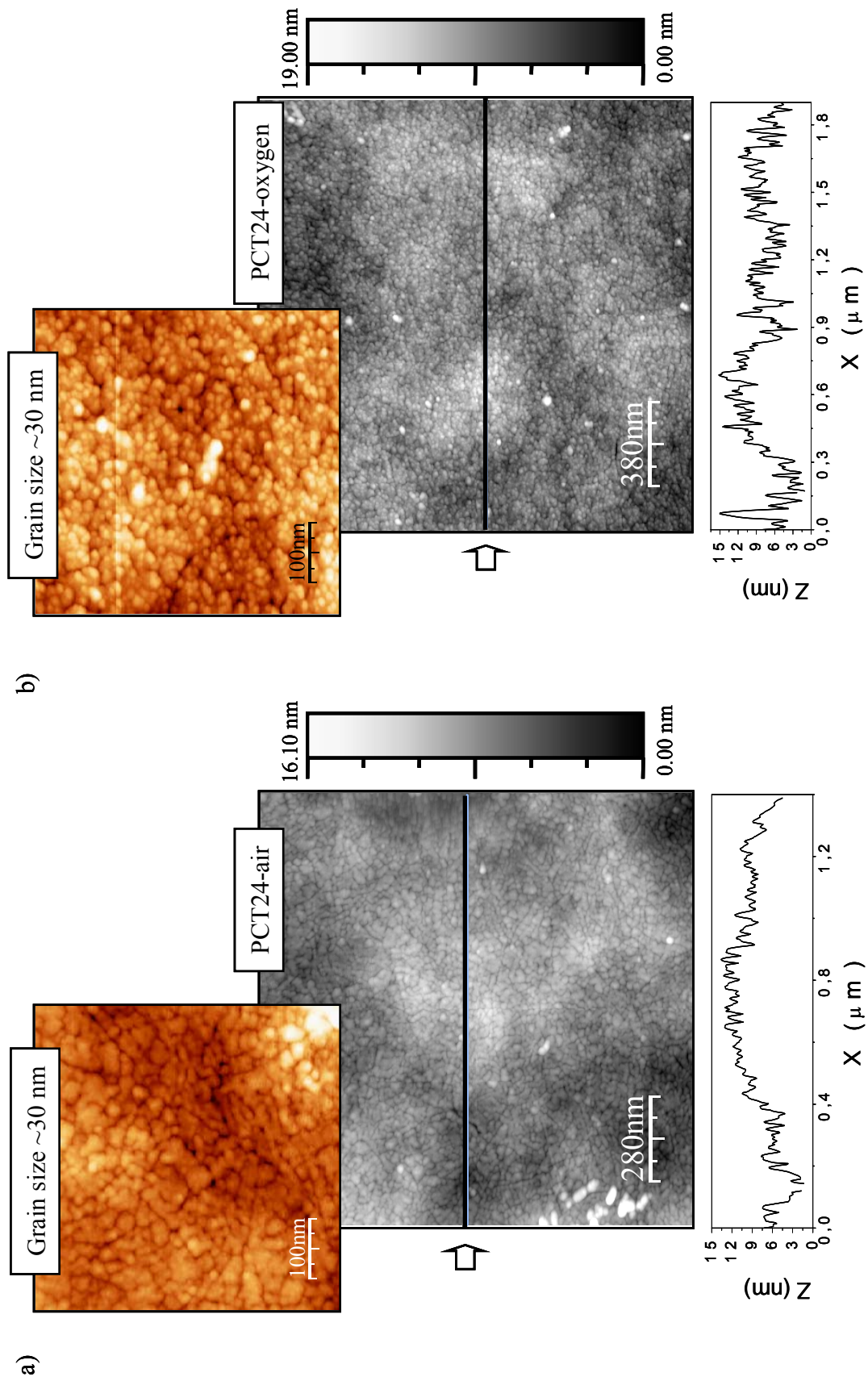


Figure 4.3.8. SFM images of the PCT24 film processed by UV-assisted RTP in air (a) and oxygen (b). Insets show line profile of the images

4.3.2.3. Films heterostructure by Rutherford Backscattering Spectroscopy (RBS)

The RBS experimental spectra of the films and their corresponding simulations are depicted in Figures 4.3.9 and 4.3.10 for the PCT24 and PCT50 films, respectively. Note that the analysis has been carried out with a 7 MeV $^{14}\text{N}^+$ beam which provides higher resolution than the 2 MeV $^4\text{He}^{2+}$ beam used in the RBS experiments of section 4.2.3.4. A good fit between the experimental and simulated curves is obtained for all the films. The film heterostructures deduced from these analyses are also shown in the figures.

The high resolution of these measurements makes possible to detect in the spectra the different PCT layers (4 layers) deposited for the fabrication of the films. Thus, the spectra show a compositional discontinuity from one layer to another, where a drop in the amount of the elements (Pb, Ca, Ti) forming the perovskite film is observed. This could be attributed to a larger porosity or roughness in these zones among the different constituent layers of the film.

For the PCT24 films, the RBS analyses show that the bulk film has an average composition of $\text{Pb}_{0.84\pm 0.08}\text{Ca}_{0.24\pm 0.02}\text{Ti}_{1.00\pm 0.10}\text{O}_{3.00\pm 0.30}$ for both films, processed in air or oxygen atmosphere. A lead gradient along the bulk film with a concentration increasing from the top to the bottom is also observed. The top surface of the films have the nominal composition of the expected perovskite, that is $(\text{Pb}_{0.76}\text{Ca}_{0.24})\text{TiO}_3$. Note that the average composition of these films is the same than that of the synthesised precursor solution, which contains a 10 mol% of lead excess (see experimental section). This lead excess is lost by volatilisation in the films processed at higher temperatures. The RBS results obtained indicate that now the lead loss by volatilisation is minimised in the PCT24 films annealed at 450 °C.

In the case of the PCT50 films, the average elemental compositions of the bulk film deduced from the RBS data are close to that of the expected perovskite $(\text{Pb}_{0.45\pm 0.04}\text{Ca}_{0.50\pm 0.05}\text{Ti}_{1.00\pm 0.10}\text{O}_{3.00\pm 0.30})$ for the film processed in air, and $\text{Pb}_{0.51\pm 0.05}\text{Ca}_{0.50\pm 0.05}\text{Ti}_{1.00\pm 0.10}\text{O}_{3.00\pm 0.30}$ for the film processed in oxygen). In these films, a 10 mol% of lead excess was also introduced during the synthesis of the precursor solutions, but now the slightly higher temperature (500 °C) at which these films were annealed respect to that used for the PCT24 films seems to favour the lead volatilisation^{289,290}.

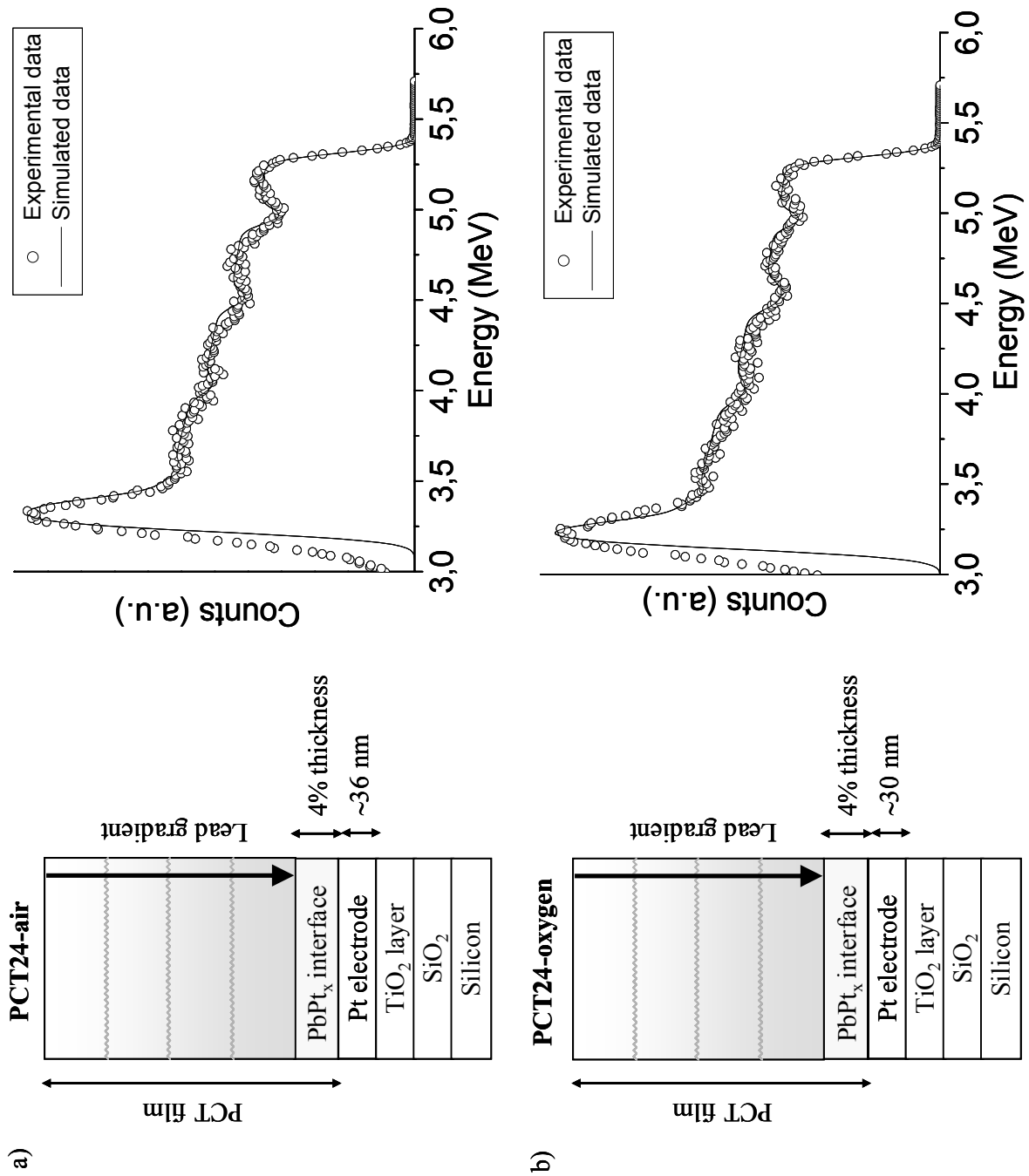


Figure 4.3.9. RBS spectra and heterostructure deduced from the RBS data of the low-temperature PCT24 films processed in air (a) or oxygen (b)

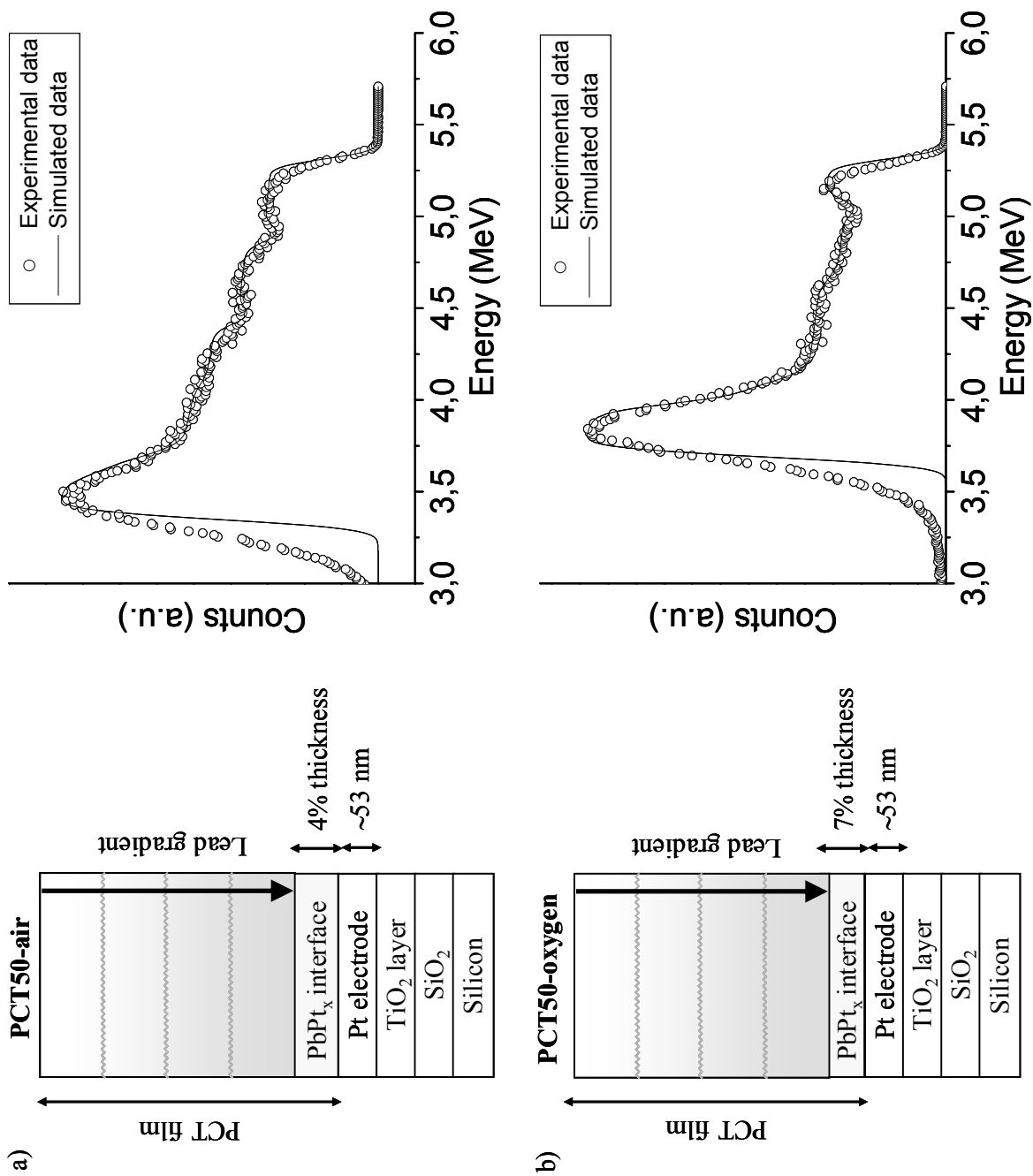


Figure 4.3.10. RBS spectra and heterostructure deduced from the RBS data for the low-temperature PCT50 films processed in air (a) or oxygen (b)

All of these films processed at low temperatures (450 °C for the PCT24 films and 500 °C for the PCT50 films) have developed very thin interfaces, around 4 % of the total film thickness (Figs. 4.3.9 and 4.3.10), much thinner than those developed in the “conventional films” shown in previous sections. Furthermore, the interdiffusion between the PCT film and the Pt bottom electrode is minimised at these low temperatures. The RBS analyses indicate that the composition of these interfaces is close to that of a PbPt_x intermetallic compound.^{291,292}

From the RBS data, thicknesses of ~272 and ~290 nm are calculated for the PCT24 films processed in air or in oxygen, respectively. For the PCT50 films, average thicknesses of ~265 and ~201 nm are obtained for the films in air or oxygen, respectively. The thickness of the Pt bottom electrode calculated from the RBS data is also indicated in Figs. 4.3.9 and 4.3.10. Films thicknesses calculated by RBS are similar to those measured by SEM (see Fig.4.3.7), which is an indication of a high bulk density of the films and a film composition close to that of the expected perovskite composition.

A summary of the most important heterostructural features deduced by RBS for the PCT films of this section is shown in Table 4.3.1.

Table 4.3.1. RBS data obtained in the PCT films processed at low temperatures

Nominal composition	Film	PCT film				Film thickness (nm)	
		PCT layer		Bottom interface		SEM	RBS ²
		Average composition ¹	Percentage of film thickness	Composition	Percentage of film thickness		
$(\text{Pb}_{0.76}\text{Ca}_{0.24})\text{TiO}_3$	PCT24 (air)	$(\text{Pb}_{0.84}\text{Ca}_{0.24})\text{TiO}_3$	96%	PbPt_x	4%	~280	~272
	PCT24 (oxygen)	$(\text{Pb}_{0.84}\text{Ca}_{0.24})\text{TiO}_3$	96%	PbPt_x	4%	~300	~290
$(\text{Pb}_{0.50}\text{Ca}_{0.50})\text{TiO}_3$	PCT50 (air)	$(\text{Pb}_{0.43}\text{Ca}_{0.50})\text{TiO}_3$	96%	PbPt_x	4%	~250	~265
	PCT50 (oxygen)	$(\text{Pb}_{0.51}\text{Ca}_{0.50})\text{TiO}_3$	93%	PbPt_x	7%	~287	~201

(1) Error of ~10 %. The formation of films with perovskite structure is assumed

(2) Thickness was calculated considering the nominal composition of the perovskite and its theoretical density

4.3.2.4. Dielectric and ferroelectric properties of the PCT films. Applications in microelectronic devices

The functionality in microelectronic devices of the PCT films obtained at temperatures compatible with those used in the Si-technology is evaluated in this section.

4.3.2.4.1. Low-temperature processed PCT24 thin films

The dielectric behaviour of the PCT24 films was analysed by measuring the variation of the dielectric constant (k') with temperature, at various frequencies. Results obtained for the films processed in air or oxygen are depicted in Figure 4.3.11. The variation of the loss tangent ($\tan \delta$) with temperature is also indicated in the figure.

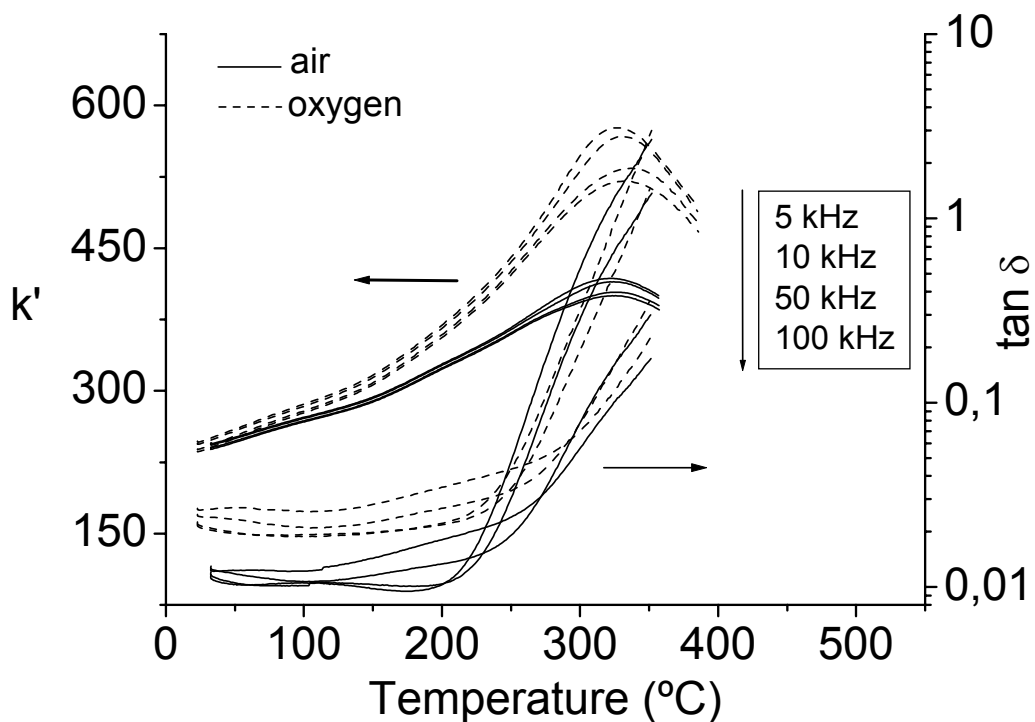


Figure 4.3.11. Variation of the dielectric constant (k') and loss tangent ($\tan \delta$) with temperature of the PCT24 films processed by UV-assisted RTP at 450 °C in air or oxygen, measured at various frequencies

A clear ferro-paraelectric transition is observed for both PCT24 films at similar temperatures ($T_m \sim 334$ and ~ 331 °C, respectively). However, higher values of the dielectric constant are obtained in the film processed in oxygen than in air (e.g. ~ 567 and ~ 413 at T_m , respectively). These values are nevertheless lower than those measured in the conventional PCT24 films, processed at 650 °C (between 1200-1600 at T_m).²⁹³ The loss tangent of the films of Fig. 4.3.11 is close to 0.01 at room temperature.

The ferroelectric hysteresis loops of these films are shown in Figure 4.3.12. The non-switching contribution to the ferroelectric domain polarisation is also depicted in this figure.

Both PCT24 films have well-defined ferroelectric hysteresis loops (Fig. 4.3.12a) with the same values of remanent polarisation ($P_r \sim 11 \mu\text{C}/\text{cm}^2$) and spontaneous polarisation ($P_s \sim 14 \mu\text{C}/\text{cm}^2$). The fact that identical P_s values are obtained for the PCT24 films processed in air or in oxygen indicates that the amount of active ferroelectric phase formed in both type of films must be very similar. However, the P_r values obtained are lower than those of $P_r \sim 25 \mu\text{C}/\text{cm}^2$ reported for the conventional films.⁹

Lower coercive fields, E_c , are obtained from the loops of Fig. 4.3.12a for the film prepared in oxygen (~ 164 kV/cm) respect to that prepared in air (~ 226 kV/cm). A larger non-ferroelectric contribution (lower capacity and higher electric displacement, D) is observed in the films prepared in air (Fig. 4.3.12b). A larger slope of the non-switching loop is indicative of a larger capacity value, whereas a lower value of D for $E = 0$ is indicative of a smaller conductivity.

Attending to the dielectric and ferroelectric properties obtained in the PCT24 films prepared at low temperatures by PCSD, differences are found if the UV-irradiation and thermal treatment of the films are carried out in air or in oxygen. As it has been explained in section 4.3.1 of this chapter, the energetic photons of the UV light here used induce the *photo-excitation* of the organics contained in the deposited gel layer.^{162,294} This enhances the decomposition and elimination from the film of the organic compounds (see Fig. 4.3.3). Therefore, an advance in the formation of a full-crystalline film is obtained, which makes possible the processing of the films at relatively low temperatures.

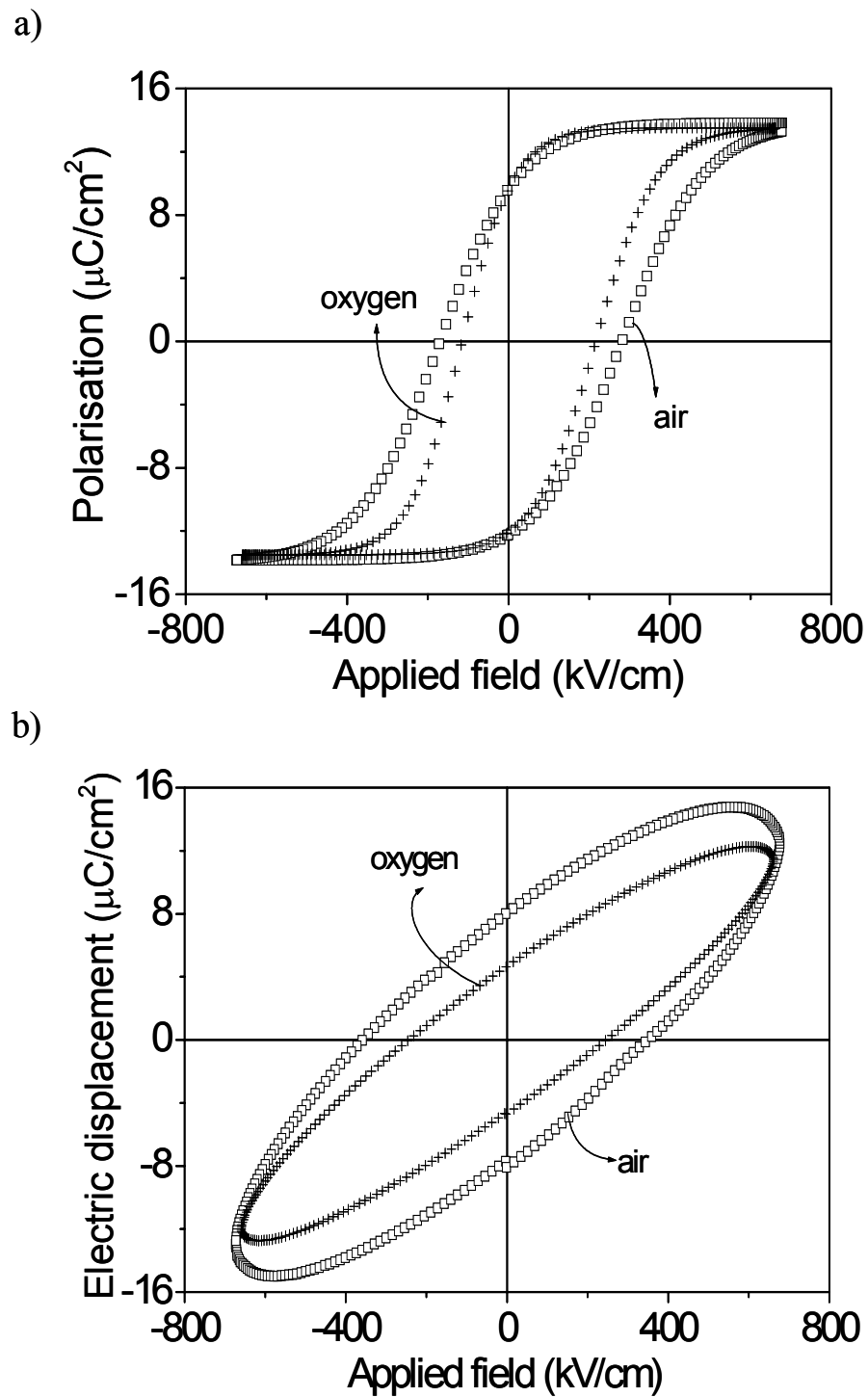


Figure 4.3.12. Ferroelectric hysteresis loops (a) and non-switching contribution to the polarisation loops (b) of the PCT24 films processed by UV-assisted RTP at 450 °C in air or oxygen

Furthermore, improved electrical properties (mainly a significant reduction of the leakage current density) have been reported for Ta₂O₅ films prepared by PCSD under UV generated ozone (*ozonolysis*).²⁸⁶ In the present work, the PCT24 films processed in a pure O₂ atmosphere show higher k' values and ferroelectric hysteresis loops with lower values of E_c (Figs. 4.3.11 and 4.3.12a, respectively). In these films, the *photo-excitation* of the organics joined to the *ozonolysis*, makes easier not only the elimination of the organics from the films and the prompt formation of the M-O-M bonds of the crystalline phase (formation of the ferroelectric perovskite phase), but also the removing of suboxides and defects. If the P_s values are an indication of the amount of ferroelectric phase (similar for the PCT24 films in air or oxygen, see Fig. 4.3.12a), the increase of k' (Fig. 4.3.11), the higher capacity and lower conductivity (non-switching contribution to the ferroelectric hysteresis loop decreases, Fig. 4.3.12b) or the decrease of E_c (Fig. 4.3.12a) are consequences of the lower amount of defects in the films processed in oxygen.

In spite of this, the dielectric and ferroelectric properties of these films are always inferior than those reported for the “conventional PCT24 films”⁹. Residual amorphous or secondary crystalline phases have not been detected in the films, that could be one of the reasons for their lower k' or P_r values when compared with those of the “conventional films”. Perhaps, other significative microstructural differences such as a markedly lower grain size (~30 nm, as deduced from the SEM and SFM measurements of section 4.3.2.2, instead of the average grain size of ~150 nm of the “conventional PCT24 films”) can be more related with this decrease in k' and P_r values. A smaller grain size would lead to a larger relative amount of grain boundaries and therefore, to a reduced dielectric and ferroelectric response. Also, the crystalline films retain the lead excess incorporated to the precursor solutions, decreasing from the top surface to the bottom of the film (see RBS data). From the study here shown, it is not possible to know where this lead excess is placed in the bulk film (grain boundaries, defective perovskite crystals, etc), but it could contribute to the decrease of the k' and P_r values of these films compared with those reported for “conventional PCT24 films”.

Figure 4.3.13 shows the field dependence dc-currents at room temperature for the PCSD processed PCT24 films. Low leakage current densities below 10^{-7} A/cm² are obtained for bias fields of 300 kV/cm (film processed in air) and 150 kV/cm (film processed in oxygen).

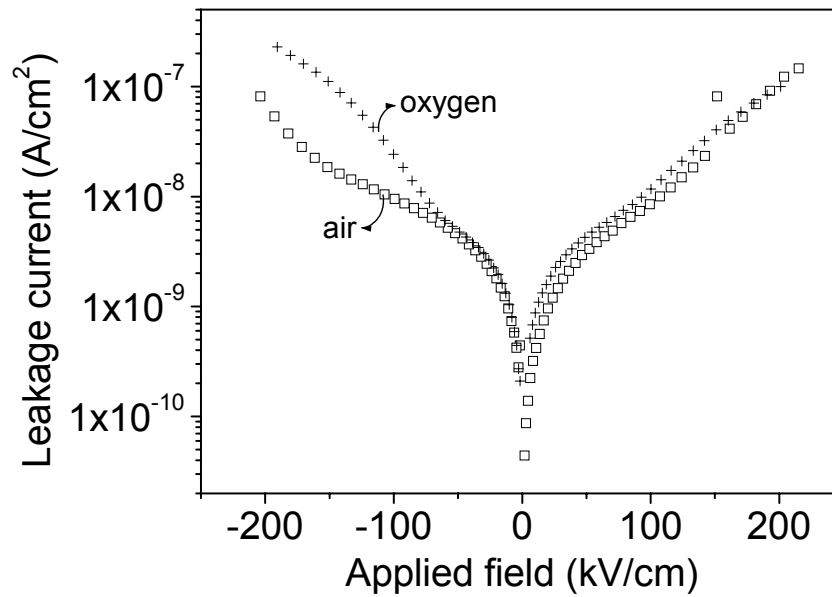


Figure 4.3.13. Leakage current densities measured for the PCT24 films processed by UV-assisted RTP at 450 °C in air or oxygen

The measurement of the evolution of the pyroelectric coefficient with time was used to evaluate the retention of the polarisation of the PCT24 films (Figure 4.3.14).

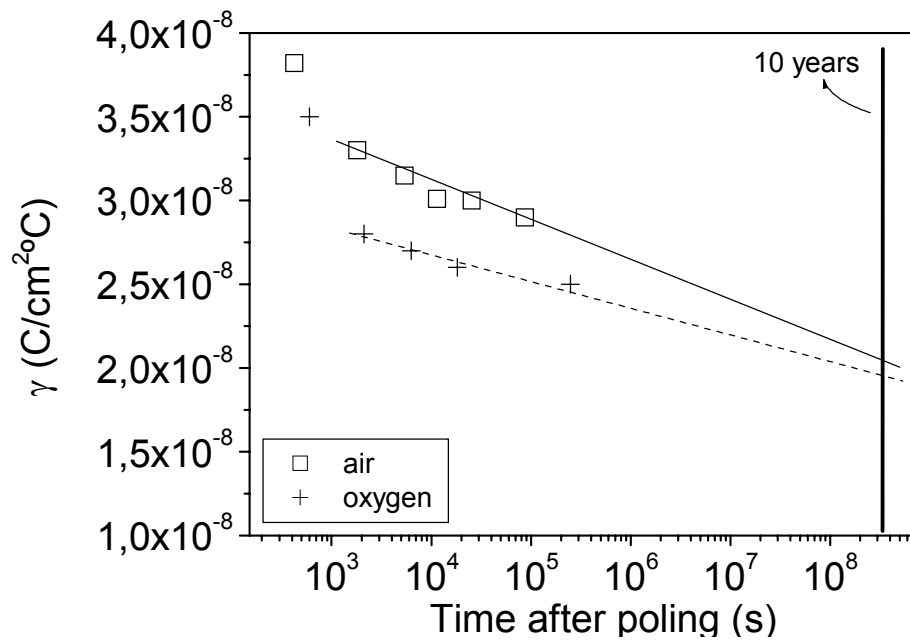


Figure 4.3.14. Variation of the pyroelectric coefficient (γ) with time for the PCT24 films processed by UV-assisted RTP at 450 °C in air or oxygen

Before any poling, the spontaneous pyroelectric coefficient measured in these films resulted to be $\gamma_s \sim 0.29 \times 10^{-8}$ C/cm²°C and $\gamma_s \sim 0.21 \times 10^{-8}$ C/cm²°C for the films processed in air or oxygen, respectively. These results suggest a significant amount of self-polarisation in the films that can be related with the positive bias obtained in their ferroelectric hysteresis loops (Fig. 4.3.12a). Values of the pyroelectric coefficient of $\gamma \sim 3.30 \times 10^{-8}$ C/cm²°C (film processed in air) and of $\gamma \sim 2.80 \times 10^{-8}$ C/cm²°C (film processed in oxygen) are measured after 30 minutes of poling the films with 16 V. Unlike the k' and P_r values, the pyroelectric coefficients of these films are comparable to those of the “conventional films”,⁷⁵ indicating their possible interest for applications in pyroelectric sensors. There was no significant difference in the pyroelectric coefficients of the films as a function of the sense of the poling field vector, which confirms that they have not considerable switching limitations associated to defects at the interfaces.

The extrapolation of the results obtained in Fig. 4.3.14 indicates that ~ 75 % of the value of the pyroelectric coefficient is maintained after a long period of time (10 years). Therefore, these PCT24 films processed at 450 °C have well defined dielectric and ferroelectric responses, with relatively high k' and P_r values, with a large retention of the polarisation with time and with low leakage current densities and loss tangent. These properties are of high interest for using these films in NVFeRAMs or sensors devices.^{61,221}

The local piezoelectric response of these films was also studied by Piezoresponse Force Microscopy (PFM), thus evaluating the piezoelectric activity of the films, of interest in MicroElectroMechanical Systems (MEMS). The local piezoelectric hysteresis loop of Figure 4.3.15 corresponds to the PCT24 film processed at 450 °C in oxygen atmosphere.

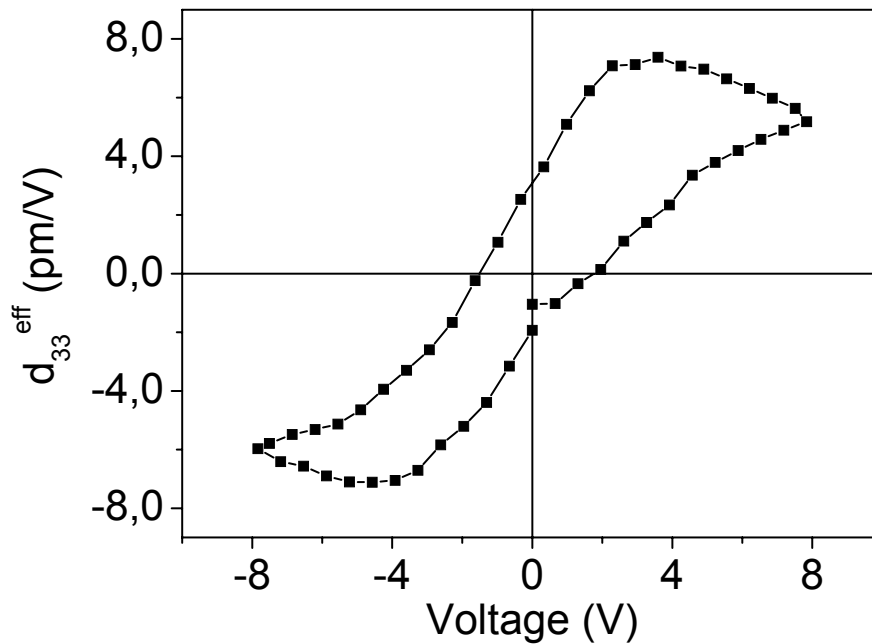


Figure 4.3.15. Local piezoelectric hysteresis loop of the PCT24 film processed by UV-assisted RTP at 450 °C in oxygen

4.3.2.4.2. Low-temperature processed PCT50 thin films

Figure 4.3.16 shows the variation of the dielectric constant (k') with temperature of the PCT50 films, measured at various frequencies. The variation of the loss tangent ($\tan \delta$) with temperature of the films is also indicated in the figure.

A diffuse transition, characteristic of this relaxor-ferroelectric composition,¹⁰ is observed for both PCT50 films. Maxima at ~ 64 and ~ 47 °C are recorded for the films processed in air and in oxygen, respectively. As in the case of the PCT24 films, higher k' values are measured for the PCT50 film processed in oxygen than in air (e.g. ~ 179 and ~ 62 at T_m , respectively), which is attributed to the lower density of defects and oxygen vacancies for the films prepared in an oxygen atmosphere, due to the *ozonolysis* phenomenon. Once more, low k' values are here obtained when comparing with those corresponding to the “conventional PCT50 films”¹⁷⁶ (~ 315 at T_m), but they are high enough to fulfil the requirements of these materials in devices. The loss tangent at room temperature measured for both films is ~ 0.01 (Fig. 4.3.16), with a low dispersion as characteristic of relaxor materials.

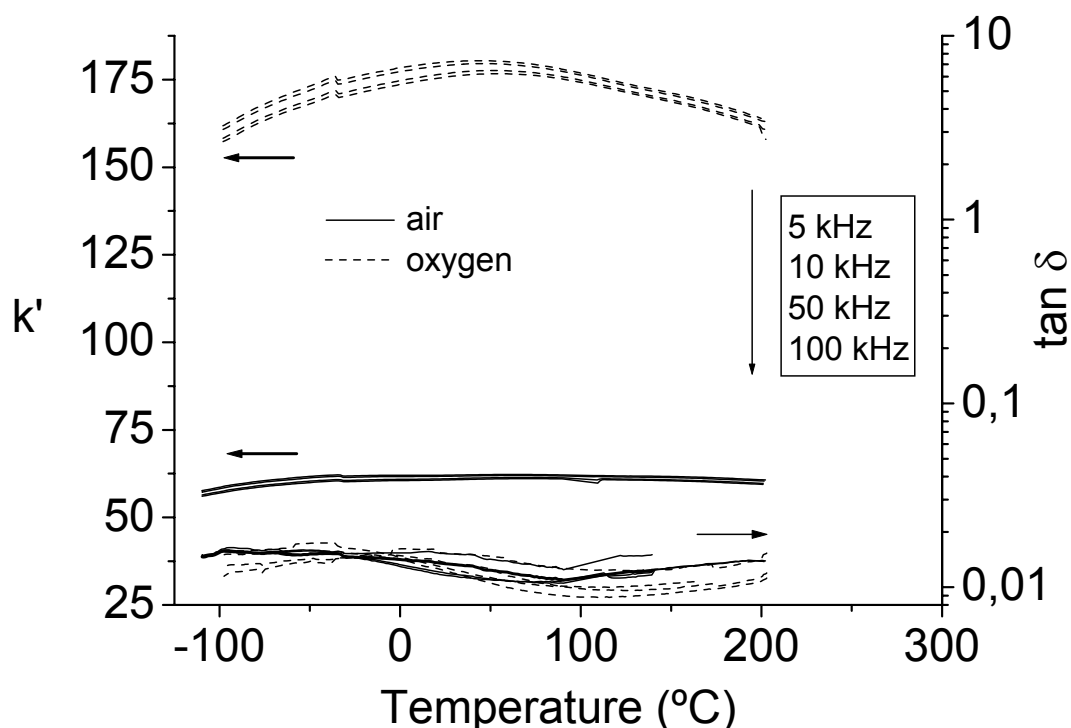


Figure 4.3.16. Variation of the dielectric constant (k') and loss tangent ($\tan \delta$) with temperature of the PCT50 films processed by UV-assisted RTP at 500 °C in air or oxygen, measured at various frequencies

Although this perovskite composition shows an almost null ferroelectric response, the ferroelectric characterisation of the films was analysed through the hysteresis loops of Figure 4.3.17.

As expected, these films have slim ferroelectric hysteresis loops at a temperature of -100 °C, well below the transition temperature. Low P_r values are obtained, although the PCT50 film processed in oxygen shows higher P_r values ($\sim 0.6 \mu\text{C}/\text{cm}^2$ at -100 °C). Values measured in “conventional PCT50 films” are near $1.5 \mu\text{C}/\text{cm}^2$.²⁹⁵ As in the case of the PCT24 films, dielectric and ferroelectric properties are improved for the films processed in oxygen. Figs. 4.3.17b and c show the ferroelectric hysteresis loops of these films measured at different temperatures, below and over the transition temperature, observing the disappearance of the switchable polarisation above this temperature.

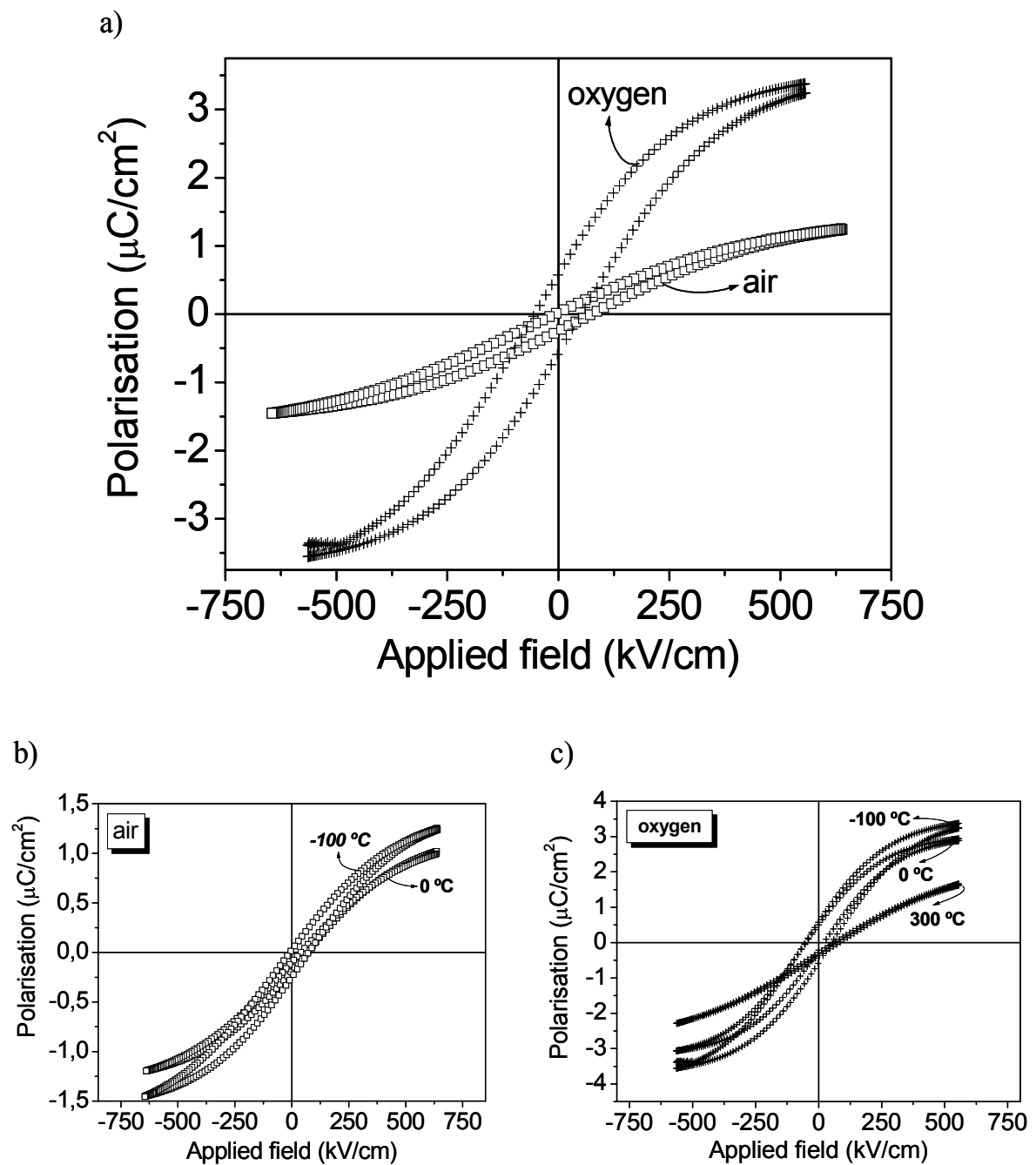


Figure 4.3.17. Ferroelectric hysteresis loops of the PCT50 films processed by UV-assisted RTP at 500°C in air or oxygen (a). Ferroelectric hysteresis loops measured in these films at temperatures below and over the transition temperature, in air (b) or oxygen (c)

Leakage current densities were also measured in the films. Figure 4.3.18 shows the field dependence dc-currents at room temperature for these films.

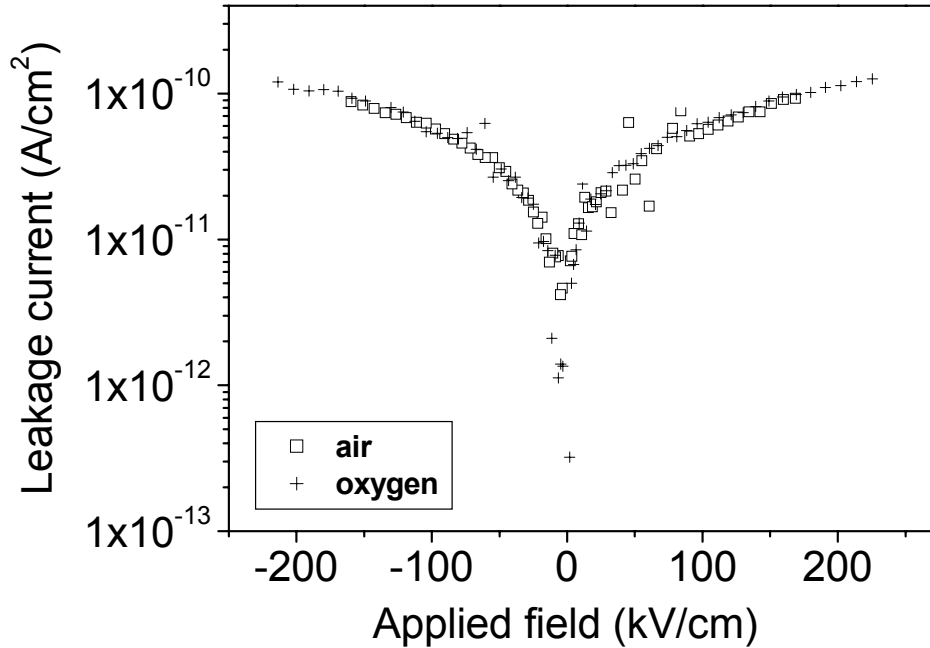


Figure 4.3.18. Leakage current densities measured for the PCT50 films processed by UV-assisted RTP at 500 °C in air or oxygen

The leakage current densities obtained in both PCT50 films show very low values, around 10^{-10} A/cm² at 200 kV/cm, that are lower than those required for computer charge storages devices (DRAMs).²²¹

Therefore, PCT50 films processed at 500 °C in air or oxygen are high- k films with possible applications as capacitors in DRAMs. Although their dielectric constants, k' , are lower than those of the “conventional PCT50 films” (see Fig. 4.3.16), they are always much higher than those of any high- k single oxide film considered for these uses (SiO₂, Ta₂O₅, etc)^{163,281,286,287}. To obtain the same k' values than the PCT films here presented, the equivalent of an only 7 nm thick film of SiO₂ should be prepared, with all the performance problems associated to the use of this so thin gate oxide layer in the device. Furthermore, the PCT50 films show very low leakage current densities ($\sim 10^{-10}$ A/cm² at 200 kV/cm, Fig. 4.3.18), which indicates that the DRAM memory could work at a low operation voltage, below 5 V. These low leakages are also important for other aspects, like the

reduction of the risk of thermal breakdown of the memory. The high diffusivity of k' with temperature of these PCT50 films moreover strengthens their possible applications in DRAMs, since this results in small variations of the dielectric constant with temperature, improving the temperature stability of the memory device. All of these facts point to the competitiveness of these materials as an alternative for DRAM devices.

4.3.3. REMARKS

- PhotoChemical Solution Deposition (PCSD) (UV sol-gel photoannealing) has made possible the fabrication of multifunctional PCT thin films at temperatures compatible with those used in the Si-technology. This low-temperature processing of PbTiO₃-based films moreover decreases the emission of toxic volatiles to the atmosphere.
- The inherent photo-sensitivity of the diol-based sol-gel PCT solutions ascribed to the acetylacetonate ligand of the titanium (IV) reagent enables the absorption of UV light. Thus, the photo-excitation of the organic compounds contained in the sol-gel derived films by the high intensity UV irradiation produces the quick elimination of the organics and the formation of single crystalline perovskite films at low temperatures.
- Perovskite PCT24 and PCT50 films with pseudocubic structures have been obtained by PCSD at 450 and 500 °C, respectively, in air or in oxygen atmosphere. The perovskite crystallisation in the PCT films seems not to be affected by the fact that is carried out in an environment of air or oxygen.
- The low temperatures used for the crystallisation of the PCT perovskite films prevent the grain growth process and therefore, nanostructured films are obtained. These films are formed by small grains with an average size of ~30 nm, independently of the composition (PCT24 or PCT50) and of the local atmosphere used during the film processing (air or oxygen).
- PCT thin films with a high bulk density and an elemental composition close to that of the expected perovskite are obtained. The low temperatures used for the processing of these films minimise the diffusion between the PCT film and the Pt bottom electrode. Thus, the films develop very thin interfaces formed by a PbPt_x intermetallic compound. Also, the low processing temperatures of the films decrease the lead loss by volatilisation. As a result, the PCT24 perovskite films retain the lead excess added to the respective precursor solution.

-
- Dielectric and ferroelectric properties of the low-temperature processed PCT thin films are in general inferior to those reported for similar films prepared at high temperatures. However, they fulfil the requirements of multifunctional devices. These properties are improved when the films are processed in oxygen atmosphere. Here, the *photo-excitation* of the organics together with their *ozonolysis* promotes the removing of defects (vacancies, suboxides, etc) from the films, giving rise to enhanced electric, dielectric and ferroelectric responses.

CAPÍTULO V

CONCLUSIONES GENERALES

Las principales conclusiones obtenidas a partir de los resultados experimentales mostrados y discutidos en la presente Tesis se resumen en los siguientes apartados:

1. Se han desarrollado dos procesos químicos en disolución para la fabricación de láminas delgadas de $(\text{Pb}_{1-x}\text{Ca}_x)\text{TiO}_3$ (PCT) con distintos contenidos de Ca^{2+} (desde 0 hasta 50 at%, $0 \leq x \leq 0.50$), haciendo uso de métodos de depósito químico de disoluciones (“Chemical Solution Deposition”, CSD) de baja toxicidad. El primer proceso se basa en una ruta disolución-gel acuosa donde se utiliza agua como único disolvente. El segundo proceso consiste en el uso de soles o disoluciones basados/as en dioles, donde el disolvente consiste en mezclas de un diol (1,3-propanodiol) y agua.
2. La ruta disolución-gel acuosa emplea exclusivamente agua como disolvente inocuo y de bajo coste. Ésto simplifica la metodología del procesado, facilitando el manejo de los reactivos y evitando también el uso de las atmósferas secas generalmente empleadas en la química sol-gel que utiliza alcóxidos de metales de transición.
3. Se han preparado disoluciones precursoras de $(\text{Pb}_{0.76}\text{Ca}_{0.24})\text{TiO}_3$ (PCT24) y $(\text{Pb}_{0.50}\text{Ca}_{0.50})\text{TiO}_3$ (PCT50) mediante la ruta disolución-gel acuosa. La inestabilidad de la disolución aumenta con el contenido de Ca^{2+} , debido a la baja solubilidad del citrato de calcio utilizado como reactivo en este sistema.
4. La elevada tensión superficial del agua dificulta el mojado de los substratos basados en silicio ($\text{Pt}/\text{TiO}_x/\text{Ti}/\text{SiO}_2/\text{Si}$) empleados para el depósito de las láminas delgadas. La hidrofiliidad del substrato se modificó con un tratamiento químico de limpieza. Dicho tratamiento mejoró el mojado del substrato por la disolución acuosa y permitió el depósito de láminas de PCT.
5. Se han obtenido láminas delgadas cristalinas de PCT24 y PCT50 mediante la ruta disolución-gel acuosa. Las láminas de PCT24 muestran respuesta ferroeléctrica, aunque sus altas densidades de corriente de fugas impiden su correcta polarización con el campo eléctrico. Por el contrario, las láminas de PCT50 exhiben bajas densidades de corriente de fugas, constantes dieléctricas relativamente altas a temperatura ambiente y transiciones ferro-paraeléctrica

difusas. Estas propiedades son adecuadas para el posible uso de estos materiales en Memorias Dinámicas de Acceso Aleatorio (“Dynamic Random Access Memories”, DRAMs) y componentes de alta frecuencia (dispositivos sintonizables con el voltaje).

6. También se han preparado láminas delgadas cristalinas de PCT mediante un método sol-gel basada en dioles. Aquí se ha estudiado el efecto del contenido de Ca^{2+} en la cristalización de la perovskita de PCT, observándose un desplazamiento de la cristalización hacia temperaturas mayores con el aumento del contenido de Ca^{2+} . La cristalización de las láminas de PCT mediante RTP (“Rapid Thermal Processing”) ocurre a temperaturas menores que en los polvos de PCT preparados con tratamientos de calentamiento convencionales.
7. Se han desarrollado tres rutas sintéticas sol-gel basadas en diol (A, B ó C) para la preparación de los precursores de PCT. Éstas difieren en el reactivo de calcio utilizado (acetato de calcio o acetilacetato de calcio) y en el protocolo de reacción seguido. Las disoluciones derivadas de la ruta A consisten en una mezcla de un sol de Pb(II)-Ti(IV) y una disolución acuosa de acetato de calcio. Mediante las rutas B y C se obtienen soles de Ca(II)-Pb(II)-Ti(IV). Los soles derivados de la ruta C sólo son estables para contenidos de $\text{Ca}^{2+} \leq 30$ at%.
8. Las disoluciones de PCT preparadas a través de la ruta A están formados por partículas agrupadas en dos distribuciones de tamaño, mientras que los soles de PCT (rutas B y C) contienen partículas de tamaño uniforme. La descomposición térmica de los polvos cerámicos derivados de las rutas B y C es más sencilla que la de los respectivos polvos cerámicos de la ruta A.
9. En los polvos cerámicos derivados de las rutas A y B, que utilizan acetato de calcio como reactivo, aparecen restos de carbonato de calcio a altas temperaturas (>600 °C). Este compuesto no se detecta en los polvos cerámicos preparados a través de la ruta C, que emplea acetilacetato de calcio. A pesar de esto, ninguno de los análisis del perfil composicional de las láminas cristalizadas a 650 °C por RTP muestra la presencia de restos de carbono en las láminas.

10. La microestructura y heteroestructura de estas láminas de PCT se ven afectadas tanto por el contenido de Ca^{2+} como por el sistema químico empleado en la preparación de la disolución. Las microestructuras de láminas de PCT24 están formadas por granos de mucho mayor tamaño (150-190 nm) que los de las láminas de PCT50 (~50 nm). En las láminas de PCT24 y PCT50 derivadas de la ruta A se forman intercaras de reacción lámina-substrato y superficies deficientes en plomo, mientras que las láminas obtenidas por las rutas B ó C presentan heteroestructuras homogéneas con una composición próxima a la de la perovskita. Estas láminas tienen mayores respuestas dieléctricas y ferroeléctricas que las láminas derivadas de la ruta A.
11. Se han preparado láminas cristalinas con estructura perovskita a bajas temperaturas (450-500 °C) mediante “PhotoChemical Solution Deposition” (PCSD). Las microestructuras de estas láminas están formadas por granos con un tamaño medio de ~30 nm. Las bajas temperaturas utilizadas en el procesado de estas láminas minimizan la difusión entre la película de PCT y el electrodo inferior de Pt, y también evitan la pérdida de plomo por volatilización.
12. Las láminas de PCT preparadas por PCSD muestran claras respuestas dieléctricas y ferroeléctricas. Estas propiedades mejoran cuando la irradiación con UV de las láminas se lleva a cabo en atmósfera de oxígeno. Aquí, la foto-oxidación de los orgánicos junto con su ozonolisis promueve la eliminación de defectos (vacantes, subóxidos), dando lugar a láminas con propiedades que satisfacen los requisitos de estos materiales en dispositivos microelectrónicos.

CHAPTER V

GENERAL CONCLUSIONS

The main conclusions obtained from the experimental results presented and discussed in this Ph.D Thesis are summarised as follows:

1. Two approaches, using low-toxic Chemical Solution Deposition (CSD) methods, have been developed in this Ph.D Thesis for the fabrication of $(\text{Pb}_{1-x}\text{Ca}_x)\text{TiO}_3$ (PCT) thin films with different Ca^{2+} contents (from 0 to 50 at%, $0 \leq x \leq 0.50$). The first approach is based on an aqueous solution-gel route in which water is used as solvent. The second one consists in the use of diol-based sols or solutions with mixtures of a diol (1,3-propanediol) and water as solvents.
2. The aqueous solution-gel route exclusively uses water as a non-hazardous and inexpensive solvent. This makes simpler the processing methodology, with an easy handling of the reagents and without the need of the dried atmospheres usually used in the sol-gel chemistry of transition metal alkoxides.
3. $(\text{Pb}_{0.76}\text{Ca}_{0.24})\text{TiO}_3$ (PCT24) and $(\text{Pb}_{0.50}\text{Ca}_{0.50})\text{TiO}_3$ (PCT50) precursor solutions have been prepared by the aqueous solution-gel route. Instability of the solution increases with the Ca^{2+} content, due to the low solubility of the calcium citrate reagent in the aqueous media.
4. The high surface tension of water hinders the wetting of the platinised silicon based substrates used for the deposition of the thin films ($\text{Pt}/\text{TiO}_x/\text{Ti}/\text{SiO}_2/\text{Si}$). A wet chemical treatment of cleaning was used to modify the hydrophilicity of the substrate. This enhances the wetting of the substrate by the aqueous solution, making possible the deposition of the PCT films.
5. Crystalline PCT24 and PCT50 thin films with perovskite structure have been obtained by the aqueous solution-gel route. The PCT24 films have ferroelectric response, although the high leakage current densities measured prevent their correct polarisation with the electric field. On the contrary, the PCT50 films exhibited low leakage current densities, relatively high dielectric constants at room temperature and diffuse ferro-paraelectric transitions. These properties are adequate for the possible use of these PCT50 films in Dynamic Random Access Memories (DRAMs) and high-frequency components (voltage tunable devices).

6. Crystalline PCT thin films have also been prepared by a diol-based sol-gel method. Here, the effect of the Ca^{2+} content on the crystallisation of the PCT perovskite has been studied, observing a displacement of the perovskite crystallisation towards higher temperatures with the increase of the Ca^{2+} content. The crystallisation of the PCT perovskite thin films by Rapid Thermal Processing (RTP) occurs at lower temperatures than in the PCT powders treated by conventional heating processes.
7. Three different diol-based sol-gel synthetic routes (A, B or C) have been developed for the preparation of the PCT precursors, which differ in the calcium reagent used (calcium acetate or calcium acetylacetonate) and in the synthetic pathway followed. Solutions derived from the route A consist in a mixture of a Pb(II)-Ti(IV) sol and a water solution of calcium acetate. On the other hand, Ca(II)-Pb(II)-Ti(IV) sols are obtained by the routes B and C. Sols derived from the route C were stable only for Ca^{2+} contents ≤ 30 at%.
8. PCT solutions prepared through the route A are constituted by two particle size distributions, whereas the PCT sols (routes B and C) are formed by particles with an uniform size. The thermal decomposition of the powders derived from the routes B and C is simpler than that of the powders derived from the route A.
9. Calcium carbonate rests are detected at high temperatures (>600 °C) in the powders derived from the routes A and B, which use calcium acetate as calcium reagent. However, these carbonate rests are not detected in the powders prepared from the route C, where the calcium acetylacetonate reagent was used. In spite of this, none compositional profile analysis of the films crystallised at 650 °C by RTP shows the presence of carbon rests in the bulk film.
10. The microstructure and heterostructure of these PCT films are affected by both the Ca^{2+} content and the solution chemistry. Microstructures of the PCT24 films are formed by much larger grains (150-190 nm) than those of the PCT50 films (~ 50 nm). Bottom interfaces and lead-deficient surfaces are formed in both PCT24 and PCT50 films derived from the route A, whereas films obtained by the route B or C present homogeneous heterostructures with a composition close to

that of the expected PCT perovskite. These films have higher dielectric and ferroelectric responses than the films derived from the route A.

11. Full-crystalline PCT films with perovskite structure have been prepared at low temperatures (450-500 °C) by PhotoChemical Solution Deposition (PCSD). The microstructures of these films are formed by grains with a mean size of ~30 nm. The low temperatures used for the processing of these films minimise the diffusion between the PCT film and the Pt bottom electrode and also avoid the lead loss by volatilisation from the film.
12. The PCT films prepared by PCSD have clear dielectric and ferroelectric responses. These properties improve when the UV-irradiation of the films is carried out in oxygen atmosphere. Here, the photo-excitation of the organics together with their ozonolysis promotes the removing of defects (vacancies, suboxides, etc) from the films, giving place to films with properties that fulfil the requirements of these materials in microelectronic devices.

References

- ¹ R.W. Schwartz. “*Electroceramic Materials and Applications: Ceramic Transactions, vol. 196*” (John Wiley & Sons, New York, 2006).
- ² N. Setter and R. Waser. “Electroceramic materials”. *Acta Mater.*, 2000, **48**, 151.
- ³ B. Jaffe, W.R. Cook and H. Jaffe. “*Piezoelectric Ceramics*” (Academic Press, New York, 1971).
- ⁴ C.A. Paz de Araujo, J.D. Cuchiaro, L.D. McMillan, M.C. Scott and J.F. Scott. “Fatigue-free ferroelectric capacitors with platinum-electrodes”. *Nature*, 1995, **374**, 5233.
- ⁵ M.L. Calzada, R. Jiménez, P. Ramos, M.J. Martín and J.Mendiola. “Ferroelectric improvements of (Pb,Ca)TiO₃ thin films”. *J. Phys. IV*, 1998, **8**, 53.
- ⁶ A. Kholkin, A. Seifert and N. Setter. “Electromechanical properties of sol-gel derived Ca-modified PbTiO₃ films”. *Appl. Phys. Lett.*, 1998, **72(25)**, 3374.
- ⁷ R. Poyato, M.L. Calzada and L. Pardo. “Effects of substrate annealing and post-crystallization thermal treatments on the functional properties of preferentially oriented (Pb,Ca)TiO₃ thin films”. *J. Appl. Phys.*, 2003, **93(7)**, 4081.
- ⁸ P. Ramos, J. Mendiola, R. Jiménez, M.L. Calzada, A. González and P. Tejedor. “IR detectors made of ferroelectric (Pb,Ca)TiO₃ thin films”. *Bol. Soc. Esp. Ceram. V.*, 2002, **41(1)**, 5.
- ⁹ J. Mendiola and M.L. Calzada. “*Ferroelectric thin films of modified lead titanate*”, in “*Handbook of Thin Film Materials. Vol. 3: Ferroelectric and Dielectric Thin Films*”. Ed. H.S. Nalwa (Academic Press, London, 2002).
- ¹⁰ R. Jiménez, C. Alemany, M.L. Calzada and J. Mendiola. “Relaxor-like behavior of Pb_{0.5}Ca_{0.5}TiO₃ thin films”. *Ferroelectrics*, 2004, **302**, 461.
- ¹¹ T. Yamamoto, M. Saho, K. Okazaki and E. Goo. “Electrical properties and microstructure of Ca modified PbTiO₃ ceramics”. *Jpn. J. Appl. Phys.*, 1987, **26(2)**, 57
- ¹² J. Mendiola, B. Jiménez, C. Alemany, L. Pardo and L. Del Olmo. “Influence of calcium on the ferroelectricity of modified lead titanate ceramics”. *Ferroelectrics*, 1989, **94**, 183.
- ¹³ D. Xiao. “Environmentally conscious ferroelectric research”. *J. Korean Phys. Soc.*, 1998, **32**, S1798.
- ¹⁴ European Union Directive **2002/95/EC on the Restriction Of the use of certain Hazardous Substances in electrical and electronic equipment** (RoHS directive).
- ¹⁵ Semiconductor Industry Association. International Technology Roadmap for Semiconductors, **2005**, International SEMATECH, Austin TX; available at <http://public.itrs.net>.
- ¹⁶ W.D. Kingery, H.H. Bowen and D.R. Uhlman. “*Introduction to Ceramics. Chapter 18: Dielectric properties*” (John Wiley & Sons, Singapore, 1991).
- ¹⁷ J. Valasek. “Piezoelectric and allied phenomena in Rochelle salt”. *Phys. Rev.*, 1921, **17**, 475.
- ¹⁸ W. Kanzig. “*Ferroelectrics and Antiferroelectrics*” (Academic Press, New York, 1957).
- ¹⁹ E. Fatuzzo and W.J. Merz. “*Ferroelectricity*” (North-Holland, Amsterdam, 1967).
- ²⁰ M.E. Lines and A.M. Glass. “*Principles and Applications of Ferroelectrics and Related Materials*” (Clarendon, Oxford, 1997).

- ²¹ F. Jona and G. Shirane. “*Ferroelectric Crystals*” (Pergamon, Oxford, 1962).
- ²² A.J. Moulson and J.M. Herbert. “*Electroceramics*” (Chapman & Hall, London, 1990).
- ²³ G.H. Haertling. “Ferroelectric ceramics: history and technology”. *J. Am. Ceram. Soc.*, 1999, **82(4)**, 797.
- ²⁴ G. Shirane, S. Hoshino and K. Suzuki. “Phase transitions in PbTiO_3 ”. *Phys. Rev.*, 1952, **80**, 1105.
- ²⁵ M.L. Calzada and L. del Olmo. “Piezoelectric behaviour of pure PbTiO_3 ceramics”. *Ferroelectrics*, 1991, **123**, 233.
- ²⁶ J.P. Remeika and A.M. Glass. “Growth and ferroelectric properties of high resistivity single crystals of lead titanate”. *Mater. Res. Bull.*, 1970, **5**, 37.
- ²⁷ V.G. Gavriyachenki, R.I. Spinko, M.A. Martynen and E.G. Fesenko. “Spontaneous polarization and coercive field of lead titanate”. *Sov. Phys. Solid State*, 1970, **12(5)**, 1203.
- ²⁸ M. McQuarrie. “Studies in the system $(\text{Ba,Ca,Pb})\text{TiO}_3$ ”. *J. Am. Ceram. Soc.*, 1957, **40(2)**, 35.
- ²⁹ D. Berlincourt. “Transducers using forced transitions between ferroelectric and antiferroelectric states”. *IEEE Trans. Sonics Ultrason.*, 1966, **SU-13**, 116.
- ³⁰ H. Takeuchi, S. Jyomura, E. Yamamoto and Y. Ito. “Electromechanical properties of $(\text{Pb,Ln})(\text{Ti,Mn})\text{O}_3$ ceramics (Ln = rare earths)”. *J. Acoust. Soc. Am.*, 1982, **72(4)**, 1114.
- ³¹ E. Sawaguchi, T. Mitsuma and Z. Ichi. “Double hysteresis loop of $(\text{Pb,Ca})\text{TiO}_3$ ceramics”. *J. Phys. Soc. Jpn.*, 1956, **11**, 1298.
- ³² T. Ikeda. “Some studies on the ternary system $(\text{Ba-Pb-Ca})\text{TiO}_3$ ”. *J. Phys. Soc. Jpn.*, 1958, **1(4)**, 335.
- ³³ Y. Yamashita, K. Yokoyama, H. Honda and T. Takahashi. “ $(\text{Pb,Ca})(\text{Co}_{1/2}\text{W}_{1/2})\text{TiO}_3$ piezoelectric ceramics and their applications”. *Jpn. J. Appl. Phys.*, 1981, **20(4)**, 183.
- ³⁴ Y. Yamashita, S. Yoshida and T. Takahashi. “Effect of MnO additive on piezoelectric properties in modified $(\text{Pb,Ca})\text{TiO}_3$ ferroelectric ceramics”. *Jpn. J. Appl. Phys.*, 1983, **22(2)**, 40.
- ³⁵ B. Jiménez, J. Mendiola, C. Alemany, L. Del Olmo, L. Pardo, E. Maurer, M.L. Calzada, J. De Frutos, A.M. González and M.C. Fandiño. “Contributions to the knowledge of calcium modified lead titanate ceramics”. *Ferroelectrics*, 1988, **87**, 97.
- ³⁶ V.V. Eremkin, V.G. Smotrakov, S.I. Shevtsova and A.T. Kozakov. “x,T phase diagram of $\text{Pb}_{1-x}\text{Ca}_x\text{TiO}_3$ crystals ($0 \leq x \leq 0.62$)”. *Phys. Solid State*, 1994, **36**, 191.
- ³⁷ S.A. Fedulov and Y.N. Venevtsev. “A study of system $\text{PbTiO}_3\text{-CaSnO}_3$ and $\text{PbTiO}_3\text{-CaZrO}_3$ ”. *Sov. Phys. Crystallogr.*, 1964, **9(3)**, 286.
- ³⁸ M. Deri. *Period. Polytech. Chem. Eng.*, 1960, **4**, 307.
- ³⁹ A.M. Glazer. “Classification of tilted octahedra in perovskites”. *Acta Crystallogr.*, 1972, **B 28**, 3384.
- ⁴⁰ G. King and E.K. Goo. “Effect of the c/a ratio on the domain structure in $(\text{Pb}_{1-x}\text{Ca}_x)\text{TiO}_3$ ”. *J. Am. Ceram. Soc.*, 1990, **73(6)**, 1534.
- ⁴¹ G. King, E. Goo, T. Yamamoto and K. Okazaki. “Crystal structure and defects of ordered $(\text{Pb}_{1-x}\text{Ca}_x)\text{TiO}_3$ ”. *J. Am. Ceram. Soc.*, 1994, **71(6)**, 454.

- ⁴² R. Ganesh and E. Goo. "Dielectric and ordering behaviour in $\text{Pb}_x\text{Ca}_{1-x}\text{TiO}_3$ ". *J. Am. Ceram. Soc.*, 1997, **80(3)**, 653.
- ⁴³ R. Ranjan, N. Singh, D. Pandey, V. Siruguri, P.S.R. Krishna, S.K. Paranjpe and A. Banerjee. "Room temperature crystal structure and relaxor ferroelectric behaviour of $\text{Pb}_{0.5}\text{Ca}_{0.5}\text{TiO}_3$ ". *Appl. Phys. Lett.*, 1997, **70(24)**, 3221.
- ⁴⁴ A. Chandra and D. Pandey. "Evolution of crystallographic phases in the system $(\text{Pb}_{1-x}\text{Ca}_x)\text{TiO}_3$: a Rietveld study". *J. Mater. Res.*, 2003, **18(2)**, 407.
- ⁴⁵ A.M. Glazer. "Simple ways of determining perovskite structures". *Acta Crystallogr.*, 1975, **A 31**, 756.
- ⁴⁶ G.A. Rossetti, W. Zhang and A.G. Khachatryan. "Phase coexistence near the morphotropic phase boundary in lead zirconate titanate (PbZrO_3 - PbTiO_3) solid solutions". *Appl. Phys. Lett.*, 2006, **88(7)**, 072912.
- ⁴⁷ M. Algueró, A. Moure, L. Pardo, J. Holc and M. Kosec. "Processing by mechano synthesis and properties of piezoelectric $\text{Pb}(\text{Mg}_{1/3}\text{Nb}_{2/3})\text{O}_3$ - PbTiO_3 with different compositions". *Acta Mater.*, 2006, **54(2)**, 501.
- ⁴⁸ N. Vottayakorn, G. Rujijanagul, X. Tan, H. He, M.A. Marquardt and D.P. Cann. "Dielectric properties and morphotropic phase boundaries in the $x\text{Pb}(\text{Zn}_{1/3}\text{Nb}_{2/3})\text{O}_3$ - $(1-x)\text{Pb}(\text{Zr}_{0.5}\text{Ti}_{0.5})\text{O}_3$ pseudo-binary system". *J. Electroceram.*, 2006, **16(2)**, 141.
- ⁴⁹ L.E. Cross. "Relaxor ferroelectrics". *Ferroelectrics*, 1987, **76**, 241.
- ⁵⁰ V.V. Lemanov, A.V. Sotnikov, E.P. Smirnova and M. Weihnacht. "From incipient ferroelectricity in CaTiO_3 to real ferroelectricity in $\text{Ca}_{1-x}\text{Pb}_x\text{TiO}_3$ solid solutions". *Appl. Phys. Lett.*, 2002, **81(5)**, 886.
- ⁵¹ B. Jiménez and R. Jiménez. "Elasting softening due to polar clusters in $\text{Pb}_{1-x}\text{Ca}_x\text{TiO}_3$ ferroelectric ceramics above the phase transition temperature". *Phys. Rev. B*, 2002, **66**, 141XX-1-7.
- ⁵² R.B. Gray. "Transducer and method of making same". **U.S. Pat. No. 2 486 560**, 1949.
- ⁵³ N. Setter. "Electroceramics: looking ahead". *J. Eur. Ceram. Soc.*, 2001, **21**, 1279.
- ⁵⁴ A.E. Feuersanger, A.K. Hagenlocher and A.L. Solomon. "Preparation and properties of thin barium titanate films". *J. Electrochem. Soc.*, 1964, **111(12)**, 1387.
- ⁵⁵ A.E. Feuersanger. "*Thin Films Dielectrics*". Ed. F. Vratney (Electrochemical Society, New York, 1969).
- ⁵⁶ A.I. Kingon, J.P. Maria and S.K. Streiffer. "Alternative dielectrics to silicon dioxide for memory and logic devices". *Nature*, 2000, **406**, 1032.
- ⁵⁷ G.E. Moore. "Cramming more components onto integrated circuits". *Electronics*, 1965, **38**, 114.
- ⁵⁸ Y. Wei, R.M. Wallace and A.C. Seabaugh. "Void formation on ultrathin thermal silicon oxide films on the Si(100) surface". *Appl. Phys. Letts.*, 1996, **69**, 1270.
- ⁵⁹ J.J. Yu. "Formation of high-quality advanced high-k oxide layers at low temperature by excimer UV lamp-assisted photo-CVD and sol-gel processing". *Chem. Res. Chinese U.*, 2004, **20(4)**, 396.
- ⁶⁰ S. Tang, Y. Wei and R.M. Wallace. "Energetics of void enlargement in thermally grown ultrathin Si-oxide on Si(001)". *Surf. Sci. Lett.*, 1997, **387**, L1057.

- ⁶¹ O. Auciello, F. Scott and R. Ramesh. "The physics of ferroelectric memories". *Phys. Today*, 1998, **51(7)**, 22.
- ⁶² Y.H. Xie, Y.Y. Lin and T.A. Tang. "Characteristics of BST thin film prepared by novel chemical solution deposition method for high-density DRAM application". *Integr. Ferroelectr.*, 2002, **47**, 113.
- ⁶³ M. Kosec, J. Holc, B. Malic and V. Bobnar. "Processing of high performance lead lanthanum zirconate titanate thick films". *J. Eur. Ceram. Soc.*, 1999, **19(6-7)**, 949.
- ⁶⁴ A.I. Kingon, S.K. Streiffer, C. Basceri and S.R. Summerfelt. "High-permittivity perovskite thin films for dynamic random-access memories". *Mater. Res. Bull.*, 1996, **21(7)**, 46.
- ⁶⁵ H. Takasu. "The ferroelectric memory and its applications". *J. Electroceram.*, 2000, **4:2/3**, 327.
- ⁶⁶ T.W. Noh, B.S. Kang, S. Seo, Y.W. So, B.H. Park, S.D. Bu, J.G. Yoon. "A new candidate materials for use in ferroelectric random access memory (FRAM)" *Ferroelectrics*, 2002, **267**, 121.
- ⁶⁷ B.H. Park, B.S. Kang, S.D. Bu, T.W. Noh, J. Lee, W. Jo. "Lanthanum-substituted bismuth titanate for use in non-volatile memories". *Nature*, 1999, **401**, 682.
- ⁶⁸ A.K. Tangatsev, V.O. Sherman, K.F. Astafiev, J. Venkatesh and N. Setter. "Ferroelectric materials for microwave tunable applications". *J. Electroceram.*, 2003, **11**, 5.
- ⁶⁹ A. Kozyrev, A. Ivanov, A. Prudan, O Soldatenkov, E Hollmann, V. Loginov, D. Ginley and T. Rivkin. "Microwave phase shifter employing SrTiO₃ ferroelectric varactors". *Integr. Ferroelectr.*, 1999, **24(1-4)**, 287.
- ⁷⁰ Z.G. Ban and S.P. Alpay. "Optimization of the tunability of barium strontium titanate films via epitaxial stresses". *J. Appl. Phys.*, 2003, **93(1)**, 504.
- ⁷¹ R. Watton. "Ferroelectric materials and devices in infrared detection and imaging". *Ferroelectrics*, 1989, **91**, 87.
- ⁷² R.W. Whatmore. "Pyroelectric devices and materials". *Rep. Prog. Phys.*, 1986, **49(12)**, 1335.
- ⁷³ A. Sixsmith, N. Johnson and R. Whatmore. "Pyroelectric IR sensor arrays for fall detection in the older population". *J. Phys. IV*, 2005, **128**, 153.
- ⁷⁴ Z.T. Song, N. Chong, H.L.W. Chan and C.L. Choy. "Electrical and pyroelectric properties of in-plane polarized lead lanthanum titanate thin film". *Appl. Phys. Lett.*, 2001, **79(5)**, 668.
- ⁷⁵ R. Poyato, A. González, M.L. Calzada and L. Pardo. "High pyroelectric coefficients of Ca modified lead titanate sol-gel thin films obtained by multiple deposition and crystallization". *Ferroelectrics*, 2002, **271**, 385.
- ⁷⁶ H.G Craighead. "Nanoelectromechanical systems". *Science*, 2000, **290**, 1532.
- ⁷⁷ A.N. Cleland and M.L. Roukes. "A nanometre-scale mechanical electrometer". *Nature*, 1998, **392**, 160.
- ⁷⁸ S. Trolier-McKinstry and P. Muralt. "Thin film piezoelectrics for MEMS". *J. Electroceram.*, 2004, **12(1-2)**, 7.
- ⁷⁹ R.A. Roy, K.F. Etzold and J.J. Cuomo. "Ferroelectric film synthesis, past and present. A select review". In *Ferroelectric Thin Films*, ed. by E.R. Myers and A.I. Kingon (Materials Research Society, San Francisco, 1990).

- ⁸⁰ S.C. Ray, M. Algueró, J. Ricote, M.L. Calzada, C. Prieto, A. de Andrés and M. García-Hernandez. "RF magnetron sputtering $\text{PbZr}_{0.5}\text{Ti}_{0.48}\text{O}_3$ thin films with (001) preferred orientation on colossal magneto-resistive layers". *Matter. Lett.*, 2006, **13-14**, 1714.
- ⁸¹ H. Fujita, S. Goto, M. Sakashita, H. Ikeda, A. Sakai, S. Zaima and Y. Yasuda. "Control of crystal structure and ferroelectric properties of $\text{Pb}(\text{Zr}_x\text{Ti}_{1-x})\text{O}_3$ films formed by pulsed laser deposition". *Jpn. J. Appl. Phys.*, 2000, **39(12B)**, 7035.
- ⁸² S.L. Swartz and V.E. Wood. "Ferroelectric thin films". *Condens. Matter News*, 1992, **1(5)**, 4.
- ⁸³ A.C. Jones and P.R. Chalker. "Some recent developments in the chemical vapour deposition of electroceramic oxides". *J. Phys. D Appl. Phys.*, 2003, **36(6)**, R80.
- ⁸⁴ A.C. Jones. "Molecular design of improved precursors for the MOCVD of electroceramic oxides". *J. Mater. Chem.*, 2002, **12(9)**, 2576.
- ⁸⁵ J. Fukushima. "Preparation of BaTiO_3 films by hydrolysis of organometallic compounds". *Am. Ceram. Soc. Bull.*, 1976, **55(12)**, 1064.
- ⁸⁶ J. Fukushima, K. Kodaira and T. Marsushita. "Preparation of ferroelectric PZT films by thermal decomposition of organometallic compounds". *J. Mater. Sci.*, 1984, **19**, 595.
- ⁸⁷ K.D. Budd, S.K. Dey and D.A. Payne. "Sol-gel processing of PbTiO_3 , PbZrO_3 , PZT and PZLT thin films". *Brit. Cer. Proc.*, 1985, **36**, 107.
- ⁸⁸ S.K. Dey, K.D. Budd and D.A. Payne. "Thin-film ferroelectrics of PZT by sol-gel processing". *IEEE T. Ultrason. Ferr.*, 1988, **35(1)**, 80.
- ⁸⁹ R. Lipeles, N. Ives and M. Leung. "Sol-gel processing of lead zirconate titanate films". Presented at the 2nd International Conference on Ultrastructure Processing of Ceramics, Glasses and Composites. Palm Coast, Florida, 1985 (poster).
- ⁹⁰ B. Malic, M. Kosec, I. Arcon and A. Kodre. "Influence of the structure of precursors on the crystallisation of PbTiO_3 thin films". *J. Sol-Gel Sci. Techn.*, 2000, **19(1-3)**, 153.
- ⁹¹ M. Kosec, B. Malic and M. Mandeljc. "Chemical solution deposition of PZT thin films for microelectronics". *Mat. Sci. Semicon. Proc.*, 2002, **5(2-3)**, 97.
- ⁹² M.K. Van Bael, D. Nelis, A. Hardy, D. Mondelaers, K. Van Werde, J. D'Haen, G. Vanhoyland, H. Van Den Rul, J. Mullens, L.C. Van Poucke, F. Frederix and D.J. Wouters. "Aqueous chemical solution deposition of ferroelectric thin films". *Integr. Ferroelectr.*, 2002, **45**, 113.
- ⁹³ M.L. Calzada, I. Bretos, R. Jiménez, J. Ricote, J. Mendiola, J. García-López and M.A. Respaldiza. "Chemical solution deposition of $(\text{Pb}_{1-x}\text{Ca}_x)\text{TiO}_3$ thin films with $x \sim 0.5$ as new dielectrics for tunable components and dynamic random access memories". *J. Am. Ceram. Soc.*, 2005, **88(12)**, 3388.
- ⁹⁴ M.C. Kao, C.M. Wang, M.S. Lee, H.Z. Chen and Y.C. Chen. "Characterization of sol-gel prepared magnesium-modified lead titanate thin films". *Appl. Phys. A-Mater.*, 2004, **78(5)**, 705.
- ⁹⁵ M.L. Calzada and A. González. "Tantalum penta-glycolate sol as a precursor of strontium bismuth tantalate ferroelectric thin films". *J. Am. Ceram. Soc.*, 2005, **88(10)**, 2702.
- ⁹⁶ R.W. Schwartz, T. Schneller and R. Waser. "Chemical solution deposition of electronic oxide films". *C. R. Chimie*, 2004, **7**, 433.
- ⁹⁷ G.H. Haertling. "PLZT thin-films prepared from acetate precursors". *Ferroelectrics*, 1991, **51**, 116.

- ⁹⁸ R. Ijima. "Factors controlling the a-axis orientation of strontium bismuth tantalate thin films fabricated by chemical solution deposition". *Appl. Phys. Lett.*, 2001, **79(14)**, 2240.
- ⁹⁹ D. Van Genechten, G. Vanhoyland, J. D'Haen, J. Johnson, D.J. Wouters, M.K. Van Bael, H. Van den Rul, J. Mullens and L.C. Van Poucke. "Phase evolution of sol-gel prepared $\text{Pb}(\text{Zr}_{0.3}\text{Ti}_{0.7})\text{O}_3$ thin films deposited on $\text{IrO}_2/\text{TiO}_2/\text{SiO}_2/\text{Si}$ electrodes". *Thin Solid Films*, 2004, **467**, 104.
- ¹⁰⁰ S.R. Gurkovich and J. D. Blum. "*Ultrastructure Processing of Glasses, Ceramics and Composites*". Ed. L.L. Hench and D.R. Ulrich (Wiley, New York, 1984).
- ¹⁰¹ N.J. Phillips, M.L. Calzada and S.J. Milne. "Sol-gel derived lead titanate films". *J. Non-Cryst. Solids*, 1992, **147-148**, 285.
- ¹⁰² F.M. Pontes, E.R. Leite, M.S.J. Nunes, D.S.L. Pontes, E. Longo, R. Magnani, P.S. Pizani and J.A. Varela. "Preparation of $\text{Pb}(\text{Zr,Ti})\text{O}_3$ by soft chemical route". *J. Eur. Ceram. Soc.*, 2004, **24(10-11)**, 2969.
- ¹⁰³ U. Schubert. "Chemical modification of titanium alkoxides for sol-gel processing". *J. Mater. Chem.*, 2005, **15**, 3701.
- ¹⁰⁴ T.J. Boyle, D. Dimos, R.W. Schwartz, T.M. Alam, M.B. Sinclair and C.D. Buchheit. "Aging characteristics of a hybrid sol-gel $\text{Pb}(\text{Zr,Ti})\text{O}_3$ precursor solution". *J. Mater. Res.*, 1997, **12(4)**, 1022.
- ¹⁰⁵ M.B. González, A.Y. Wu and P.M. Vilarinho. "Influence of solvents on the microstructure and dielectric properties of $\text{Ba}_{0.5}\text{Sr}_{0.5}\text{TiO}_3$ thin films prepared by a diol-based sol-gel process". *Chem. Mater.*, 2006, **18(7)**, 1737.
- ¹⁰⁶ B. Malic, M. Kosec, I. Arcon and A. Kodre. "Homogeneity issues in chemical solution deposition of $\text{Pb}(\text{Zr,Ti})\text{O}_3$ thin films". *J. Eur. Ceram. Soc.*, 2005, **25(12)**, 2241.
- ¹⁰⁷ I. Arcon, B. Malic, M. Kosec and A. Kodre. "EXAFS study of PZT sols". *Mat. Res. Bull.*, 2003, **38(15)**, 1901.
- ¹⁰⁸ K. Kato. "Low-temperature synthesis of $\text{SrBi}_2\text{Ta}_2\text{O}_9$ ferroelectric thin films through the complex alkoxide method: Effects of functional group, hydrolysis and water vapour treatment". *Jpn. J. Appl. Phys.*, 1998, **37**, 5178.
- ¹⁰⁹ L.D. McMillan, C.A. Paz de Araujo, T.L. Roberts, J. Cuchiaro, M.C. Scott, J.F. Scott. "Liquid source CVD". *Integr. Ferroelectr.*, 1992, **2**, 351.
- ¹¹⁰ L.E. Scriven "*Physics and application of dip-coating and spin-coating*". In *Better Ceramics Through Chemistry III*, ed. by C.J. Brinker, D.E. Clark, and D.R. Ulrich (Materials Research Society, Pittsburgh, 1988).
- ¹¹¹ R.W. Schwartz, J.A. Voigt, C.D. Buchheit and T.J. Boyle. "Densification and crystallization of zirconia thin films prepared by sol-gel processing". *Ceram. Trans. Ferroic Mater.: Design, Prep. Char.*, 1994, **43**, 145.
- ¹¹² R.W. Schwartz, T.L. Reichert, P.G. Clem, D. Dimos and D. Liu. "A comparison of diol and methanol-based chemical solution deposition routes for PZT thin film fabrication". *Integr. Ferroelectr.*, 1997, **18**, 275.
- ¹¹³ J.L. Keddie and E.P. Giannelis. "Effect of heating rate on the sintering of titanium-dioxide thin-films-Competition between densification and crystallization". *J. Am. Ceram. Soc.*, 1991, **74**, 2669.

- ¹¹⁴ A. Wu, P.M. Vilarinho, I. Reaney and I.M.M. Salvado. "Early stages of crystallisation of sol-gel-derived lead zirconate titanate thin films". *Chem. Mater.*, 2003, **15(5)**, 1147.
- ¹¹⁵ R.W. Schwartz. "Chemical solution deposition of perovskite thin films". *Chem. Mater.*, 1997, **9**, 2325.
- ¹¹⁶ E. Yamaka, H. Watanabe, H. Kimura, H. Kanaya, and H. Ohkuma. "Structural, ferroelectric and pyroelectric properties of highly c-axis oriented $\text{Pb}_{1-x}\text{Ca}_x\text{TiO}_3$ thin film grown by radio-frequency magnetron sputtering". *J. Vac. Sci. Technol. A*, 1988, **6(5)**, 2921.
- ¹¹⁷ H. Maiwa and N. Ichinose. "Preparation and properties of $(\text{Pb,Ca})\text{TiO}_3$ thin films by multiple-cathode sputtering". *Jpn. J. Appl. Phys.*, 1997, **36**, 5825.
- ¹¹⁸ M.J. Martín, J. Mendiola and C. Zaldo. "Influence of deposition parameters and substrates on the quality of pulsed-laser-deposited $\text{Pb}_{1-x}\text{Ca}_x\text{TiO}_3$ ferroelectric films". *J. Am. Ceram. Soc.*, 1998, **81**, 2542.
- ¹¹⁹ A. Tsuzuki, H. Murakami, K. Kani, K. Watari and Y. Torii. "Preparation and ferroelectric properties of sol-gel-derived $(\text{Pb,Ca})\text{TiO}_3$ thin films". *J. Mater. Sci. Lett.*, 1991, **10**, 125.
- ¹²⁰ R. Sirera, M.L. Calzada, F. Carmona and B. Jiménez. "Ferroelectric thin films of calcium modified lead titanate by sol-gel processing". *J. Mater. Sci. Lett.*, 1994, **13**, 1804.
- ¹²¹ R. Sirera, D. Leinen, E. Rodríguez-Castellón and M.L. Calzada. "Processing effects on the compositional depth profile of ferroelectric sol-gel Ca-PbTiO_3 thin films". *Chem. Mater.*, 1999, **11(12)**, 3437.
- ¹²² V.V. Shvartsman, M.L. Calzada, R. Poyato, L. Pardo and A.L. Kholkin. "Microstructure and local piezoelectric properties of $(\text{Pb,Ca})\text{TiO}_3$ thin films". *Ferroelectrics*, 2003, **296**, 229.
- ¹²³ A.L. Kholkin and M.L. Calzada. "Calcium modified lead titanate thin films for electromechanical applications". *J. Phys. IV*, 1998, **8**, 195.
- ¹²⁴ A. Seifert, P. Muralt and N. Setter. "High figure-of-merit porous $\text{Pb}_{1-x}\text{Ca}_x\text{TiO}_3$ thin films for pyroelectric applications". *Appl. Phys. Lett.*, 1998, **72(19)**, 2409.
- ¹²⁵ A. Seifert, L. Sagalowicz, P. Muralt and N. Setter. "Microstructural evolution of dense and porous pyroelectric $\text{Pb}_{1-x}\text{Ca}_x\text{TiO}_3$ thin films". *J. Mater. Res.*, 1999, **14**, 2012.
- ¹²⁶ D.S.L. Pontes, E.R. Leite, F.M. Pontes, E. Longo and J.A. Varela, "Microstructural, dielectric and ferroelectric properties of calcium-modified lead titanate thin films derived by chemical processes". *J. Eur. Ceram. Soc.*, 2001, **21**, 1107.
- ¹²⁷ Y. Torii, A. Tsuzuki and H. Murakami. "Sol-gel processing of highly orientated PbTiO_3 -based thin films". *J. Mater. Sci. Lett.*, 1994, **13**, 1364.
- ¹²⁸ R. Sirera and M.L. Calzada. "Multicomponent solutions for the deposition of modified lead titanate films". *Mater. Res. Bull.*, 1995, **30(1)**, 11.
- ¹²⁹ H. Li, X. Tang, Q. Li, Y. Liu, Z. Tang, Y. Zhang and D. Mo. "Optical functions of Ca-modified PbTiO_3 thin films determined by spectroscopic ellipsometry". *Solid State Commun.*, 2000, **114**, 347.
- ¹³⁰ H. Shen, J. Chen and G. Chen. "Seeding acceleration of perovskite crystallization in lead calcium titanate thin films". *J. Non-Cryst. Solids*, 1997, **220**, 231.

- ¹³¹ C.M. Wang, Y.T. Huang, Y.C. Chen, M.S. Lee and M.C. Kao. "Characterization of calcium-modified lead titanate thin films derived from a diol-based sol-gel process". *Jpn. J. Appl. Phys.*, 2000, **39**, 3579.
- ¹³² F.M. Pontes, D.S.L. Pontes, E.R. Leite, E. Longo, E.M.S. Santos, S. Mergulhao, A. Chiquito, P.S. Pizani, F. Lanciotti Jr., T.M. Boschi and J.A. Varela. "Influence of Ca concentration on the electric, morphological and structural properties of (Pb,Ca)TiO₃ thin films". *J. Appl. Phys.*, 2002, **91(10)**, 6650.
- ¹³³ F.M. Pontes, D.S.L. Pontes, E.R. Leite, E. Longo, A. J. Chiquito, M.A.C. Machado, P.S. Pizani and J.A. Varela. "A Raman and dielectric study of a diffuse phase transition in (Pb_{1-x}Ca_x)TiO₃ thin films". *Appl. Phys. A*, 2004, **78**, 349.
- ¹³⁴ S. Chewasatn and S.J. Milne. "Sol-gel synthesis and electrical characterization of (Pb,Ca)TiO₃ thin films". *J. Mater. Sci.*, 1997, **32(3)**, 575.
- ¹³⁵ D. Bao, X. Wu, L. Zhang and X. Yao. "Preparation, electrical and optical properties of (Pb,Ca)TiO₃ thin films using a modified sol-gel technique". *Thin Solid Films*, 1999, **350**, 30.
- ¹³⁶ D. Bao, L. Zhang, and X. Yao. "Compositionally step-varied (Pb,Ca)TiO₃ thin films with enhanced dielectric and ferroelectric properties". *Appl. Phys. Lett.*, 2000, **76(8)**, 1063.
- ¹³⁷ M.L. Calzada, I. Bretos, R. Jiménez, J. Ricote and J. Mendiola. "X-ray characterisation of chemical solution deposited PbTiO₃ films with high Ca doping". *Thin Solid Films*, 2004, **450(1)**, 211.
- ¹³⁸ <http://www.unep.org/Documents/Default.asp?DocumentID=78&ArticleID=1163>.
- ¹³⁹ T.W. Dekleva, J.M. Hayes, L.E. Cross and G.L. Geoffroy. "Sol-gel processing of lead titanate in 2-methoxyethanol investigations into the nature of the prehydrolyzed solutions". *J. Am. Ceram. Soc.*, 1988, **7(5)**, C-280.
- ¹⁴⁰ W. Sakamoto, Y. Yura, D. Kawasaki, T. Yogo and S.I. Hirano. "Chemical processing and properties of (Sr,Ca)₂(Nb,Ta)₂O₇ thin films". *Integr. Ferroelectr.*, 2002, **45**, 49.
- ¹⁴¹ M.H.M. Zai, A. Akiba, H. Goto, M. Matsumoto and E.M. Yeatman. "Highly (111) oriented lead zirconate titanate thin films deposited using a non-polymeric route". *Thin Solid Films*, 2001, **394(1-2)**, 97.
- ¹⁴² Y. Miyamoto, T. Tsuchiya, I. Yamaguchi, T. Manabe, H. Niino, A. Yabe, T. Kumagai, T. Tsuchiya and S. Mizuta. "Preparation of epitaxial Pb(Zr,Ti)O₃ thin films using coating pyrolysis process". *Appl. Surf. Sci.*, 2002, **197**, 398.
- ¹⁴³ Y. Suyama, T. Noritake and M. Nagasawa. "Formation of BaTiO₃ from a barium titanate isopropoxide complex". *Jpn. J. Appl. Phys.*, 1997, **36(9B)**, 5939.
- ¹⁴⁴ Y. Takahashi and Y. Matsuoka. "Dip-coating of TiO₂ films using a sol derived from Ti(O-i-Pr)₄-diethanolamine-H₂O-i-PrOH system". *J. Mater. Sci.*, 1988, **3**, 2259.
- ¹⁴⁵ K.D. Budd, S.K. Dey and D.A. Payne. "The effects of hydrolysis conditions on the characteristics of PbTiO₃ gels and thin films". In *Better Ceramics Through Chemistry II*, ed. by C.J. Brinker (Materials Research Society, Palo Alto, 1986).
- ¹⁴⁶ G. Yi and M. Sayer. "An acetic acid/water based sol-gel PZT process I: Modification of Zr and Ti alkoxide with acetic acid". *J. Sol-Gel Sci. Tech.*, 1996, **6**, 65.

- ¹⁴⁷ C.T. Lin, L. Li, J.S. Webb, M.S. Leung and R.A. Lipeles. "Deposition and characterization of photoconductive PZT thin films". *J. Electrochem. Soc.*, 1995, **142(6)**, 1957.
- ¹⁴⁸ B. Lee and J. Zhang. "Preparation, structure evolution and dielectric properties of BaTiO₃ thin films and powders by an aqueous sol-gel process". *Thin Solid Films*, 2001, **388**, 107.
- ¹⁴⁹ T. Asai, E.R. Camargo, M. Kakihana and M. Osada. "A novel aqueous solution route to the low-temperature synthesis of SrBi₂Nb₂O₉ by use of water-soluble Bi and Nb complexes". *J. Alloy. Compd.*, 2000, **309**, 113.
- ¹⁵⁰ J. Schäfer, W. Sigmund, S. Roy and F. Aldinger. "Low temperature synthesis of ultrafine Pb(Zr,Ti)O₃ powder by sol-gel combustion". *J. Mater. Res.*, 1997, **12(10)**, 2518.
- ¹⁵¹ Y. Narendar and G.L. Messing. "Synthesis, decomposition and crystallization characteristics of peroxy-citrato-niobium: an aqueous niobium precursor". *Chem. Mater.*, 1997, **9**, 580.
- ¹⁵² J. Livage, M. Henry and C. Sanchez. "Sol-gel chemistry of transition metal oxides". *Prog. Solid State Ch.*, 1988, **18**, 259.
- ¹⁵³ P. Gonnard and L. Simon-Seveyrat. "Environmentally conscious electroceramics". In *Conference Notes*, ed. by M. Kosec, D. Kuscer and B. Malic (Processing of Electroceramics, Bled, 2003).
- ¹⁵⁴ M.L. Calzada, L. Pardo, H. Guillon, I. Bretos, A. González, R. Poyato and R. Jiménez. "Low temperature CSD processing of ferroelectric thin films". In *Conference Notes*, ed. by M. Kosec, D. Kuscer and B. Malic (Processing of Electroceramics, Bled, 2003).
- ¹⁵⁵ E. Bescher, Y. Xu and J.D. McKenzie. "New low temperature multiphase ferroelectric films". *J. Appl. Phys.*, 2001, **89(11)**, 6341.
- ¹⁵⁶ T. Kijima, Y. Kawashima, Y. Idemoto and H. Ishiwara. "Effect of high pressure oxygen annealing on Bi₂SiO₅-added ferroelectric thin films". *Jpn. J. Appl. Phys.*, 2002, **41**, L1164.
- ¹⁵⁷ C.K. Kwoka and S.B. Desu. "Low temperature perovskite formation of lead zirconate titanate thin films by a seeding process". *J. Mater. Res.*, 1993, **8(2)**, 339.
- ¹⁵⁸ K. Maki, N. Soyama, S. Mori and K. Ogi. "Lowering of crystallisation temperature of sol-gel derived Pb(Zr,Ti)O₃ thin films". *Integr. Ferroelectr.*, 2000, **30**, 193.
- ¹⁵⁹ Y. Fujimori, T. Nakamura and H. Takasu. "Low-temperature crystallisation of sol-gel derived Pb(Zr,Ti)O₃ thin films". *Jpn. J. Appl. Phys.*, 1999, **38**, 5346.
- ¹⁶⁰ M.L. Calzada, A. González, R. Poyato and L. Pardo. "Photo-sensitive sol-gel solutions for the low-temperature UV-assisted processing of PbTiO₃ based ferroelectric thin films". *J. Mater. Chem.*, 2003, **13**, 1451.
- ¹⁶¹ M.L. Calzada, I. Bretos, R. Jiménez, H. Guillon and L. Pardo. "Low-temperature processing of ferroelectric thin films compatible with silicon integrated circuit technology". *Adv. Mater.*, 2004, **16(18)**, 1620.
- ¹⁶² H. Imai. "Ultraviolet (UV) irradiation". In *Handbook of Sol-gel Science and Technology. Processing, Characterization and Applications*, ed. by S. Sakka. "Volume I. Sol-gel Processing", ed. by H. Kozuka (Kluwer Academic Publishers, Boston, 2005).
- ¹⁶³ T. Ohishi, S. Maekawa and A. Katoh. "Synthesis and properties of tantalum oxide-films prepared by the sol-gel method using photoirradiation". *J. Non-Cryst. Solids*, 1992, **147**, 493.

- ¹⁶⁴ H. Imai and H. Hirashima. "Novel modification method of sol-gel thin films: densification of silica gel films with electronic excitation". *J. Ceram. Soc. Jpn.*, 1994, **102**, 1094.
- ¹⁶⁵ N. Hasakuma, H. Hirashima, T. Fukui, M. Toki, K. Awazu and H. Imai. "Photoreduction of amorphous and crystalline ZnO films". *Jpn. J. Appl. Phys.*, 2002, **41**, 3909.
- ¹⁶⁶ N. Hasakuma, T. Fukui, M. Toki, K. Awazu and H. Imai. "Photoinduced hydroxylation at ZnO surface". *Thin Solid Films*, 2003, **445**, 284.
- ¹⁶⁷ Y. Nakao, T. Nakamura, K. Hoshiba, K. Sameshima, A. Kamisawa, K. Abe, N. Soyama and K. Ogi. "Micro-patterning of $\text{PbZr}_x\text{Ti}_{1-x}\text{O}_3$ thin films prepared by photo sensitive sol-gel solution". *Jpn. J. Appl. Phys.*, 1993, **32**, 4141.
- ¹⁶⁸ N. Soyama, G. Sasaki, T. Atsuki, T. Yonezawa and K. Ogi. "Pattern of dielectric thin films from photo sensitive sol-gel solution". *Jpn. J. Appl. Phys.*, 1994, **33**, 5268.
- ¹⁶⁹ O. Soppera, C. Croutxé-Barghorn, C. Carré and D. Blanc. "Design of photoinduced relief optical devices with hybrid sol-gel materials." Pattern of dielectric thin films from photo sensitive sol-gel solution". *Appl. Surf. Sci.*, 2002, **186**, 91.
- ¹⁷⁰ S. Hirai, K. Shimakage, M. Sekiguchi, K. Wada and A. Nujui. "Zirconium oxide coating on anodized aluminum by sol-gel process combined with ultraviolet irradiation at ambient temperature". *J. Am. Ceram. Soc.*, 1999, **82(8)**, 2001.
- ¹⁷¹ Z.S. Guan. "Effects of UV irradiation on the intensity, structure and hydrophilicity of sol-gel TiO₂ films in high-humidity". *Acta Chimica Sinica*, 2003, **61(12)**, 2025.
- ¹⁷² J.Y. Zhang and I.W.Boyd. "Characterization of lead-zirconate-titanate (PZT) films formed by photo-decomposition of metal organic polymer". *Jpn. J. Appl. Phys.*, 1999, **38**, L393.
- ¹⁷³ T. Hayashi and D. Togawa. "Preparation and properties of $\text{SrBi}_2\text{Ta}_2\text{O}_9$ ferroelectric thin films using excimer UV irradiation and seed layer". *J. Appl. Phys.*, 2001, **40**, 5585.
- ¹⁷⁴ T. Hayashi, N. Iizawa, D. Togawa, M. Yamada, W. Sakamoto, K. Kikuta and S.I. Hirano. "Excimer UV processing of $(\text{Bi,Nd})_4\text{Ti}_3\text{O}_{12}$ ferroelectric thin films by chemical solution deposition method". *Jpn. J. Appl. Phys.*, 2003, **42**, 5981.
- ¹⁷⁵ A. Hardy, D. Nelis, G. Vanhoyland, M.K. Van Bael, J. Mullens, L.C. Van Poucke, J. D'Haen and D.J. Wouters. "Aqueous CSD of ferroelectric $\text{Bi}_{3.5}\text{La}_{0.5}\text{Ti}_3\text{O}_{12}$ (BLT) thin films". *Integr. Ferroelectr.*, 2004, **62**, 205.
- ¹⁷⁶ I. Bretos, J. Ricote, R. Jiménez, J. Mendiola and M.L. Calzada. "Processing of chemical solution deposited Ca-modified PbTiO_3 films for high frequency components and dynamic random access memories". *Integr. Ferroelectr.*, 2004, **61**, 105.
- ¹⁷⁷ S.J. Milne and S.H. Pyke. "Modified sol-gel process for the production of lead titanate films". *J. Am. Ceram. Soc.*, 1991, **74(6)**, 1407.
- ¹⁷⁸ A. Hardy, K. Van Werde, G. Vanhoyland, M.K. Van Bael, J. Mullens and L.C. Van Poucke. "Study of the decomposition of an aqueous metal-chelate gel precursor for $(\text{Bi,L a})_4\text{Ti}_3\text{O}_{12}$ by means of TGA-FTIR, TGA-MS and HT-DRIFT". *Thermochim. Acta*, 2003, **397(1-2)**, 143.
- ¹⁷⁹ M. Kourgiantakis, M. Matzapetakis, C.P. Raptopoulou, A. Terzis and A. Salifoglou. "Lead-citrate chemistry. Synthesis, spectroscopic and structural studies of a novel lead(II)-citrate aqueous complex". *Inorg. Chim. Acta*, 2000, **297**, 134.

- ¹⁸⁰ T. Li, Y. Zhu, S.B. Desu, C-H. Peng and M. Nagata. "Properties of SrBi₂Ta₂O₉ ferroelectric thin films prepared by a modified metalorganic solution deposition technique" *Appl. Phys. Lett.*, 1996, **68(5)**, 616.
- ¹⁸¹ D.C Bradley, R.C. Mehrotra, I.P. Rothwell and A. Singh. "Alkoxo and Aryloxo Derivatives of Metals" (Academic Press, London, 2001).
- ¹⁸² N.J. Philipps, S.J. Milne, N.J. Ali and J.D. Kennedy. "A preliminary Nuclear Magnetic resonance investigation of the titanium diisopropoxide bis(2,4-pentadionate) propanediol sol-gel precursor system". *J. Mater. Sci. Lett.*, 1994, **13**, 1535.
- ¹⁸³ M.L. Calzada, R. Sirera, F. Carmona and B. Jiménez. "Investigations of a diol-based sol-gel process for the preparation of lead titanate materials". *J. Am. Ceram. Soc.*, 1995, **78(7)**, 1802.
- ¹⁸⁴ Y.L Tu, M.L. Calzada, N.J. Phillips and S.J. Milne. "Synthesis and electrical characterization of thin films of PT and PZT made from a diol-based sol-gel route". *J. Am. Ceram. Soc.*, 1996, **79(2)**, 441.
- ¹⁸⁵ R. Sirera. "Síntesis por sol-gel de soluciones de titanato de plomo modificado para la preparación de láminas delgadas ferroeléctricas". Tesis doctoral. Univ. Autónoma de Madrid (1997).
- ¹⁸⁶ M. Algueró. "Relaciones entre la microestructura y las propiedades de láminas delgadas ferroeléctricas de (Pb, La)TiO₃". Tesis doctoral. Univ. Autónoma de Madrid (1998).
- ¹⁸⁷ M.L. Calzada, M. Algueró and L. Pardo. "Chemistry-crystallization-microstructure relations of sol-gel derived lanthanum modified lead titanate thin films". *J. Sol-Gel Sci. Techn.*, 1998, **13**, 837.
- ¹⁸⁸ A. González. "Láminas delgadas y ultradelgadas de tantalato de estroncio y bismuto obtenidas a partir de derivados de glicolato de tántalo para su uso en memorias ferroeléctricas no volátiles". Tesis doctoral. Univ. Autónoma de Madrid (2002).
- ¹⁸⁹ M.L. Calzada, M.J. Martín, P. Ramos, J. Mendiola, R. Sirera, M.F. Da Silva and J.C Soares. "Effect of compositions and annealing conditions on the properties of sol-gel prepared calcium-modified lead titanate thin films". *J. Phys. Chem. Solids*, 1997, **58(7)**, 1033.
- ¹⁹⁰ S. Sakka. "Viscosity and spinnability of gelling solutions". In "Handbook of Sol-gel Science and Technology. Processing, Characterization and Applications", ed. by S. Sakka. "Volume II. Characterization and Properties of Sol-gel Materials and Products", ed. by R.M. Almeida (Kluwer Academic Publishers, Boston, 2005).
- ¹⁹¹ J.M. Albella, A.M. Cintas, T. Miranda, J.M. Serratosa. "Introducción a la Ciencia de los Materiales" (CSIC, Madrid, 1993).
- ¹⁹² B.P. Straughan and S. Walker. "Spectroscopy. Volume 2" (Chapman & Hall, London, 1976).
- ¹⁹³ J.M. Albella. "Láminas Delgadas y Recubrimientos. Preparación, Propiedades y Aplicaciones" (CSIC, Madrid, 2003).
- ¹⁹⁴ R. Pecora, "Dynamic Light Scattering: Applications of Photon Correlation Spectroscopy" (Plenum Press, New York, 1985).
- ¹⁹⁵ B.J. Berne and R. Pecora, "Dynamic Light Scattering with Applications to Chemistry, Biology and Physics" (Wiley-Interscience, New York, 1976).
- ¹⁹⁶ E.N. Kaufmann "Characterization of Materials. Volume 1" (Wiley-Interscience, New York, 2003).

- ¹⁹⁷ J. Mullens. "EGA-Evolved gas analysis". In "Handbook of Thermal Analysis and Calorimetry. Volume I. Principles and Practice", ed. by M.E. Brown (Elsevier Science, Amsterdam, 1998).
- ¹⁹⁸ R. Singh. "Rapid isothermal processing". *J. Appl. Phys.*, 1988, **63(8)**, R59.
- ¹⁹⁹ Web page of JIPELEC division, QUALIFLOW. Available at <http://www.jipelec.com/index.htm>.
- ²⁰⁰ H.Y. Lee and H.G. Kim. "Chemical vapor-deposition of PbTiO₃ films onto TiO₂-Si" *J. Mater. Sci-Mater. El.*, 1991, **2(3)**, 183.
- ²⁰¹ D.E. Bornside, C.W. Macosko and L.E. Scriven. "On the modeling of spin coating". *J. Imag. Technol.*, 1987, **13(4)**, 122.
- ²⁰² J. Mendiola, M.L. Calzada, P. Ramos, M.J. Martín and F. Agulló-Rueda. "On the effects of stresses in ferroelectric (Pb,Ca)TiO₃ thin films". *Thin Solid Films*, 1998, **315**, 195.
- ²⁰³ W.K. Chu, J.M. Mater and M.A. Nicolet. "Backscattering Spectroscopy" (Academic Press, New York, 1978).
- ²⁰⁴ F.J. García Lopez, F.J. Ager, M. Barbadillo, F.J. Madrigal, M.A. Ontalba, M.A. Respaldiza and M.D. Ynsa. "CNA: the first accelerator-based IBA facility in Spain". *Nucl. Instrum. Meth. B.*, 2000, **B161-B163**, 1137
- ²⁰⁵ L.R. Doolittle. "A semiautomatic algorithm for Rutherford backscattering analysis". *Nucl. Instrum. Meth. B*, 1986, **15(1-6)**, 227.
- ²⁰⁶ SIMRA version 5.0. M. Mayer. Max-Planck-Institut für Plasmaphysik, 1997-2002.
- ²⁰⁷ M. Faraldos, C. Goberna. "Técnicas de Análisis y Caracterización de Materiales" (CSIC, Madrid, 2002).
- ²⁰⁸ R.A. Vaia, M.S. Weathers and W.A. Basset. "Anomalous peaks in grazing incidence thin film X-ray diffraction". *Powder Diffr.*, 1994, **9(1)**, 44.
- ²⁰⁹ F.A. Jenkins and H.E. White. "Fundamentals of Optics" (Mc Graw-Hill. Tokyo, 1976).
- ²¹⁰ B.K. Vainshtein. "Modern Crystallography I" (Springer-Verlag, Berlin, 1981).
- ²¹¹ J.I. Goldstein, D.E. Newbury, P. Echlin, D.C. Joy, C. Fiori and E. Lifshin. "Scanning Electron Microscopy and X-Ray Microanalysis" (Plenum Press, New York, 1981).
- ²¹² D.B. Williams and C.B. Carter. "Transmission Electron Microscopy" (Plenum Press, New York, 1996).
- ²¹³ R. Jiménez, A. González, M.L. Calzada and J. Mendiola. "Study of electrolytic laminated ferroelectric thin films from electroded substrates". *J. Mater. Res.*, 2000, **15(5)**, 1041.
- ²¹⁴ S.V. Kalinin, R. Shao and D.A. Bonnell. "Local phenomena in oxides by advanced scanning probe microscopy". *J. Am. Ceram. Soc.*, 2005, **88(5)**, 1077.
- ²¹⁵ H. Bässler. "Optical Techniques to Characterize Polymer Systems" in "Brillouin Spectroscopy and its Application to Polymers" ed. by J.K. Krüger (Elsevier, Amsterdam, 1989).
- ²¹⁶ M. Montagna. "Characterisation of sol-gel materials by Raman and Brillouin spectroscopies". In "Handbook of Sol-gel Science and Technology. Processing, Characterization and Applications", ed. by S. Sakka. "Volume II. Characterization and Properties of Sol-gel Materials and Products", ed. by R.M. Almeida (Kluwer Academic Publishers, Boston, 2005).

- ²¹⁷ J.K. Krüger, C. Ziebert, H. Schmitt, B. Jiménez and C. Bruch. "Evidence of an elastic instability between the amorphous and the microcrystalline state of Ca-modified lead titanate as revealed by Brillouin spectroscopy". *Phys. Rev. Lett.*, 1997, **78**, 2240.
- ²¹⁸ R.J. Jiménez-Riobóo, M.L. Calzada, J.K. Krüger and P. Alnot. "Elastic properties by Brillouin spectroscopy of sol-gel (Pb,Ca)TiO₃ films". *J. Appl. Phys.*, 1999, **85(10)**, 7349.
- ²¹⁹ M. Cardona and Guntherodt. "Topics in Applied Physics vol. 51" in "Light Scattering in Solids III" ed. by J.R. Sandercock. (Springer, Berlin, 1982).
- ²²⁰ J.K. Krüger, J. Ems, J. Brierley and R.J. Jiménez-Riobóo. "A new Brillouin scattering technique for the investigation of acoustic and opto-acoustic properties: application to polymers". *J. Phys. D Appl. Phys.*, 1998, **31**, 1913.
- ²²¹ J.F. Scott. "Ferroelectric Memories" (Springer, Heilderberg, 2000).
- ²²² M.L. Calzada, A. Gonzalez, J. García-López and R. Jiménez. "Crystallization, heterostructure, microstructure, and properties of ferroelectric strontium bismuth tantalate films derived from tantalum glycolate solutions". *Chem. Mater.*, 2003, **15**, 4775.
- ²²³ P. Ramos "Estudio de la ferroelectricidad en láminas delgadas de titanato de plomo modificados, obtenidas por sol-gel". Tesis doctoral. Univ. Autónoma de Madrid (1996).
- ²²⁴ L. Pardo, J. Mendiola and C. Alemany. "Theoretical treatment of ferroelectric composites using Monte-Carlo calculations". *J. Appl. Phys.*, 1988, **64(10)**, 5092.
- ²²⁵ M. Alexe and A. Gruverman. "Nanoscale Characterisation of Ferroelectric Materials: Scanning Probe Microscopy Approach" (Springer-Verlag, Berlin, 2003).
- ²²⁶ A. Gruverman, O. Auciello, R. Ramesh and H. Tokumoto "Scanning force microscopy of domain structure in ferroelectric thin films: imaging and control". *Nanotechnology*, 1997, **8**, A38.
- ²²⁷ R. Dat, D.J. Lichtenwalner, O. Auciello and A.I. Kingon. "Polycrystalline La_{0.5}Sr_{0.5}CoO₃ PbZr_{0.53}Ti_{0.47}O₃ La_{0.5}Sr_{0.5}CoO₃ ferroelectric capacitors on platinized silicon with no polarization fatigue". *Appl. Phys. Lett.*, 1994, **64(20)**, 2673.
- ²²⁸ R. Jiménez, P. Ramos, M.L. Calzada and J. Mendiola. "Piroelectricidad en láminas delgadas de titanato de plomo". *Bol. Soc. Esp. Ceram. V.*, 1998, **37(2-3)**, 117.
- ²²⁹ M. Yoshimura. "Importante of soft solution processing for advanced inorganic materials". *J. Mater. Res.*, 1998, **13(4)**, 796.
- ²³⁰ K. Van Werde, D. Mondelaers, G. Vanhoyland, D. Nelis, M.K. Van Bael, J. Mullens, and L.C. Van Poucke. "Thermal decomposition of the ammonium zinc acetate citrate precursor for aqueous chemical solution deposition of ZnO". *J. Mater. Sci.*, 2002, **37**, 81.
- ²³¹ M.L. Calzada, B. Malic, R. Sirera and M. Kosec. "Thermal-decomposition chemistry of modified lead-titanate aquo-diol gels used for the preparation of thin films". *J. Sol-Gel Sci. Techn.*, 2002, **23**, 221.
- ²³² S. Javoric, M. Kosec and B. Malic. "Water-based synthesis of La_{0.5}Sr_{0.5}CoO₃ (LSCO) electrodes for ferroelectric thin films". *Integr. Ferroelectr.*, 2000, **30**, 309.
- ²³³ D. Nelis, M.K. Van Bael, H. Van den Rul, J. Mullens, L.C. Van Poucke, G. Vanhoyland, , J. D'Haen, W. Laureyn and D.J. Wouters. "Ferroelectric SrBi₂Nb₂O₉ thin films by aqueous chemical solution deposition". *Integr. Ferroelectr.*, 2002, **45**, 205.

- ²³⁴ D. Van Genechten. *Internal report*. Laboratory of Inorganic and Physical Chemistry of the University of Hasselt, at Diepenbeek (Belgium).
- ²³⁵ J. Mendiola, C. Alemany, R. Jiménez, E. Maurer and M.L. Calzada. "Ca modified PbTiO₃: from the bulk ceramic to the film". *Bol. Soc. Esp. Ceram. V.*, 2004, **43(3)**, 620.
- ²³⁶ D. Bao, X. Wu, L. Zhang and X. Yao. "Preparation, electrical and optical properties of (Pb,Ca)TiO₃ thin films using a modified sol-gel technique". *Thin Solid Films*, 1999, **350**, 30.
- ²³⁷ P. Ramos, J. Mendiola, F. Carmona, M.L. Calzada and C. Alemany. "Effect of electrical treatment on the polarization of modified PbTiO₃ thin films". *Phys. Status Solidi. A*, 1996, **156(1)**, 119.
- ²³⁸ I.W. Boyd and J.Y. Zhang. "Photo-induced growth of dielectrics with excimer lamps". *Solid. State Electron.*, 2001, **45**, 1413.
- ²³⁹ K.M. Rittenmeyer and R.Y. Ting. "Piezoelectric and dielectric properties of calcium and samarium modified lead titanate ceramics for hydroacoustic applications". *Ferroelectrics*, 1990, **110**, 171.
- ²⁴⁰ I. Bretos, J. Ricote, R. Jiménez, J. Mendiola, R. Jiménez-Rioobó and M.L. Calzada. "Crystallisation of Pb_{1-x}Ca_xTiO₃ ferroelectric thin films as a function of the Ca²⁺ content". *J. Eur. Ceram. Soc.*, 2005, **25**, 2325.
- ²⁴¹ D. Leinen, R. Sirera, E. Rodríguez-Castellón and M.L. Calzada. "XPS depth profile análisis of sol-gel calcium-modified lead titanate thin films". *Thin Solid Films*, 1999, **354**, 66.
- ²⁴² D. Leinen, A. Fernández, J.P. Espinós and A.R. González-Elipse. "XPS and ISS study of NiTiO₃ and PbTiO₃ subjected to low-energy ion-beam bombardment. I. Influence of the type of ion (Ar⁺ or O₂⁺)". *Surf. Interface Anal.*, 1993, **20**, 941.
- ²⁴³ C.S. Gopinath, S.G. Hegde, A.V. Ramaswamy and S. Mahapatra. "Photoemission studies of polymorphic CaCO₃ materials". *Mater. Res. Bull.*, 2002, **37**, 1323.
- ²⁴⁴ K.S. Kim, T.J. O'Learly and N. Winograd. "X-ray photoelectron spectra of lead oxides". *Anal. Chem.*, 1973, **45**, 2214.
- ²⁴⁵ D.L. Blachard Jr. and D.R. Baer. "The interactions of Co, Mn and water with calcite surfaces". *Surf. Sci.*, 1992, **276**, 27.
- ²⁴⁶ V.I. Bukhtiyarov, A.I. Nizovskii, H. Bluhm, M. Hävecker, E. Kleimenov, A. Knop-Gericke and R. Schlögl. "Combined in situ XPS and PTRMS study of ethylene epoxidation over silver". *J. Catal.*, 2006, **238**, 260.
- ²⁴⁷ L. Pardo, M.L. Calzada, S.J. Milne, J. Ricote and B. Jiménez. "Microstructure development of diol-based sol-gel processed lead titanate thin films". *J. Phys. Chem. Solids*, 1995, **56(1)**, 15.
- ²⁴⁸ J. Ricote, D.L. Corker, R.W. Whatmore, S.A. Impey, A.M. Glazer, J. Dec and K. Roleder. "A TEM and neutron diffraction study of the local structure in the rhombohedral phase of lead zirconate titanate". *J. Phys. Condens. Matter*, 1998, **10**, 1767.
- ²⁴⁹ D.L. Corker, A.M. Glazer, R.W. Whatmore, A. Stallard and F. Fauth. "A neutron diffraction investigation into the rhombohedral phases of the perovskite series PbZr_{1-x}Ti_xO₃". *J. Phys. Condens. Matter*, 1998, **10**, 6251.
- ²⁵⁰ F.W. Martín. "Metastable cubic form of lead titanate observed in titania nucleated glass ceramics". *Phys. Chem. Glasses*, 1965, **6(4)**, 143.

- ²⁵¹ M.A. Subramanian, G. Aravamudan and G.V. Subba Rao. "Oxide pyrochlores. A review". *Prog. Solid State Ch.*, 1983, **15**, 55.
- ²⁵² J.I. Langford and J. Tapia. "X-ray diffraction studies of thin gold films using the variance method". *J. Appl. Cryst.*, 1974, **7**, 421.
- ²⁵³ C.J. Brinker and G.W. Scherer. "*Sol-gel Science*" (Academic Press, Boston, 1990).
- ²⁵⁴ C.C. Hsueh and M.L. Mecartney. "Microstructural development and electrical properties of sol-gel prepared lead zirconate-titanate thin films". *J. Mater. Res.*, 1991, **6 (10)**, 2208.
- ²⁵⁵ S.D. Ramamurthi and D.A. Payne. "Structural investigations of prehydrolyzed precursors used in the sol-gel processing of lead titanate". *J. Am. Ceram. Soc.*, 1990, **73(8)**, 2547.
- ²⁵⁶ K. Nakamoto. "*Infrared and Raman Spectra of Inorganic and Coordination Compounds*" (John Wiley & Sons, New York, 1997).
- ²⁵⁷ C.D.E. Lakeman and D.A. Payne. "Processing effects in the sol-gel preparation of PZT dried gels, powders and ferroelectric thin layers". *J. Am. Ceram. Soc.*, 1992, **75(11)**, 3091.
- ²⁵⁸ C.D.E. Lakeman, X. Zhengkui and D.A. Payne. "On the evolution of structure and composition in sol-gel derived lead zirconate titanate thin layers". *J. Mater. Res.*, 1995, **10(8)**, 2042.
- ²⁵⁹ A.G. Fredrickson. "*Principles and Applications of Rheology*" (Prentice-Hall, Englewood Cliffs, New Jersey, 1964).
- ²⁶⁰ R.A. Assink and R.W. Schwartz. "¹H and ¹³C NMR investigations of Pb(Zr,Ti)O₃ thin-film precursor solution". *Chem. Mater.*, 1993, **5**, 511.
- ²⁶¹ D. Hennings, G. Rosenstein and H. Schreinemacher. "Hydrothermal preparation of barium titanate from barium-titanium acetate gel precursors". *J. Eur. Ceram. Soc.*, 1991, **8**, 107.
- ²⁶² S.S. Sengupta, L. Ma, D.L. Adler and D.A. Payne. "Extended x-ray absorption fine structure determination of local structure in sol-gel-derived lead titanate, lead zirconate, and lead zirconate titanate". *J. Mater. Res.*, 1995, **10(6)**, 1345.
- ²⁶³ E.I. Tsyganova and L.M. Dyagileva. "The reactivity of metal β-diketonates in the thermal decomposition reaction". *Russian Chemical Reviews*, 1996, **65(4)**, 315.
- ²⁶⁴ R. Jiménez, I. Bretos, J. Ricote, C. Alemany, M.L. Calzada and J. Mendiola. "Size effects on Pb_{0.5}Ca_{0.5}TiO₃ thin films". *J. Eur. Ceram. Soc.*, 2005, **25(12)**, 2319.
- ²⁶⁵ R.W. Schwartz, T.J. Boyle, S.J. Lockwood, M.B. Sinclair, D. Dimos and C.D. Buchheit. "Sol-gel processing of PZT thin-films. A review of the state-of-the-art and process optimization strategies". *Integr. Ferroelectr.*, 1995, **7(1-4)**, 259.
- ²⁶⁶ K. Kushida, K.R. Udayakumar, S.B. Krupadinhi and L.E. Cross. "Origin of orientation in sol-gel-derived lead titanate films". *J. Am. Ceram. Soc.*, 1993, **76(5)**, 1345.
- ²⁶⁷ K. Nashimoto, M.J. Cima, P.C. McIntyre and W.E. Rhine. "Microstructure development of sol-gel derived epitaxial LiNbO₃ thin-films". *J. Mater. Res.*, 1995, **10(10)**, 2564.
- ²⁶⁸ C. Chen, D.F. Ryder Jr., and W.A. Spurgeon. "Synthesis and microstructure of highly oriented lead titanate thin-films prepared by a sol-gel method". *J. Am. Ceram. Soc.*, 1989, **72(8)**, 1495.
- ²⁶⁹ W.H. Shih and Q. Lu. "Ultrafine titanate powders processed via a precursor-modified sol-gel method". In *Amorphous Insulating Thin Films*, ed. by J. Kanicki, W.L. Warren, R.A.B. Devine and M. Matsumura (Materials Research Society, Pittsburgh, 1993).

- ²⁷⁰ R.W. Schwartz, J.A. Voigt, B.A. Tuttle, D.A. Payne, T.L. Reichert and R.S. DaSalla. "Comments on the effects of solution precursor characteristics and thermal processing conditions on the crystallization behaviour of sol-gel derived lead zirconate titanate thin films". *J. Mater. Res.*, 1997, **12(2)**, 444.
- ²⁷¹ J. Ricote, R. Poyato, M. Algueró, L. Pardo and M.L. Calzada. "Texture development in modified lead titanate thin films obtained by chemical solution deposition on silicon-based substrates". *J. Am. Ceram. Soc.*, 2003, **86(9)**, 1571.
- ²⁷² Y. Xu and J. Mackenzie. "Ferroelectric thin films prepared by sol-gel processing". *Integr. Ferroelectr.*, 1992, **1**, 17.
- ²⁷³ G. Yi and M. Sayer. "Sol-gel processing of complex oxide films". *Am. Ceram. Soc. Bull.*, 1991, **70(7)**, 1173.
- ²⁷⁴ K. Kato, K. Suzuki, D.S. Fu, K. Nishizawa and T. Miki. "Chemical approach using tailored liquid sources for traditional and novel ferroelectric thin films". *Jpn. J. Appl. Phys.*; Part 1, 2002, **41(11B)**, 6829.
- ²⁷⁵ A. González, R. Jiménez, J. Mendiola, C. Alemany and M.L. Calzada. "Ultrathin ferroelectric strontium bismuth tantalate films". *Appl. Phys. Lett.*, 2002, **81(14)**, 2599.
- ²⁷⁶ G.A.C.M Spierings, G.J.M. Dormans, W.G.J. Moors, M.J.E. Ulenaers and P.K. Larsen. "Stresses in Pt/Pb(Zr,Ti)O₃/Pt thin-film stacks for integrated ferroelectric capacitors". *J. Appl. Phys.*, 1995, **78**, 1926.
- ²⁷⁷ J.G. Cheng, X.J. Meng, B. Li, J. Tang, S.L. Guo, J.H. Chu, M. Wang, H. Wang and Z. Wang. "Ferroelectricity in sol-gel derived Ba_{0.8}Sr_{0.2}TiO₃ thin films using a highly diluted precursor solution". *Appl. Phys. Lett.*, 1999, **75(14)**, 2132.
- ²⁷⁸ S. Hoffman and R.M. Waser. "Dielectric properties, leakage behaviour, and resistance degradation of thin films of the solid solution series Ba(Ti_{1-y}Zr_y)O₃". *Integr. Ferroelectr.*, 1997, **17**, 141.
- ²⁷⁹ D. Dimos and C. H. Mueller. "Perovskite thin films for high-frequency capacitor applications". *Ann. Rev. Mater. Sci.*, 1998, **28**, 397.
- ²⁸⁰ J.Y. Zhang and I.W. Boyd. "Efficient XeI* excimer ultraviolet sources from a dielectric barrier discharge". *J. Appl. Phys.*, 1998, **84**, 1174.
- ²⁸¹ N. Tohge, K. Shinmou and T. Minami. "Effects of UV-irradiation on the formation of oxide thin films from chemically modified metal-alkoxides". *J. Sol-Gel Sci. Techn.*, 1994, **2**, 581.
- ²⁸² European project **BRPR-CT98-0777**. "Microfabrication with UltraViolet-Assisted Sol-Gel Technology (MUVAST)".
- ²⁸³ L. Pardo, R. Poyato, A. González and M.L. Calzada. "Low temperature preparation of piezoelectric thin films by ultraviolet-assisted rapid thermal processing". *Mat. Sci. Semicon. Proc.*, 2002, **5(2-3)**, 77.
- ²⁸⁴ A. González, R. Poyato, L. Pardo and M.L. Calzada. "Photo-activated Ca-PbTiO₃ solutions for the preparation of films at low temperatures". *Ferroelectrics*, 2002, **271**, 1635.
- ²⁸⁵ D.W. Barnum. "Electronic absorption spectra of acetyl-acetonato complexes - I". *J. Inorg. Nucl. Chem.*, 1961, **21**, 221

-
- ²⁸⁶ I.W. Boyd and J.Y. Zhang. "Low temperature photoformation of tantalum oxide". *Microelectron. Reliab.*, 2000, **40(4-5)**, 649.
- ²⁸⁷ M. Brinkmann, V.Z.H. Chan and E.L. Thomas. "Room-temperature synthesis of a-SiO₂ thin films by UV-assisted ozonolysis of a polymer precursor". *Chem. Mater.*, 2001, **13**, 967.
- ²⁸⁸ Y. Zhang, R.H. Terril and P.W. Bohn. "Ultraviolet photochemistry and ex-situ ozonolysis of alkanethiol self-assembled monolayers on gold". *Chem. Mater.*, 1999, **11**, 2191.
- ²⁸⁹ A.I. Akimov, V.V. Panevchik and G.K. Savchuk. "Kinetics of lead-oxide volatilization from pressed LZT ceramics". *Inorg. Mater.*, 1994, **30(9)**, 1103.
- ²⁹⁰ N.A. Basit, H.K. Kim and J. Blachere "Temperature dependence of lead loss in rf magnetron sputtering of a stoichiometric Pb(Zr,Ti)O₃ target". *Thin Solid Films*, 1997, **302**, 155.
- ²⁹¹ S.-Y. Chen, I.-W. Chen. "Texture development, microstructure evolution and crystallisation of chemically derived PZT thin films". *J. Am. Ceram. Soc.*, 1998, **81**, 97.
- ²⁹² Z. Huang, Q. Zang and R.W. Whatmore. "The role of an intermetallic phase on the crystallisation of sol-gel processed lead zirconate titanate thin films". *J. Mater. Sci. Lett.*, 1998, **17**, 1157.
- ²⁹³ R. Jiménez, M.L. Calzada and J. Mendiola. "Conditioning effects on RTP (Pb,Ca)TiO₃ thin films". *Thin Solid Films*, 1998, **335**, 292.
- ²⁹⁴ H. Imai, A. Tominaga, H. Hirashima, M. Toki and N. Asakuma. "Ultraviolet-reduced reduction and crystallization of indium oxide films". *J. Appl. Phys.*, 1999, **85(1)**, 203.
- ²⁹⁵ J. Mendiola, R. Jiménez, P. Ramos, I. Bretos and M.L. Calzada. "Dielectric properties of Pb_{0.5}Ca_{0.5}TiO₃ thin films". *J. Appl. Phys.*, 2005, **98**, 024106-1.